Tribocorrosion of Total Hip Replacements

by

James Edward Tilston Hesketh

Submitted in accordance with the requirements for the degree of

Doctor of Philosophy

The University of Leeds

School of Mechanical Engineering

December 2012

The candidate confirms that the work submitted is his own, except where work which has formed part of jointly authored publications has been included. The contribution of the candidate and the other authors to this work has been explicitly indicated below. The candidate confirms that appropriate credit has been given within the thesis where reference has been made to the work of others.

In all papers, the primary author completed paper drafting and experimental measurements. All authors listed on the paper completed proof reading and amendments prior to paper submission. Elastohydrodynamic film modelling was run by Dr Qingen Meng. Transmission electron microscope sample preparation and operation was undertaken by Dr Michael Ward.

Papers contributing to this thesis

James Hesketh, Xinming Hu, Duncan Dowson, Anne Neville, *Tribocorrosion reactions between metal-on-metal and metal-on-polymer surfaces for total hip replacement*, Proceedings of the Institution of Mechanical Engineers, Part J: Journal of Engineering Tribology, 2012, 226, p.p.564-574, 2012

Featured in Chapters 3-5 and 10

James Hesketh, Xinming Hu, Yu Yan, Duncan Dowson, Anne Neville, *Biotribocorrosion: Some electrochemical observations from an instrumented Hip Joint Simulator,* Tribology International, **59**, p.p. 332-339, 2013

Featured in Chapters 6-10

Yu Yan, Anne Neville, James Hesketh, Duncan Dowson, *Real-time corrosion measurements to assess biotribocorrosion mechanisms with a hip simulator,* In press - Tribology International, 2012

Featured in Chapters 6-8 and 10

James Hesketh, Qingen Meng, Duncan Dowson, Anne Neville, *Biotribocorrosion of metal-on-metal hip replacements: How surface degradation can influence metal ion formation,* Submitted to the Leeds-Lyon special issue of Tribology international, 2012

Featured in Chapters 6-10

James Hesketh, Michael Ward, Duncan Dowson, Anne Neville, *The Composition of Tribo-films Produced in Metal-on-Metal Hip Bearings,* pending submission

Featured in Chapters 9-10

Acknowledgements

I am deeply grateful to my primary supervisor Professor Anne Neville with whom it has been a privilege to work. Her patient guidance and enthusiastic encouragement, throughout all the highs and lows, not only made this work possible, but also made it enjoyable.

I would like to thank Professor Duncan Dowson for his supervision and support. His insightful comments and advice throughout our many meetings have been an enormous contribution to this work. I am also indebted to my two former supervisors, Dr Yu Yan and Dr Xinming Hu, whose advice and support helped form the foundation of this study.

I would like to thank Dr Qingen Meng for his generous help in the running of elastohydrodynamic lubrication simulations and Dr Michael Ward for his help regarding the use of transmission electron microscopy. The discussions with Professor Rik Brydson on the interpretation of electron energy loss spectrographs have been great help, for which I am very grateful.

I would like to thank the IETSI and IMBE technicians for their continuous help with the preparation and smooth operation of the experimental laboratory work. In addition, I am indebted to the secretaries and receptionists and IT staff in mechanical engineering who have helped in many ways over the past three years, in particular Jackie Kidd and Fiona Slade, Graham Blyth, Ted Allwood, Margret Gibson and Jane Tillotson.

I would also like to thank my fellow members of Professor Neville's research group for making a great working environment that has been both entertaining and educational, and has been a pleasure to be a part of.

Finally, I would like to thank my close friends and family for their positive influence throughout the duration of my studies. The encouragement and support of my mother, father and sister have helped me more than I can say, and I am truly grateful.

Abstract

The performance of metal-on-metal total hip replacements is largely determined by their propensity to degrade *in vivo*. Degradation occurs through the complex interactions between wear and corrosion (termed tribocorrosion) and leads to the production of metallic particulate debris and metallic ions. The interaction of these degradation products with the body can lead to serious health complications, within patients, and is an important factor in determining the success of prostheses.

Testing was undertaken on a reciprocating pin-on-plate tribometer and a single station hip joint simulator. Each test rig was instrumented, with a 3-electrode electrochemical cell, to enable *in-situ* corrosion monitoring during tribological testing. Testing was focused around 36mm metal-on-metal bearing surfaces in both saline and bovine serum solutions but consideration was also given to metal-on-polymer interfaces.

Corrosion was found to contribute substantially to material degradation within metal-on-metal contacts, both in the tribometer and in the hip simulator. Within metal-on-polymer interfaces, the material degradation, due to corrosion, was negligible when compared with metal-on-metal surfaces. *In-situ* corrosion measurements were influenced by the variance in tribological conditions of the bearing. These unique findings enabled, for the first time, observations of both the corrosion and tribological performance of the bearing to be assessed in real-time.

Contents

List of Figures

Nomenclature

Chapter 2

M – Metal species

n – Valence number

G – Gibbs Free energy

G_0 – Standard free energy of a cell reaction

R – Ideal gas constant

T – Temperature

F – Faraday constant

E – Potential difference between two half-cells

E_0 – Standard potential difference across a cell

Λ – Lambda ratio

h_{min} – Minimum lubricating/elastohydrodynamic film thickness

R_a – Average surface roughness

η – Dynamic viscosity

η_0 - Standard dynamic viscosity

α – pressure viscosity coefficient

p – Pressure

H_{min} – Dimensionless minimum elastohydrodynamic film thickness

U - Dimensionless speed parameter ($\eta_0 u/E'R_x$)

W – Dimensionless load parameter ($w/ E'R_x^2$)

w – Load

k – Ellipticity ratio (unity for spherical components)

d – Diameter of femoral head

c_d – Diametrical clearance

Ω – Angular velocity

E' – Effective elastic modulus

T – Total degradation due to tribocorrosion

C – Degradation due to pure corrosion

W – Degradation due to wear

S – Degradation due to synergy between corrosion and wear

C_w – Degradation due to wear-enhanced corrosion

W_C – Degradation due to corrosion-enhanced wear

Chapter 3

P_{max} - Maximum Hertzian contact pressure

P_{mean} – Mean Hertzian contact pressure

R – Effective radius $(1/R_x + 1/R_y)^{-1}$

$R_{x/y}$ – Radius in x/y direction $(1/R_A + 1/R_B)^{-1}$

$R_{A/B}$ – Radius of surface A/B

Chapter 4

ΔE – Change in potential

Δi – Change in current

R_p – Polarisation resistance

β_a – Anodic Tafel constant

βc – Cathodic Tafel constant

Chapter 5

m – Mass of corroded material

Q – Total charge transfer

M – Atomic mass

z – Number of electrons lost in anodic half reaction

Chapter 6

λ – Wavelength

h – Planck's constant

m_0 – Electron rest mass

e – Charge on an electron

U – Accelerating voltage

c – Speed of light in a vacuum

n – Integer

d –Atomic plane spacing

θ – Angle of incident wave

E – Energy

Φ – Work function of spectrometer

Chapter 8

I_{corr} – Total corrosion current

I_{corr} – Corrosion current density

A – Surface area

a – Contact patch half width

I – External current caused by applied overpotential

α – Symmetry coefficient between 0-1 (usually close to 0.5)

η – Test electrode overpotential

n – Number of electrons lost in anodic half reaction

Chapter 10

I – Current generated by indentation/abrasion

I_0 – Baseline current

A_1 – Constant determined experimentally

t - Time

t_0 – Time at 0 seconds

τ – Time constant for repassivation

i – Current density response to single particle impact

i_s – Stable current density in the absence of impingement

t_j – Time of continuous gait

V – Volume loss of material

p_0 – Yield pressure

a – Real contact area

τ – Shear rate

v – Linear sliding velocity

Chapter 1 Introduction

1.1 Motivation

In 2011 over 83,000 total hip replacements were implanted in England and Wales (1). 93% of these procedures were for the treatment of osteoarthritis. Osteoarthritis is a particularly painful and debilitating condition and THR has proved to be effective in treating the end stage of the disease by restoring motion and eliminating pain.

Despite currently being the most effective treatment for osteoarthritis, THRs may sometimes fail. This can happen for a number of reasons the most popular being, aseptic loosening, dislocation/subluxation and implant failure. When failure occurs a patient must undergo revision surgery. This involves removal of all or part of the original implant and replacement with a new component. Revision surgery is more complex than primary surgery; it takes about twice as long and costs around twice much as primary surgery.

Increasing popularity of the procedure coupled with large incidences of revision surgery place a financial burden on the National Health Service as well as expose patients to the inherent risks involved with major surgery. Hence, research into this field promises widespread returns both in terms of patient health and monetary savings (2-4).

One current issue plaguing the world of total hip replacements is negative media attention (5, 6) prompted by the higher than expected failure rate associated with some modern metal-on-metal prostheses (1). Evidence collected from patients suggests that corrosion of the joints had taken place (7, 8), despite degradation formerly being considered as a purely mechanical system. By considering this system in terms of both electrochemical and

mechanical influences, a novel approach was be undertaken in the investigation of these joints.

1.2 Aims and Objectives

- To investigate the degradation of metal-on-metal hip bearing materials in a tribocorrosion environment.
- To extend studies of the sliding interface beyond tribometer studies to the use of an electrochemically instrumented hip simulator.
- To determine the significance of corrosion, in terms of material degradation and metal ion release, for metal-on-metal bearing surfaces.
- To investigate the formation of tribologically formed layers at the bearing interface, as well as their effect on the performance of it.
- To link tribology models to the measurement of corrosion *in-situ*.

1.3 Thesis Outline

Following the literature review presented in the next chapter, the apparatus, methodology and results are split into two parts. Part 1 relates to experiments performed on a pin-on-plate tribometer, whilst Part 2 relates to experiments performed on a hip simulator.

The methodology and results for each part are further subdivided into separate experimental procedures adopted on the different test rigs. Part 1 contains details of two separate procedures referred to as ‘Procedure A’ and

‘Procedure B’. Part 2 contains details of 3 separate procedures referred to as ‘Procedure 1’, ‘Procedure 2’ and ‘Procedure 3’.

Extensive surface analysis was performed following the procedures undertaken in Part 2, and for this reason is presented separately in Chapter 9.

A diagram of the experimental structure undertaken in this thesis is shown in Figure 1.1.

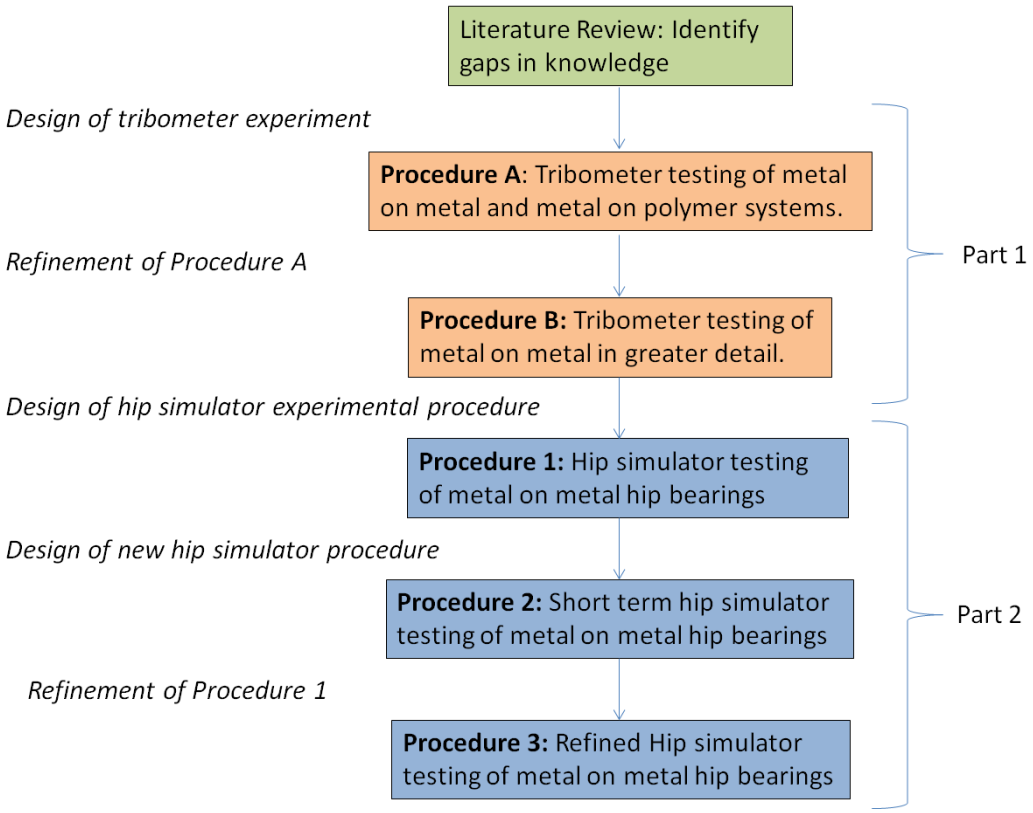

Figure 1.1: Experimental structure of thesis.

Chapter 2 Literature Review

2.1 Total Hip Replacement (THR)

2.1.1 Introduction

Information from the UK 'National Joint Registry' shows that over 250,000 people in UK have at least one total-hip-replacement (THR) or hip resurfacing. Predominantly, these contain one of four bearing material combinations: metal-on-polymer (MoP), ceramic-on-ceramic (CoC), ceramic-on-polymer (CoP) and metal-on-metal (MoM). Their estimated abundance is 64.4%, 12.6%, 11.0% and 7.9% respectively, with an additional 4.0% comprising an alternative or unknown design. In the case of THRs as opposed to hip resurfacing, the bearings are used in combination with a femoral-stem that is either cemented, un-cemented or a hybrid. The choice of bearing surface and fixation mechanism is determined by the surgeon and based on a number of factors (1) .

In the UK, estimates in the National Joint Registry indicate that the risk of revision surgery is greatest for MoM bearing surfaces, and that the cemented stems are the fixation mechanism most prone to failure (1). It is difficult to determine whether this reflects shortcomings in prosthesis designs, or is a reflection of the cohort of patients in which a specific device is favoured. Metal-on-metal bearings tend to be implanted predominantly in younger (on average 63 years) male patients, as opposed to MoP bearings that are implanted into older (on average 73 years) female patients. Such factors as these may be important when estimating the level of expected use and the vigour with which such prosthesis are likely to be used.

2.1.2 Metal-on-Polymer (MoP)

John Charnley first conceived the use of MoP bearing surfaces in 1959. His design, known as 'the Charnley Low Friction Arthroplasty (LFA)', comprised a monolithic stainless steel stem and head, which articulated against a polytetrafluoroethylene (PTFE) acetabular cup. The design was engineered to minimise frictional torque, by combining low sliding friction with a small head diameter of just 22.2mm. Although the design produced very low friction, the wear rate limited the life of design to around 3 years. For this reason PTFE was replaced with Ultra-High-Molecular-Weight-Polyethylene (UHMWPE) which greatly improved its wear resistance. The low friction arthroplasty was a huge success for many years, considered by many to be the 'gold standard' of total hip replacements. The maximum life of these prostheses was usually determined by the rate of polymeric wear; this gave an average life span of approximately 16 years, although some reports suggest that survivorship could greatly exceed this on occasion. Following the success of the LFA, Müller pioneered the use of CoCrMo in MoP articulations; an idea that led on to further designs including those of a modular system created by Weber (9, 10).

Modern MoP designs make use of a polymer surface made from UHMWPE. It has been shown that gamma irradiation of this polymer at approximately 50kGy can induce cross-linking in the polymer chains, improving its wear resistance. At doses greater than this subsurface oxidation can occur, which compromises its fatigue resistance. Laboratory investigations have demonstrated that by doping UHMWPE with vitamin E, the oxidation by irradiation can be mitigated (11, 12). This has the potential to allow a greater irradiation dose to be used, which may further improve the wear resistance of the material without compromising its fatigue life.

An issue, which limits the effectiveness of MoP designs, is their propensity to produce micron scale polymeric wear debris (10, 13). Although chemically inert, the size of this debris means it can have deleterious effects when liberated into the body (14). Polymeric wear debris of the 0.1-1μm scale has been shown to be the most effective in stimulating a macrophagic response.

This results in the production of cytokines, in particular TNF-α, leading to bone reabsorption and osteolysis (15). Studies have shown that osteolysis is a major cause for aseptic loosening in MoP THRs and can lead to premature prosthesis revision (14, 16-19).

2.1.3 Ceramic-on-Ceramic (CoC)

Ceramic-on-ceramic bearings were first conceived by Boutin in the 1970s (10, 20). Despite initial popularity in Europe the design had lost favour by the 1980s due to issues with fracture and fixation (20). By the 1990s, improvements in manufacture headed to the development of high purity alumina with reduced grain sizes (10, 21, 22). This new generation of ceramics were more resilient to fracture and contributed to the renewed popularity of CoC THRs (10)

Ceramic-on-ceramic bearings are renowned for their outstandingly low volumetric wear rates. They produce considerably lower wear rates than: MoP, CoP and even MoM designs (10, 20, 23). The superior wear resistance of CoC bearings can be partly attributed to their extremely hard surfaces (7.6GPa<Vickers hardness<17.5GPa)(24, 25), and low surface roughness (5nm<R_a<10nm)(23, 26). It has been shown that, like MoM bearings, MoC bearings also exhibit a ‘running-in’ period. After this, a shift towards partial or full fluid film lubrication is made (10, 22). The wear debris produced in CoC contacts tends to be of the nanometre scale (13, 23), and is generally much less biologically reactive than MoP particles (13, 21).

Despite these developments, there are some concerns with the performance of CoC bearings. Improvements in material manufacture have not completely eliminated the risk of femoral head fracture. In addition, stripe wear and grain pull-out has been identified on the surfaces of ceramic bearings (20, 22), which may be a concern for long-term implantation.

2.1.4 Ceramic-on-Polymer (CoP)

An alternative soft-on-hard bearing combination to MoP is CoP. These consist of an acetabular cup made of UHMWPE and a femoral head made from either alumina or zirconia. The ceramic surfaces used are smoother and harder than their metal counter parts, which results in a reduction to the volumetric wear of the polymer cup (10, 13). Zirconia is used in conjunction with alumina because of its superior fracture toughness (10).

2.1.5 Metal- on-Metal (MoM)

Metal-on-metal THRs were first widely implanted in the 1960s, popularised by the 'McKee-Farrer' (10). This design was initially made from a stainless steel head and cup, which was replaced by the use of the more wear resistant cobalt-chromium (CoCr). These early joints were generally associated with high failure rates, although reports of well functioning joints lasting in excess of 20 years have been recorded. In the 1990's a renaissance in the use of MoM bearing surfaces was observed. This was fuelled by the advantages offered over MoP bearings in terms of volumetric wear rate and particle size. Although much more abundant, the smaller size of metallic particles makes them less likely to induce osteolysis than MoP debris.

Modern MoM THRs are almost exclusively made from some form of CoCr alloy usually containing Molybdenum (Mo) and/or Nickel (Ni). Alloys can be separated into high- or low-carbon designs depending on their carbon content. High-carbon alloys tend to have a greater hardness and a greater wear resistance than low-carbon alloys (27). It has also been shown that high-carbon alloys contain precipitated carbides, whereas low-carbon alloys tend to contain carbon in solid solution (27, 28).

The resurgence of MoM THRs has been hindered in recent years due to fear of the effects of the release of metallic debris into the body. Metal-on-metal hip replacements have attracted a significant amount of media attention following higher than expected failure rates in some prosthesis (5, 6). Instances of soft-tissue inflammation and hypersensitivity have led to a number of restrictions to the use of MoM bearing surfaces in the UK. To date the MHRA has issued medical device alerts relating to the use of metal-on-metal bearing surfaces in hip replacements, some of these being amendments to previous alerts or instructions involving specific devices (29). The use of these alerts has resulted in restrictions on the use of some combinations of MoM devices, as well as invoking mandatory blood ion monitoring for patients already implanted with certain MoM prostheses.

2.2 Corrosion of Biomaterials

2.2.1 Introduction

Corrosion is the degradation of a material, usually a metal, by chemical interaction with its environment. It involves a transfer of a species from that of a high-energy state to a lower energy state i.e. from a pure metal to a metal oxide. Usually this transformation involves the transfer of electrons, and where this is the case it is defined as an electrochemical process, simultaneous reduction and oxidation take place, termed redox. This can be demonstrated by the oxidation and reduction (named anodic and cathodic respectively) reactions taking place as a metal corrodes in an aqueous environment. This is shown in Equations (2.1) and (2.2).

$$M \rightarrow M^{n+} + ne^{-} \tag{2.1}$$

$$\frac{1}{2}\, O_2 + H_2O + 2e^{-} \rightarrow 2OH^{-} \tag{2.2}$$

Where,

M – Metal species

n – Valence number

Whenever metals are implanted into the body corrosion can take place. This is a concern because of the damage caused to implants by corrosion and the effects that corrosion debris can have on patient health.

For corrosion to proceed spontaneously it must be thermodynamically favourable. This can be determined from the Gibbs free energy see Equation (2.3).

$$\Delta G = \Delta G_0 + RT\, ln \frac{[product][product]}{[reactant][reactant]} \quad (2.3)$$

Where,

G – Gibbs Free energy

G_0 – Standard free energy of a cell reaction

R – Ideal gas constant

T – Temperature

If $\Delta G > 0$ then the reaction requires energy to be supplied in order for it to occur, if $\Delta G < 0$ then the reaction releases energy and can happen spontaneously. This considers the energy associated with enthalpy and entropy however, there is also energy associated with the separation of charge. This charge separation is known as the electrical double layer and its behaviour is similar to that of a capacitor; a rise to a potential across the interface between the metal and the solution occurs. Figures 2.1 and 2.2 show how potential can vary across the double layer.

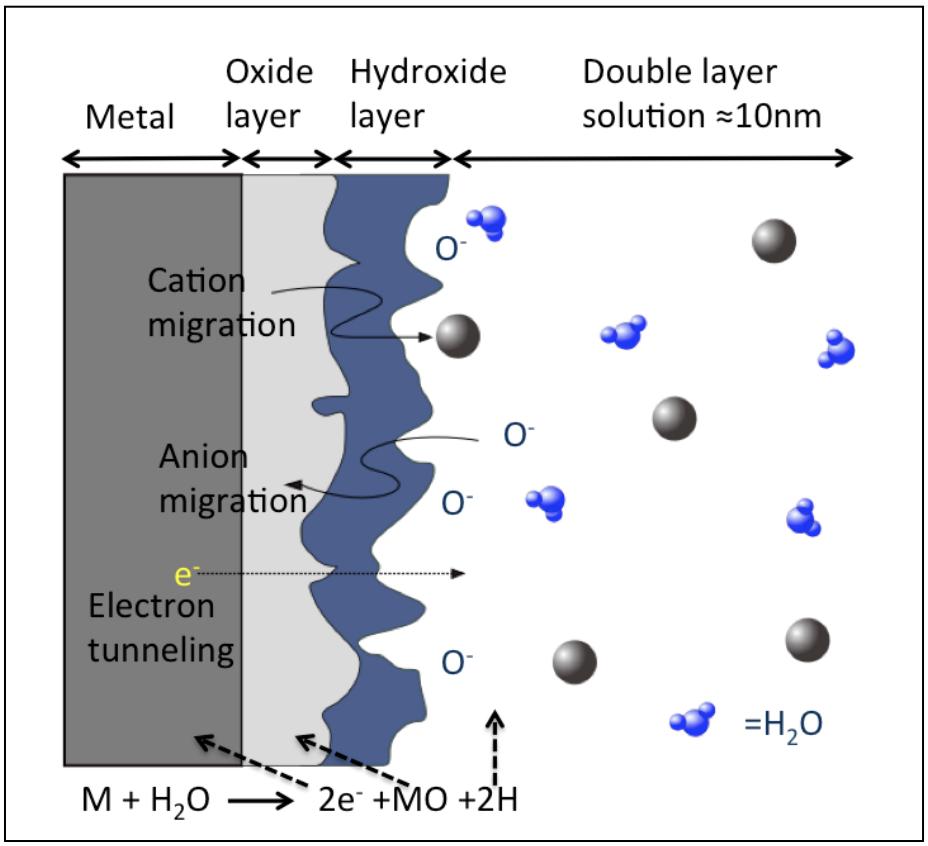

Figure 2.1: The interface of a metal surface in contact with an aqueous environment, where the metal is covered by an oxide layer, through which metal ions can pass into the solution as shown (30).

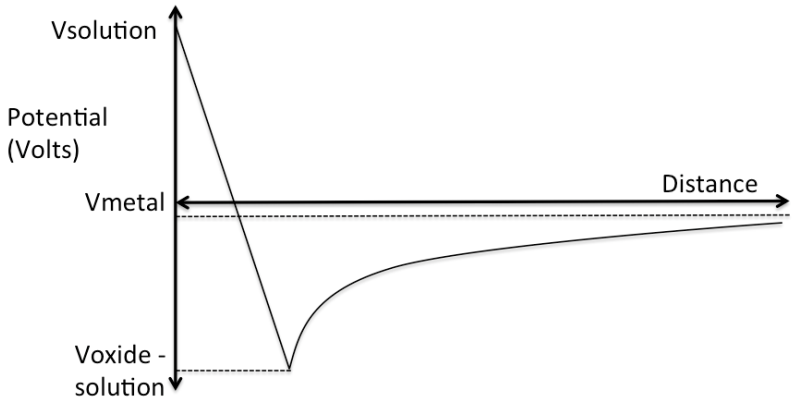

Figure 2.2: Variation of potential across the oxide/EDL interface (30).

This potential can be represented by Equation (2.4).

$$\Delta G = -nFE \quad (2.4)$$

Where,

G – Gibbs Free energy

n – Valence number

F – Faraday constant

E – Potential difference between two half-cells

Hence, under equilibrium conditions the electrical energy and chemical energy are equal and can be combined to give the Nernst Equation (shown in Equation (2.5).

$$\Delta E = \Delta E_0 + \frac{RT}{nF} \ln \frac{[products]}{[reactants]} \quad (2.5)$$

Where,

E – Potential difference between two half-cells

E_0 – Standard potential difference across a cell

R – Ideal gas constant

T – Temperature

F – Faraday constant

n – Valence number

This potential gives rise to the electrochemical series, from which the relative reactivity of metals is established. It is important to note that this scale does not indicate the rate at which a reaction will proceed; it is only a comparison of the tendency for a reaction to occur. The electrochemical series for some metals is shown in Figure 2.3.

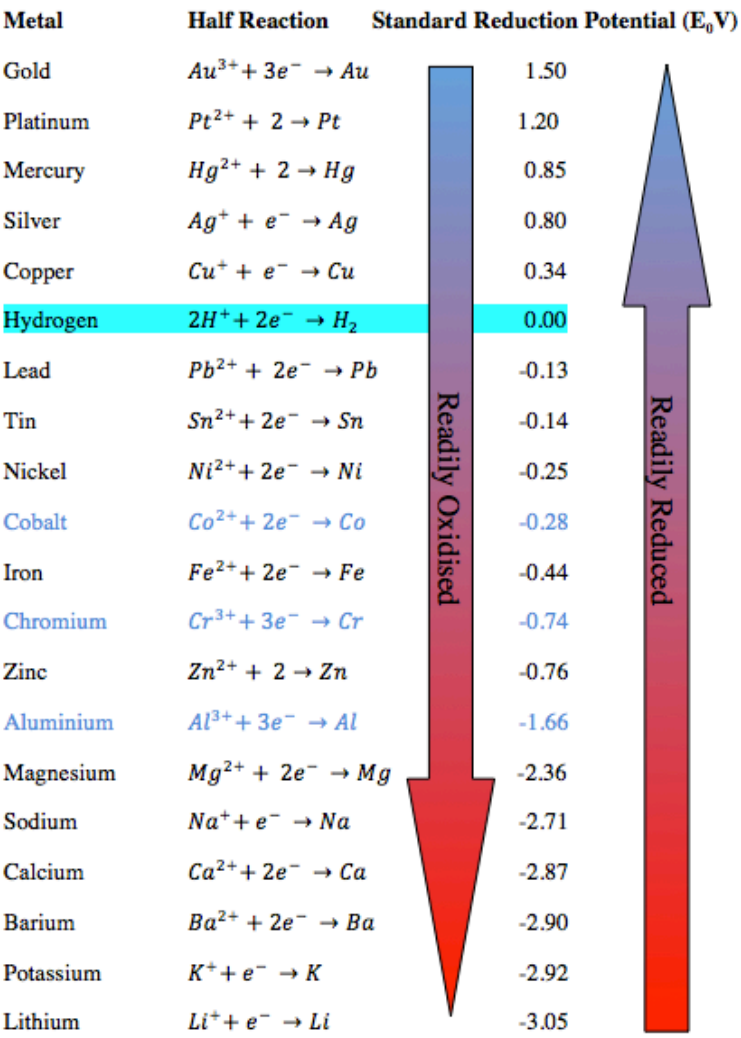

Figure 2.3: Standard reduction potentials for some active and passive metals (metals commonly used in orthopaedics are shown in blue).

It can be seen from Figure 2.3 that some widely used biomedical alloys have a low potential indicating a strong tendency to oxidise, but are still considered to be corrosion resistant. This can be explained by reaction kinetics. Materials such as gold obtain their corrosion resistance by having a very noble potential. However, corrosion resistant materials with a very negative potential, such as aluminium, obtain their corrosion resistance from kinetic barriers, which limit the rate of reaction. This usually occurs as a result of the formation of a very dense metal oxide film that spontaneously forms on the surface of the metal as a result of corrosion. Its formation impedes further corrosion from taking place by acting as a physical barrier between the oxidative species in the electrolyte and the metal surface. These oxide layers are known as passive films, as they limit the rate of

corrosion of the metal to a level at which the metal can be deemed passive (extremely corrosion resistant). The corrosion behaviour of materials can be investigated in the laboratory using a similar setup to that shown in Figure 2.4 (31). In this configuration a potentiostat is used to pass a current through the working electrode and the auxiliary electrode whilst immersed in an electrolyte. When corrosion of the working electrode takes place metal ions leave its surface and a current is drawn from it. Simultaneously a current is supplied to the counter electrode and cations are drawn towards its surface. With this configuration, a potential can be applied to the working electrode. This is done with reference to the reference electrode. When this is undertaken, the current is measured. Useful information can then be obtained from graphical plots of the current produced at a given potential. The behaviour of both an active and passive material under anodic polarisation is shown in Figure 2.5, where E_b is the breakdown potential, E_{pp} is the passivation potential and E_{corr} is the open circuit potential (OCP).

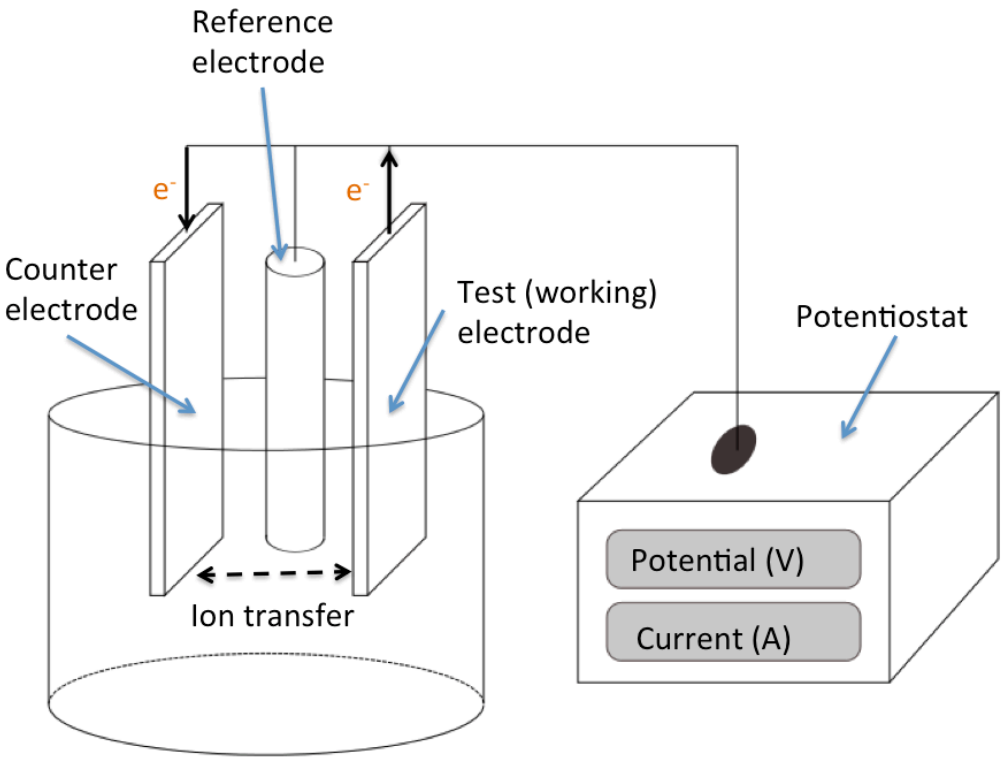

Figure 2.4: Diagram of a 3-electrode electrochemical test cell.

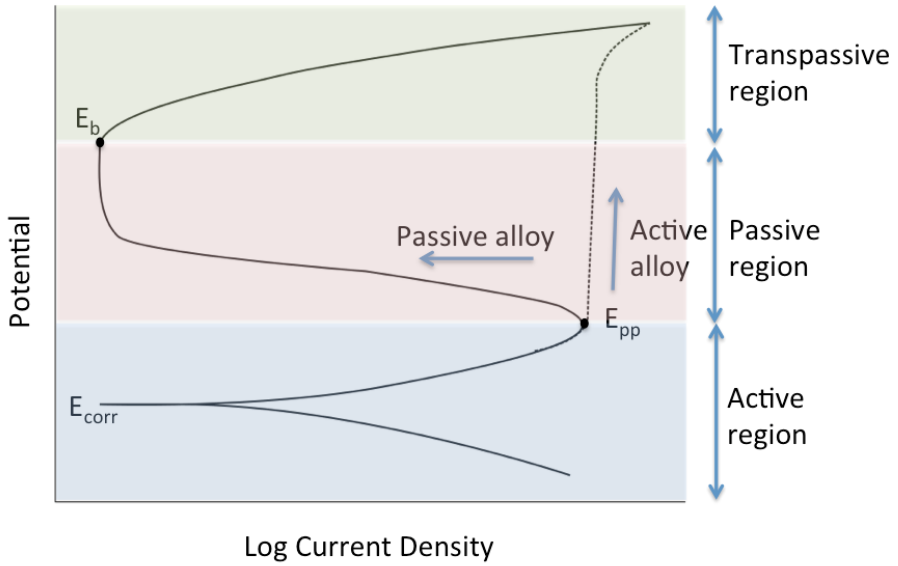

Figure 2.5: Example anodic polarisation scan for a passive and an active alloy showing corrosion potential (E_{corr}) passivation potential (E_{pp}) and breakdown potential (E_b).

The passive film that develops on the surface of species is dependent on the applied potential. It has been suggested that oxide film formation will proceed to maintain a constant electric field across the interface of the metal surface and the solution. When a negative potential is applied the film thickness reduces to maintain a high electric field (10^6-10^7 V/cm) but when a positive potential is applied the film will thicken. This technique has been used in many studies to predict the thickness of metal oxide films (32-34). Under large anodic potentials the film will lose its stability and will breakdown. This results in the loss of passivity from the metal and is accompanied by a large increase in current flow.

2.2.2 Corrosion of Total-Hip-Replacements

Most metals exposed to aqueous electrolytes will succumb to some level of general corrosion over the whole exposed surface, but in specific instances localised corrosion may also proceed causing a high level of damage to be

concentrated over a small area. For THRs this usually takes the form of pitting or crevice corrosion.

Numerous studies have found evidence of crevice corrosion and pitting on the necks and stems of retrieved THRs. Studies have demonstrated that titanium and steel stems are particularly vulnerable when coupled with CoCr heads (35-37). It is thought that this is caused by the formation of a galvanic cell between the passive CoCr and the crevice-corroded steel/titanium. In this scenario the CoCr acts as a net cathode, which increases the anodic dissolution of the coupled metal.

The mechanism by which crevice corrosion can cause the loss of passivity has been outlined by Oldfield *et al* (38, 39), it can be split into four stages (40).

1. Depletion of oxygen within the crevice solution.
2. Increase in acidity and chloride content of the crevice solution.
3. Permanent breakdown of the passive film and the onset of rapid corrosion.
4. Finally, propagation of crevice corrosion.

Crevices form due to tight geometries between surfaces; in total hip replacements this occurs at the interface between the head/neck taper found in modular designs, or at the stem/cement interface of cemented devices. Initially, within the crevice the surfaces corrode at a passive rate and generally water is reduced forming OH^- ions as shown in Equation (10.2).

$$2H_2O + e^- \rightarrow H_2 + OH^- \qquad (2.6)$$

If the rate of oxygen consumption in the anodic reaction exceeds the rate of oxygen diffusion into the crevice, then over time the crevice will become deoxygenated. Once deoxygenated, the cathodic reaction ceases to take place within the crevice and moves outside. This induces a mini galvanic circuit between the anodic reactions within the crevice and the external cathodic reactions (see Figure 2.6). Metal ions formed in the crevice are hydrolysed, as their concentration increases metal hydroxides begin to precipitate from the solution. The precipitation of these metal hydroxides removes OH^- ions from the solution leaving an increased concentration of H^+

ions, which then lowers the pH. The large H^+ concentration causes cations to migrate from the crevice and anions, specifically Cl^-, to enter it. The reduced pH and increased chloride ion content can render the electrolyte aggressive enough to breakdown the passive film at the crevice walls. The rate of corrosion will then increase from that of a passive alloy to that of an active alloy. As corrosion proceeds, anodic dissolution of the surface takes place and the crevice is propagated. Under these conditions corrosion can take place in the form of pitting, in which the anodic reaction takes place over a very small area at a high rate (39, 40). Pitting takes place by a very similar mechanism to crevice corrosion, a large H^+ ion concentration develops in the pit causing rapid penetration of the surface (35, 39).

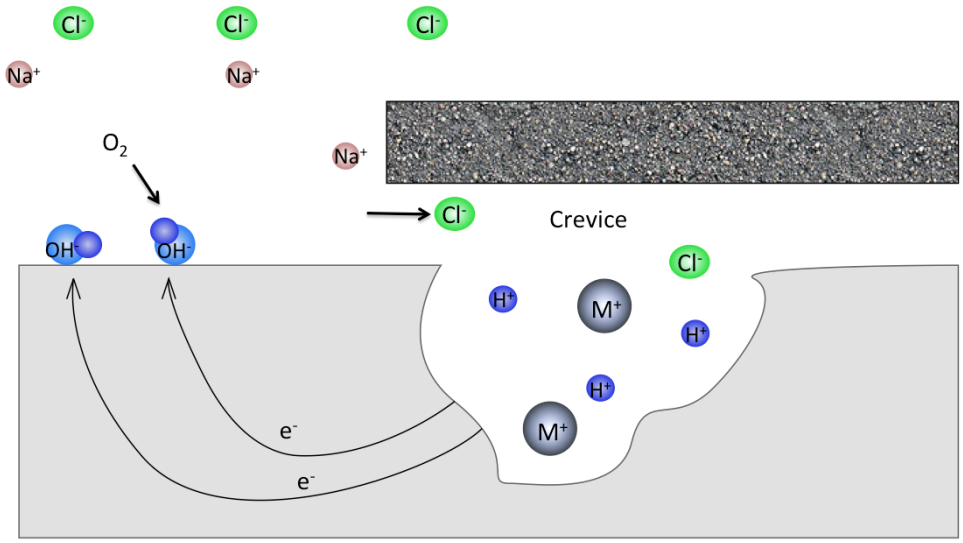

Figure 2.6: Crevice corrosion in a saline environment.

Retrieval studies performed on modular femoral hip prostheses revealed substantial corrosion damage around the head/neck interface. This was exhibited as inter-granular corrosion, pitting and the removal of machining marks (35, 36). In both studies it was found that corrosion of single-metal assemblies, either consisting of titanium or CoCr, showed little evidence of corrosion damage, or were devoid of observable damage altogether. Whilst mixed-metal assemblies consisting of a CoCr head and titanium stem/neck, were corroded as previously stated. In a study of 139 components, 25

displayed definite corrosion damage and an absence of fretting (35). There appeared to be a direct correlation between the implantation duration and the level of degradation of the explants. Corrosion was not observed on either single- or mixed-metal assemblies that were implanted for under 9 months. Additionally, every component that was implanted for at least 40 months displayed evidence of corrosion damage.

The corrosion of metals is heavily affected by environmental factors such as, pH, temperature, chloride concentration and the presence of other compounds; for example, inhibitors and organic species. The environment within the body consists largely of aqueous, chloride rich solutions, which are suitable conditions for corrosion to arise. As THRs are implanted within the joint capsule, it is important to understand the effects of proteins on corrosion. Studies have shown that for some biomaterials such as CoCr the presence of proteins caused a considerable increase in the rate of anodic dissolution of the metal (41, 42). Albumin was shown to cause an increase in the dissolution of cobalt by over 20 times and almost 5 times for chromium. However, it had very little effect on the dissolution of aluminium, no effect on titanium and inhibited the dissolution of molybdenum (41). In addition, sites within the joint capsule have frequently been shown to suffer from inflammation following surgery, which can cause a reduction in pH from 7.4 to 5.5 (43, 44).

2.3 Cobalt Chromium (CoCr) Alloys

2.3.1 Strain Induced Transformation

During wear testing, it has been shown that alloys of cobalt can undergo a phase transformation from a face-centred-cubic (FCC) crystal structure to a hexagonally closed packed (HCP) one. This occurs as a result of strain-induced transformations (SITs) from γ- to ε-martensite, arising from shear

occurring at the alloy surface (45-50). This phenomenon has been detected on numerous occasions in a variety of different conditions including, pin-on-plate tribometer studies, hip simulator studies and from explanted hip bearing surfaces. It was detected through the use of X-ray diffraction (XRD) and transmission electron microscopy (TEM) (28, 46, 50-53). XRD spectra have been used to identify the formation of wear-induced ε-martensite. This was achieved through observation of prominent spectral peaks occurring at approximately $2\theta=44^0$ and $2\theta=47^0$ corresponding to the <0001> and <$1\bar{0}11$> planes of the HCP lattice (52). The HCP planes are illustrated in Figure 2.7. TEM images have been used to identify subsurface ε-martensite observed as orientated needles present within the top 1μm of both simulator tested and explanted hip bearing surfaces (46).

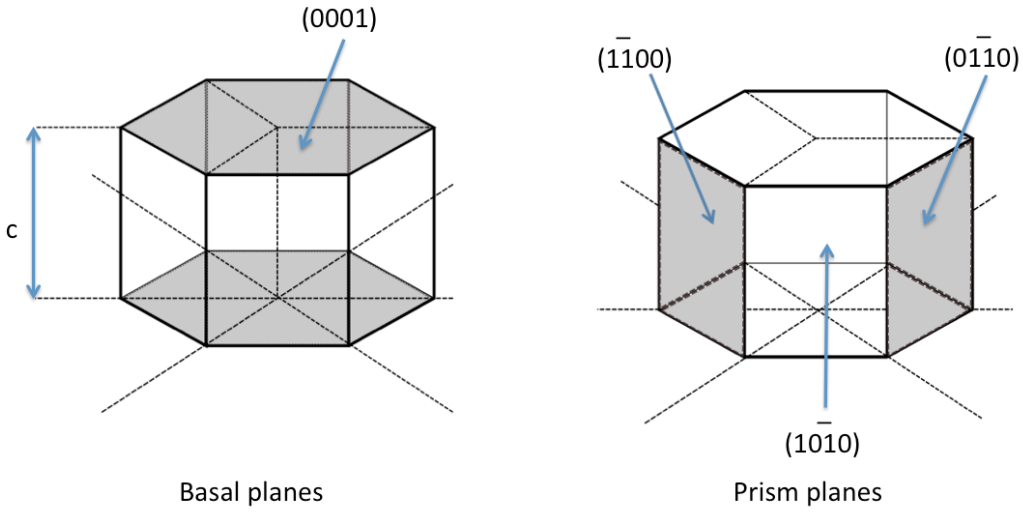

Figure 2.7: HCP basal and prism planes.

CoCr alloys are susceptible to SITs owing to their low stacking fault energy. This can result in the formation of Shockley partials as lattice dislocations become dissociated; propagation of Shockley dislocations down close packed plains can lead to twinning in the alloy (47-49). This produces strain hardening in the alloy since both twins and ε-martensite platelets will impede plastic deformation (46, 48). It has been shown that strain hardening occurs normal to the direction of shear since the HCP basal planes orientate parallel to shear (51-53). Observations determined that basal plane orientation only occurs within the top 30nm of the surface, not extending

beneath the tribofilm. In dry conditions this has been shown to reduce both friction and galling (51).

Despite the associated strain hardening of SITs it was advocated by Varano *et al* (28) that FCC-HCP phase transformation is detrimental to the wear performance of CoCr alloys . This concept was justified by the suggestion that HC-CoCr alloys have superior wear rates compared to low-carbon ones, due to the effect of carbon on stabilizing the FCC phase and inhibiting SIT. However, it was demonstrated that when heat treatment was used to induce FCC-HCP phase transformation there was little effect on the wear resistance of the alloy. These ideas conflict with those presented by Bücher *et al* (46) who believe SIT from FCC to a HCP structure to be beneficial in reducing wear through strengthening of the alloy.

It was established by Bücher *et al* (46) that CoCr alloys form a nano-crystalline layer in the top few hundred nanometres of the surface. In this region crystallites are approximately 40nm in diameter but may reach as low as 10nm. Evidence suggests that the generation of round nano-scale wear debris arises as a consequence of the removal of these crystallites from the bearing surface. Whilst the larger needle like particles observed in patients could be produced by the fracturing of the HCP ε-martensite needles, observed in the subsurface of the alloy (46). This would suggest that SIT serves to reduce wear by acting as a precursor to the formation of a nano-crystalline layer reducing the average globular particle size, but may also be responsible for the simultaneous release of larger needle like particles. The role of the nano-crystalline layer in the wear mechanisms of CoCr alloys could suggest that wear is dominated by the structure present in the top few hundred nanometres; this may explain why authors have found wear performance to be largely independent of the bulk grain size.

2.3.2 Metallic Ion Release and Patient Health

Patients implanted with THRs have been shown in many cases to experience increased concentrations of metal ions (8, 54, 55). The levels of specific metal ions are dependent on a number of factors such as the type of prosthesis implanted, the time since surgery and how the joint is functioning in terms of wear or loosening. Metal ions are usually detected using Inductively Coupled Plasma Spectroscopy (ICPS) on samples taken from patients' joint capsules, whole blood, serum and renal excretions (7, 8, 54, 56). Studies have shown that patients with prostheses containing a MoM bearing surface have significantly greater levels of Co and Cr than patients implanted with MoP or CoP bearings (8, 55). It can be inferred from this that the majority of Co and Cr ions detected arise from degradation of MoM bearing surfaces. This is consistent with the observed correlation between the metal ion concentration measured in the serum and the joint capsules of patients, and the level of degradation on their MoM bearing surface (56).

Metal ions are formed when a metal corrodes, which can take place either from the bulk surface or from the surface of the wear debris. Observations of corrosion debris in patients have confirmed that the latter occurs both intra and extra-cellularly, and high ion concentrations may be detected in distant lymph nodes, away from the prosthesis (57, 58). It has been posited that the level of renal excretion of Co closely matches the estimated rate of production, assuming immediate ionisation of the wear debris (59). This would suggest Co does not accumulate internally, in the same way that Cr does (59, 60). Studies of both the short- and medium–term ion release in patients have demonstrated that metal ion concentrations tend to increase over the first 1-2 years, but have declined after 4-5 years (7, 54). This has been attributed to the reduction of wear taking place following running-in; however, the reductions in metal ion concentrations are less dramatic than would be expected, based on the reduced wear rate (7). This may be partially explained by the previously discussed observations of a Cr containing passive film, which formed on the surface of wear particles (61). The presence of a chromium oxide passive film would substantially reduce their rate of anodic dissolution. Particles produced during the running-in

stage could continue to ionise well into the medium-term, causing a delayed release of ions. This effect would be enhanced by the difference in particle size produced in both the short- and medium-term. As previously discussed, Catelas *et al* (62) observed that particles produced in the first 0.25 million cycles were larger than those produced at around 2 million cycles. These particles would have a smaller surface area per unit mass than those produced later. It has been shown that the rate of chromium release from CoCr is proportional to particle surface area, hence a reduction in particle size can lead to an increase in the rate of ion production (63).

Cobalt chromium alloys tend to form mostly Co^{2+} and Cr^{3+} ions, although more toxic Cr^{6+} ions may also be produced (59, 60). Co^{2+} has been shown to be more toxic than Cr^{3+} by its propensity to cause a greater release of TNA-α upon exposure, even at reduced doses (60). It has also been demonstrated that cobalt can kill synovial fibroblasts, monocytes and chondrocytes at given concentrations more readily than chromium (59). Cr^{6+} is produced in significantly less abundance than Cr^{3+} but is substantially more toxic. When Cr^{6+} is reduced it can produce a number of intermediate species, which cause further reactions to proceed, leading to genetic lesions (60). Positive metal ions will readily react with most proteins, as they are mostly zwitterions (contain both a positive and negative charge) that are negative in neutral or alkaline conditions. This causes changes in the body's pH and produces organometallic complexes, which can cause hypersensitivity in patients (57, 59, 60, 64). It has been shown that Co and Cr ion concentration in the joint capsule are at least an order of magnitude greater than those measured in the serum. This may be the cause of inflammation and necrosis observed in the joint capsule of patients experiencing joint loosening. Suggestions that local effects of metal ions may be dose-dependent concur with these findings (8, 56, 57).

2.3.3 Cobalt Chromium Alloy Passivity

It was shown that when immersed in simulated physiological fluid, the rate of dissolution of pure molybdenum and cobalt greatly exceeded that of chromium. However when alloyed, the release of Mo and Co were greatly reduced at the expense of a small increase in the release of Cr (65). The relative release of Co from the alloy exceeded its stoichiometric amount indicating that it was preferentially leached out (65, 66).

The resistance of cobalt chromium to corrosion can be attributed to its formation of a passive film (32-34, 65-67). The passive film is a thin oxide layer that forms spontaneously on the surface of the alloy. It chiefly comprised of Cr(III) oxide which, makes up approximately 90% with the remainder comprising of oxides of Mo and Co (34, 66, 68). When in aqueous solution, a hydroxide layer has been found to form on the outside of the oxide layer. The presence of this oxide/hydroxide layer gives CoCr alloys electrochemical properties that closely mirror those of pure Cr (33, 66, 68).

Under an applied anodic potential the amount of Co and Mo in the passive film is increased. This results in thickening of the film, but also causes a decrease in passivity due to the greater solubility of Mo and Co oxides (34). When the potential is increased into the transpassive region, the preferential release of Co is less pronounced and the relative dissolution of the alloying elements approaches their stoichiometric quantities (66). The properties of the passive film can also be affected by immersion in a solution containing complexing species such as EDTA. It was found that the presence of EDTA reduced the thickness of the passive film and reduced its passivity (68). Alternatively, when exposed to PBS solution the passive film was found to increase in thickness over time, also increasing in passivity (66).

2.4 Tribology of Metal-on-Metal Total Joint Replacements

2.4.1 Introduction

The formal definition of tribology is the science and technology of interacting surfaces in relative motion, and related subjects and processes. This includes the study of friction lubrication and wear. Total joint replacements provide a unique set of tribological engineering problems due to their biological operating environment. These issues typically relate to the production of wear debris, which is liberated into the body, and lubrication using a natural lubricant that cannot be artificially replaced.

2.4.2 Lubrication Regimes

Lubrication falls into 3 basic categories: boundary, mixed and fluid film. In boundary conditions the separation of the two opposing surfaces is almost entirely supported by elastic deformation of the surface asperities. The surfaces are covered with a very thin film of lubricant that serves to reduce friction. In these conditions, the wear rate is relatively large and friction is not greatly affected by the bulk properties of the lubricant. In mixed conditions the partial separation of the surfaces arises from a combination of the relief of elastic deformation of the surfaces and also from the pressure exerted by a thicker interstitial lubricating film. In moving from boundary to mixed lubrication the wear rate is reduced, owing to a lessening in the severity of mechanical contact between opposing asperities. In fluid-film conditions the surfaces are completely supported by fluid pressure since the lubricating film is thick enough to completely separate opposing asperities. Under these conditions wear is at its minimum and friction is dominated by fluid rheology (69).

Using the film thickness and surface roughness, the lubricating regime can be estimated from the lambda ratio. The lambda ratio is defined below (Equation (2.7)).

$$\Lambda = \frac{h_{min}}{\sqrt{(R_a)^2_{surface\ 1} + (R_a)^2_{surface\ 2}}} \tag{2.7}$$

Where,

h_{min} – Minimum lubricating/elastohydrodynamic film thickness

R_a – Average surface roughness

Generally lambda ratios below 1 indicate that a system is operating in the boundary regime, and ratios above about 3 (70) or 5 (71), depending on the test geometries, indicate fluid-film lubrication is taking place. Mixed lubrication exists between these two ratios, with lower values indicating a more severe mixed regime. It is important to consider that this only gives an indication and that other factors, such as surface skew, are not taken into account. Figure 2.8 shows a Stribeck curve, which relates certain operating parameters to lubrication regime and friction.

It should be noted that although this approach is useful in estimating the lubricating regime in which a system resides, there are a number of limitations to its approach. Film thickness is generally determined numerically with the assumption that surfaces are smooth. This value is then used in conjunction with the materials roughness (R_a) to determine the degree of mechanical contact. This is illustrated in Figure 2.9. Hence the influence of R_a on lubricant film thickness is usually ignored. In addition, there is no differentiation between two surfaces of equal R_a but with different roughness profiles.

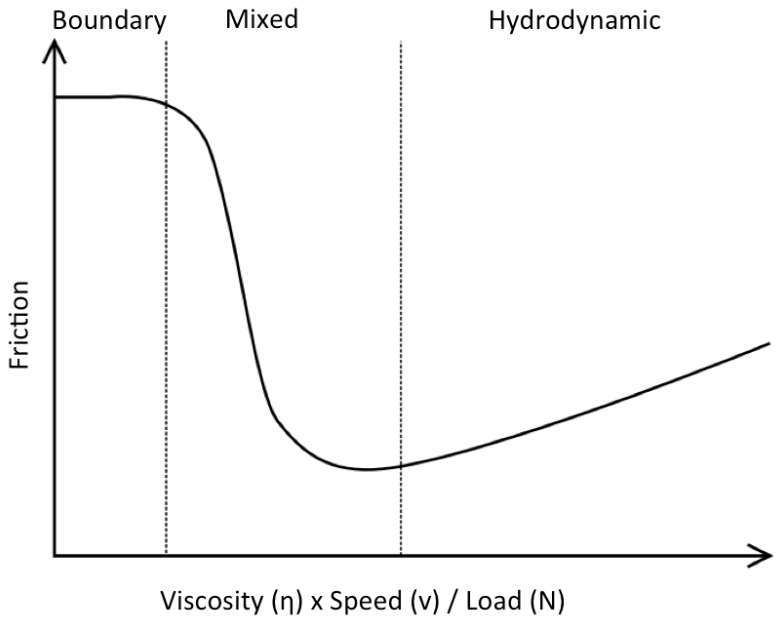

Figure 2.8: Example Stribeck diagram illustrating: boundary-, mixed- and fluid-film-lubrication regimes.

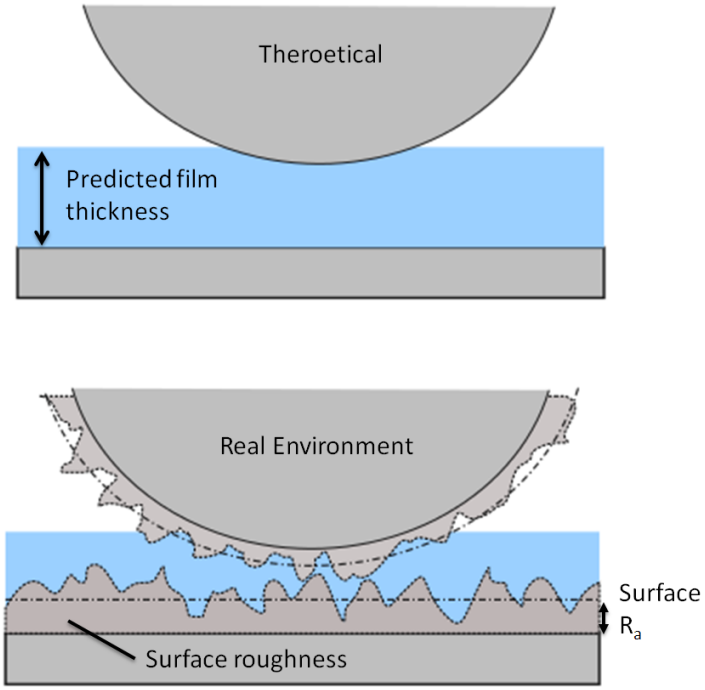

Figure 2.9: Determination of Lambda ratio from a theoretically smooth surface.

2.4.3 Elastohydrodynamic Lubrication

It has been observed that many systems involving classically unfavourable tribological parameters, such as high loading or poor conformity, perform as though operating in a state of fluid-film lubrication. For many years this contradicted lubrication theory, and the high performance of components such as gears could not be explained. It was later demonstrated that this was due to a phenomena known as elastohydrodynamic lubrication (EHL) (69, 72). Elastohydrodynamic lubrication arises from two formerly overlooked factors that are significant in tribologically severe conditions: variation of the lubricant properties, notably viscosity with pressure, and deformation of the opposing surfaces (69, 72). Lubricants such as mineral oils have a pressure-viscosity dependence that can be modelled approximately by the Barus Equation, see (2.8).

$$\eta = \eta_0 \, exp(\alpha p) \tag{2.8}$$

Where,

η – Dynamic viscosity

η_0 - Standard dynamic viscosity

α – pressure viscosity coefficient

p – Pressure

It can be seen that under increased pressure the viscosity will increase and cause the formation of a thicker lubricating film. However, this effect alone is often not significant enough to promote the low friction and wear that have been observed in practice. Under severe loading, surface deformation can drastically alter the geometry of a lubricating film and hence the pressure distribution at the interface (69, 72). Pioneering work by Dowson and Hamrock led to a non-dimensionalised solution to the governing elastic and lubrication equations. An example of this equation when applied to contacts, such as synovial joints, is given below (Equation (2.9)) (73, 74). Since lubricants such as synovial fluid and bovine serum are essentially isoviscous

under the conditions experienced in natural joints, the lubrication regime resides within the elastic-isoviscous region of EHL (74).

$$H_{min} = \frac{h_{min}}{R_x} = 7.43(1 - 0.85e^{0.31k})U^{0.65}W^{-0.21} \quad (2.9)$$

Where,

H_{min} – Dimensionless minimum elastohydrodynamic film thickness

U - Dimensionless speed parameter ($\eta_0 u/E'R_x$)

W – Dimensionless load parameter ($w/ E'R_x^2$)

k – Ellipticity ratio (unity for spherical components)

h_{min} – Minimum lubricating/elastohydrodynamic film thickness

R_x – Equivalent radius in the x-direction

In MoM THRs the film thickness is in the order of tens of nanometres whilst elastic deformations are in the order of tens of micrometres. This large ratio indicates that elastohydrodynamic action must be considered when analysing the lubrication of prostheses of this type. By considering the ball and cup of a hip as a two dimensional problem it can be solved using the equation described by Dowson and Hamrock (73) (see Equation (2.9)).

This equation can be simplified by making the ellipticity ratio equal to 1 and assuming that the diametrical clearance between the head and cup is small, relative to their diameters. When expressed in terms of the individual variables the following equation is given (2.10). Displaying the equation in this manner is useful as it demonstrates the relative significance of each term on film thickness (74).

$$h_{min} = 0.66685d^{2.19}c_d^{-0.77}\eta^{0.65}\Omega^{0.65}w^{-0.21}(E')^{-0.44} \quad (2.10)$$

Where,

c_d – Diametrical clearance

Ω – Angular velocity

E' – Effective elastic modulus

w – Load

h_{min} – Minimum lubricating/elastohydrodynamic film thickness

η – Dynamic viscosity

From these parameters designers can vary only the head/cup diameter, the clearance between the two, and the effective elastic modulus. From Equation (2.10) it can be seen that a large head diameter accompanied by a small clearance and a low modulus of elasticity will favour the formation of a greater minimum film thickness. In recent years, full 3D modelling of EHL film thickness by computational methods has been possible. Studies have predicted the significant effects of radius and clearance on minimum EHL film thickness (75-77). Small increases in head/cup radii cause substantial increases in the film thickness and reductions in the contact pressure. Typically the lubricating fluid is modelled as being a Newtonian, isoviscous, incompressible fluid. Studies have demonstrated that this is an accurate approximation for the operating conditions found within MoM joint prostheses (78), particularly at the very high shear rates (10^5-$10^6 s^{-1}$) encountered in hip joint replacements. The significance of radius and clearance on the lubrication on MoM THRs has been demonstrated in both numerical simulations, and through laboratory experiments. (10, 74, 79-84). Figure 2.10 demonstrates the average film thickness predicted by Equation (2.10) for a range of MoM bearing diameters and clearances. The values obtained are based on a typical gait frequency, viscosity and body mass.

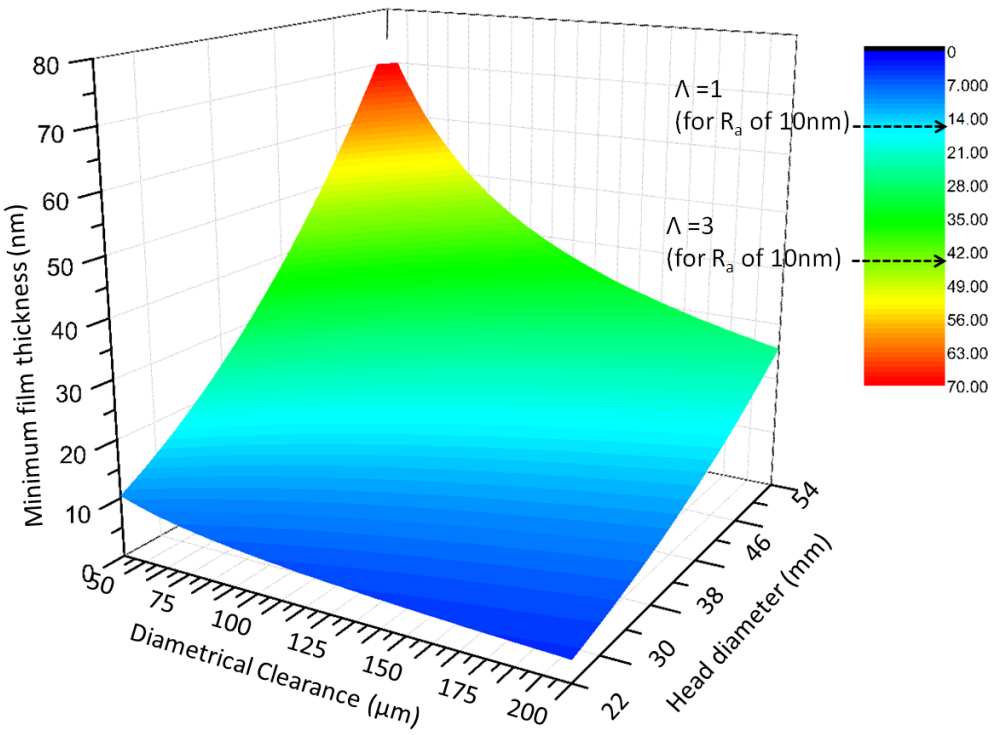

Figure 2.10: Average minimum film thickness variation with clearance and head diameter.

Dowson *et al* (81, 82) detected the cyclic film thicknesses between MoM bearings by using an electrical resistivity technique. In one investigation the effect of different lubricants on the film of 36mm bearings was assessed; whilst in another study, the effects of bearing size were determined. It was found that protein-containing lubricants provided the greatest separation of the bearing surfaces, providing longer periods of separation than the more viscous carboxy-methyl-cellulose (CMC). It was also determined that 100% bovine serum provided significant improvements in the longevity of lubrication than the 25% bovine serum solution (81). This may indicate the significant role of adsorbed proteins on lubricating the interface. When comparing the effects of head diameter all tests were run using 25% bovine serum solution. When comparing 16, 22.25, 28 and 36mm bearings it was observed that surface separation did not take place between 16mm and 22.25mm joints. This observation was also reflected in the relative wear rates of the two joints; the larger bearing experienced greater wear caused by the larger relative sliding distance between its surfaces. For the 28mm and 36mm joints, separation of the surfaces was evident for both, and accounted for the vastly increased longevity of the larger bearings. This was

also demonstrated in their wear rates, the 36mm bearing showed substantial reductions in wear compared to the 28mm joint, and can be explained by the superior lubrication afforded by its increased diameter. The results observed were in complete agreement with the predicted values of lambda, which suggest that the two smaller joints would have lambda ratios of less than 1, whilst the 28mm and 36mm bearings were calculated to operate in the mixed lubrication regime (82). These observations have been confirmed in other studies. It was also found that by using bearings with diameters larger than 36mm, such as 54mm, that further gains in terms of lubrication and wear could be made (85). In the same study it was also demonstrated that diametrical clearance played an important role in the lubrication of both 36mm and 54mm diameter bearings. For each bearing diameter the wear rate was reduced when bearings with smaller clearances were used (85). These findings coupled with EHL theory, demonstrate that from a purely tribological perspective MoM hips should be designed with as large diameter and as small a clearance as is feasible. This combination would result in the greatest lubricating film thickness and the greatest opportunity to achieve hydrodynamic lubrication throughout longer periods in the gait cycle (74, 79, 81, 85). It has been demonstrated in a study of results spanning over 70 tests undertaken in 8 different laboratories, from the USA, Canada and the UK, that running-in- and steady-state-wear are both heavily affected by EHL film thickness (74). A noteworthy reduction in wear rate can be achieved upon increasing the EHL film thickness towards 25nm, but films beyond this yield diminishing returns in terms of wear.

2.4.4 Wear Mechanisms

For studies investigating the wear between CoCr MoM interfaces, the governing wear mechanisms are very much dependent on the exact experimental set up. In linear tribometer experiments many authors have observed scratching of the surfaces in the direction of motion, either caused by 2^{nd} or 3^{rd} body abrasion (86-89). In some studies, pitting and surface fatigue have also been observed, and is attributed to high contact pressure developed by the pin plate geometry (87, 89). Similar observations have

been made in hip simulator studies, which demonstrate that these mechanisms arise at locations of increased stress (90). It has been demonstrated by several authors that when a rotating motion is introduced, in addition to sliding in the tribometer, the wear rate of MoM contacts can be significantly reduced (86, 88, 91). This is explained by a self-polishing mechanism, whereby raised metal is folded back into the wear scar. This concept is supported by observations of roughness being either, independent of wear or significantly reduced when compared to simple sliding tests. Tribometer tests incorporating both sliding and rotation appear to produce a more realistic wear mechanism than sliding alone. Simulator studies of MoM bearings have demonstrated that average surface roughness (R_a) is not critically altered by wear, but that the surface skew may change as peaks are worn flat and valleys deepened by self-polishing (26, 79, 82, 92). Figure 2.11 demonstrates the effect of self-polishing motion on the wear of CoCr pins (88).

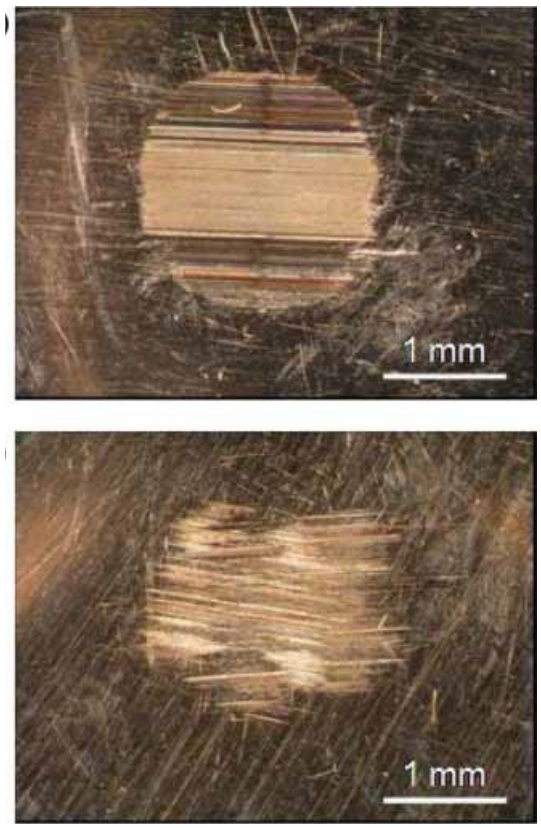

Figure 2.11: Wear of pin surface after sliding only (top); wear of pin surface after sliding and rotating (88).

An example of the change in surface topography of 2 femoral heads as a result of simulator testing is shown in Figure 2.12 (92). Increased roughness in the loaded regions of MoM hip bearing surfaces has been reported, but it was also acknowledged that self-polishing had taken place (20). Adhesive wear is not frequently observed between CoCr MoM bearing surfaces, despite being a major failure mechanism when like metals come into contact (93, 94). This has been explained by the subsurface micro-structural changes that take place as a result of wear induced strain in the alloy (46).

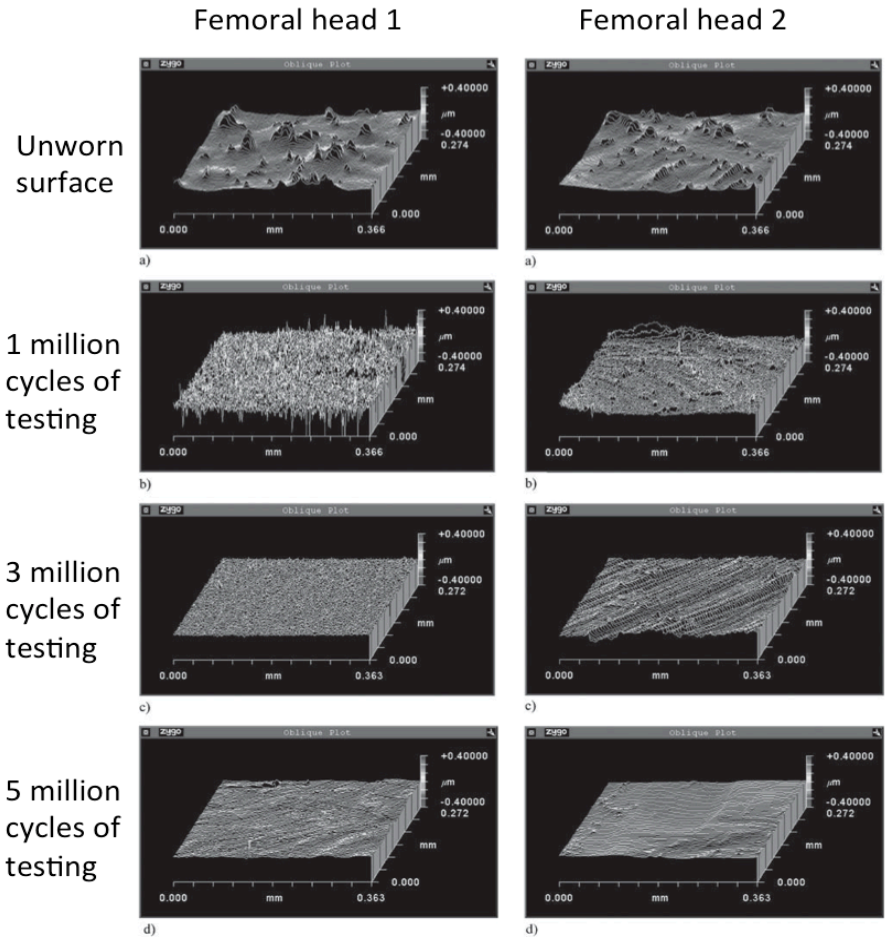

Figure 2.12: Change in surface topography as a result of material degradation (92).

Numerous wear studies on CoCr MoM contacts have reported that they exhibit running-in (20, 82, 85, 92, 95-98). Running-in is characterised by an initial high wear rate that subsides over time to a lower rate, often referred to as the steady-state. This phenomena has been observed in both tribometer

studies and in hip simulator studies. The initial high level of metal ions in patients with MoM THRs suggests that it also happens *in vivo.* Typically running-in occurs over the first 0.5 million (M) -1.0 million (M) cycles in hip simulator testing, however, it has been shown that factors such as bearing size can influence this (82, 85). There is no definitive answer to what causes running-in, however, during operation the surface roughness can be reduced which, limits the mechanical interaction of the surfaces. It has also been suggested that the local reductions in clearance taking place at the wear scar may promote more favourable lubrication between the surfaces (20, 62, 92, 98). It has also been shown that reductions in surface skew can take place and were observed with a reduction in friction, characteristic of that approaching fluid film lubrication (92). Other studies have demonstrated that tribological layers may form on the surface as a result of interaction with the lubricant and that the action of these layers may serve to reduce wear (99-102).

2.4.5 Effect of Carbon Content

There are a variety of different CoCr alloys used in MoM THR bearings that contain different amounts of other alloying elements such as molybdenum and nickel. In general these alloys can be split into two categories: those containing a high carbon content, typically around 0.2-0.35%, and those containing a low carbon content, typically around 0.05-0.07%. In the low-carbon alloy, the bulk of the carbon resides in solid solution (86) although the sparse presence of carbides has been observed (103, 104). Increasing the carbon content of the alloy encourages the precipitation of carbides, which cause a refinement of the grain structure and an increase in the hardness of the alloy (86, 103, 104). Studies on the wear characteristics of both high- and low-carbon alloys have demonstrated differences in their performance, both in tribometer studies and hip simulators. In general the wear rate of low-carbon alloys is greater than in high-carbon alloys. This effect is heightened in the extreme conditions found during linear sliding in the tribometer (27, 86, 91, 103, 104). Under simultaneous sliding and rotation, a self-polishing action takes place, which

reduces the total wear. This action was more effective on the low-carbon alloy (91), possibly due to its increased ductility. When high- and low-carbon alloys are paired together, tribometer studies have shown that the combined pin/plate wear rates are greater than for high-carbon/high-carbon pairings, and are less than low-carbon/low-carbon pairings. However, in some instances, pairing of high and low-carbon alloys can increase the wear of the low-carbon surface (86, 103).

In addition to varying the carbon content of alloys, the microstructure can be altered by a variety of different heat treatments. In general the carbide fraction is decreased with increasing temperature and exposure time (105). Bowsher (106) found that, when comparing a cast alloy to a heat treated alloy, heat treatment produced both finer grains and finer carbides. In this study there was no significant difference in the wear characteristics between the as-cast and heat treated samples, despite showing differing microstructures. Varano *et al* (107) found that cast CoCr outperformed wrought or heat treated samples in wear tests. However, the effect of heat treatment, which dissolved carbides and coarsened the grain structure, was beneficial to the reduction of wear when compared to the wrought specimens.

2.4.6 Particle Generation

During normal use the bearing surfaces of MoM hip replacements are subject to wear. Wear rates are usually measured as an estimated volume loss from explants, or a measured mass loss from simulator tests. They are typically in the region of 0.1 mm^3/million cycles in steady state conditions (74). A proportion of this material loss forms metallic particles that are liberated into the joint capsule. Estimates based on typical particle size and wear rates predict that as many as 10^{14} particles may be released from the bearing surface each year (46, 61).

In a study by Catelas *et al* (62) over 1000 wear particles were characterised from hip simulator tests. It was found that most particles were round or oval in shape, although some needle-like particles were also identified. Figure 2.13 shows some of the particles imaged in this study, during both running-in and steady state conditions. These results were consistent with a survey of particles found in the tissue of patients who were undergoing revision of MoM hip replacements (57, 61). Catelas *et al* (62) demonstrated that, on average, particles were generally larger in the first 0.25 million cycles compared with 1.75-2 million cycles; these were 52nm and 46nm respectively. It was also shown that a greater amount of needle-like particles were liberated in the early cycles. Martensitic needles may be more easily released from the subsurface under severe running-in wear as opposed to steady state conditions. Similar particle sizes have been measured both *in-vivo* and in other simulator studies, with particle sizes rarely exceeding 100nm (13, 46, 96, 108). Table 2.1 presents the particle sizes from a number of studies. All particles were produced from MoM articulation, either *in vivo* or *in vitro*. Laboratory experiments were all performed on hip simulators employing a physiologically representative gait cycle.

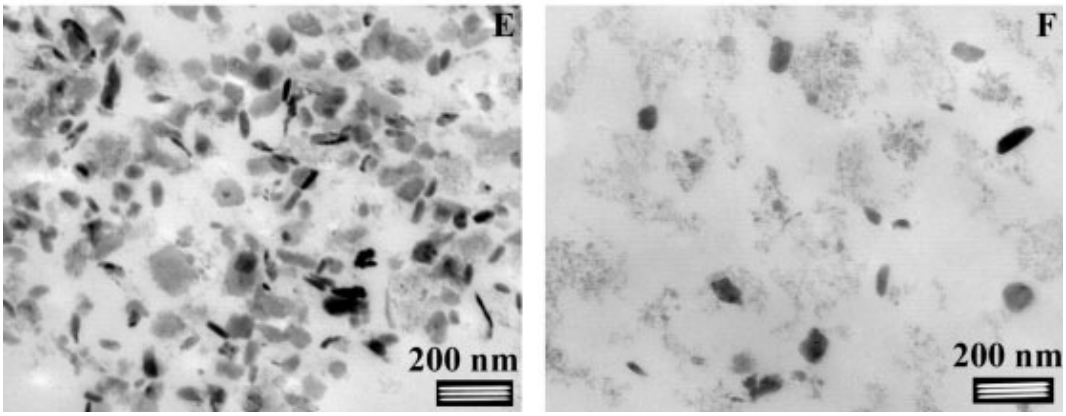

Figure 2.13: TEM images of particles produced during running-in (E) and steady state (F) from low-carbon MoM articulation (62).

Name	Year	*Vitro/ Vivo*	Bearing Diameter (mm)	Operation Conditions	Time of particle sample (Million cycles)	Size range (nm)	Average diameter (nm)	Number of particles measured
Doorn (61)	1998	*Vivo*	28-45	-	Following revision	6-834	42	>308
Tipper (13)	2002	*Vitro*	-	Standard gait	0-5	9-66	30±5	>100
Catelas (62)	2003	*Vitro*	28	Standard gait	0-0.25	14-253	20-84	3129
					1.75-2	11-225	17-76	1599
Catelas (109)	2006	*Vivo*	28-50	-	Following revision	-	29-59	9970
Bowsher (96)	2006	*Vitro*	40	Standard gait	2.5-3.0	10-1500	99-135	314
				Simulated jogging	3.0-3.6	10-1500	132-169	378
Brown (108)	2007	*Vitro*	28	Standard gait	0.67-1	8-116	35	150
				Micro separation	1.17-1.5	8-107	36	150
					3.67-4	6-146	31	150

Table 2.1: Summary of measured particles from in vivo and in vitro studies.

In an effort to determine the size and shape of particles under realistic conditions, authors have measured the particles released under loading cycles of increased severity compared with the commonly used Paul-type loading, which replicates an ideal walking cycle. Bowsher *et al* (96) compared particles produced in a hip simulator under walking conditions and jogging conditions and found significant differences between the two. The two different loading cycles are shown in Figure 2.14 (96). Under jogging conditions there was a 7-fold increase in total wear volume, which translated

to a 14-fold increase in the total number of particles. Particles were also larger, with a greater proportion having a needle-like shape. The change in particle shape and volume caused by the more extreme jogging cycle had an overall effect of increasing the particle surface area by a factor of 20. This astonishing increase could have significant implications when considering the *in-vivo* dissolution of such particles. Brown *et al* (108) investigated the effects of increased loading severity on particle morphology; this was achieved through the use of a loading profile containing micro-separation. Micro-separation causes the femoral head to make contact with the rim of the cup prior to striking its centre, resulting in a greater wear volume. Despite this, micro-separation produced no statistically significant difference to particle size or shape for MoM bearing surfaces.

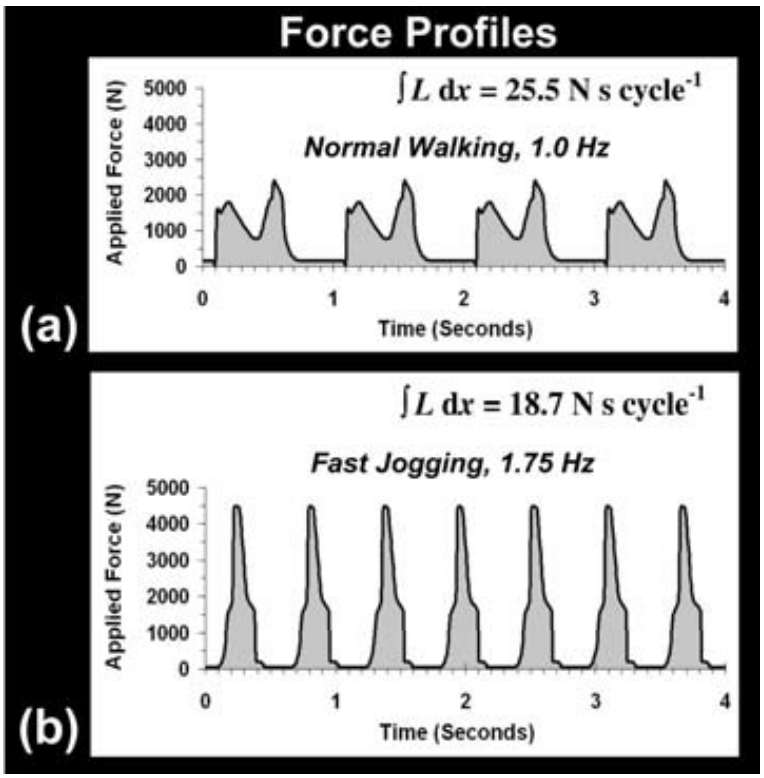

Figure 2.14: 'Force profiles timed over 4 s for (a) normal walking cycles (2450 N maximum; 1 Hz) and (b) simulated fast-jogging cycles (4500 N maximum; 1.75 Hz)' (96).

Studies of the chemical composition of metallic wear particles have shown that they can differ stoichiometrically from that of the bulk alloy. Doorn *et al* (61) identified particles from periprosthetic tissue consisting of an

amorphous CoCr layer surrounded by a crystalline chromium oxide layer. It has also been shown that the cobalt content of particles varied from no cobalt to an equal amount of cobalt, as is found in the base alloy (61, 110). This was explained by the idea that cobalt preferentially dissolves from particles originally consisting of CoCr (110). In contrast, Catelas *et al* (62) identified 3 types of particle from simulator studies: particles containing no cobalt, particles containing more Cr than Co, and finally, particles which contained both a low or absent carbon content and a greater abundance of Co than Cr. The fact that Catelas *et al* found particles with more Co than Cr, when others did not, may be explained by the differences in particle environment and dwelling times. The environment in a hip-simulator may be less corrosive than that found *in vivo*. In addition, hip-simulator tests accelerate the wear rate, producing a year's worth of debris in 12 days but without also accelerating the particle dissolution rate. These two factors could contribute to variations in the chemical changes taking place in the particles up to the point when they were measured.

Studies have shown that once particles are released into the joint capsule they are not confined to it and are disseminated around the body. Debris is sufficiently small to be transported by the lymphatic system where it has been found to accumulate at lymph nodes. Where this is the case, necrosis of the nodes has been observed (58). Particles were also found to accumulate in organs, particularly the liver, spleen and in bone marrow. The amount of disseminated wear material was greatest in patients who had experienced prosthesis loosening, or whose prosthesis contained a highly worn bearing surface (58). Despite the mobility of wear debris, a vast amount remains in or local to the joint capsule and is an additional cause for concern regarding patient health.

2.4.7 Surface Engineering

One technique for minimising the wear of MoM THRs is through surface engineering. This usually involves the coating of one or more bearing

surfaces with a thin hard coating. Fisher *et al* (111, 112) conducted two studies, which investigated the potential merits of utilising surface engineering to improve the wear resistance of 28mm MoM bearing surfaces. In one study (111), differential hardness bearings were coated with either no coating, the same coating, or a combination of coatings. These were applied by either arc evaporative physical vapour deposition or plasma assisted chemical vapour deposition, which produced thin coatings of between 2-12μm. The coatings tested were titanium-nitride (TiN), chromium-nitride, chromium-carbonitride (CrCN) and diamond like carbon (DLC). For both heads and cups, the wear rate over 2 million cycles was significantly reduced by the use of coatings, irrespective of the coating used. The presence of coatings had a notable effect on the release of metallic ions, reducing the concentration by at least 20 times. Overall CrN and CrCN were identified as demonstrating significant potential for reducing wear. After 5 million cycles the wear rate, compared to uncoated samples, was diminished by 36 times. In a different study (112), low-carbon femoral heads were coated with the same coatings as previously mentioned, but the high-carbon cups were not. For CrN, CrCN and DLC the wear rate was reduced on both the head and the uncoated cup. However, for TiN the overall wear rate was increased. This manifested as increased wear of the cup since the TiN coating provided superior protection of the head. Despite this, the ion concentrations for bearings with a coated head were lower than those without. This observation raises questions when comparing the performance of the uncoated bearing and the bearing with a TiN coated head. In determining which one gave the superior performance it is necessary to first establish whether it is more important to reduce the total wear volume or the total ion release. These findings demonstrate a great potential for surface engineering in the design of modern MoM prostheses, and is reflected by the on-going research into coatings for THRs in recent years (113-116).

2.4.8 Biological Lubrication and the Influence of Proteins

Total joint replacements are lubricated by a biological fluid that resembles the native synovial fluid prior to surgery (117, 118). It contains a combination

of dissolved salts, proteins, hyaluronic acid and phospholipids. The most abundant protein present is human serum albumin (HSA), but a-1-globulin, a-2-globulin, b-globulin, and c-globulin are also present. It has been demonstrated that patients suffering from osteoarthritis or rheumatoid arthritis have greater total protein concentration in their joint fluid than healthy patients. In addition, they also demonstrate a depletion of hyaluronic acid. In laboratory tribology experiments, bovine serum solution is frequently used as a simulated biological lubricant. It contains the same proteins as are present in human joint fluid, albeit in differing ratios, and a different total protein concentration (117, 118). Current guidelines recommend diluting serum to a total protein concentration of 17g/l, although this has been demonstrated to be inconsistent with that measured *in vivo* (117). In addition, upon dilution with distilled water the osmolality of bovine serum is reduced, hence it has been recommended that dilution with phosphate buffered saline (PBS) may be more relevant (117). Another potential shortcoming of using bovine serum is the absence of hyaluronic acid, which has a strong influence over fluid viscosity and its shear rate dependence (118). Figure 2.15 is a ribbon diagram of the HSA molecule, showing its secondary structure (shown in red)(119).

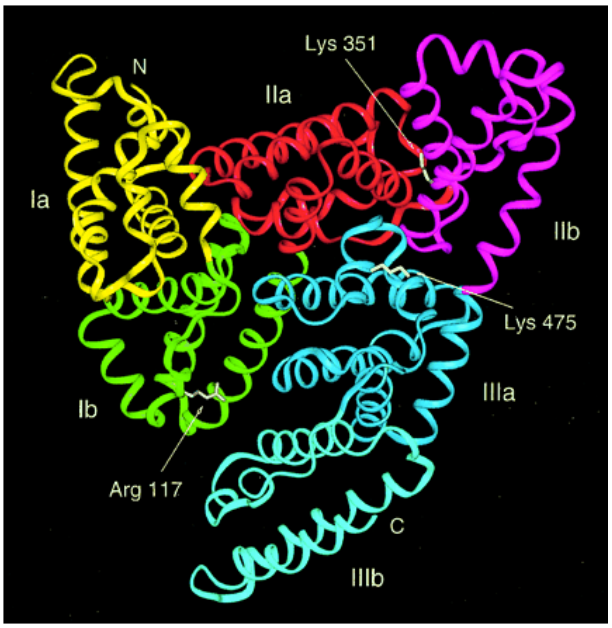

Figure 2.15: : 'Schematic drawing of the HSA molecule. Each subdomain is marked with a different color (yellow for subdomain Ia; green, Ib; red, IIa; magenta, IIb; blue, IIIa; and cyan, IIIb). N- and C-termini are marked as N and C, respectively. Arg117, Lys351 and Lys475, which may be binding sites for long-chain fatty acids, are colored white.'

Proteins are long chain biological molecules consisting of carbon chains and side chains that contain both an amino (NH_2) group and a carboxyl group (COOH). Protein chains are folded into a 3 dimensional shape containing 4 levels of structure. As previously mentioned, proteins are zwitterions and their net charge is dependent on the pH of the solvent in which they are dissolved (60). Each protein has an iso-electric point at which it has no net charge. In solutions with a pH lower than the iso-electric point, the amino group becomes protonated by the excess H^+ ions present in the solution to form $-NH_3^+$. This gives the protein a net positive charge. In solutions with a pH higher than the iso-electric point, the presence of OH^- ions in the solvent causes the carboxyl group to lose a H^+ ion. This forms $–COO^-$, which gives the molecule a net negative charge. The pH of joint fluid is approximately 7.4, which is greater than the iso-electric point of the contained proteins, rendering them with a net negative charge.

The way in which proteins affect the friction and wear of biomaterials is complex and is subject to wide variability caused by the precise conditions imposed. The influence has been shown to be dependent on protein type, protein concentration, material, surface wettability, lubrication regime, loading conditions, shear rate, the presence of dissolved salts, surface charge, time, pH and the structure of the protein (natural or denatured) (120-133).

When a biomaterial surface is exposed to a proteinaceous solution, proteins in the solution adsorb onto the material surface. Depending on the wettability of the surface and the nature of the protein this can occur though either hydrophilic or hydrophobic reactions (130, 131). Pin-on-plate tests have demonstrated that for MoP tribo-couples the presence of albumin can increase the wear due to increased surface adhesion (128, 134). However, studies have also shown that upon increasing the adsorption of albumin, by altering the wettability of the surface, the friction in MoP contacts can be reduced (130). It should be considered that lower friction does not always translate to lower wear. Natural albumin will adsorb to a polymer surface by hydrophilic attraction and will form a thick, uniform, low shear film that can reduce friction (121, 130). The presence of this film can inhibit polymeric

transfer to a metallic counter-surface, which may result in increased wear (128, 134). Denatured protein will tend to adsorb via strong hydrophobic reactions (121). This produces a denser, thicker film, which affords a greater degree of surface protection without the lubrication advantages associated with low shear resistance (121, 130). Albumin has little effect on CoC systems, as the amount of adsorbed protein is limited by the low wettability of commonly used ceramics such as alumina (134). For MoM tribo-couples, the presence of proteins has been shown to reduce friction and wear (128, 129, 134). This is caused by a multitude of factors that will be discussed in more detail.

Upon separate investigation of the lubricating properties of albumin and globulin, it has been demonstrated that they offer different properties. When lubricating CoCr MoM surfaces, solutions rich in globulin provide coefficients of friction close to those obtained for synovial fluid, and lower than that for albumin (129, 135). In addition, when solutions of bovine serum albumin (BSA) and bovine serum globulin (BSG) were exposed to temperatures of 60^0C, it was found that there was a loss of BSA but not of BSG from the solution, indicating the superior thermal stability of BSG to BSA (136). Although 60^0C is above the normal expected operating temperatures of a THR, flash temperatures are expected to reach as high as 67^0C (87, 102). Conversely, when used in a hip simulator wear test, BSG was found to degrade under the action of shear at a greater rate than BSA, altering the BSA/BSG ratio by 24% over 500,000 cycles (136). Studies performed on the lubricating film thickness between CoCr femoral heads and a rotating glass disk revealed that BSG solution formed considerably thicker films than BSA or serum solutions. This thicker film served to significantly reduce wear on the femoral head, when compared with either BSA or serum (120, 132).

The adsorption of albumin onto metallic biomaterials is affected by a number of different factors. As previously discussed, wettability of a surface and protein conformation may affect adsorption mechanisms. In addition to this, it has been demonstrated that the presence of magnesium cations can substantially increase the adsorption of albumin on to stainless steels (125). It is thought that the cations act as bridges between the metal surface and the protein, although this effect was not observed in the presence of calcium

cations, which may be attributed to their greater atomic radii. Other studies have also demonstrated that albumin adsorption is affected by the presence of phosphates which competitively adsorb onto metal surfaces (42). Mechanical factors also affect protein adsorption. During pin-on-disk experiments, preferential adsorption within the wear track of both UHMWPE and CoCr was observed using fluorescent staining (as illustrated in Figure 2.16) (134, 137). This may be an effect of increased protein denaturing, however, in the case of CoCr the wear track could have an increased surface activity due to depassivation. In addition, the effect of pH on the film developed between a CoCr/glass interface has been investigated (133). It was shown that increasing the pH from 7.4 to 8 resulted in a substantial increase in film thickness, but interestingly, it also increased the wear rate.

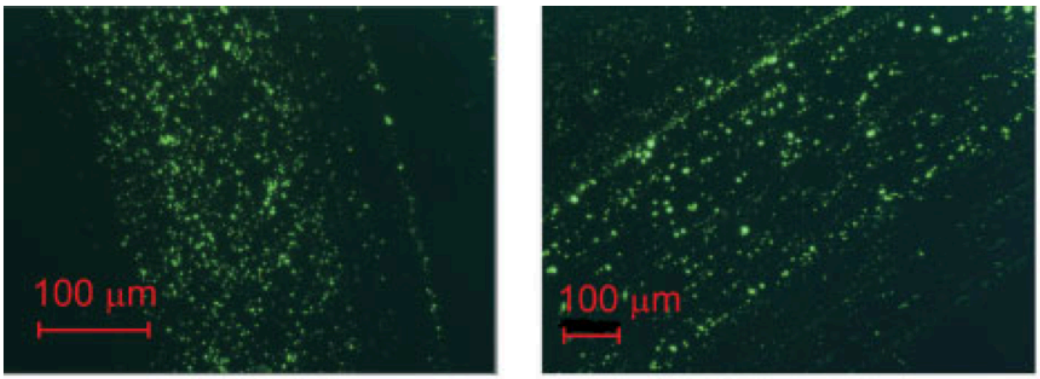

Figure 2.16: 'Fluorescent images on CoCrMo after sliding against a UHMWPE pin at a load of 2 N in (a) BSF, (b) BSA' (137).

It is known that proteinaceous solutions reduce both the friction and wear between MoM surfaces relative to saline solutions (129, 134, 135). This may not be surprising considering that the addition of proteins to a solution increases its viscosity. For most pin-on-plate tests and hip simulator tests, this would produce more favourable lubrication. However, it has also been demonstrated that proteinaceous solutions provide more favourable lubrication for MoM surfaces than carboxymethylcellulose (CMC), despite its higher viscosity (81, 135). This is an important finding, which demonstrates that the interactions of proteins at the metal/solution interface play an important role in reducing friction and wear. It has been observed in different wear studies that proteins may precipitate from solution due to denaturing

from temperature and shear (134, 136). Upon denaturing, the protein containing solution has been shown to increase in viscosity (134). This is in agreement with experimental evidence, which suggests that close to the metal surface, albumin forms a high viscosity gel-like layer capable of separating the surfaces, even in static conditions (120, 127, 132, 133). Repeated experiments between a CoCr femoral head and a rotating glass disk have utilised optical interferometry to explore the effects of proteins on lubricating film thickness (120, 132, 133). Observations of the film behaviour under an array of different test conditions suggested that proteins form a biphasic lubricating film, comprising a thin film adhered to the surface and a thick gel-like viscous overlay. This is caused by shear-induced protein aggregation at the inlet, where aggregated proteins form a viscous precipitate that adheres to the surface, which then acts as a lubricating film. Observations made in these studies demonstrated that the behaviour of proteinaceous lubricants departed from that predicted by current EHL theory. There was a much greater sensitivity to the effects of loading, and the effect of entrainment velocity on film thickness was dependent on protein concentration (120, 132, 133). These studies may explain the observations, made by Dowson (81), Scholes and Unsworth (135, 138, 139), of improved lubrication in protein containing solutions compared with CMC, despite their lower viscosity.

Proteinaceous films have been observed on bearing surfaces of metallic biomaterials that have been either explanted (46, 101, 102), or tribologically tested *in vitro* (46, 87, 106, 133). These layers are referred to as tribofilms or tribo-chemical reaction layers (TRLs) (often referred to as tribolayers). These differ from the adsorbed protein layers that form outside the contact region, as they are much thicker, ~100nm, compared with those in the non-contacting region ~1nm (101). It has also been reported that they are more compact and resilient to removal (133). Figure 2.17 shows the macroscopically visible TRLs reported by Wimmer *et al* (102).

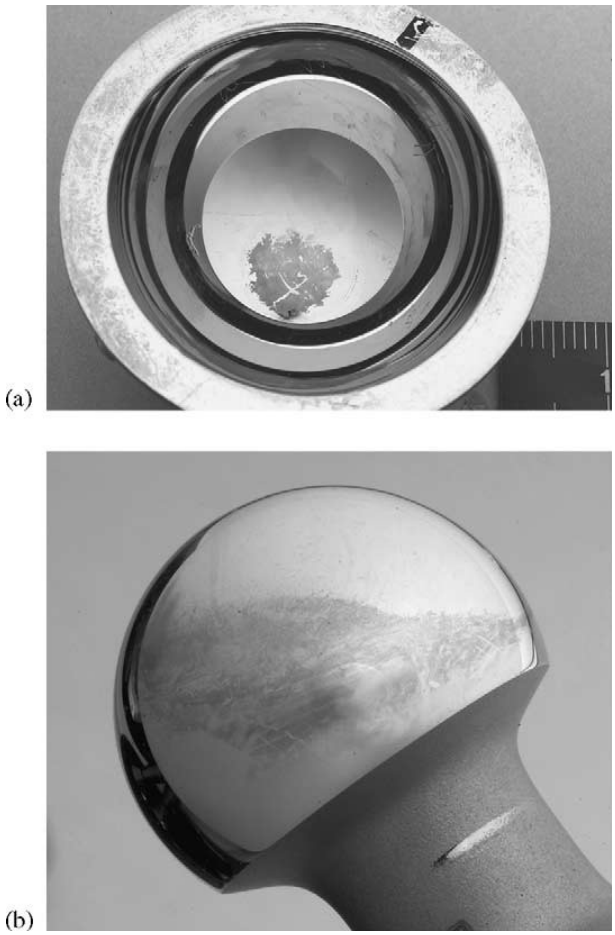

Figure 2.17: ‘Cup (a) and head (b) of an explanted McKee–Farrar prosthesis.’ (102)

The composition of TRLs is rich in carbon, which has been identified as organic, confirming it originated from proteins present in the lubricant (102). Other elements such as phosphorus, sulphur, nitrogen and oxygen were also identified using energy dispersive X-ray spectroscopy (EDX). It has been proposed that these layers are not simply made from layers of denatured protein, but chemical reactions took place to form an complex organometallic layer (101). Despite elevated flash temperatures and mechanical stress, the time taken to form an organometallic layer would be expected to exceed that of the *in vitro* test time. This was explained by the mechanism of ‘mechanical mixing’, of the organic layer and the alloy substrate (101). It has also been identified that, within this layer, debris can become trapped and, in some situations, may become compacted and fused together in surface grooves. This mechanism is thought to reduce the surface roughness and reduce wear (46).

Recent investigation of the carbon rich TRLs formed on MoM bearing surfaces suggests that partial graphitisation may be taking place within the film (100). This remarkable notion has been qualified through the use of electron energy loss spectroscopy (EELS) and Raman spectroscopy. EELS spectra of the carbon k-edge from a sample of the TRL revealed a prominent sp^2 π* component which was deemed indicative of graphitisation. Upon investigation, with Raman spectroscopy, the presence of a D- and G-line peak were identified at 1383cm^{-1} and 1567cm^{-1}. The shift in G-line position from 1580cm^{-1} in pure graphite suggested that the sample was between nano-crystalline graphite and amorphous carbon with 80% sp^2 bonding. This estimate is close to the 82% sp^2 bonding predicted from the EELS spectra after calibrating against highly ordered pyrolytic graphite (HOPG) (100). In the study, the effect of beam damage, from the TEM (in which EELS was conducted), was considered, however, this was not done for Raman spectroscopy. Usual mechanisms for graphitisation require pressure and temperature in excess of those expected in MoM hip prostheses, even when under the influence of catalysis (140, 141). It was also suggested that graphitisation in TRLs could promote solid lubrication, since graphite is a known lubricant in both dry and aqueous conditions (100). An issue with this concept is the lack of long range ordering in the carbon contained in the TRL. Graphite gains its lubricating properties through inter-lamella shearing of its graphene layers, which requires a high level of ordering that is not present in partially nano-graphitised carbon (142, 143).

2.5 Biotribocorrosion

2.5.1 Introduction

Hitherto, corrosion and tribology have been considered exclusively. This simplification is useful for describing the underlying principles of each, however, in a MoM bearing system, corrosion and tribological mechanisms occur simultaneously in the presence of organic species. The concurrent

interaction of tribology and corrosion, including their effect over one another, is termed tribocorrosion. In a tribocorrosion system, the total surface degradation (*T*) can be attributed to three main mechanisms. These are: degradation due to pure corrosion reactions (*C*), degradation due to pure mechanical wear (*W*), and the change in the level of degradation caused by the synergism (*S*) between corrosive damage and mechanical damage. The synergism term can further be divided into two sub-categories: the change in corrosion rate as a result of mechanical wear (C_w), and the change in mechanical wear rate as a result of corrosion *(W_c).* This is demonstrated in Equation (2.11) and (2.12).

$$T = C + W + S \tag{2.11}$$

$$S = C_w + W_c \tag{2.12}$$

Where,

T – Total degradation due to tribocorrosion

C – Degradation due to pure corrosion

W – Degradation due to wear

S – Degradation due to synergy between corrosion and wear

C_w – Degradation due to wear-enhanced corrosion

W_C – Degradation due to corrosion-enhanced wear

Modelling tribocorrosion in this way has been implemented with reasonable success in both erosion-corrosion and sliding contact systems. Electrochemical testing in the absence of wear gives *C*, which can be subtracted from the corrosion rate in tribological conditions to give C_w. To obtain the level of pure mechanical wear, a cathodic potential is usually applied to the sample during testing. This is done to suppress the anodic dissolution of the alloy, so that material degradation is exclusively caused by wholly mechanical interactions (*W*). By subtraction of *C,* and W from the total degradation under normal conditions, the contribution from W_c and C_w can be obtained. In practice, there are weaknesses with this approach, which

arise from the use of cathodic protection. If a sufficiently negative potential is applied, then water ceases to be thermodynamically stable and significant hydrogen evolution can proceed. It has been shown that hydrogen enbrittlement of metals will affect their wear behaviour and can cause substantial variability in results. Other issues with cathodic protection can arise in the presence of adsorbent species in the electrolyte, such as proteins or inhibitors. By varying the net surface charge, the mechanisms that govern species adsorption can be altered, changing the way they interact with the environment. Nakanishi *et al* (123) demonstrated that by varying the charge across both a silicone/steel and a silicone/titanium tribological interface, the relative adsorption of HA and γ-globulin was affected. This resulted in changes in friction and wear, depending on the strength of the electric field between the surfaces. In THRs there are a number of interfaces that succumb to degradation by tribocorrosion reactions. This can occur as a result of micro-motion between interfaces such as the stem/cement junction, the head/neck interface or as a result of relative motion between the bearing surfaces (see Figure 2.18).

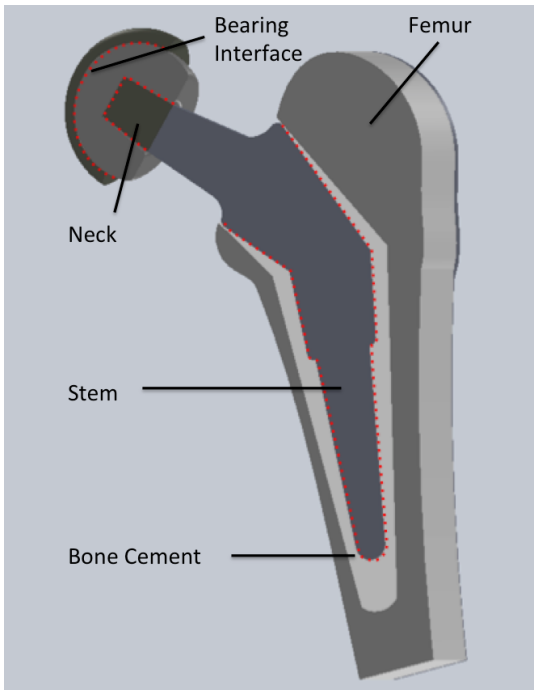

Figure 2.18: Total hip replacement, with tribocorrosion-prone areas highlighted.

2.5.2 Laboratory studies of biotribocorrosion

A slightly different method of characterising tribocorrosion relies on splitting the total degradation into a mechanical factor (k_m) and a chemical factor (k_c). The chemical factor is defined as the material degradation due to anodic dissolution, hence it includes both C and C_w (defined in the synergism model) but does not differentiate between them. The mechanical factor is the remaining damage, and can be thought of as a combination of W and W_c from the synergism model. By comparing the ratio of k_c/k_m, the degradation mechanism can be characterised by one of four systems. In a sliding contact, these are: wear $(k_c/k_w \leq 0.1)$, wear-corrosion $(0.1 < k_c/k_w < 1.0)$, corrosion-wear $(1.0 < k_c/k_w \leq 10)$ and corrosion $(k_c/k_w > 10)$. In erosion-corrosion systems, these are: erosion, erosion-corrosion, corrosion-erosion and corrosion. Degradation in a tribocorrosion environment is significantly affected by the mechanism of particle generation, and their egress from the interface. This was shown to be significant through the work of Barril *et al* (144), who found that tribometer stiffness affected the anodic current during the fretting of Ti6Al4V. It was thought that, in stiffer contacts, particles were ejected from the interface more readily, whereas reduced stiffness increased the tendency for particles to become trapped and deform in the contact (144).

Yan *et al* (95, 104, 145) demonstrated that the degradation of CoCr alloys, in conditions simulating those found on THRs bearing surfaces, was dominated by tribocorrosion mechanisms. Mechanical abrasion caused damage to the Cr_2O_3 passive layer within the wear scar. This resulted in local depassivation of the alloy and accelerated ion release. It was shown that in solutions of 50% bovine serum, corrosion and synergy contributed, by 20-24%, towards the degradation of HC-CoCr, when sliding was performed against a SiN ball (95, 104). These values were even higher for LC-CoCr, with corrosion and synergy making up 31% of material loss. When experiments were repeated in both Dulbecco's Modified Eagle's Medium (DMEM) and 0.3% NaCl, the proportion of corrosion and synergy was altered. In DMEM the proportion was the highest, making up 47% and 50% for HC- and LC-CoCr respectively, whereas, in 0.3% NaCl proportions were within 5% of those

measured in bovine serum (104). This highlights the significance of ions and biological species present in the solution. Serum contains proteins and DMEM contains amino acids whereas NaCl solution only contains ions. The presence of amino acids and proteins in Serum and DMEM, was shown to adversely affect the breakdown potential under sliding, when compared to 0.3% NaCl as shown in Figure 2.19. This did not, however, govern the total material loss, as DMEM was found to produce the lowest wear rates for both HC- and LC-CoCr.

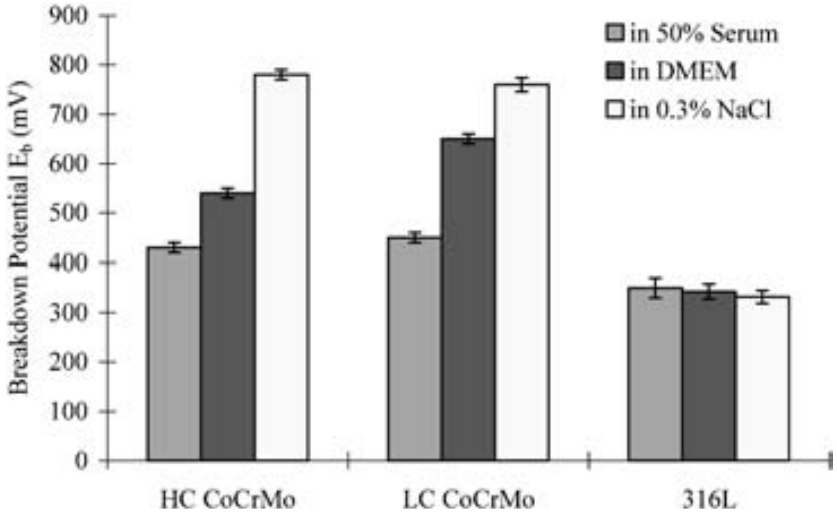

Figure 2.19: Breakdown potential, for different materials in different solutions (104).

Interestingly, and contrary to other studies, serum was found to produce the greatest wear rates (104), which generally show that proteins present in serum tend to reduce wear of CoCr (44, 129, 134, 135). This could be an artefact of the test setup; contact pressure between the ball and pin was in the region of 800MPa, which is substantially greater than that achieved in standard hip simulator testing. This increased loading severity could produce high volumes of abrasives, leading to a critically increased level of 3rd-body wear. In sliding contact, the addition of 3rd-body debris increases wear in both serum and NaCl solutions (44, 146-148). When larger concentrations of abrasives are present, the effects are more pronounced in serum. It has been shown that in the absence of 3rd body abrasives serum is effective at reducing the material degradation due to tribocorrosion between alumina and CoCr (149).

In addition to tribometer studies, Yan *et al* (150, 151) preformed studies on a pendulum hip simulator integrated with an electrochemical cell. Tests were performed on 36mm, HC-CoCr, MoM bearing surfaces. These studies showed that a similar breakdown of the surfaces occurred in the simulator as in the tribometer. Upon the transition from static conditions to dynamic, loaded conditions, the passive film on the CoCr surface was mechanically damaged, leading to corrosion. In both test configurations, this was demonstrated by a negative shift in OCP at the onset of dynamic loading, which remained low, only recovering upon a return to static conditions. Furthermore, the OCP was found to be greatly affected by the simulator loading cycle, and the presence of 3^{rd}-body wear particles (151). A considerably lower OCP was measured when the loading cycle reflected a twin-peak Paul-type cycle, with a 2kN peak load, as opposed to a constant 300N load. This may reflect an increase in the severity of contact brought about by the more aggressive loading cycle (150). In moving from a tribometer to a hip simulator, the action of mechanical depassivation increases in complexity since the lubrication regime moves from boundary- to mixed-lubrication. In the mixed-lubrication regime, it is more difficult to predict the influence of factors such as: gait frequency, and load, on mechanical depassivation. When aliquots of Co nano-particles were added to the bearing interface, the OCP shifted in the negative direction, indicating increased depassivation (151). This is demonstrated in Figure 2.20. The presence of particles may affect electrochemical measurements in a number of different ways. Pure Co particles that are smeared onto the interface will actively corrode, and since they are electrochemically coupled to the surface by contact, they will contribute towards any electrochemical observation made of it (152). Similar effects on OCP have been observed with SiC and Al_2O_3 particles; with increasing particle concentration, both the total material degradation and level of depassivation increased (44, 147, 148). Additionally, the roughness (R_a) of metal THR bearing surfaces is of the nano-scale, as are the lubricating films generated (75, 79). Hence, particles introduced to the interface may increase the degree of MoM contact, reducing the effective lambda ratio of the joint, and increasing the level of 3^{rd}-body abrasion depassivation. This mechanism is more detrimental when harder abrasives are present (148). Pure Co particles are relatively soft in

comparison to CoCr, suggesting that the level of 3rd-body abrasion they impart is diminutive.

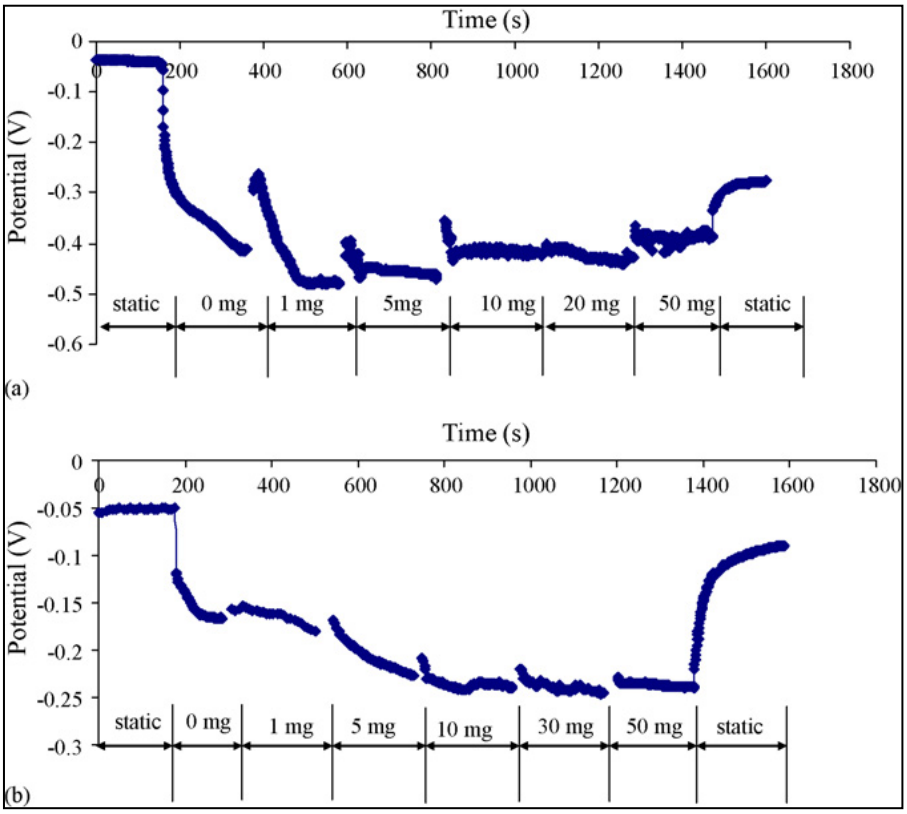

Figure 2.20: 'OCP as a function of time with different weight of particles at 300N in (a) 0.3% NaCl and (b) 25% serum.' (151)

As previously mentioned, tribocorrosion can also take place in regions where fretting is prevalent. Goldberg *et al* (32, 153, 154) demonstrated that the head/neck interface in MoM THRs suffers from mechanically assisted crevice corrosion, due to fretting. Electrochemical testing was undertaken, during fretting, on head/neck couples that were made from aluminium, CoCr, or a combination of both. It was found that upon the initiation of fretting there was a negative shift in OCP for all material combinations. This was accompanied by an increase in the fretting current, due to mechanical abrasion of the passive film (153, 154). When loading ceased, there was not an immediate recovery in OCP, as has been observed in other tribocorrosion systems. This was indicative of the initiation of crevice corrosion. Based on the total level of metal ion release, it was determined that mixed-metal tribo-couples were more susceptible to this mechanism of degradation, than

either CoCr/CoCr or Ti6Al4V/ Ti6Al4V (153). It was also shown that, in static tests, Ti6Al4V provided superior corrosion resistance over a wide range of applied potentials compared to CoCr. However, the oxide layer on Ti6Al4V is less robust and a greater corrosion current ensues in dynamic conditions, compared to CoCr (154).

When considering the tribocorrosion performance of components such as those demonstrated by Yan *et al* and Goldberg *et al,* it is important to consider that, in reality, these systems occur concurrently and are electrochemically coupled (see Figure 2.18). By having numerous systems, each of which contain passive and active regions coupled together, multiple galvanic cells may be produced, leading to complex corrosion reactions.

2.6 Summary of the Literature Review

Metal-on-metal THRs show good performance in terms of wear and corrosion due to the use of robust CoCr alloys which are self-passivating. Care must be taken, however, when estimating the *in vivo* performance of these materials based on *in-vitro* testing. Individual tribology and corrosion performance of an alloy may not accurately indicate its tribocorrosion performance. It has been demonstrated that passive biomaterials can become depassivated chemically, in the case of crevice corrosion, and mechanically, by 2^{nd}- and 3^{rd}- body abrasion, including fretting. In addition, even tribocorrosion testing of components may be unrepresentative of the *in-vivo* environment because components are usually tested individually rather than as an entire electrochemically coupled system.

Part 1 Tribometer Testing

Tribometer studies are useful in providing an initial insight into how a material combination will perform in a simplified situation. By reducing a complex tribological system, such as a THR bearing, to a simple pin-on-plate sliding configuration, individual mechanisms can be isolated and investigated. Part 1 includes the findings from two separate tribometer experiments. The first investigated the tribocorrosion performance of HC- and LC-CoCr alloys in MoM contact, in addition to MoP contact between LC-CoCr and UHMWPE. The second was a more detailed investigation of MoM contact between HC-CoCr/HC-CoCr couples. Details of the equipment and testing methods used for the two experiments are given in the following chapter.

Chapter 3 Tribometer Apparatus

3.1 Instrumented Tribometer

All the tests conducted in both experiments were performed on a Biceri reciprocating pin-on-plate tribometer. The plate samples used were 35mm diameter CoCr plates polished using a Buehler automatic polishing machine. A diagram of the tribometer is shown in Figure 3.1. For this configuration two different pin geometries were used: truncated cone polymer pins made from GUR 1050, which is a non-irradiated UHMWPE; and hemi spherically-tipped CoCr pins with a tip radius of 100mm. A normal load was applied to the pin sample through a pivoted beam and dead weight and reacted by the reciprocating plate, as illustrated in Figure 3.1. For the polymer pins, the contact pressure at the pin/plate interface was the normal load divided by the pin surface area (initially 12.6 mm^2). For the metallic pins the pressure was calculated using Hertzian contact analysis.

The contact was modelled as a sphere against a flat surface (Figure 3.2), which gave rise to an uneven pressure distribution across a circular contact patch. The pressure was calculated using Equation (3.1). Although Hertzian contact analysis is used to model dry contact, it can be used with reasonable efficacy for contacts operating in the boundary-lubrication regime. The plate and lubricant bath were driven across a linear slider bearing by a crank mechanism, causing them to slide in a linear reciprocating path. The stroke length could be varied to be between 5mm and 20mm at a frequency of 0-2Hz, but it was set to 10mm and 1Hz for all tests performed. This produced a constant normal load and a sliding velocity that varied sinusoidally over each cycle. The friction force imparted on the cantilever arm, by the pin/plate interface, was resisted by contact with a load cell. Measurement of the oscillatory force against the load cell enabled calculation of the friction between the static pin and the reciprocating plate. This data was fed into a Labview programme, where it was converted into a coefficient of friction between the pin and plate.

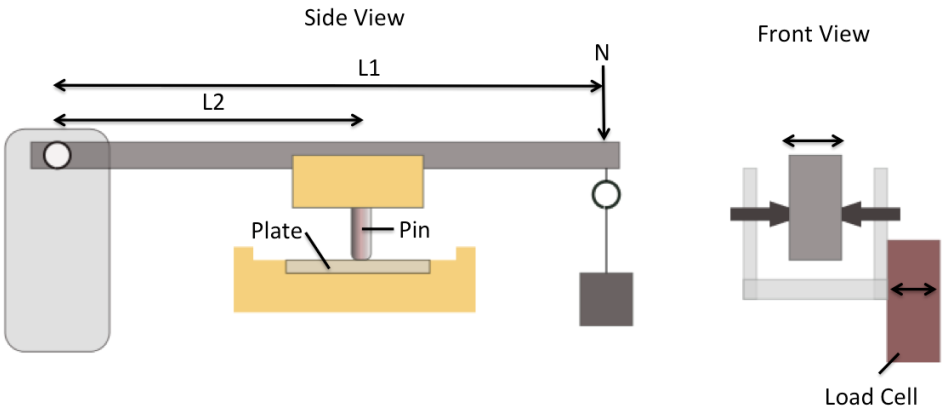

Figure 3.1: Tribometer and load cell configuration.

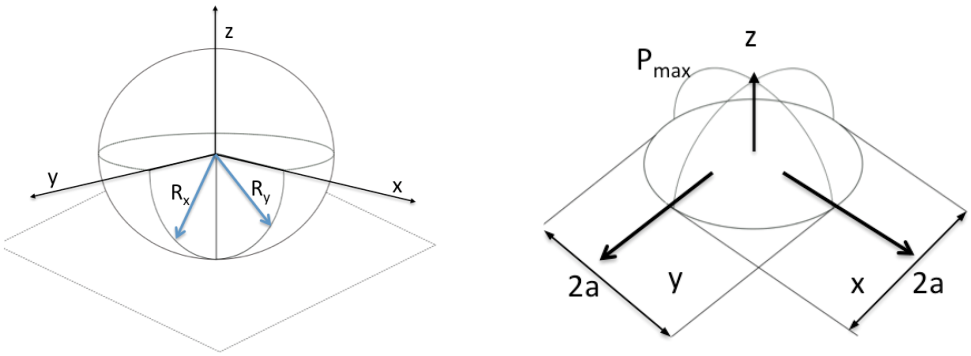

Figure 3.2: Spherical contact and associated pressure distribution.

$$P_{max} = \frac{2}{3}P_{mean} = \frac{1}{2\pi}\left(\frac{3wE'^2}{R^2}\right)^{\frac{1}{3}} \quad (69, 155) \qquad (3.1)$$

P_{max} - Maximum Hertzian contact pressure

P_{mean} – Mean Hertzian contact pressure

R – Effective radius $(1/R_x + 1/R_y)^{-1}$

$R_{x/y}$ – Radius in x/y direction $(1/R_A + 1/R_B)^{-1}$

$R_{A/B}$ – Radius of surface A/B

w – Load

E' – Effective elastic modulus

In order to permit electrochemical testing, the tribometer was instrumented with a 3-electrode, electrochemical cell. The 3-electrode cell consisted of: a working electrode, a silver/silver chloride (Ag/AgCl) reference electrode, and a platinum (Pt) counter electrode. In each test the working electrode was the metallic test specimen. This was the plate for MoP tests, and the combined pin and plate for MoM tests. The reference electrode used was a non-refillable, glass, RE-5B/RE-6, supplied by Bioanalytical Systems, Inc (Basi). The counter electrode was a piece of Pt mesh with a surface area of approximately 4cm^2. The counter and reference electrode were positioned either side of the working electrode, within 2cm of it. This small separation distance was maintained to reduce the effects of solution resistance on electrochemical measurements. All electrodes were connected to a Versastat 4 potentiostat, which was controlled using VersaStudio software. An illustration of this configuration is shown in Figure 3.3. To prevent the samples becoming electrochemically coupled to the metal tribometer, sample holders made from Delrin were used. Delrin is a poor thermal conductor; hence temperature control was maintained by encasing the entire tribometer in an insulated Perspex case, and heating from within using a 60w bar heater. This was regulated to within ±0.5^{0}C by a thermocouple positioned in the lubricant bath.

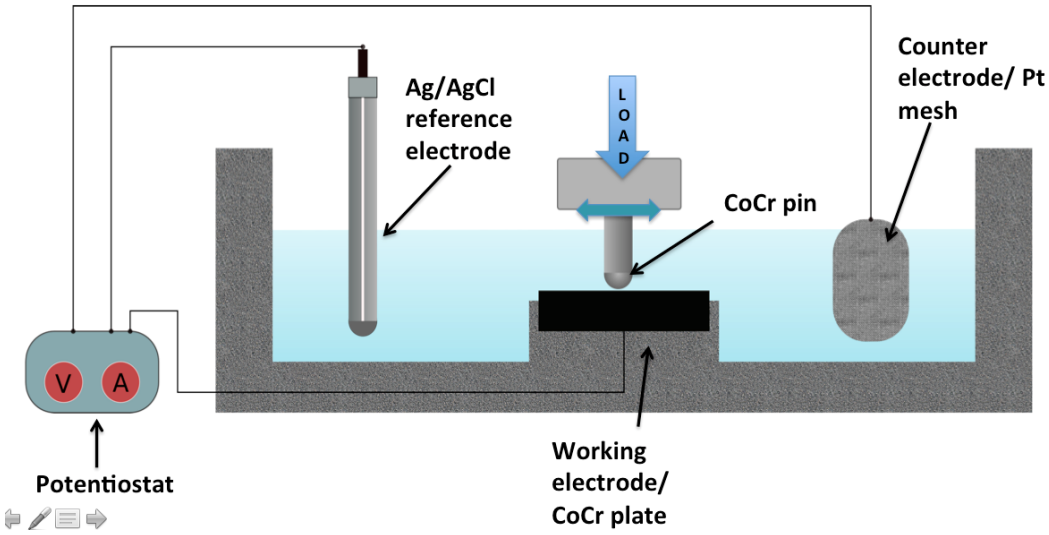

Figure 3.3: Tribometer instrumented with a 3-electrode cell.

3.2 Potentiostat

A potentiostat is a piece of electronic hardware that maintains the potential of a working electrode with respect to a reference electrode by adjusting the current supply to a counter electrode. The first 3-electrode potentiostats were used by Hickling (156) in 1942. The simple function of a potentiostat is to measure the potential difference between the working electrode and the reference electrode, and to apply a current through the counter electrode. The current is measured as an iR voltage drop over a series resistor (R_m). Several potentiostats were used in the studies outlined in this thesis: a Versastat 4 supplied by Princeton Applied Research, A Solartron SI 1280 supplied by Ametek and an Autolab PGstat 101.

3.3 Scanning Electron Microscope (SEM) and Focused Ion Beam (FIB) Etching

A Philips XL30 SEM was used to enable visual examinations of the sample surfaces to be made under high magnifications. The microscope was instrumented with secondary electron detectors, and back-scattered electron detectors, as well as an energy-dispersive spectrometer to enable EDX analysis. Image intensity from back-scattered electrons is related to the atomic mass of sample material. This facilitated determination of the elemental distribution of a surface, which would otherwise be unachievable using secondary-electron images. In addition, focused ion beam (FIB) etching was used to expose cross-sections of the sample (Figure 3.4). An FEA Nova 200 Nanolab dual beam FIB was also used to allow cross-sectional SEM images to be taken of the sample surfaces. Bulk etching was performed at 30keV, with a beam current of 5nA. Polishing was performed with a beam current between 0.1nA and 50pA and SEM images were taken at 5keV. Sputter coating was applied to the surface before a thicker 1 mm Pt layer was applied by a gaseous injection system. This was done in order to

protect the surface from the ion beam. Samples prepared in this manner enabled visual inspection by SEM of both tribofilms and the subsurface alloy.

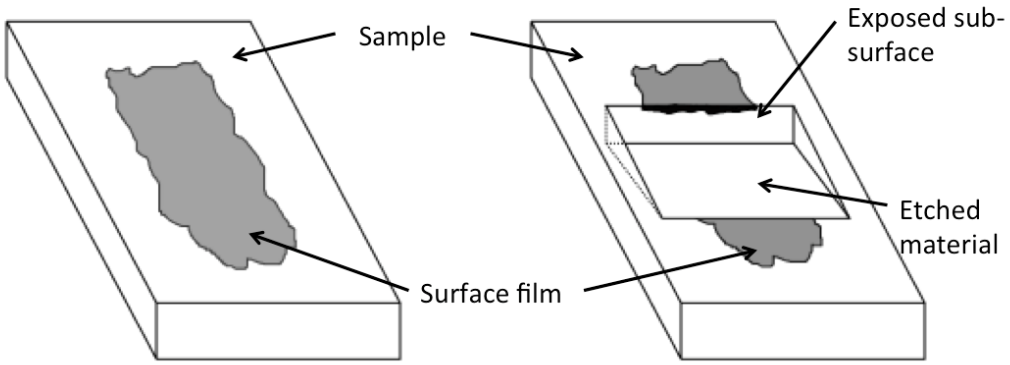

Figure 3.4: Diagram of sample prepared by focused ion beam etching.

3.4 Energy Dispersive X-Ray (EDX) Analysis

When a high-energy electron beam from the SEM reaches the sample surface, inner shell electrons may become excited to higher energy states. This results in the formation of an electron hole, which is subsequently filled by an outer shell electron from a higher energy state. The transition from a high-energy state to a lower energy state results in the emission of an X-ray of equal magnitude to the energy associated with the change in state. Since the X-ray energy corresponds to the specific energy levels within an element they can be used to identify the elemental composition of a surface. In addition, the quantity of X-rays produced is affected by the abundance of the element emitting them; hence the quantity of a specific element can be ascertained to within a reasonable level of accuracy, depending on the sample being analysed. Although EDX is considered a surface analysis technique, electrons do penetrate the subsurface and the signal measured reflects a volume of material rather than a surface area. The depth of penetration is largely influenced by atomic number; elements of a low atomic number are penetrated more readily than elements with a high atomic number.

3.5 Scanning White Light Interferometry

White light interferometry was performed using a Wyko laser interferometer. Interferometry is an example of non-contacting profilometry, and enables precise measurements of surface topography to be made. White light is focused onto the surface and reflected back; this produces interference with a reference light source, reflected from an internal mirror. When the optical path length of the two light signals differs by less than half of the coherence length of the light, diffraction fringes are produced. White light is used as it has a low coherence length and enables a finer resolution to be obtained. Images taken using interferometry were post-processed in Talymap Gold to give statistical parameters relating to surface roughness such as R_a. CoCr samples were ideal for analysis by interferometry due to their high reflectivity, however, CoCr pins were more challenging to image as their domed surfaces were prone to scatter light.

3.6 Inductively Coupled Plasma Mass Spectroscopy (ICP-MS)

Inductively coupled plasma mass spectroscopy is a technique capable of performing a chemical assay on given samples, to within parts per trillion accuracy. Detection can be performed on most elements with the exception of: H, C, N, O, Fl, Cl, Po, At, Fr, Ra and Ac, as well as some lanthanides and actinides. Samples are usually liquids, however, some gaseous samples and solids may also be analysed using specific preparation techniques. Liquid samples are vaporised by a nebuliser forming a fine aerosol. The aerosol is then subjected to a high-energy plasma beam, which ionises the atomic species. An ion lens focuses the charged particles onto a detector; this beam consists of species ionised in the spectrometer and species that were present as dissolved ions in the initial sample. Species are then separated based on their mass/charge ratio and directed towards the detector. Ions strike the detector causing a release of electrons. This enables quantification

to be made based on the current produced when compared to a calibration curve of known standards. Some limitations to the use of this technique arise when samples contain a colloidal suspension. This can be an issue for proteinaceous solutions or those containing nano-scale particles, which must first be removed before ICP-MS can be assumed.

3.7 Centrifuge

Centrifugation was used to separate agglomerated proteins and metallic particles from serum prior to ICP measurement. The centrifuge used was an Eppendorf 5415C with a maximum rotation speed of 14,000 revs/minute, giving a centripetal acceleration 15,996g.

Chapter 4 Tribometer Materials and Methods

Tribometer testing was split into two procedures referred to as Procedure A and Procedure B. Procedure A was performed as an initial investigation of both MoM and MoP tribocouples. Procedure B was a more detailed investigation of MoM contact only, in which the experimental procedure had been refined.

4.1 Electrochemical Measurements

4.1.1 Open Circuit Potential

Open circuit potential (OCP or free corrosion potential E_{corr}) is the electrochemical potential measured between the working and reference electrodes. The potential is achieved when the electrode is not polarised, that is to say, when no net current is flowing in the circuit between the working and counter electrodes. In this condition, the rates of the anodic and cathodic reactions at the surface of the working electrode are equal. A change in OCP demonstrates a change in the rate of anodic and cathodic half reactions, and can be used to give a semi-quantitative assessment of the level of passivation of the working electrode sample (114). A shift of OCP towards more negative values is indicative of an increase in the ratio of products in the anodic half reaction of the metal. When a substantial negative shift in OCP takes place this may be interpreted as a breakdown of passivity of the surface. Analogously, when the OCP becomes considerably more positive (ennobled) this is usually interpreted as the recovery of the film and the restoration of passivity (104, 157, 158), however it may also be caused by a change in the cathodic reaction.

4.1.2 Linear Polarisation Resistance (LPR)

Linear polarisation resistance is a widely used electrochemical technique used for measurement of corrosion rate. A linearly varying potential is applied to the sample, evoking a linearly increasing measured current between the working and counter electrode. An example LPR plot is shown in Figure 4.1. The change in current as a function of the applied potential gives the polarisation resistance (R_p). This can be used in conjunction with the Stern and Geary (159) Equation (3.1) to calculate the rate of corrosion (I_{corr}) of the sample. Linear polarisation is considered to be a non-destructive technique due to the low level of polarisation from OCP (±70mV and ±50mV in this study). The time taken for a single LPR test can be deduced from the scan rate and the scan range. Typical scan rates are between 0.167mV/sec-0.25mV/sec and occur over a 40mV-140mV range. Hence, the R_p calculated from a single LPR test is indicative of the corrosion rate over a period of minutes. It cannot be used to interpret short-term events such as oscillations in tribocorrosion occurring over a single cycle.

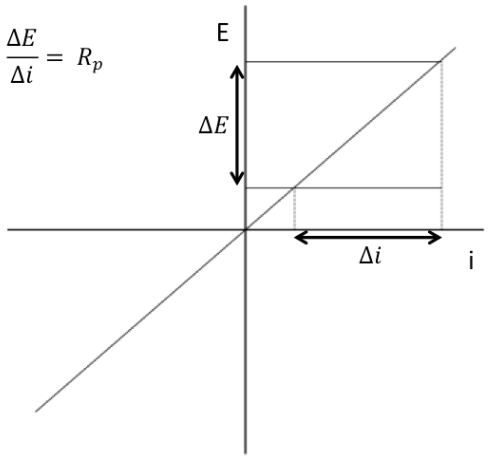

Figure 4.1: Illustration of a typical LPR plot.

Where,

ΔE – Change in potential

Δi – Change in current

$$I_{corr} = \frac{\beta_a \beta_c}{2.303 R_p (\beta_a + \beta_c)} \quad (4.1)$$

Where.

R_p – Polarisation resistance

β_a – Anodic Tafel constant

βc – Cathodic Tafel constant

I_{corr} – Corrosion current

4.1.3 Tafel Plotting

A Tafel plot is produced from data obtained from two separate electrochemical tests; an anodic polarisation test and a cathodic polarisation test. The Tafel region is approximately ±250mV from OCP. The data is plotted on a E vs. log i plot, on which there is a linear relationship between potential and the logarithmic current (or logarithmic current density), in the approximate ranges of +50mV to +250mV (Vs. OCP) and -50mV to -250mV (Vs. OCP), as shown in Figure 4.2. By comparing the rate of logarithmic increase in current to the applied potential, the constants β_a and β_c, known as the anodic- and cathodic-Tafel constants (measured in mV/decade), can be obtained. These are necessary for calculating i_{corr} (corrosion current) density) or I_{corr} (corrosion current) from the Stern Geary (159) Equation (4.1).

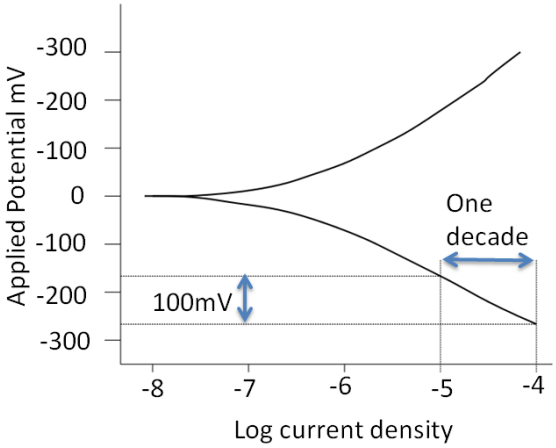

Figure 4.2: Schematic representation of the polarisation diagrams (anodic and cathodic) which comprise a complete Tafel plot.

4.1.4 Cathodic Protection

In order to suppress the anodic dissolution of the working electrode, it can be supplied with a cathodic current. The surface is given a net negative charge, which inhibits oxidation of the alloy from taking place. This technique is used to de-couple the electrochemical and mechanical effects leading to material loss. For tests performed under the influence of cathodic protection, it is considered that the total material loss is uniquely attributable to pure mechanical wear.

The potential applied must be sufficiently negative to inhibit the dominating anodic half reaction of the metal, whilst being of a level that will avoid evoking hydrogen evolution. This is determined by inspection of the relevant Pourbaix diagram. Figure 4.3 shows that, at pH 7.4, the anodic half reaction for the oxidation of cobalt $Co \rightarrow Co^{2+} + 2e^{-}$ is thermodynamically unfavourable when a potential below -0.5V (Vs the standard hydrogen electrode (SHE)) is applied (160). It can be seen, however, that hydrogen evolution also becomes favourable below a potential of -0.5V (Vs SHE). This diagram only gives a basic understanding of the stability of cobalt in an aqueous environment at 25^{0}C. The conditions found in the tribometer depart from this due to the increased temperature and presence of ionised species

in the electrolyte. For this reason cathodic protection was applied at -0.602V(SHE) or -0.8V (Ag/AgCl) (27, 88, 161).

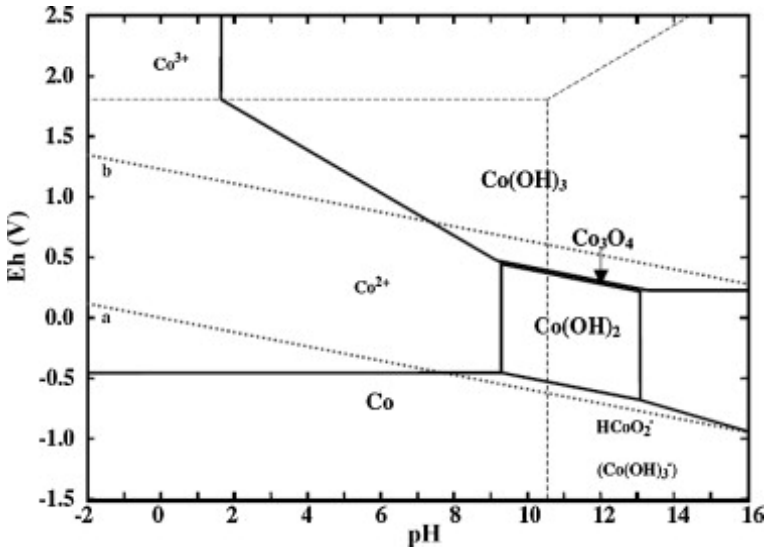

Figure 4.3: Pourbaix diagram for cobalt - water system (referenced against the standard hydrogen electrode) (162).

An important consideration when running tribocorrosion tests under the influence of cathodic protection is the influence of polarisation. This affects the ability of species in the solution to effectively adsorb and desorb from the bearing surface. It has been demonstrated that surface charge can influence the adsorption of charged species, such as proteins (123), as has been presented in section 2.5.2.

4.2 Tribometer Procedure A

Pin-on-plate tribometer tests were performed on a reciprocating tribometer, instrumented with a three-electrode electrochemical cell, as described earlier. In all tests performed, the plate specimen consisted of either a low-carbon (LC) or high-carbon (HC) wrought CoCr plate. The sliding length was 10mm and was maintained at a frequency of 1Hz. This reflects the frequency of oscillation typically measured during normal gait, as well as the

sliding length that a 36mm hip experiences between heel-strike and toe-off (163). Plates were passivated in 30% nitric acid for 30 minutes to develop a uniform passive film across the surface. The pins used were truncated-cone polymer pins and hemi-spherically tipped LC/HC-CoCr pins. Table 4.1 gives details of the pin/plate tribocouples. Two different lubricants were used: 0.35% NaCl solution and 25% foetal bovine serum. This was done in order to isolate the effects of organic species present in the serum. Both solutions had a conductivity of 0.68mS/cm, however, serum contains a greater chloride content, equivalent to 0.9% NaCl(aq). Tribological contact was maintained for a period of 6 h at 37^0C to approximate *in-vivo* temperatures. During the test, linear polarisation resistance (LPR) tests were performed to determine the polarisation resistance (Rp). This was done at the start of the test and every 90 minutes thereafter, and again 30 minutes following the end of the dynamic test. In between linear polarisation the OCP was measured and recorded.

The materials and roughness of the pins and plates were selected to represent materials currently used in commercially available THRs. The load used was selected to give initial contact pressures comparable to the initial maximum Hertzian contact pressures experienced during a normal walking cycle. These were calculated using Equation (3.1). In the tribometer, the initial contact pressure developed was 2.5MPa and 58.4MPa for the MoP and MoM configuration respectively. These were based on a 75kg body transmitting 4 times body weight during heel strike, for CoCr-MoM and MoP 36mm THRs, with 100 and 225 mm diametrical clearance, respectively. The resulting contact areas between the pin and plate were 12.6 mm^2 and 0.023mm^2 for MoP and MoM, respectively. Assuming dry Hertzian contact, the maximum contact area expected between a MoP and MoM hip bearing surface would be approximately 990mm^2 and 75mm^2, respectively. Due to the geometry of the polymer pin, it does not entrain a lubricating film when properly aligned. The metal pin, however, has a domed surface that may entrain a fluid film. Using the Dowson-Hamrock equation (73, 74) , the film thickness was calculated to be sufficiently thin to be considered as a severe mixed or boundary film. To improve reliability, each test condition was repeated three times.

Hemi-spherically tipped pins are commonly used for tribometer studies, as they do not produce edge loading, even when slightly misaligned. It is difficult to produce polymer pins with a hemispherically tipped surface, which

is why truncated cone pins were used instead. The truncated cone design allows the pin body to have the necessary girth to resist flexion caused by friction at the pin surface, whilst has a reduced surface area to increase the pressure at the contact interface. Anodic and cathodic Tafel constants of 120mV were used in the calculation of corrosion current.

Pin	Plate	Initial Contact Pressure (MPa)	Pin (R_a)	Plate (R_a)
UHMWPE	LC CoCr	2.5	0.8-1.0μm	<10nm
LC CoCr	LC CoCr	58.4	<10nm	<10nm
HC CoCr	HC CoCr	58.4	<10nm	<10nm

Table 4.1: Material combination, contact pressure and surface roughness for Procedure A tribocouples.

Tribofilms developed on the surfaces were imaged using FIB SEM (see 3.3) and a chemical assay was performed using EDX (see 3.4). Following testing the surface topography of pins and plates was mapped using white light interferometry (see section 3.5).

4.3 Tribometer Procedure B

The same instrumented tribometer configuration and lubricants were used as described in Procedure A. In addition, the stroke length of 10mm and frequency of 1Hz was also maintained. In this procedure, however, only high-carbon CoCr pins and plates were investigated, two repetitions were performed under each condition. The pins and plates were passivated using the procedure previously described and a greater load was applied to account for the reduction in pressure caused by the domed pin being worn flat. A 126N load was applied to generate an initial Hertzian contact pressure of 210MPa. The initial point-contact, caused by the domed surface of the

pin, became a flat area-contact as it began to wear. This caused a decrease in contact pressure over the duration of the test, finally reaching a value of approximately 30MPa. The calculated change in contact pressure, as a function of wear is shown in Figure 4.4.

To assess the contribution of corrosion to total material degradation, both lubricant tests were run under free corrosion conditions and under the influence of cathodic protection (CP), as described in section 4.1.4. Throughout the test, open circuit potential (OCP), friction, and LPR were measured. LPR was performed at the start of each test, and every hour thereafter, until the cessation of friction, whereupon it was measured once more after 10 minutes. For LPR measurements, the scan range used was ± 70mV from OCP at a rate of 0.25mV/sec. Tafel slopes were obtained to determine the Tafel constants necessary for converting polarisation resistance into corrosion current. For two tests at each condition, lubricant samples were taken, and ICP-MS (see section 3.6) was used to measure the concentration of metallic ions. To prepare for ICP-MS, samples were diluted in a 1:1 ratio with 5% nitric acid, and centrifuged at 14,000 rpm for 10 minutes. The supernatant was collected and passed through a 1µm filter prior to further dilution in a 1:4 ratio with 2.5% nitric acid. Table 4.2 gives details of the pin/plate tribocouples.

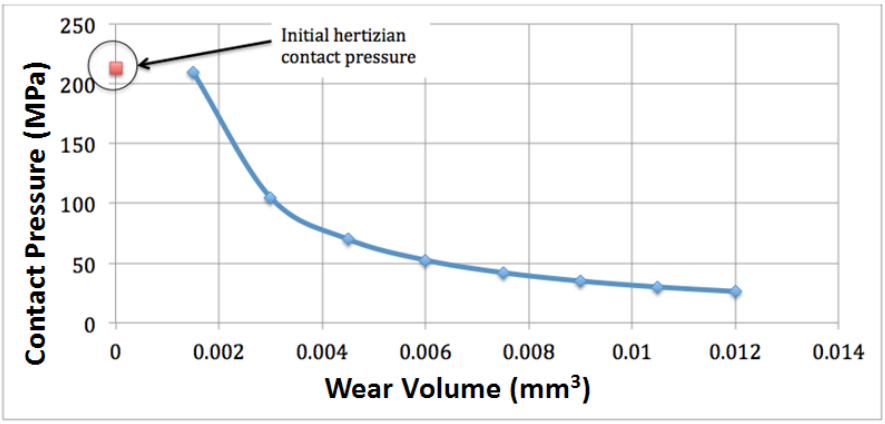

Figure 4.4: Change in contact pressure as a function of pin wear.

Polarisation Conditions	Pin	Plate	Initial Contact Pressure (MPa)	Pin (R_a)	Plate (R_a)
Free corrosion	HC CoCr	HC CoCr	210	<10nm	<10nm
Cathodic Protection	HC CoCr	HC CoCr	210	<10nm	<10nm

Table 4.2: Material combination, contact pressure and surface roughness for Procedure B tribocouples.

Chapter 5 Tribometer Results

5.1 Results from Procedure A (Testing of MoM and MoP sliding pairs)

5.1.1 Open Circuit Potential

For all tests, the transition from static to dynamic conditions was met with an immediate negative shift in OCP. This is shown for MoP, LC-MoM and HC-MoM couples in Figures 5.1, 5.3 and 5.5 respectively, and quantified in Figures 5.2, 5.4 and 5.6. A negative shift may be interpreted as an increase in the anodic dissolution of the surface caused by mechanical depassivation of the passive film formed on the surface before testing, as previously discussed.

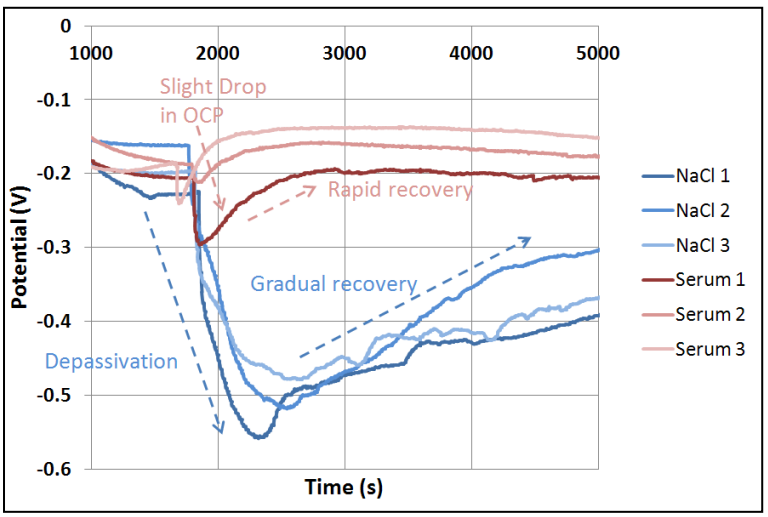

Figure 5.1: Initial open circuit potential response for 3 replicates of metal-on-polymer couples tested in either NaCl(aq) or serum solution over the first 5000s.

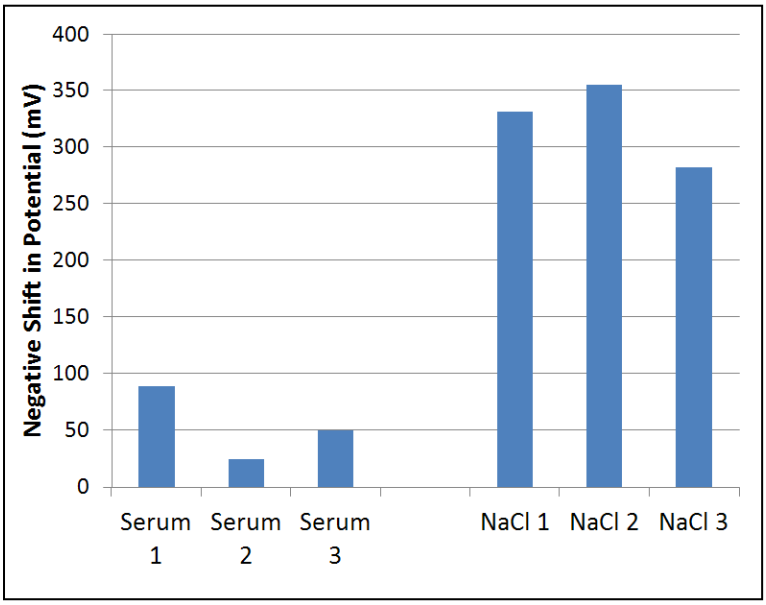

Figure 5.2: Negative shift in open circuit potential at the onset of motion for metal-on-polymer samples tested in either NaCl(aq) or serum solution.

Figure 5.1 shows the initial OCP response for the MoP systems at the onset of motion. In a solution of NaCl, there was an immediate negative shift in potential. This was followed by a gradual recovery in potential. When serum solution was used, there was a slight negative shift in OCP, followed by a rapid ennoblement. The magnitude of the negative shift in OCP for each of the tests is shown in Figure 5.2. It can be seen that the change in OCP for tests performed in serum was relatively small. However, in NaCl(aq) the negative shift was much greater, and took longer to recover. This suggested that the proteins present in serum initially provided a level of protection against mechanical depassivation. It has been shown that serum can inhibit polymeric transfer between MoP surfaces, leading to an increase in wear (128, 134).

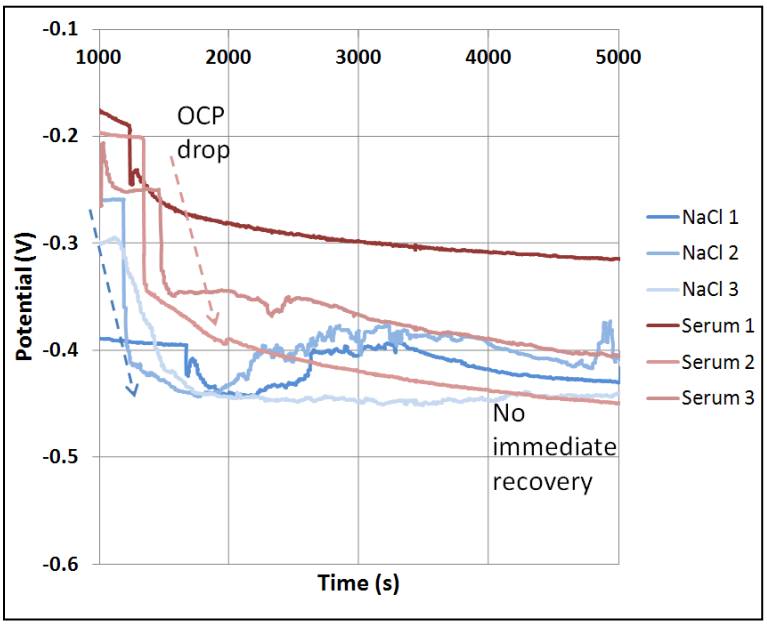

Figure 5.3: Initial open circuit potential response for low-carbon metal-on-metal couples tested in either NaCl(aq) or serum solution over the first 5000s.

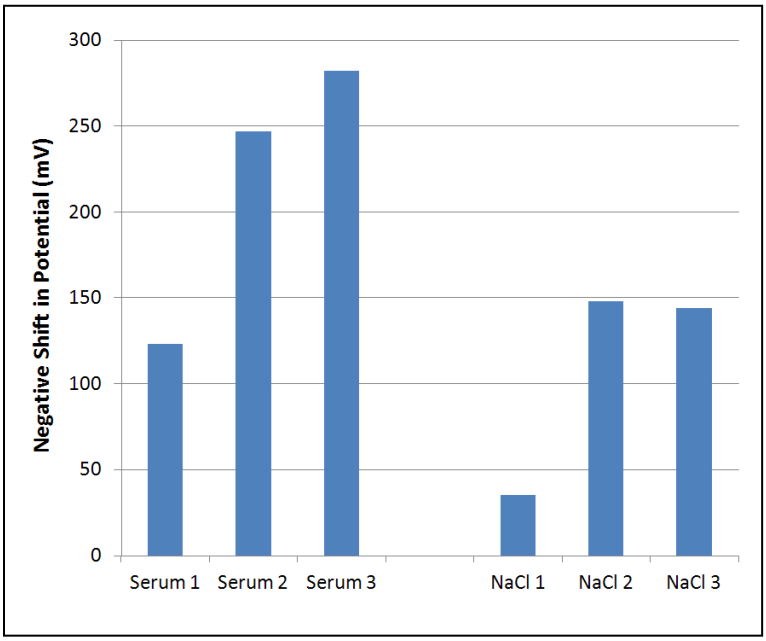

Figure 5.4: Negative shift in open circuit potential at the onset of motion for low-carbon metal-on-metal samples over the first 5000s.

For the LC MoM couples, there was a negative shift in potential at the start of motion (shown in Figure 5.3). Unlike the MoP samples, the OCP of MoM

samples continued to decrease after 5000s. This indicated that there was no recovery of the passive film during this period, and a depassivation/repassivation equilibrium was created. For LC MoM samples, the greatest negative shift occurred in serum. However, it should be noted that for the tests performed in NaCl, 'Test 1' showed little initial depassivation. This is because its initial OCP (prior to motion) was substantially more negative than for the other tests. This could have been caused by accidental depassivation during the experimental test setup.

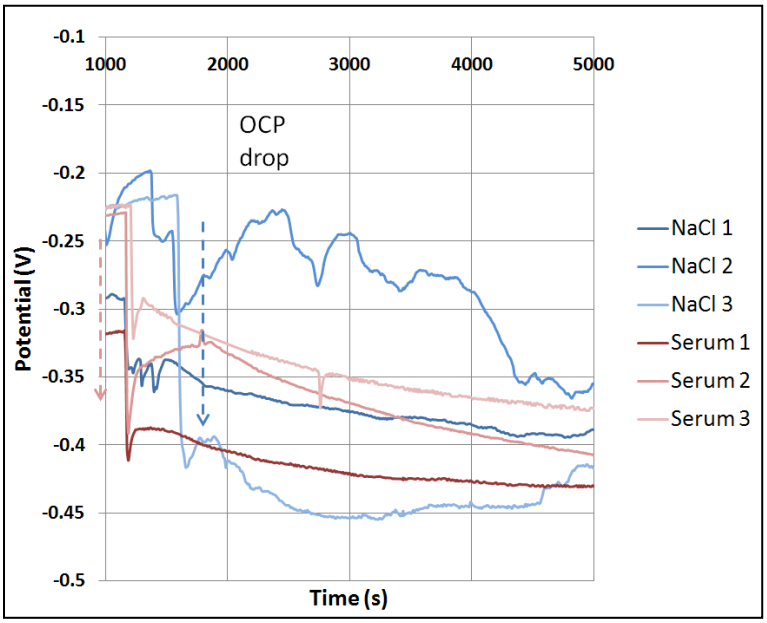

Figure 5.5: Initial open circuit potential response for high-carbon metal-on-metal couples tested in either NaCl(aq) or serum solution over the first 5000s.

For the HC MoM couples there was also a negative shift at the start of motion (shown in Figure 5.5), however there was no clear difference between the shift of potential in serum or NaCl(aq). The potential of the first test in serum and the first test in NaCl were slightly more negative than any of the others. This could suggest that the reference electrode potential might have drifted, causing a shift in the measured potential of the sample. Small changes in potential can be attributed to fluctuations in temperature or the chloride concentration in which electrodes are stored. In addition, disposable reference electrodes (such as the RE-5 and RE-6 used in this experiment)

have a finite lifespan for which they maintain a constant potential. After which the potential will drift and the electrode must be replaced.

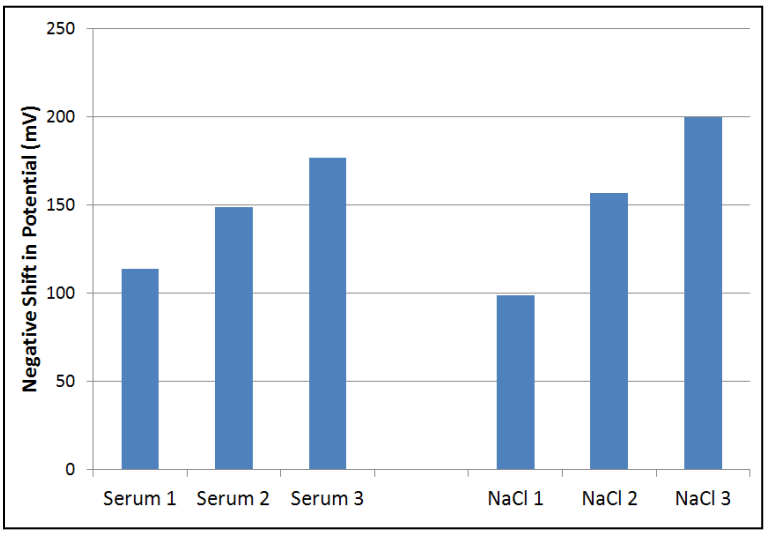

Figure 5.6: Negative shift in open circuit potential at the onset of motion for high-carbon metal-on-metal samples tested in either NaCl(aq) or serum solution.

Comparing MoM and MoP tests, it can be seen that the negative shift at the onset of motion was greatest for MoP tests in serum. This occurred despite lower contact pressure in the MoP system and the soft UHMWPE counter face. However, this may be explained by the greatly increased contact area in the MoP system compared to the MoM system, 12.6mm^2 as opposed to ≈0.1mm^2.

The response of OCP over the entire test duration for each of the materials pairs are shown in Figures 5.7-5.9 Figure 5.7. It is clear that the response in OCP is sensitive to both the lubricant and the material of the pin and plate.

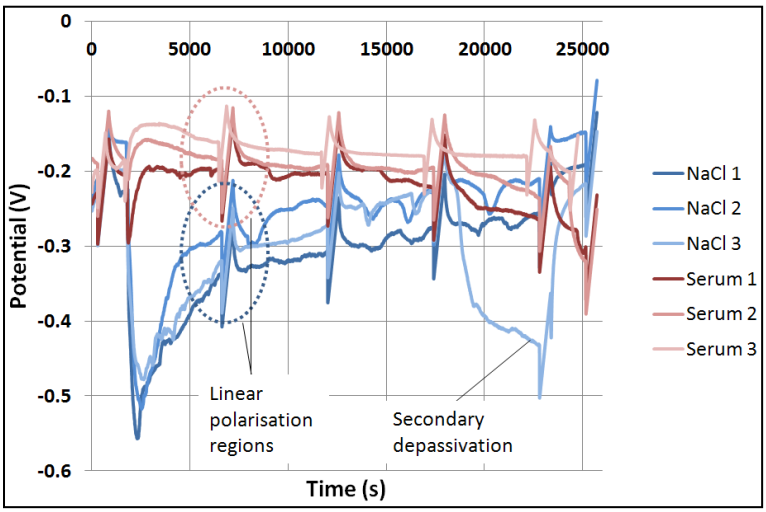

Figure 5.7: Open circuit potential response for 3 replicates of metal-on-polymer couples tested in either NaCl(aq) or serum solution over the test duration.

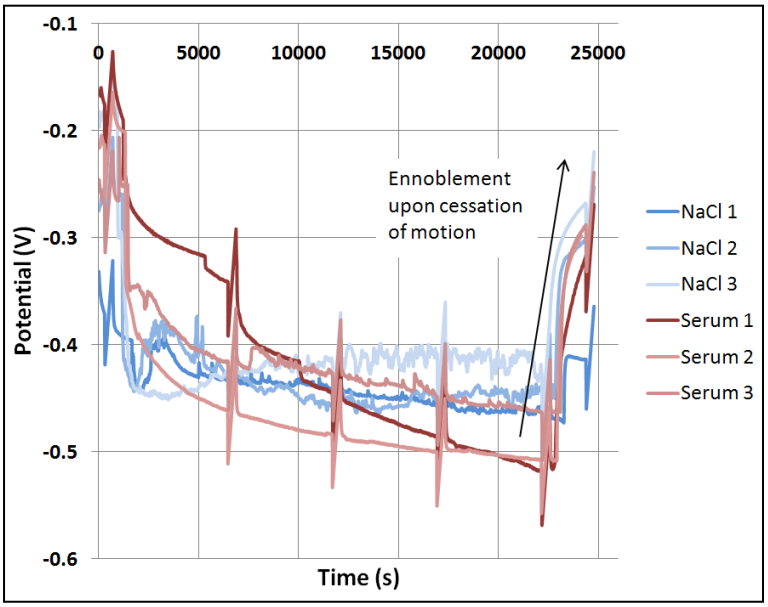

Figure 5.8: Open circuit potential response for low-carbon metal-on-metal couples tested in either NaCl(aq) or serum solution over the test duration.

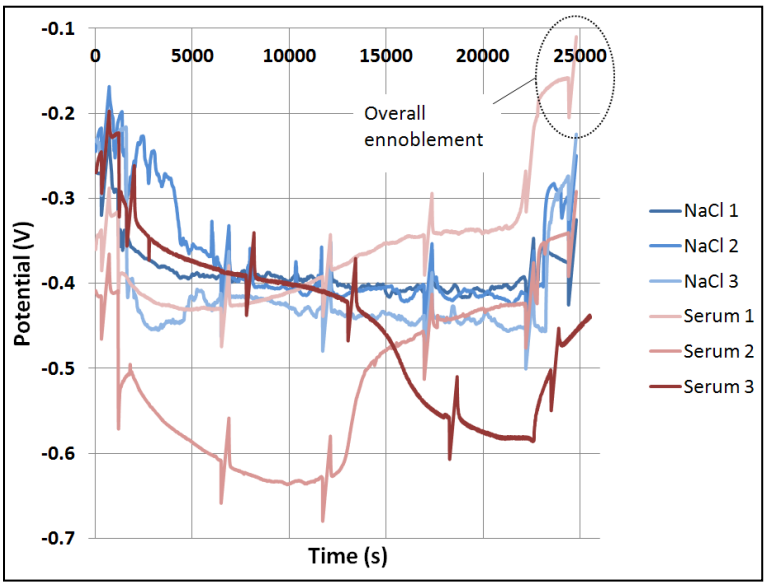

Figure 5.9: Open circuit potential response for high-carbon metal-on-metal couples tested in either NaCl(aq) or serum solution over the test duration.

Figure 5.7 shows that there was little variation in OCP for the MoP pairs following the initial depassivation repassivation, with the exception of the third test performed in NaCl(aq). In this test there appeared to be a secondary depassivation event. This may be attributable to the action of 3rd body debris, such as a metal carbide, becoming lodged in the pin counter face and scratching the metal surface.

Figure 5.8 shows that the low-carbon alloy was depassivated, and remained depassivated for the duration of sliding, only recovering upon the return to static conditions. The tests performed in serum appeared to have a continuously decreasing potential over the test duration whereas the tests performed in NaCl(aq) had a fairly constant potential following depassivation.

Figure 5.9 shows a fairly large amount of variability between the behaviour of the high-carbon samples tested in serum. The first test performed in serum finished with a potential more noble than at the start of the test. It is unlikely that the surface would be more passive at the end of the test hence it may indicate that the sample was initially in a state of partial depassivation (this could occur by accidental scratching during the test set up).

5.1.2 Corrosion Current (measured by LPR)

As indicated by the response in OCP, the sliding action between the pin and plate caused an increase in corrosion, indicated by a reduction in polarisation resistance of the entire sample. This was converted into a corrosion current from the whole surface, as previously outlined. The variation of total corrosion current for MoP couples is shown in Figure 5.10 and, for MoM couples in Figure 5.11. It is clear that the increase in corrosion caused by depassivation was substantially greater for MoM tribo-couples than for MoP tribo-couples. This was supported by interferometry images showing severe abrasion of the MoM surfaces, and SEM images showing minor wear of the MoP surfaces. It should be noted, however, that despite the absence of considerable wear to the plate, there was an increase in corrosion current, although not enough to suggest that the surface had become depassivated. For MoM tribocouples, the vast increase in current suggested that localised depassivation had taken place.

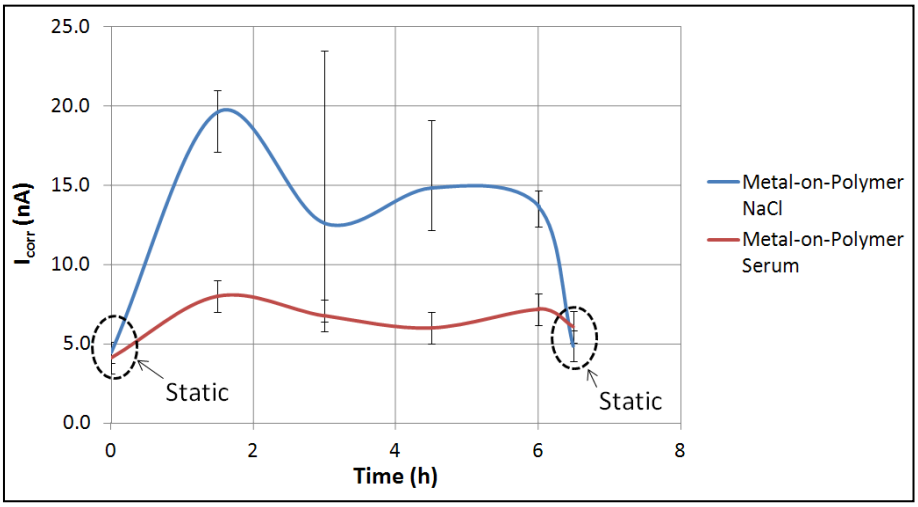

Figure 5.10: Variation of corrosion current for metal-on-polymer couples over the test duration tested in either NaCl(aq) or serum solution at 1Hz for a sliding distance of 216m.

Typically, in corrosion studies, the corrosion rate per unit area (known as the corrosion current density) is calculated to compare the rate at which surface dissolution took place. This is more complex for a tribocorrosion system as

there is a passive region and a depassivated region, as shown in Figure 5.12. In this configuration the regions outside of the wear scar are assumed to corrode with the passive current density, measured prior to the onset of sliding. Regions inside the wear scar are assumed to corrode with a current density, which would balance the increased current over the whole sample during sliding.

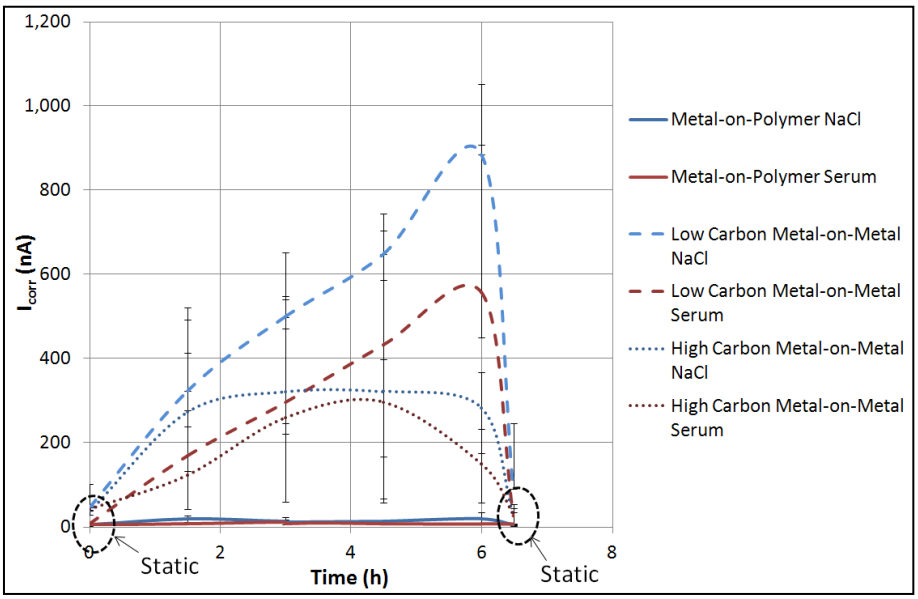

Figure 5.11: Variation of corrosion current for metal-on-metal and metal-on-polymer couples over the test duration tested in either NaCl(aq) or serum solution at 1Hz for a sliding distance of 216m.

It has been shown that under anodic polarisation, over a single cycle, the current is proportional to the absolute sliding velocity of the pin (161). Since a single LPR measurement takes minutes to complete, the cyclic variation in current density caused by the sliding velocity of the pin is disregarded for this analysis. For MoP tests, the area of metal contacted by the pin over one cycle was 52.6mm^2, which is 8.4% of the entire sample. For MoM samples, elevated corrosion also took place from the pin surface. The initial wear scar size was 2.5mm^2, which accounted for 0.33% of the total metal surface exposed to the electrolyte. However, this area increased rapidly as the domed pin surface was worn away. The currents tended to be lower for high-carbon samples, and lower for tests run in serum, although not significantly. The large variability of the measurements shown in Figure 5.11 reflect the

inherent difficulties with measuring currents in the sub μA scale, where noise is a considerable portion of the measured signal.

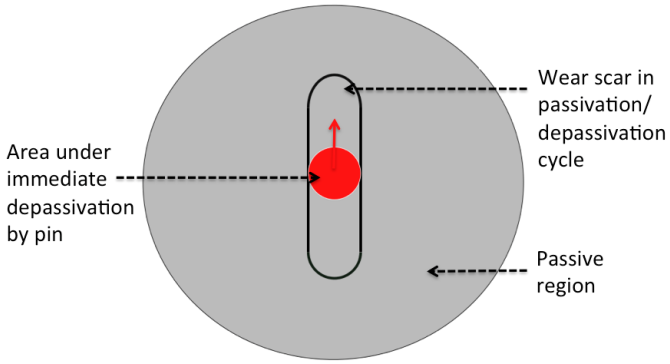

Figure 5.12: Plate specimen showing wear scar, passive and depassivated regions.

As explained previously, corrosion current can be converted into a mass loss using Faraday's Equation (5.1). This was done for each of the test conditions; the results are shown in Figure 5.13. Showing the mass loss due to corrosion in this way emphasises the increased anodic dissolution in between MoM sliding pairs.

$$m = \left(\frac{Q}{F}\right)\left(\frac{M}{z}\right) \tag{5.1}$$

Where,

m – Mass of corroded material

Q – Total charge transfer

M – Atomic mass

z – Number of electrons lost in anodic half reaction

F – Faraday constant

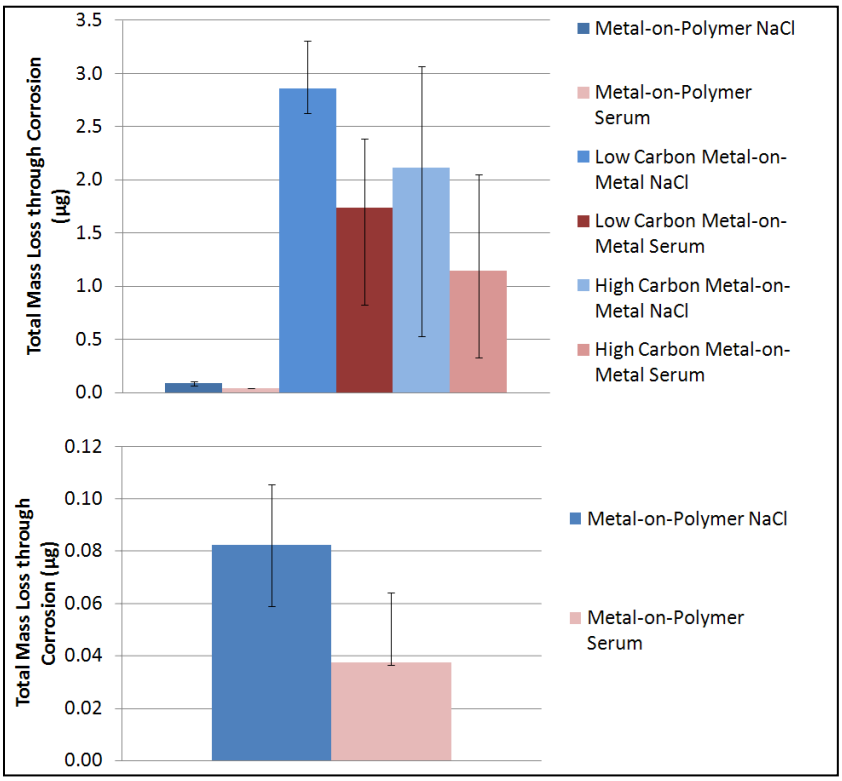

Figure 5.13: Total electrochemical mass loss over the test duration tested in either NaCl(aq) or serum solution at 1Hz for a sliding distance of 216m.

5.1.3 Scanning Electron Microscopy

Visual inspection of the surfaces of polymer pins, and their corresponding low-carbon metal plates, after testing showed them to be largely unworn. To investigate this in greater detail SEM images were taken of the surfaces of both worn pins and plates. To view non-conducting polymer pins in the SEM, they were splutter coated with a thin (approximately 40nm) gold layer.

Scanning electron microscopy images showed that pin surfaces, from both serum and NaCl(aq) lubricated tests, retained most of their original machining marks (Figures 5.14-5.16) which indicated that the wear of the pin surfaces was very mild. For pins that had been lubricated in NaCl(aq), mild wear, observed as the absence of visible machining marks, appeared to have taken place at the edge of the flat surfaces as shown in Figures 5.17-5.18.

Edge wear is indicative of misalignment of the pins, which is a common problem when using flat tipped pins. For pins lubricated in serum, edge wear was less apparent; however, under larger magnifications slight smearing of the pin surface could be seen and may have indicated adhesive wear (Figure 5.19).

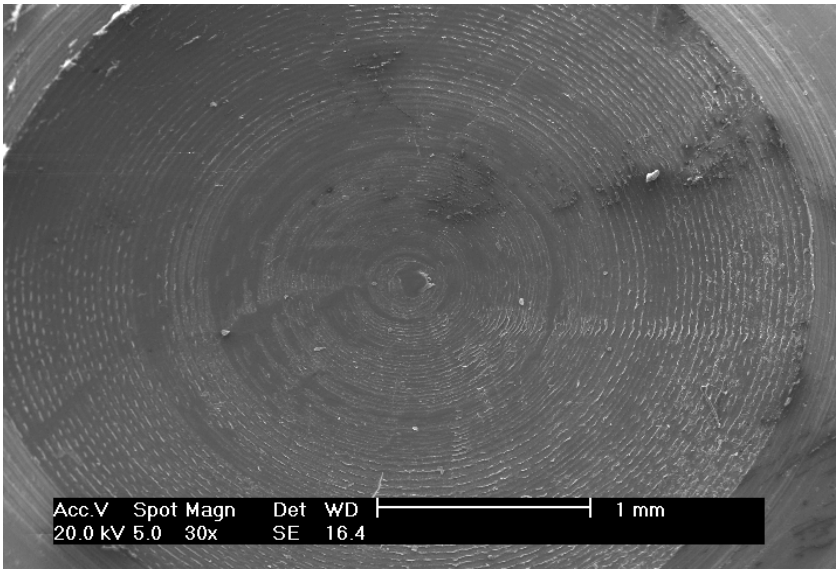

Figure 5.14: Polymer pin surface after testing in NaCl(aq) at 1Hz for a sliding distance of 216m.

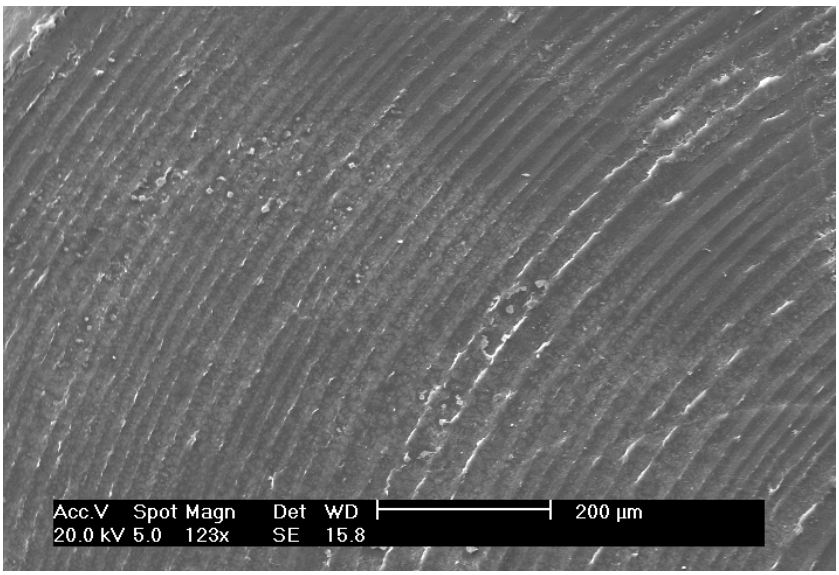

Figure 5.15: Polymer pin surface showing machining marks after testing in NaCl(aq) at 1Hz for a sliding distance of 216m.

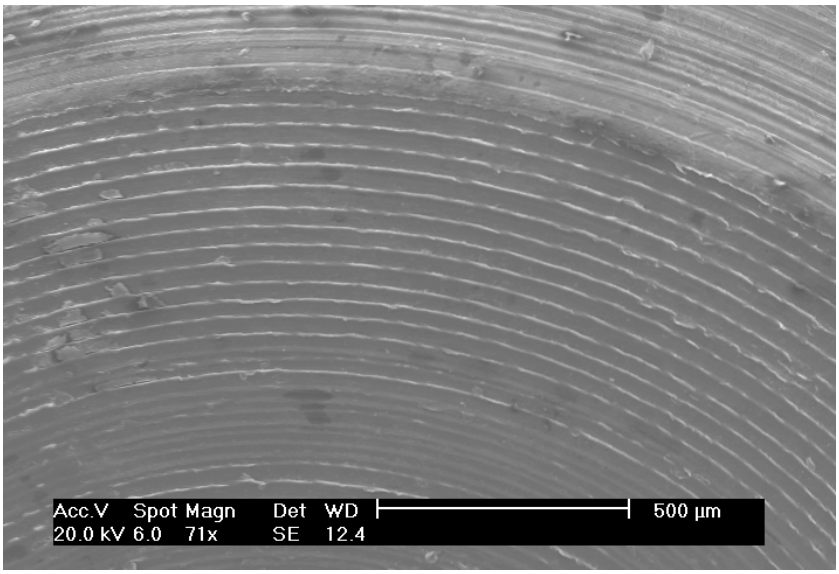

Figure 5.16: Polymer pin lubricated showing machining marks after testing in serum at 1Hz for a sliding distance of 216m.

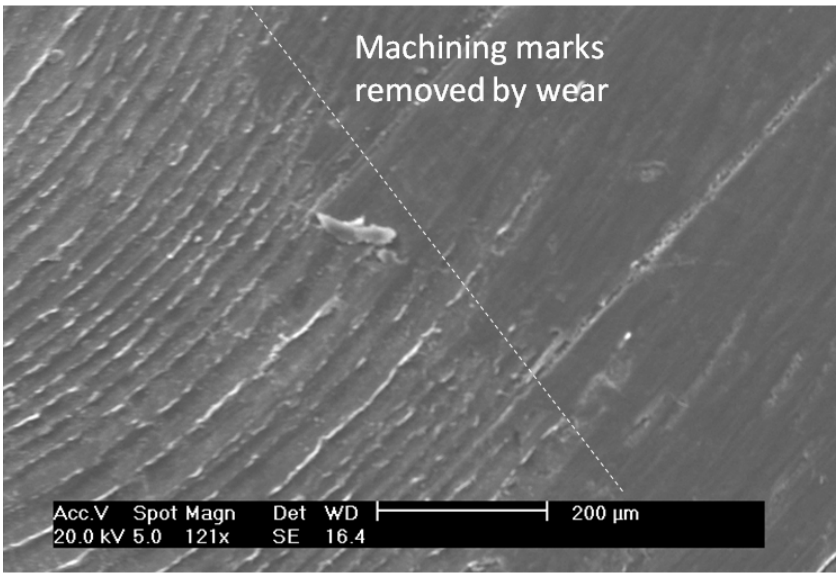

Figure 5.17: Polymer pin surface showing the partial removal of machining marks after testing in NaCl(aq) at 1Hz for a sliding distance of 216m.

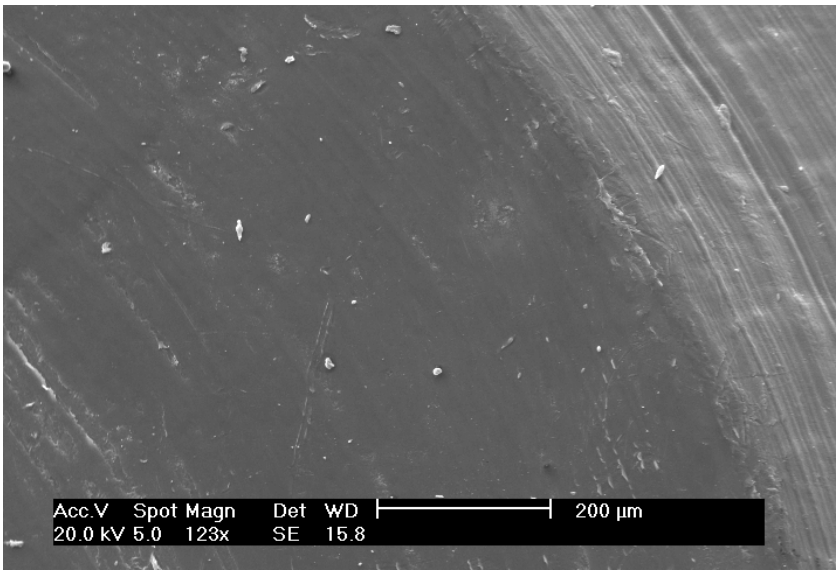

Figure 5.18: Edge of polymer pin surface showing removal of machining marks after testing in NaCl(aq) at 1Hz for a sliding distance of 216m.

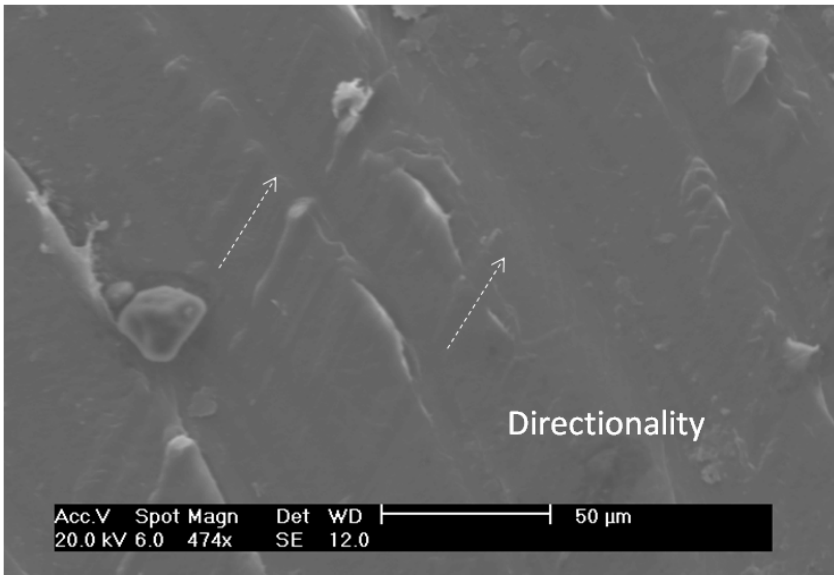

Figure 5.19: Polymer pin surface, displaying slight directional smearing after testing in NaCl at 1Hz for a sliding distance of 216m.

Images of plate surfaces lubricated in NaCl(aq) also indicated that the wear that had taken place was only very mild (Figure 5.20). This was not surprising as the softer polymer pins would only be able to scratch the surface if loose or embedded 3rd body debris, such as carbides, were present. Scratches in the direction of motion were identifiable, although

these were often isolated. In addition, samples that had been lubricated in NaCl(aq) contained dark carbon rich streaks across the surface in the worn regions, indicating a surface deposited layer. The surfaces that had been lubricated with serum were entirely covered in an adherent carbon rich layer originating from the lubricant. In order to assess the level of wear of these surfaces, they were cleaned in acetone to remove their respective carbon layers. The ease with which the organic layer was removed from the sample tested in serum suggested that it comprised physically adsorbed protein, as opposed to a chemically adhered biofilm, such as that reported by Yan *et al* (99). However, the carbon layer adhered to the sample tested in NaCl(aq) was tenacious, and remained in place after cleaning with acetone. This suggested that it was a polymeric transfer film, originating from the pin surface. Previous studies have indicated that polymer transfer can occur as a result of sliding between UHMWPE and metals, but is inhibited by the adsorption of proteins onto the metallic surfaces (124, 137). Following removal of the organic layer, surface scratches on the serum-lubricated plate could be observed as shown in Figures 5.20-5.23.

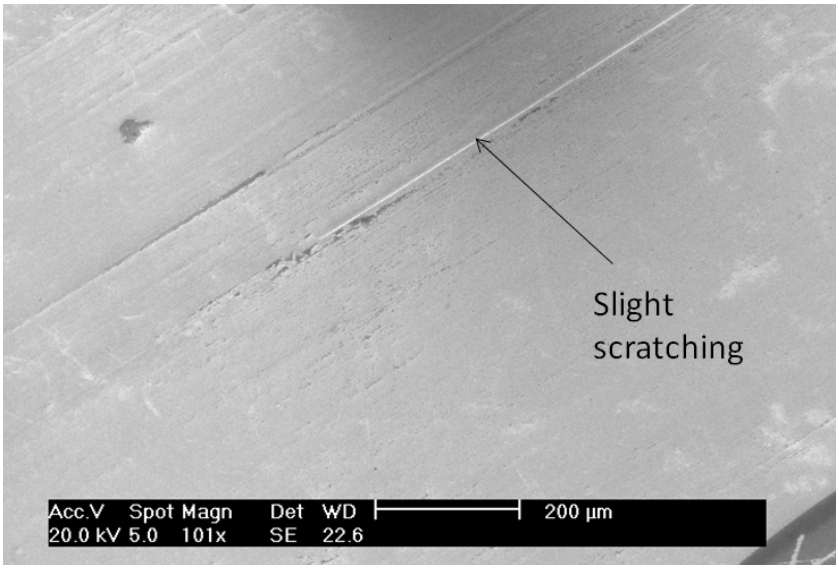

Figure 5.20: Plate indicating little evidence of wear after testing in NaCl(aq) at 1Hz for a sliding distance of 216m.

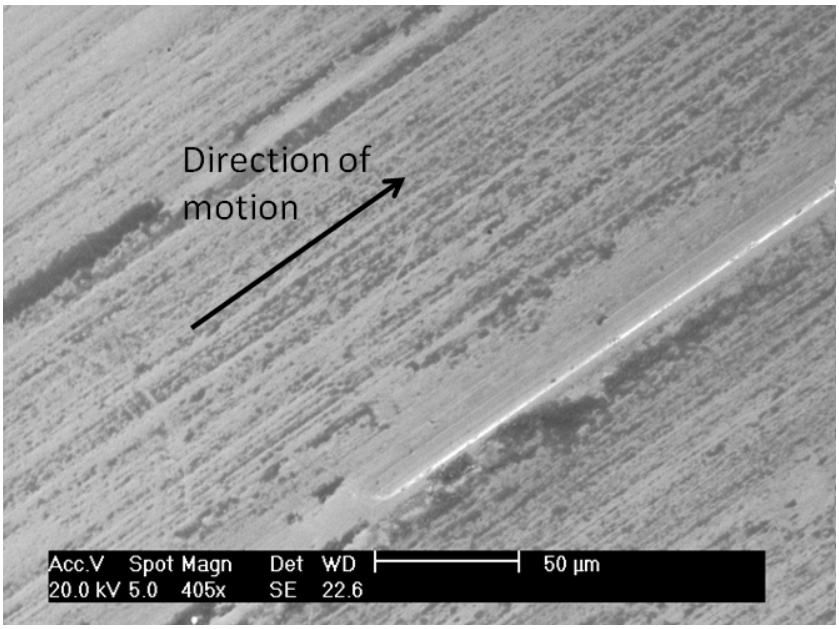

Figure 5.21: Increased magnification of surface showing the presence of black patches in the direction of motion after testing in NaCl(aq) at 1Hz for a sliding distance of 216m.

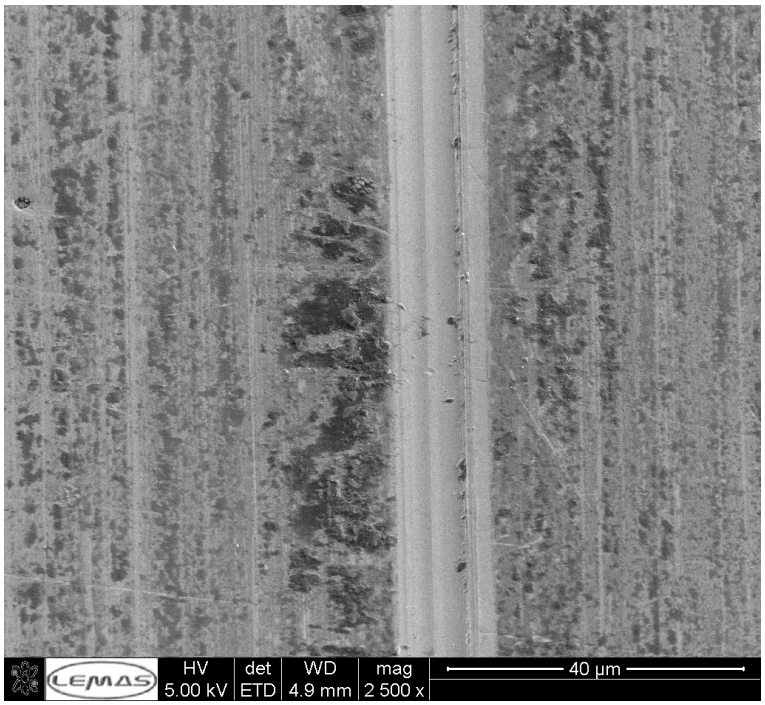

Figure 5.22: High magnification image showing dark surface deposits after testing in NaCl(aq) at 1Hz for a sliding distance of 216m.

.

Figure 5.23: High magnification image showing surface deposits after testing in NaCl(aq) at 1Hz for a sliding distance of 216m.

For MoM tribocouples, visible wear scars were evident on both the pin and plate, when lubricated by either NaCl(aq) or serum. By viewing these wear scars under the SEM, it was evident that they comprised a number of parallel ploughed valleys and peaks. Within these marks, evidence of plastic deformation could be observed. It is clear from Figures 5.24-5.26 that the level of wear between MoM sliding surfaces was considerably more severe than between MoP surfaces. Figures 5.24 and 5.25 show that similar abrasive wear took place on both the surfaces of the metal pin and plate as well as evidence plastic deformation. In Figure 5.26, evidence of plastic deformation can be seen, as well as evidence of the formation of shard-like particles.

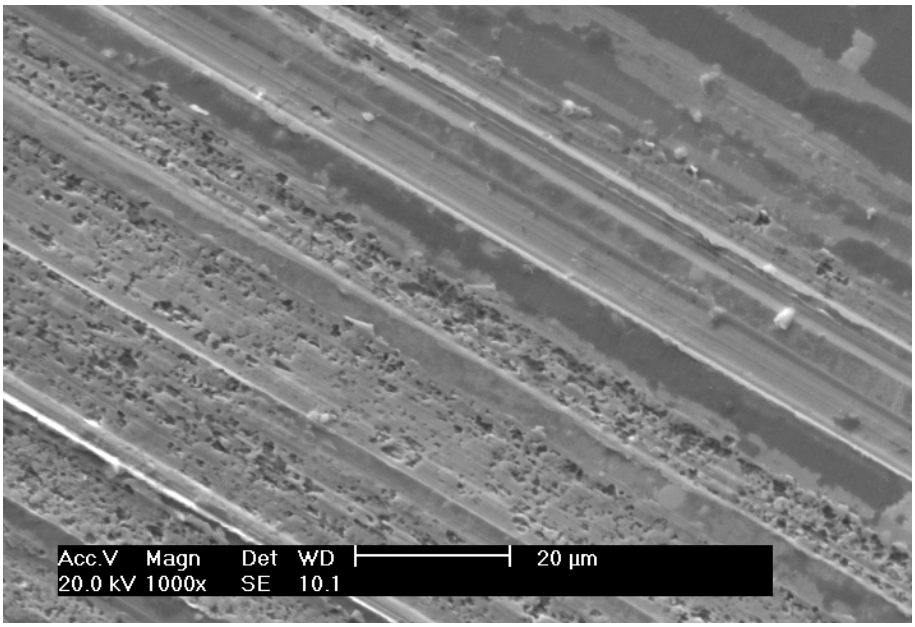

Figure 5.24: Pin surface, showing deep scratches after high-carbon MoM contact in serum at 1Hz for a sliding distance of 216m.

.

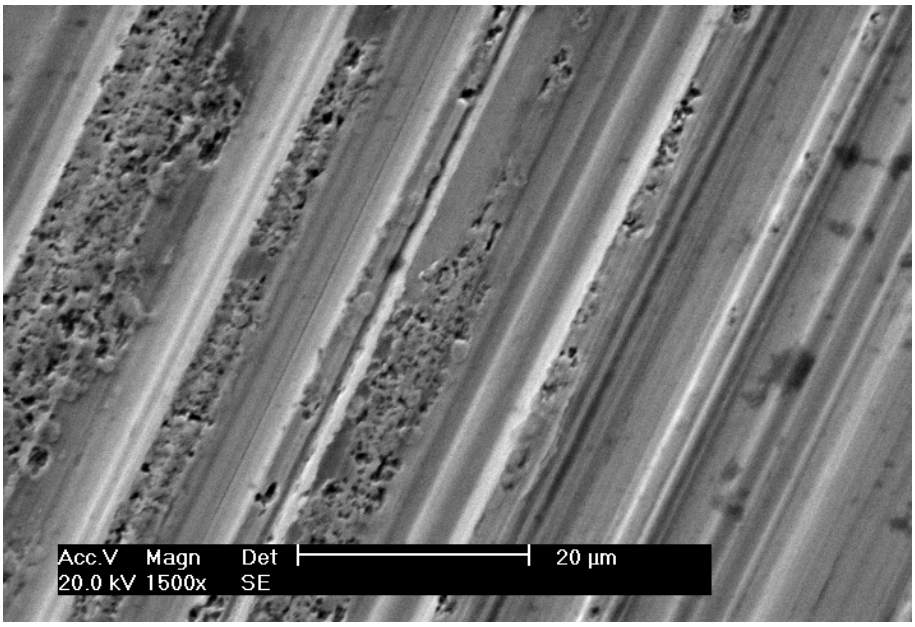

Figure 5.25: Plate surface, showing deep scratches following high-carbon MoM contact in serum at 1Hz for a sliding distance of 216m.

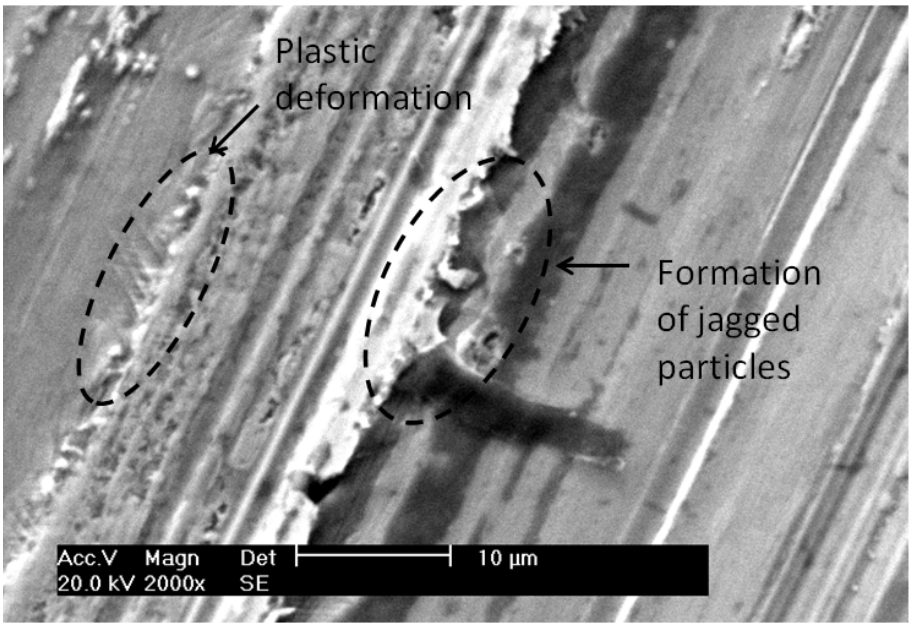

Figure 5.26: Image showing plastic deformation of surface following high-carbon MoM contact in serum at 1Hz for a sliding distance of 216m.

Typically *in vivo*, the wear rate of MoP hip replacements is substantially greater than for MoM hip replacements (10, 164) but this was not reflected in the tribometer. This could be explained by the difference in lubrication between MoP and MoM bearing surfaces. For THRs, lubricating film thicknesses are larger in MoP hip replacements but the smooth surfaces produced on MoM designs lead to an increased lambda ratio. MoP joints operate between the boundary- and severe mixed-lubrication regimes, whereas MoM joints operate between the mixed- and fluid-film regime (10). This was not reflected in the tribometer since the pins and plates used do not entrain fluid in the same way as a full prosthesis does. In the tribometer, both tribo-couples were tested in the boundary regime, which may account for the high level of wear on the MoM surfaces.

5.1.4 Focused Ion Beam Scanning Electron Microscopy

The surface deposits produced in both lubricants were investigated using electron microscopy. FIB etching was used to allow cross-sectional images

of the film to be taken. The procedure for this was outlined in 3.3. Images of the sample preparation are given in Figures 5.27, 5.28, 5.29, 5.32 and 5.33. Viewing the films in this manner enabled measurements of their thickness to be taken. The black film developed in the presence of NaCl(aq) measured up to 262nm thick in places (shown in Figures 5.30 and 5.31). The thickness of this film varied by a substantial percentage over a short distance. This transfer film had the appearance of the 'lumpy' film described by Makinson *et al* (165) and Crocket *et al* (137). The organic films had a maximum height of 300nm (see Figures 5.34 and 5.35). It was also observed that the organometallic film appeared to contain particles embedded within it. These particles appear similar to 'roll up' (148, 166) particles that form as a result of proteins reacting with metallic debris. SEM images of this area, however, suggest that coverage was patchy and the thickness of this layer appeared to vary across the surface (Figure 5.32).

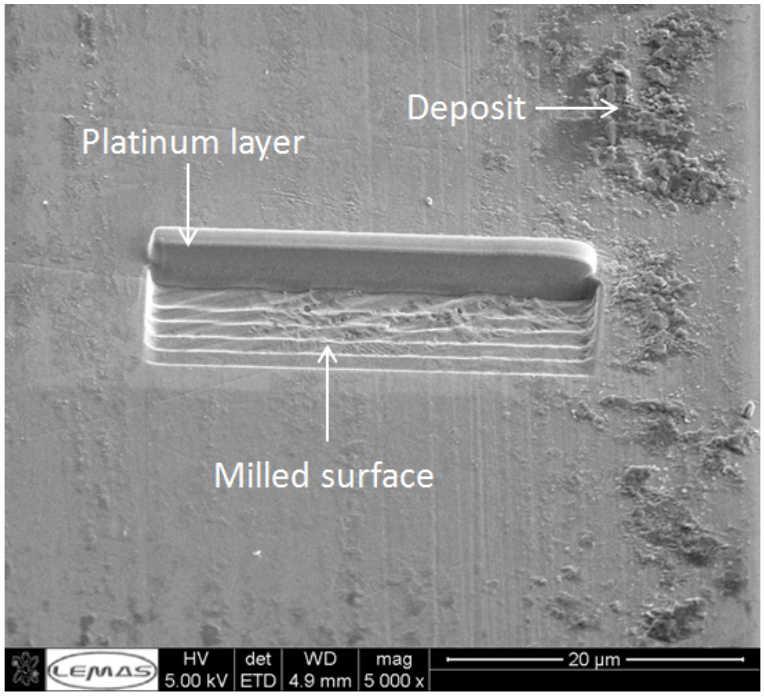

Figure 5.27: Plate surface after FIB preparation, following testing in NaCl(aq) at 1Hz for a sliding distance of 216m.

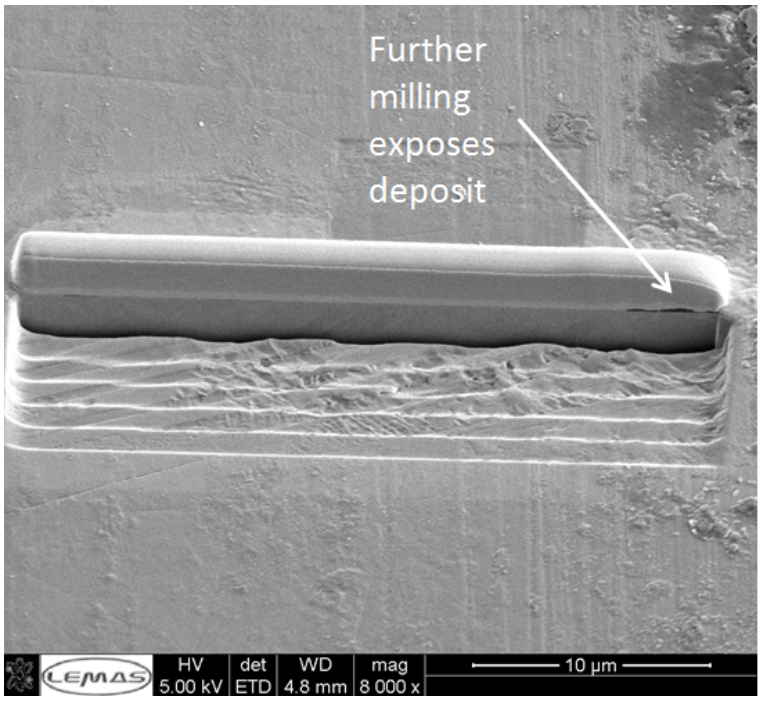

Figure 5.28: Plate sample after FIB preparation showing surface film following testing in NaCl(aq) at 1Hz for a sliding distance of 216m.

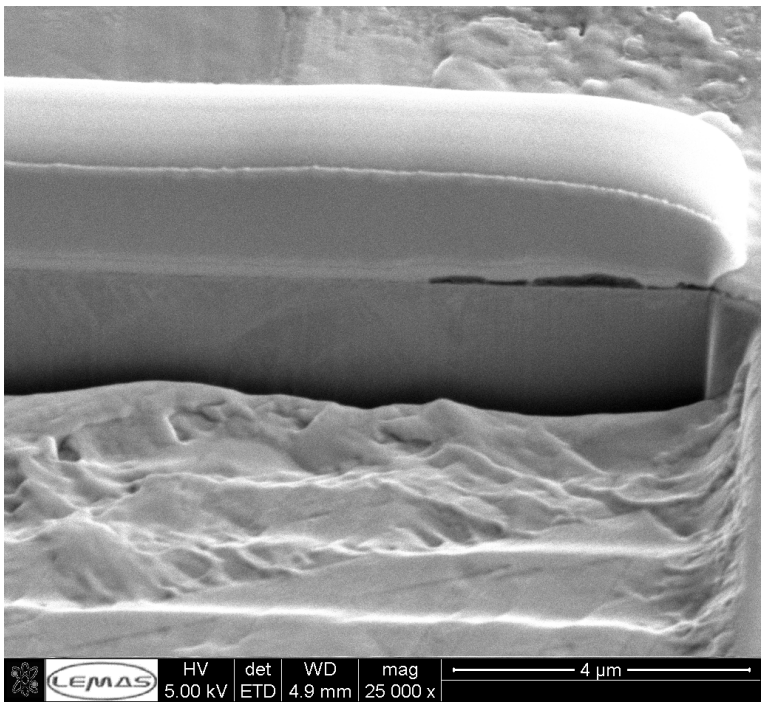

Figure 5.29: Plate sample after FIB preparation showing surface film following testing in NaCl(aq) at 1Hz for a sliding distance of 216m.

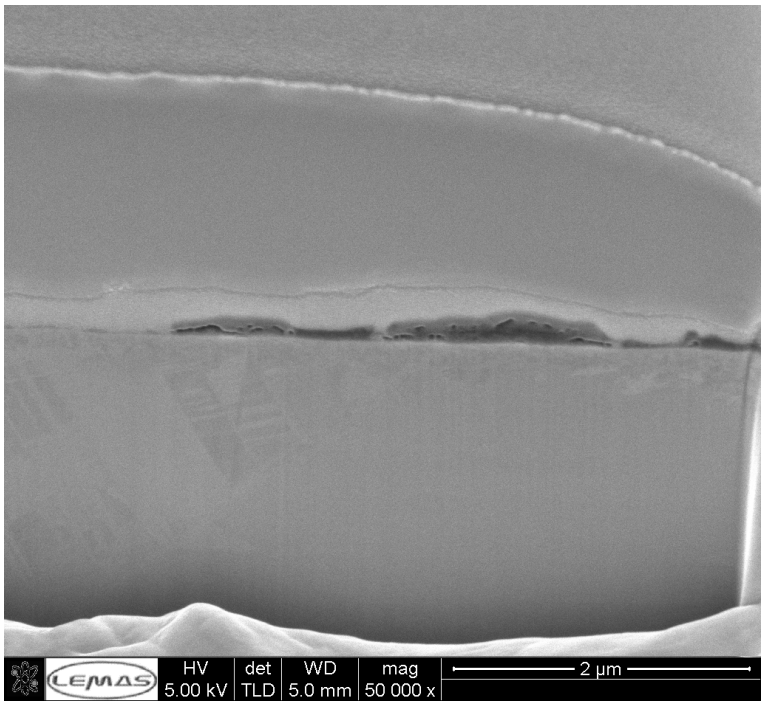

Figure 5.30: FIB SEM image showing film cross-section following testing in NaCl(aq) at 1Hz for a sliding distance of 216m.

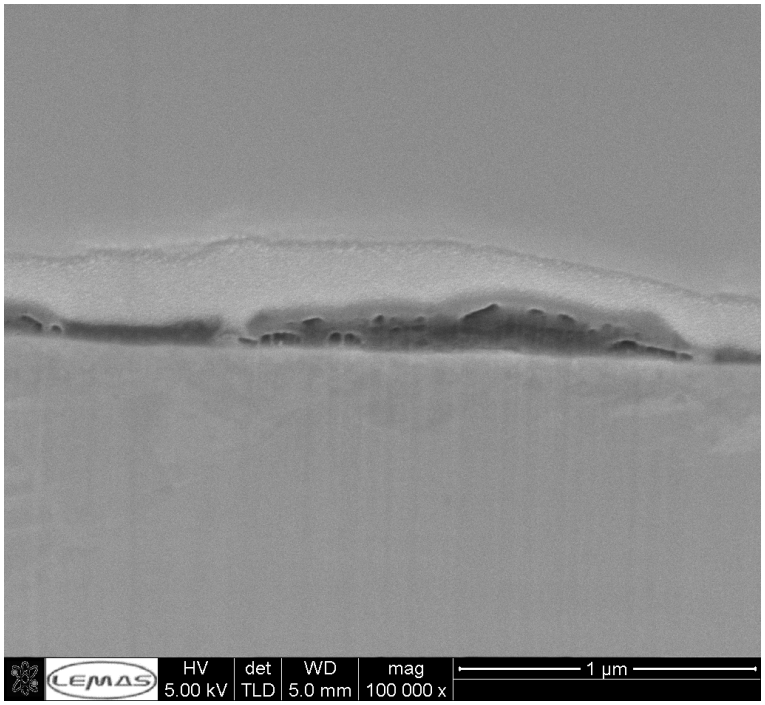

Figure 5.31: FIB SEM image showing film cross-section following testing in NaCl(aq) at 1Hz for a sliding distance of 216m.

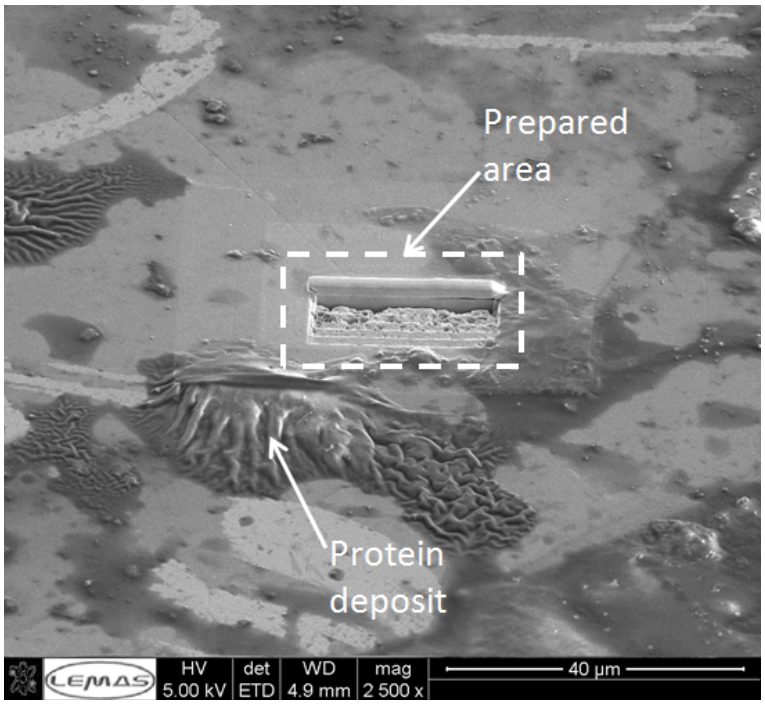

Figure 5.32: Plate surface after FIB preparation, following testing in serum at 1Hz for a sliding distance of 216m.

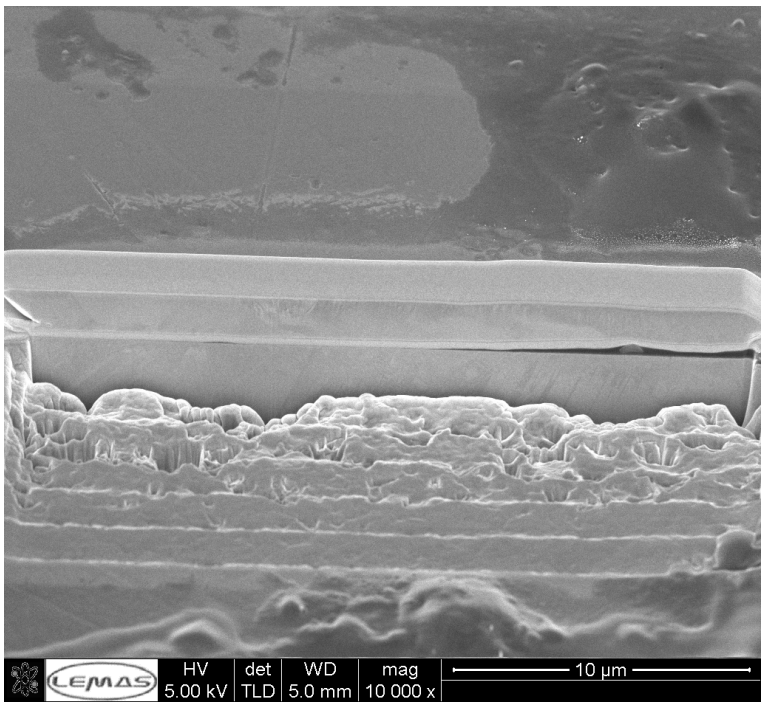

Figure 5.33: Plate sample after FIB preparation showing surface film following testing in serum at 1Hz for a sliding distance of 216m.

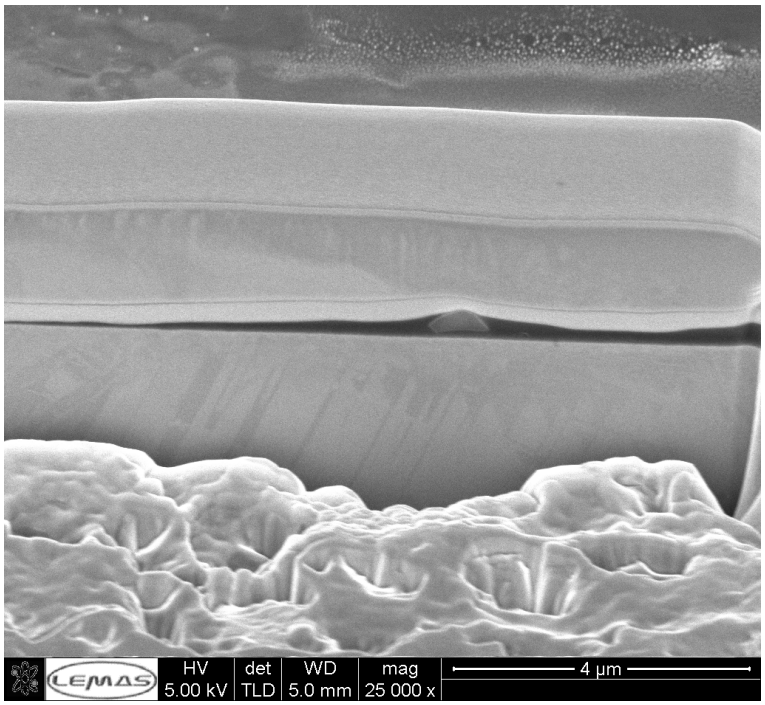

Figure 5.34: FIB SEM image showing film cross-section following testing in serum at 1Hz for a sliding distance of 216m.

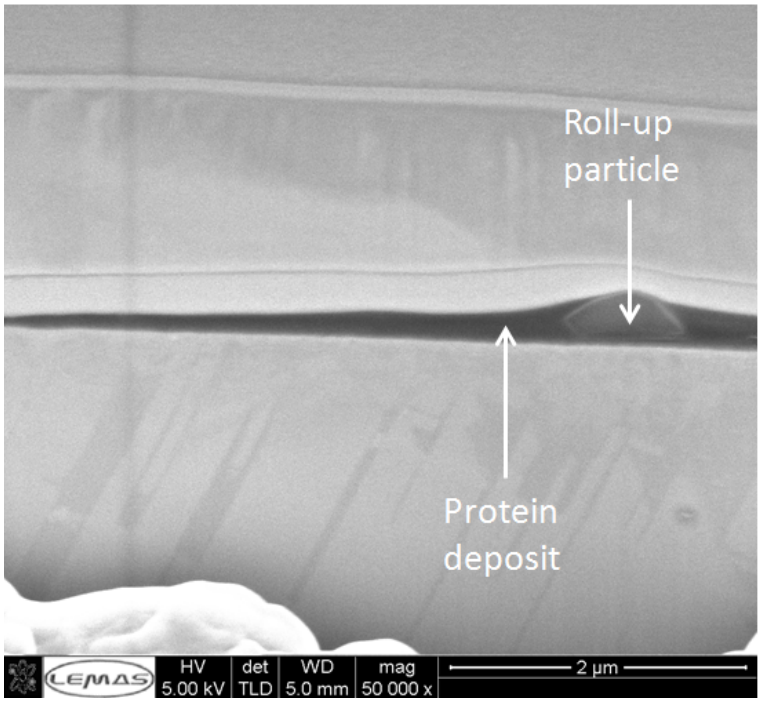

Figure 5.35: FIB SEM image showing film cross-section following testing in serum at 1Hz for a sliding distance of 216m.

5.1.5 White Light Interferometry

White light interferometry was used to analyse the wear of the surfaces of both pins and plates that had been tested in MoM contact. Figures 5.36-5.43 show 3D images of the samples tested in both NaCl(aq) and serum. It was observed that surfaces lubricated in NaCl(aq) showed signs of more severe surface abrasion, and had much rougher surface profiles than those tested in serum. This can be ascribed to the known boundary lubricating properties of proteins (128, 129, 134). Although the surfaces of samples tested in serum were generally smoother, they showed signs of increased roughening at the edges of the wear scars. The raised material at the edge of the wear scars could be generated as a result of plastic deformation or the egress of particles. The high-carbon samples showed less evidence of severe abrasive wear compared to the low-carbon samples, which is consistent with previous findings. In general, the harder high-carbon alloy is more resistant to abrasion than the softer low-carbon alloy (27, 86, 89, 91, 103). The difference between samples tested in NaCl(aq) and serum was less pronounced for high-carbon tribo-couples. As with the low-carbon samples, high-carbon plates displayed increased roughening, in the form of raised material, towards the edge of the wear scar, although to a lesser extent.

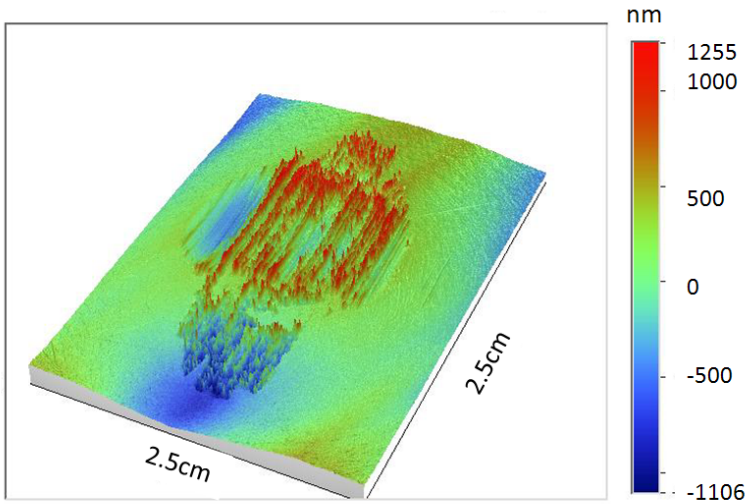

Figure 5.36: Interferometry image of a low-carbon pin, tested against a low-carbon plate in NaCl(aq) at 1Hz for a sliding distance of 216m.

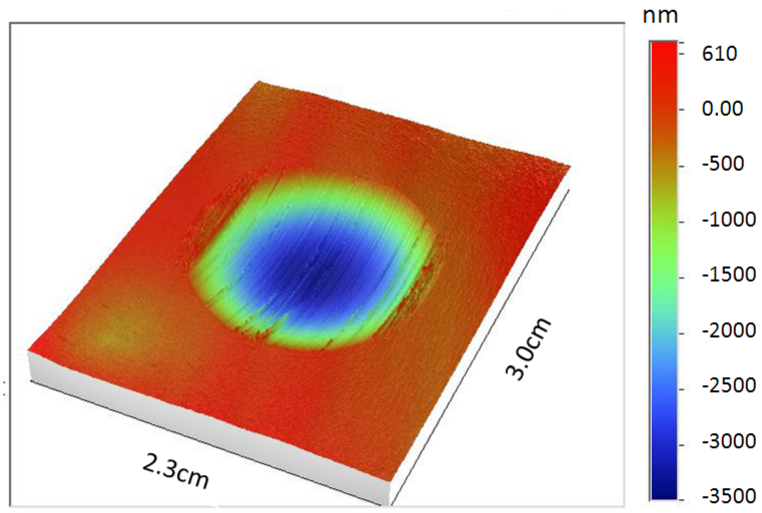

Figure 5.37: Interferometry image of a low-carbon pin, tested against a low-carbon plate in serum at 1Hz for a sliding distance of 216m.

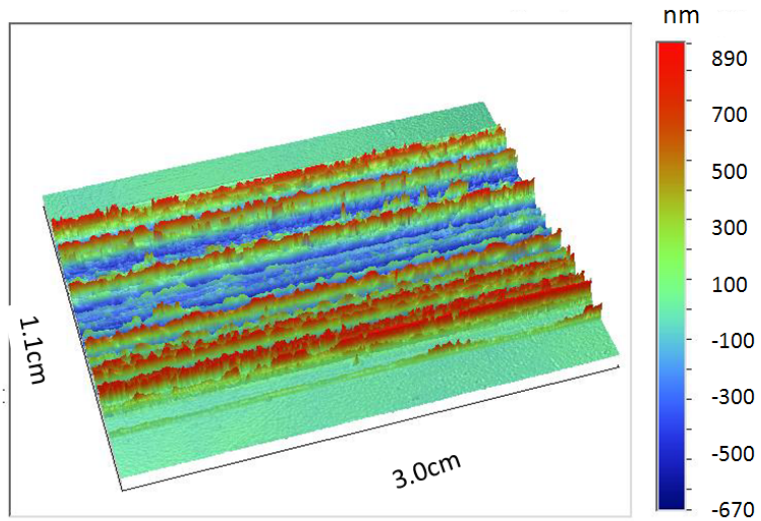

Figure 5.38: Interferometry image of a low-carbon plate, tested against a low-carbon pin in NaCl(aq) at 1Hz for a sliding distance of 216m.

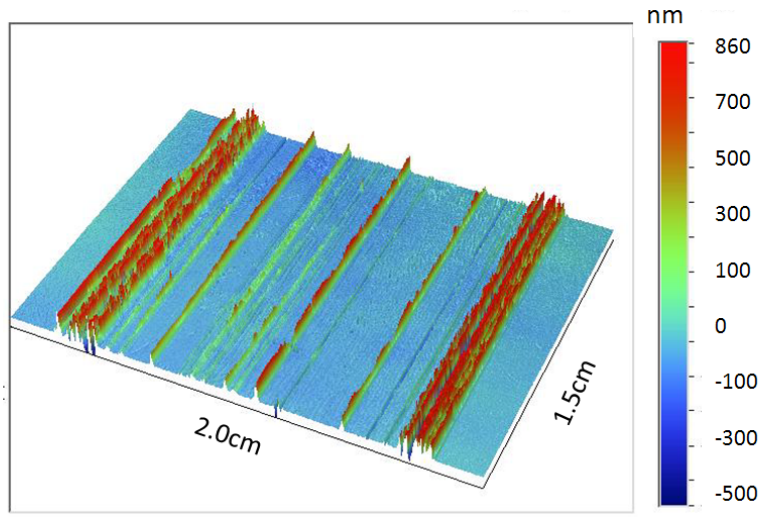

Figure 5.39: Interferometry image of a low-carbon plate, tested against a low-carbon pin in serum at 1Hz for a sliding distance of 216m.

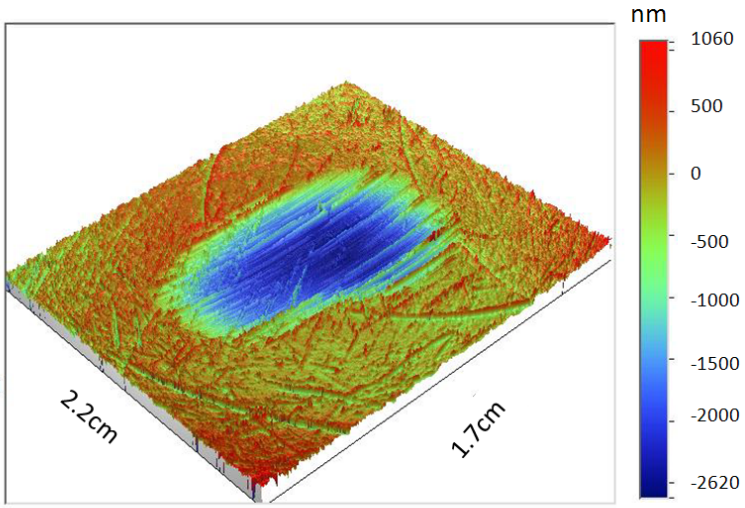

Figure 5.40: Interferometry image of a high-carbon pin, tested against a high-carbon plate in NaCl(aq) at 1Hz for a sliding distance of 216m.

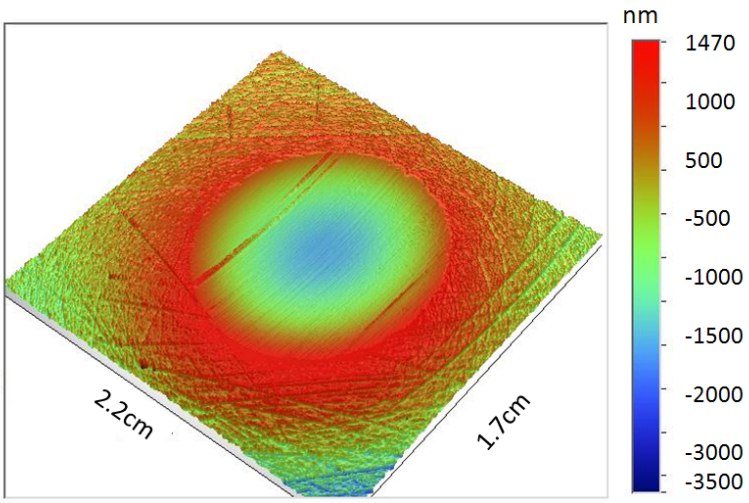

Figure 5.41: Interferometry image of a high-carbon pin, tested against a high-carbon plate in serum at 1Hz for a sliding distance of 216m.

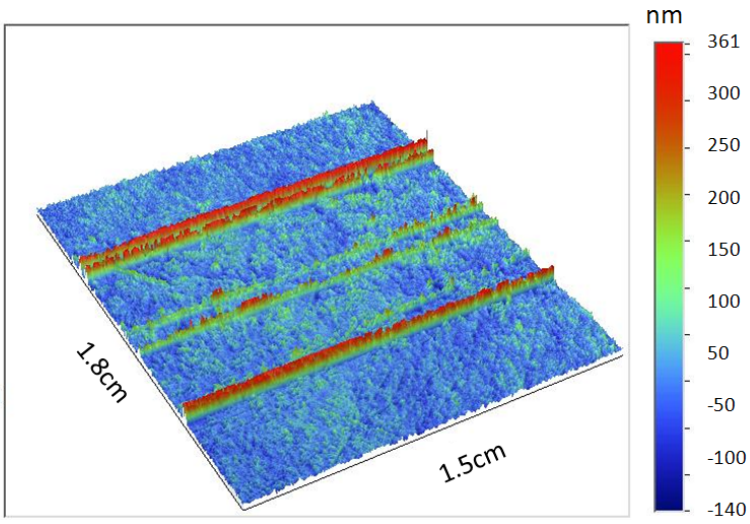

Figure 5.42: Interferometry image of a high-carbon plate, tested against a high-carbon pin in NaCl(aq) at 1Hz for a sliding distance of 216m.

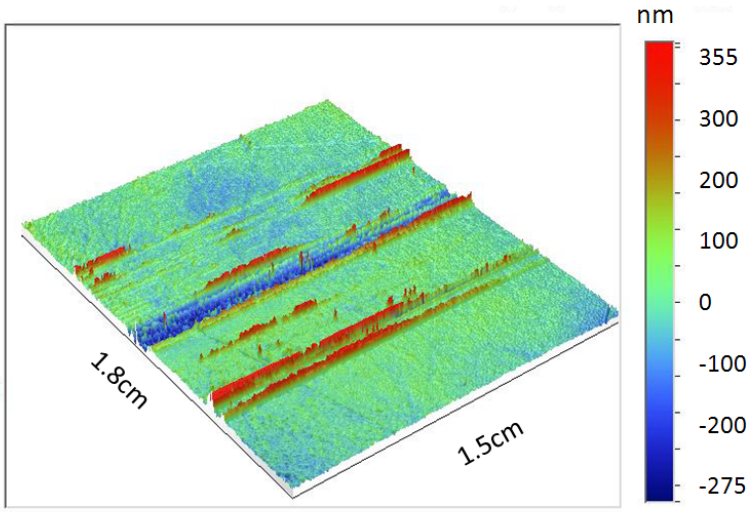

Figure 5.43: Interferometry image of a high-carbon plate, tested against a high-carbon pin in serum at 1Hz for a sliding distance of 216m.

5.2 Results from Procedure B (MoM testing with metal ion measurements)

5.2.1 Mass Loss

Due to the increased load employed in Procedure B, there was an increase in total mass loss relative to the tests performed in Procedure A, despite the reduced test duration. The mass losses produced by Procedure B were large enough to be measured gravimetrically.

The average mass loss at the end of the test indicated that wear was greater in NaCl (aq) than in serum solution (Figure 5.44). This is consistent with the observations made from Procedure A, indicating that more severe MoM abrasion took place in NaCl(aq) than serum. It also supports previous findings that demonstrate the boundary lubricating properties that proteins offer to MoM interfaces (128, 129, 134).

The average wear rate was also affected by the application of cathodic protection (CP). It reduced the total gravimetric wear by 41% and 47%, in NaCl(aq) and serum correspondingly. This is shown in Figure 5.44. CP

inhibits the dissolution of the alloy, effectively eliminating pure corrosion, wear enhanced corrosion and corrosion enhanced wear, leaving only pure wear (see Equations (2.11) and (2.12)). The difference between tests run with and without cathodic protection is equal to the magnitude of pure corrosion and the synergy between corrosion and wear.

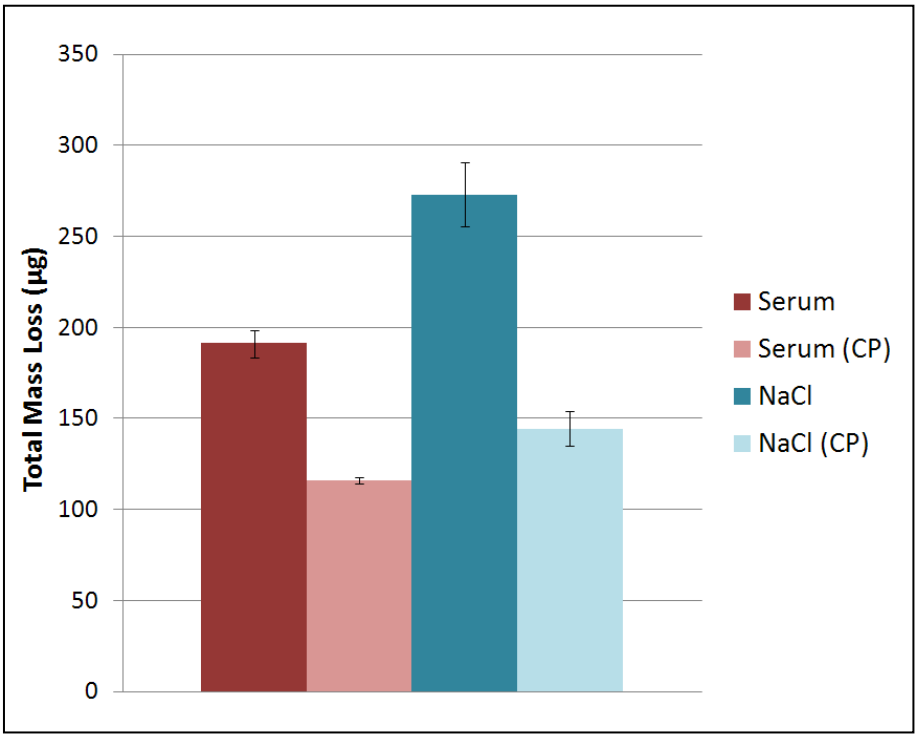

Figure 5.44: Total gravimetric mass loss over the test duration tested in either NaCl(aq) or serum solution in the presence and absence of cathodic protection (CP), at 1Hz for a sliding distance of 144m.

5.2.2 Friction

Friction was considerably lower in serum than NaCl(aq). This can be explained by the boundary lubricating properties of the proteins found within serum, as previously discussed in section 2.4.8. For tests run in serum under the effects of CP, a slight increase in friction was observed. This may be attributed to the net surface charge, caused by cathodic protection affecting the adsorption of different serum constituents at the pin/plate

interface. Nakanishi *et al* (123) demonstrated that by varying the charge across a tribo-couple in proteinaceous solutions, the friction and wear could be changed. It was shown that, due to the presence of both hydrophilic and hydrophobic species, a variation in surface charge could alter the relative adsorption of these species. The final coefficients of friction for each test condition are shown in Figure 5.45.

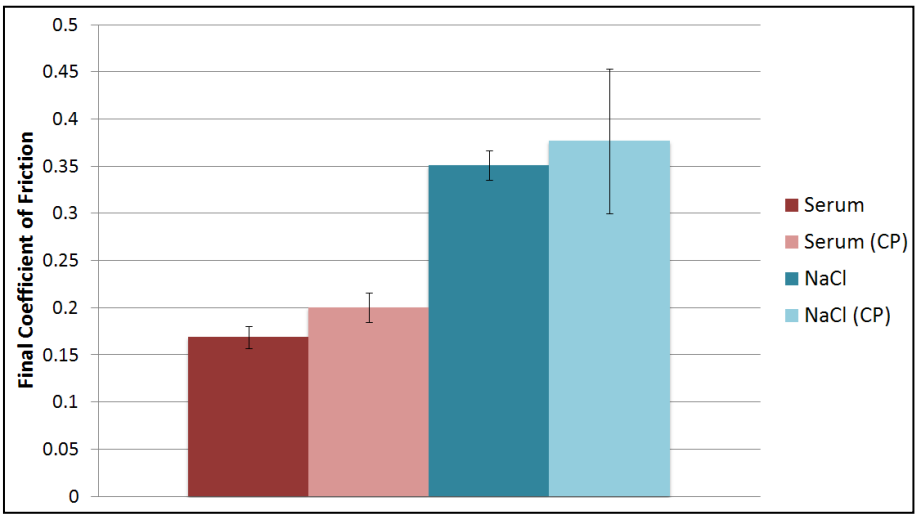

Figure 5.45: Final coefficient of friction over the test duration tested in either NaCl(aq) or serum solution at 1Hz for a sliding distance of 144m.

5.2.3 Open Circuit Potential

Upon the initiation of motion, all tests produced an immediate negative shift in potential, indicative of depassivation, which is consistent with the observations made from Procedure B. This remained low for the entire test duration indicating that depassivation was sustained. At the cessation of motion, the potential was observed to ennoble for the next 10 minutes, reaching a value close to that measured at the start of the test. These observations were made for tests run both in NaCl(aq) and serum. In serum, the initial drop in potential was lower than in NaCl(aq), -450mV as opposed to -350mV, towards the end of the test it showed a slight ennoblement of

approximately +100mV. The response of the OCP in both test conditions is shown in Figure 5.46.

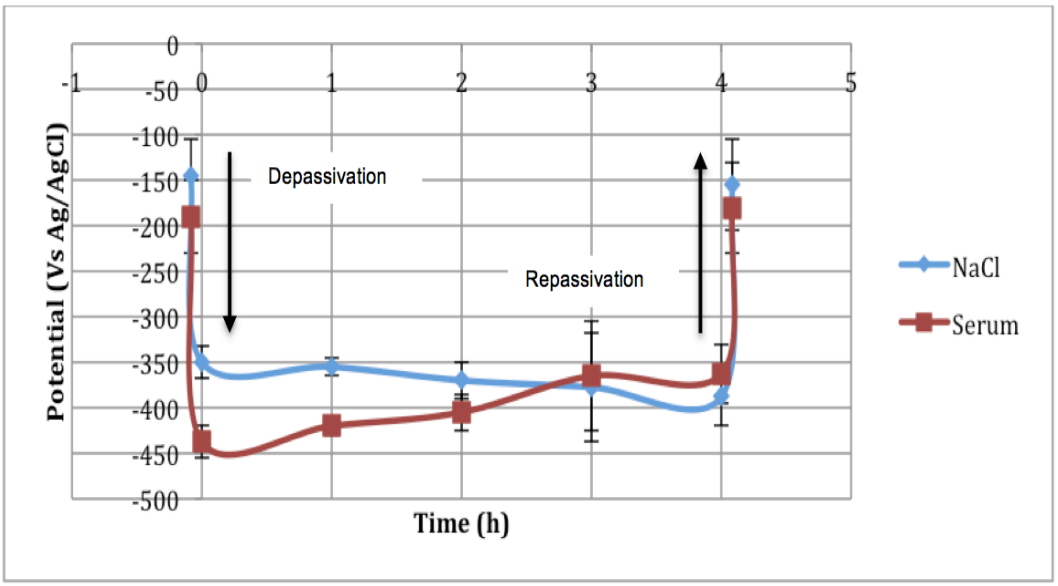

Figure 5.46: Behaviour of open circuit potential over test duration tested in either NaCl(aq) or serum solution at 1Hz for a sliding distance of 144m.

A greater negative shift would normally represent a greater rate of anodic dissolution, however, measurements of polarisation resistance revealed a lower corrosion current in serum than in NaCl(aq). This may be attributed to the effects of proteins on the anodic and cathodic Tafel slopes, as illustrated in Figure 5.47. When passive implant alloys corrode in simulated biological solutions, it has been shown that the presence of proteins in bovine serum can cause an increase in the anodic Tafel constant and a reduction in the cathodic Tafel constant (167), hence the OCP may be lower under sliding in serum without the corrosion rate being higher.

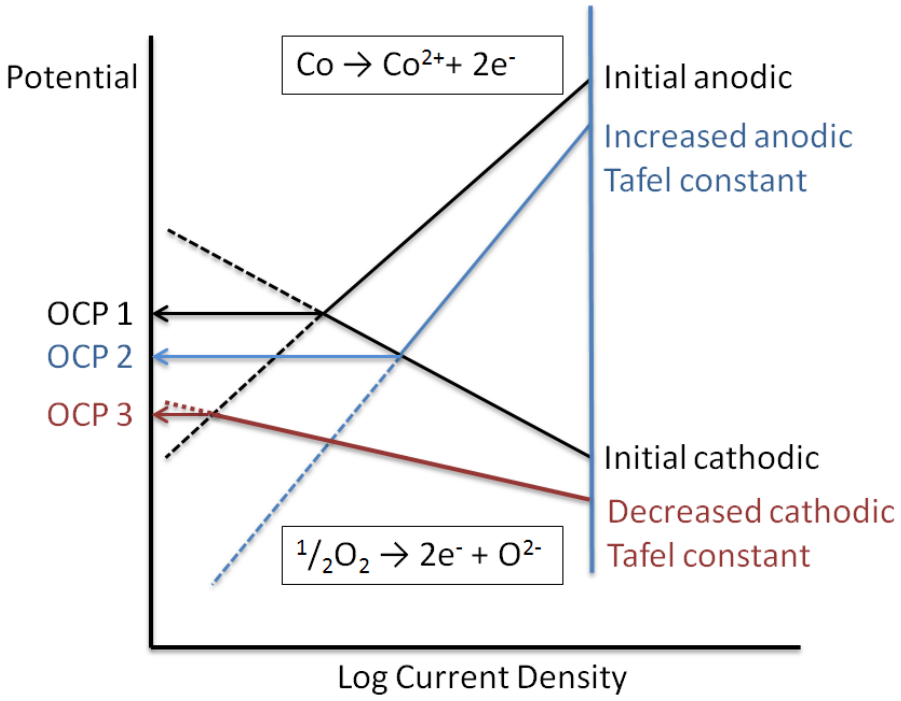

Figure 5.47: Evans diagram illustrating the effect of protein on the corrosion of Co in neutral pH aqueous solution.

5.2.4 Corrosion Current

Measurements of polarisation resistance were converted into a corrosion current over the test duration by using the Stern Geary Equation (3.1). Anodic Tafel slopes measured during sliding in serum and NaCl are shown in Figure 5.48. Cathodic Tafel slopes measured during sliding in serum and NaCl are shown in Figure 5.49. For the calculation of ICorr from R_p, anodic and cathodic Tafel constants of approximately 130mV/dec and 250mV/dec were measured in serum and approximately 190mV/dec and 150mV/dec were measured in NaCl(aq) respectively. The variation in calculated corrosion current over the test duration is shown in Figure 5.50.

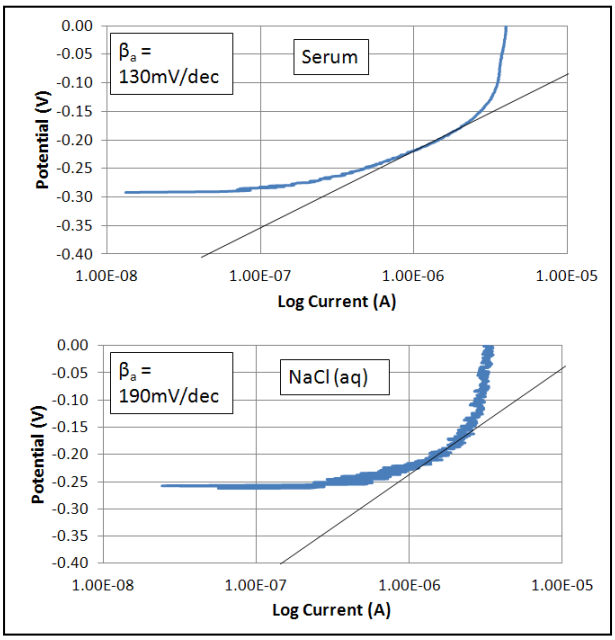

Figure 5.48: Anodic Tafel slopes measured during sliding in Serum (top) and NaCl(aq) (bottom).

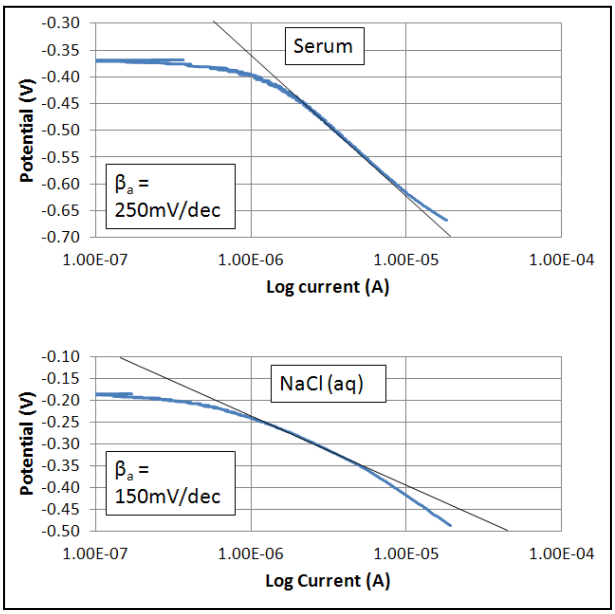

Figure 5.49: Cathodic Tafel slopes measured during sliding in Serum (top) and NaCl(aq) (bottom).

In static conditions the average corrosion current was approximately 0.05μA in NaCl(aq) and 0.07μA in serum. Upon mechanical depassivation, at the pin/plate interface, this immediately increased to 15μA in NaCl(aq) and 6μA in serum. It has already been demonstrated that wear was less severe in

serum than in NaCl(aq), due to the presence of improved boundary lubrication. It follows that the level of wear-induced depassivation in serum is less than NaCl(aq), despite serum being slightly more corrosive in static conditions. Measurements of I_{corr}, 15 minutes after motion was stopped, showed that complete recovery of the passive film had not taken place in either serum or NaCl(aq). Following 15 minutes of film recovery in static conditions, I_{corr} was still substantially greater than it was prior to the onset of sliding, remaining at approximately 0.3μA in NaCl(aq) and 0.4μA in serum.

The increase in load used in Procedure B caused a substantial increase in corrosion current compared to Procedure A. This is to be expected because the increased contact pressure causes more severe asperity contact in the boundary lubrication regime, which leads to more severe abrasion of the passive film and hence an increased corrosion current. Compared to Procedure A, the results in Procedure B show a greater difference between the corrosion current produced in serum compared to NaCl(aq). This could be due to two influences. The lubricating effects of proteins may be more effective under the more severe loading employed in Procedure B. The increased current in Procedure B may have enabled more accurate determination of the results compared to Procedure A.

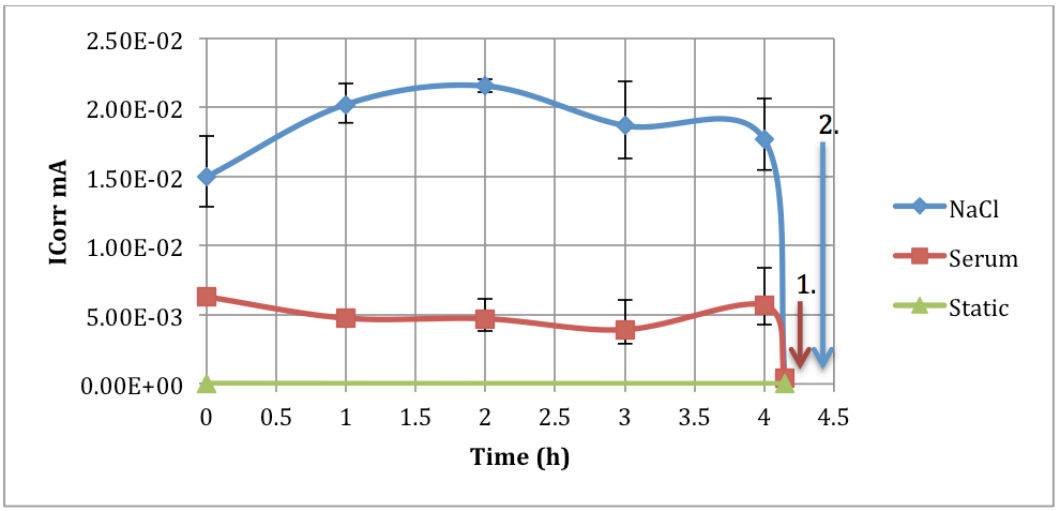

Figure 5.50: Behaviour of corrosion current (ICorr) over test duration over the test duration tested in either NaCl(aq) or serum solution at 1Hz for a sliding distance of 144m.

Although tribometer tests are only an approximation to the response of a material *in vivo,* these findings illustrate that the rate of metallic ion release remains elevated for some time following periods of mechanical depassivation. Interestingly, there was only mild variation in the current during dynamic conditions in both serum and NaCl(aq), despite the constant reduction of contact pressure throughout the test. An explanation for this could be that the increasing surface area offset the decreasing pressures as the contact patch between the pin and plate grew with wear. The change in theoretical contact pressure, as a result of uniform wear to the pin surface, is shown in Figure 4.4.

The corrosion current over the test duration was converted into a mass loss, as mentioned previously, to give the level of damage associated with pure corrosion (C) and wear-enhanced corrosion ($\bar{C}$). In addition, the mass loss associated with 4 hours 15 minutes of corrosion at the static corrosion rate, measured at the start of the test, was calculated. This gave the lone contribution of pure corrosion (C). The measured mass loss under cathodic protection gave the contribution of pure wear (W). This then enabled the contribution of corrosion-enhanced wear ($\bar{W}$) to be obtained without direct measurement (see (2.11) and (2.12)). The percentage contribution of each towards the total mass loss is given in Figures 5.51-5.52.

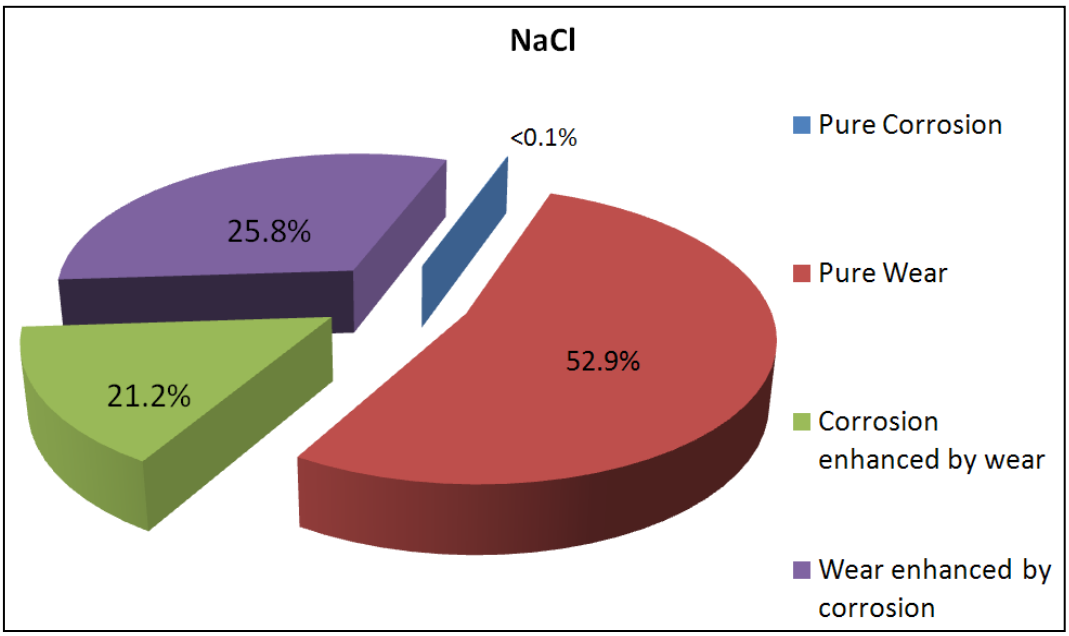

Figure 5.51: Proportions of total material loss in NaCl(aq).

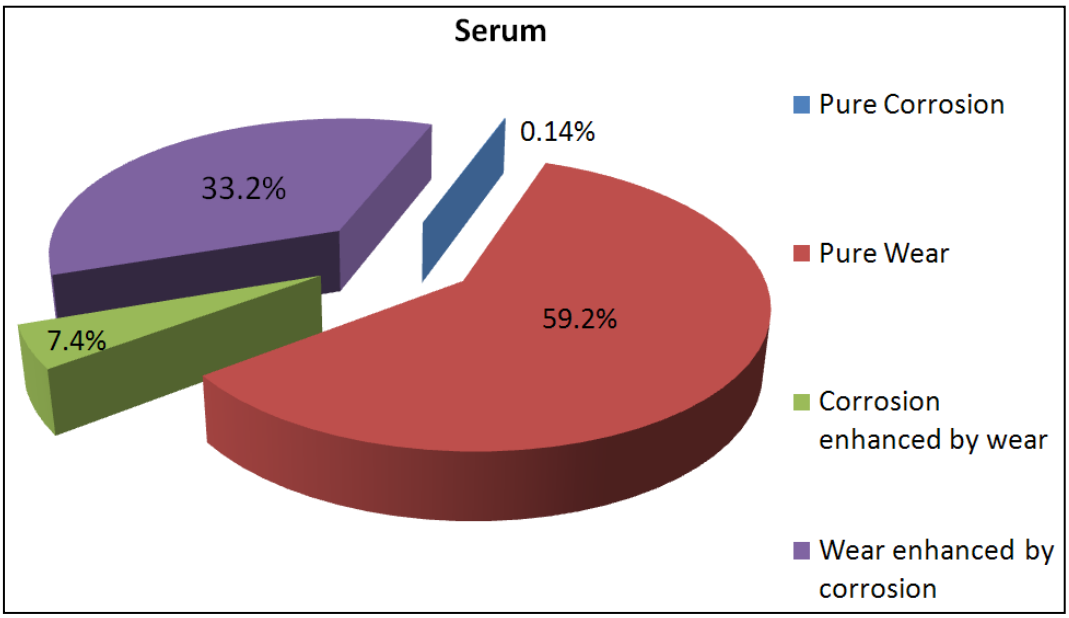

Figure 5.52: Proportions of total material loss in serum.

5.2.5 ICP-MS

Inductively coupled plasma mass spectroscopy (ICP-MS) of solution samples revealed that the highest total concentrations of metal ions were found in the tests that had not been cathodically protected. It was also shown that for either cathodically protected, or non-cathodically protected samples ion release was greater in serum than in NaCl(aq). This trend was observed for the release of Co and Cr ions, however the increased ion release in serum was more pronounced for Cr than for Co, shown in Figures 5.53-5.54.

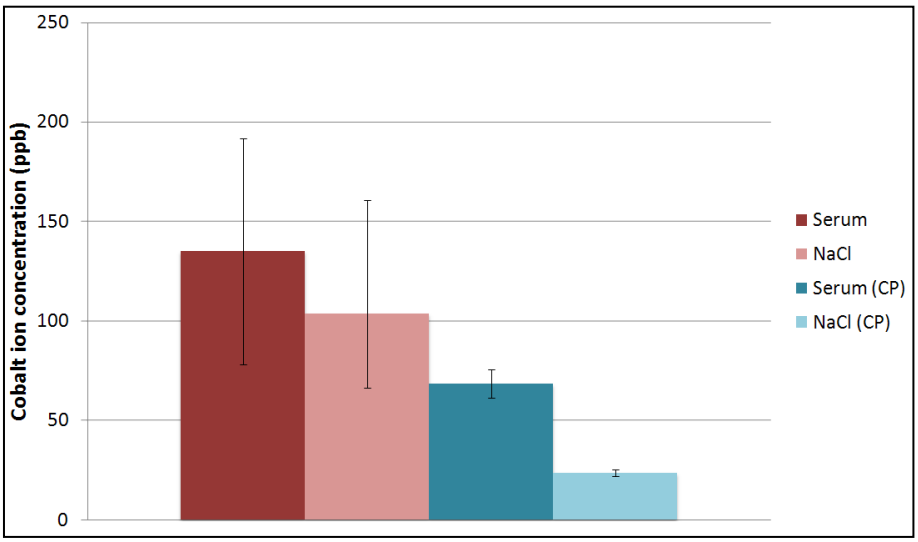

Figure 5.53: Measured cobalt ion concentrations measured after a total sliding distance of 144m between MoM samples.

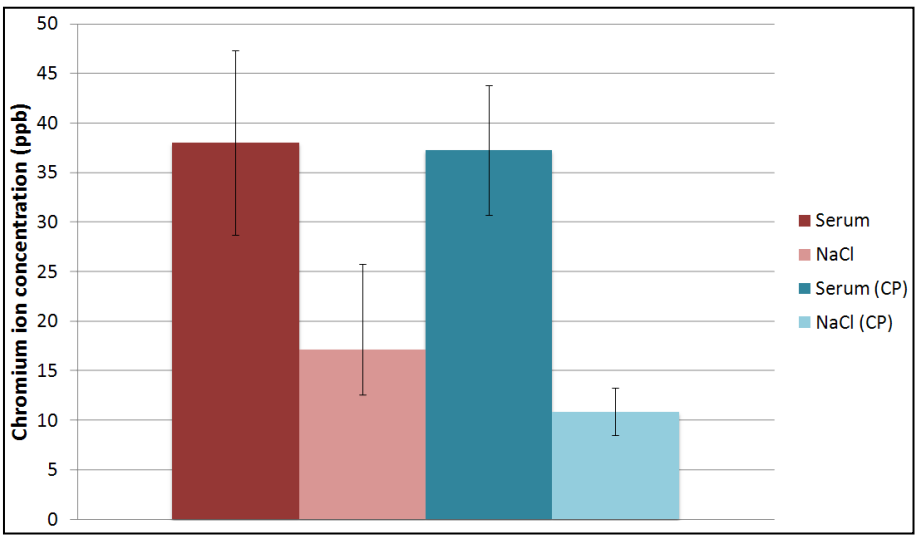

Figure 5.54: Measured chromium ion concentration measured after a total sliding distance of 144m between MoM samples.

From the metal ion measurements, it is possible to infer the amount of particle dissolution over the duration of the test. The relative contribution of debris dissolution and depassivation to ion release can also be calculated. For tests run in the absence of cathodic protection, the concentration of ions in solution accounted for 39% and 28% of the total material loss in serum and NaCl(aq) respectively. The ions detected were produced by the passive dissolution of the alloy outside of the wear scar, the dissolution of the

depassivated alloy within the wear scar and the dissolution of the wear debris. The contribution to ion release from the passive region was a fraction of the pure corrosion and was small enough to be neglected. The relative contributions of depassivation and debris dissolution in serum were 19% and 81% respectively, and 25% and 75% in NaCl(aq) respectively. This is illustrated in Figure 5.55.

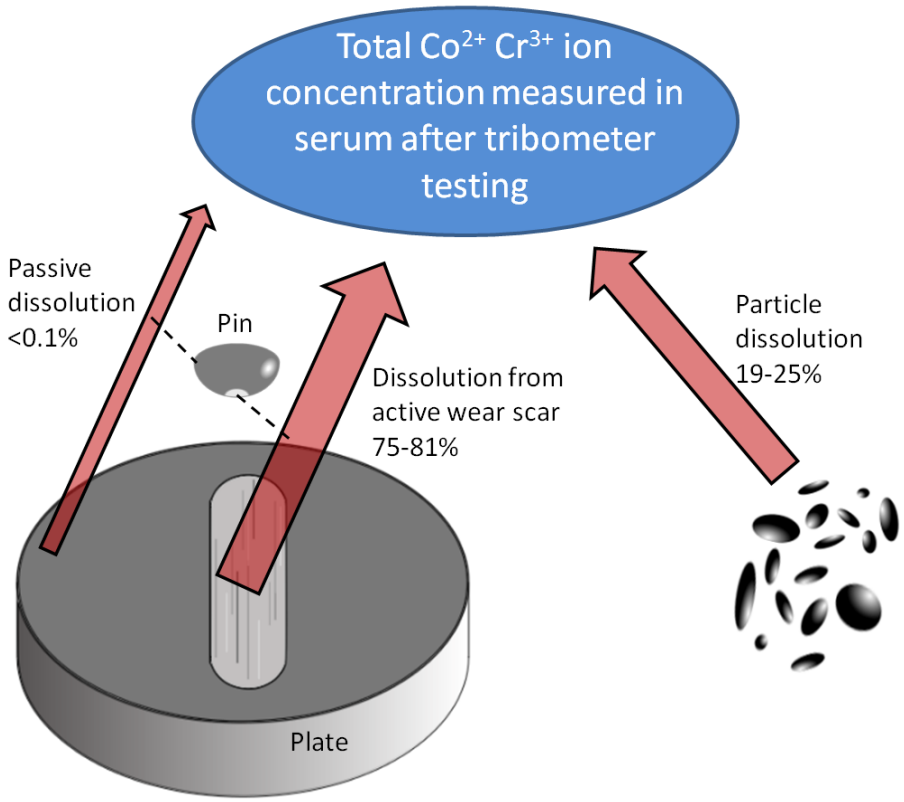

Figure 5.55: Sources of metal ions during tribometer testing after a sliding distance of 144m between MoM samples.

Cathodic protection inhibits the contribution of depassivation to metal ion formation; the ions that are formed are produced by the dissolution of the debris. Comparing samples run with and without CP, it can be seen that the amount of debris that dissolved was different. For tests run in serum, a slightly greater percentage of the debris was ionised with CP (40%) than without (34%). However, in NaCl(aq), only a very small proportion of the debris was ionised with CP (6%) compared to without CP (8%). These observations may be attributed to the effects of corrosion on wear. The reactions which cause re-growth of the passive film, and hence oxide

generation, are inhibited by CP which may lead to the production of particles with a reduced metal-oxide/metal alloy ratio. Particles with a reduced metal-oxide/metal alloy ratio have a reduced resistance to dissolution, and a greater capacity for ion release. These particles would more readily dissolve in serum, as studies have shown that metal ion release from CoCr alloys is greatly enhanced by the presence of bovine serum albumin (41, 66). Another factor that may affect the dissolution rates of particles with CP is the effect of particles being trapped in the wear scar, or remaining in contact with the plate surface. In the absence of CP, these particles would continue to corrode, and may possibly depassivate if they remain in the wear scar. However, under the influence of CP, these particles would be protected from dissolving for as long as they remain in electrical contact with the polarised surface. This may explain the reduction in particle dissolution observed in the NaCl(aq) environment whilst under CP.

It is interesting to observe that, although tests in serum produced lower corrosion currents and lower wear rates, the total metallic ion release was greater than in NaCl(aq). This can be attributed to the greater chloride content in the 25% serum solution compared to the 0.36% NaCl(aq) solution, and by the acceleratory effect of proteins on corrosion, as discussed earlier. Under free corrosion conditions there was a preferential release of cobalt. This is consistent with studies that have investigated the ion release from CoCr in simulated physiological solutions. It has been found that the ratio of cobalt ion released will exceed its stoichiometric abundance in the alloy in both saline and proteinaceous solutions (41, 66). Under the influence of CP the ratio of the release of cobalt to chromium was approximately 2:1, which is very close to their relative abundance in the alloy. This may indicate, as previously mentioned, the influence of CP on the dissolution of particles, either by altering their morphology, or by inhibiting their dissolution as they remain in contact with the polarised surface.

It is important to consider that, in serum, only 34% of the debris produced had ionised by the end of the 4-hour test; however, the contribution to ion release was still a substantial fraction of the total. This may be important when considering the use of blood ion concentrations as a diagnostic tool for patients with MoM hip replacements. Ion release caused by the latent dissolution of particles may exceed that caused by immediate depassivation and short-term particle dissolution. As a result, long-term studies on the

dissolution of CoCr based particles may be of relevance in interpretation of blood-ion concentrations in patients implanted with MoM prostheses.

5.3 Tribometer Summary

Wear enhanced corrosion can take place in MoP contacts, but is mitigated by the adsorption of proteins to the surfaces.

MoM contact results in severe depassivation within the wear scar even under low contact pressure, but is exacerbated by an increase in pressure.

The proteins present in serum reduce the level of wear-enhanced corrosion between MoM surfaces.

Cathodic protection reduced the total material loss under sliding, due to the inhibition of oxidation reactions at the surface.

Pure mechanical wear accounted for 52.9% and 59.2% of the total material loss between MoM surfaces in NaCl(aq) and serum respectively. Pure corrosion contributed less than 0.1%, and the remaining material loss was caused by the synergism between corrosion and wear.

Part 2 Hip Simulator Testing

Introduction

A hip simulator allows the testing of actual hip components in conditions approximating those found *in vivo.* Compared to a tribometer, a hip simulator provides a more realistic simulation of the operational environment. However, the complexity in setting up and instrumenting a hip simulator for electrochemical studies make it more time consuming and expensive than a tribometer. The hip simulator was used to determine whether the initial findings on the tribometer would translate to a more realistic environment, and to advance these concepts to a level where they provide useful insights about the operation of metal-on-metal joints *in vivo.*

Chapter 6 Hip Simulator Apparatus

6.1 Instrumented Hip Simulator

All tests were run on a Prosim Deep Flexion hip simulator, shown in Figure 6.1. All the components used were 36mm diameter metal-on-metal hip bearing surfaces. Cups were cemented into place at a 45^0 inclination angle using polymethyl methacrylate (PMMA) bone cement, and heads were attached to a resin neck with a 12/14 taper which was screwed into a polymer base plate. The whole configuration was sealed within a silicone gaiter, as shown. The gaiter was flooded with approximately 450ml of lubricant/electrolyte, which was heated to 37^0C ±0.5^0C by an external heated fan, regulated by an internal thermocouple. To permit electrochemical measurements, the simulator was instrumented with a 3-electrode electrochemical cell. In this cell, the hip bearing operated as the working electrode. The combined platinum counter electrode and Ag/AgCl reference electrode (supplied by Thermo Scientific) were housed within the gaiter. Prior to testing, the potential of the reference electrode was checked and noted. This was then repeated at the end of the test and compared to the initial value to ensure that the potential had not drifted throughout the experiment. All electrodes were connected to an external potentiostat using coaxial cable.

A diagram of the instrumented hip simulator is given in Figure 6.2. The simulator was used to provide a load and motion cycle which was representative of a normal gait cycle. The periodic loading and displacement used over a single cycle are shown in Figure 6.3. The load was applied pneumatically and calibrated between each test.

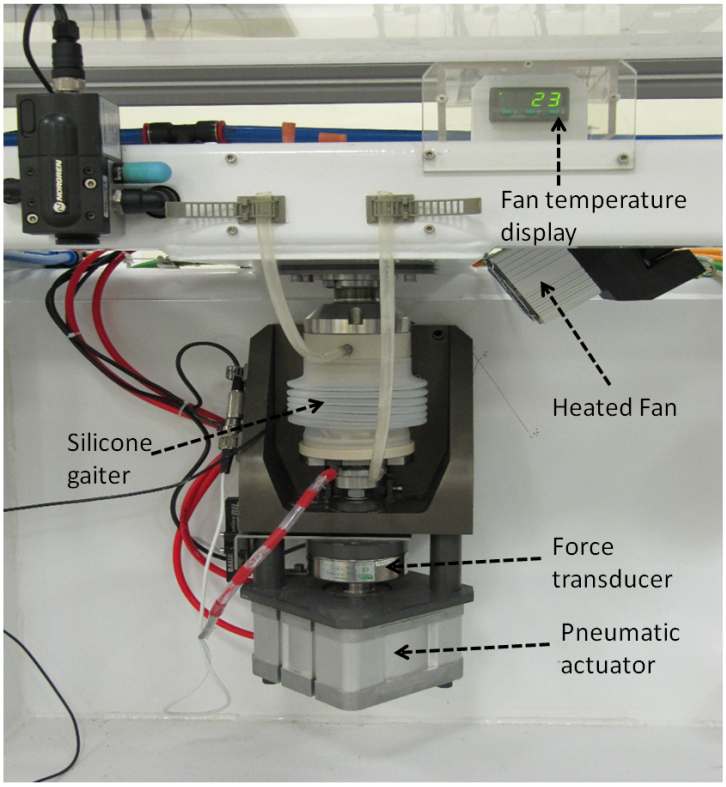

Figure 6.1: Components of the Prosim instrumented hip joint simulator.

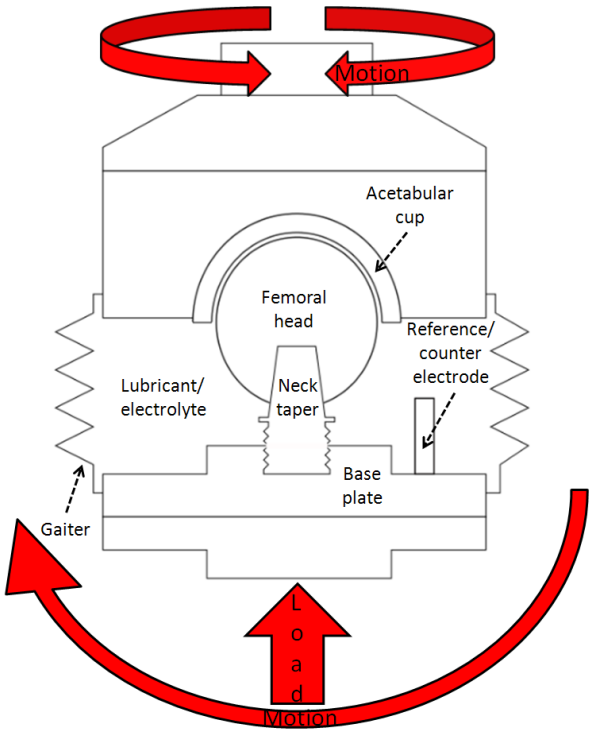

Figure 6.2: Diagram of an instrumented hip simulator.

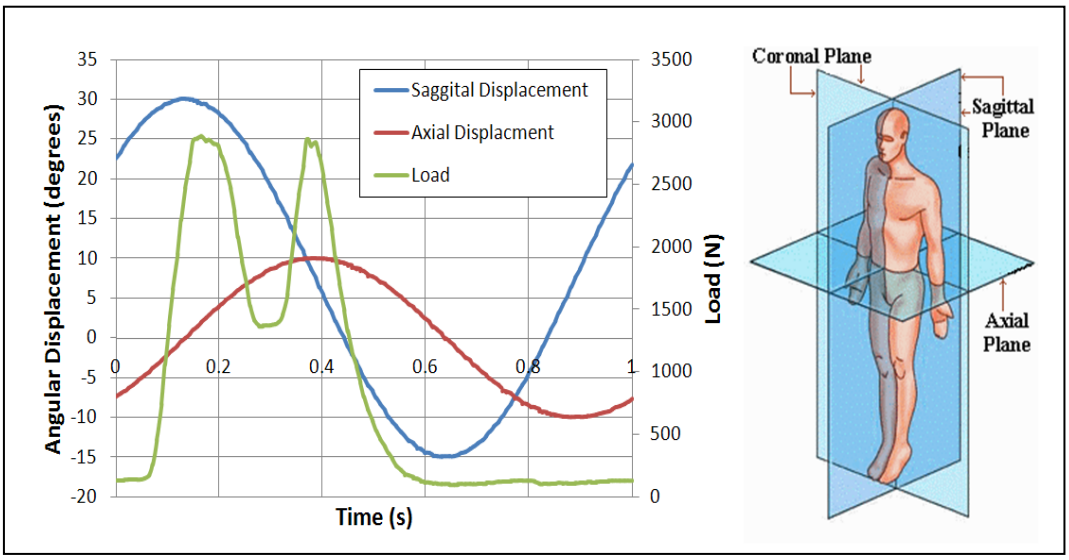

Figure 6.3: Hip simulator load and displacement profile shown with the bodily planes (168).

Two different lubricants were used in the hip simulator. The first was bovine serum, diluted to 25% v/v with ultra pure water, and supplemented with 0.03% v/v sodium azide solution. The second was bovine serum diluted to a total protein concentration of 17g/l with phosphate buffered saline (PBS) and supplemented with 0.03% v/v sodium azide solution. The motivation for diluting to 17g/l of protein, and diluting with PBS rather than distilled water, was that literature has demonstrated that this produces a solution with a comparable osmolality to that of natural fluid (117).

6.2 Transmission Electron Microscopy

A transmission electron microscope (TEM) operates much like an SEM, however, the beam of electrons is transmitted through an ultra thin sample. The beam is then focused onto a fluorescent screen or is detected with a charge-coupled device. Since the beam is transmitted, as opposed to reflected, a number of techniques can be used in conjunction with TEM.

These include electron energy loss spectroscopy (EELS) and selected area electron diffraction (SAED).

Focused ion beam transmission electron microscope (FIBTEM) sections were prepared from the femoral heads using an FEI Nova 200 Nanolab dual beam scanning electron microscope (SEM)/FIB, fitted with a Kleindiek micromanipulator. The ion column was operated at 30kV and 5kV and at beam currents between 5nA and 0.05nA, and the electron column at 5kV and 29pA. The surface was initially covered in a 40nm gold spluttered coating. The site of interest was then protected with a 200nm electron deposited platinum layer, and then a 1-micron thick platinum layer deposited using the gallium ion beam. Surrounding material was then removed using the ion beam, and a section from the site of interest was removed using the micromanipulator and attached to a TEM support grid. The section was then thinned to <100nm. TEM imaging, SAED and energy dispersive X-ray (EDX) mapping was carried out using a FEI Tecnai F20 FEGTEM operated at 200keV and fitted with a Gatan SC600 CCD camera and a high angle annular dark field (HAADF) scanning (S)TEM detector. EELS analysis was carried out using a Philips CM200 FEGTEM operated at 197 keV and fitted with a Gatan GIF 200 imaging filter. All image, diffraction pattern processing and EELS spectrum processing was performed using Gatan Digital Micrograph software. Several steps in the sample preparation are illustrated in Figure 6.4.

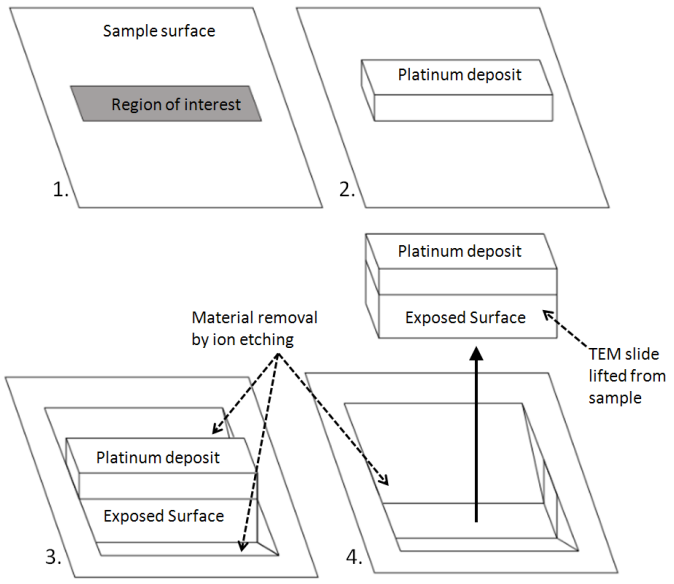

Figure 6.4: Schematic of basic steps in TEM slide preparation.

6.3 Electron Energy Loss Spectroscopy

Electron energy loss spectroscopy (EELS) is a technique for determining the chemical composition of a material. EELS is a type of absorption spectroscopy and is usually employed in a TEM. A beam of electrons is allowed to interact with a material, whereupon electrons are scattered. The scattered beam is analysed spectroscopically to produce an energy spectrum (169). Electrons are either scattered elastically or inelastically. The former are used in imaging and the formation of diffraction patterns, whilst the latter are used to form EELS spectra. When a beam of electrons interacts with atoms in the sample it is possible for the beam to excite inner shell electrons. Species in the beam then lose energy that is equal to the ionisation energy of a core electron released as a result of the interaction. Electron energy loss is used to identify the particular atoms present within the sample. For example, a high volume of transmitted electrons that have lost 285eV would indicate the presence carbon (285eV is the ionisation energy of a carbon K 1s electron). EELS was performed by an electron energy loss imaging filter (Gatan GIF 200) in diffraction mode, with a convergence and collection angle of approximately 1 and 1.7 mrads, in order to satisfy magic angle conditions for spectroscopy of graphitic materials (170).

6.4 Selected Area Electron Diffraction

Selected area electron diffraction (SAED) relies on the wave-like nature of an electron beam as it passes through a sample. The sample acts like a diffraction grating to the beam, which is scattered according to its De-Broglie wavelength. Due to the high accelerating voltages (200keV) used in the TEM, electron speeds are great and relativistic effects must be accounted for (see Equation (6.1)). Interference of two waves occurs when the path difference between them is equal to an integer multiple of their wavelength (see Figure 6.5) as demonstrated by Bragg's law (see Equation (6.2)).

$$\lambda = \frac{h}{\sqrt{m_0 eU}} \frac{1}{\sqrt{1 + \frac{eU}{2m_0 c^2}}} \tag{6.1}$$

$$n\lambda = 2dsin\theta \tag{6.2}$$

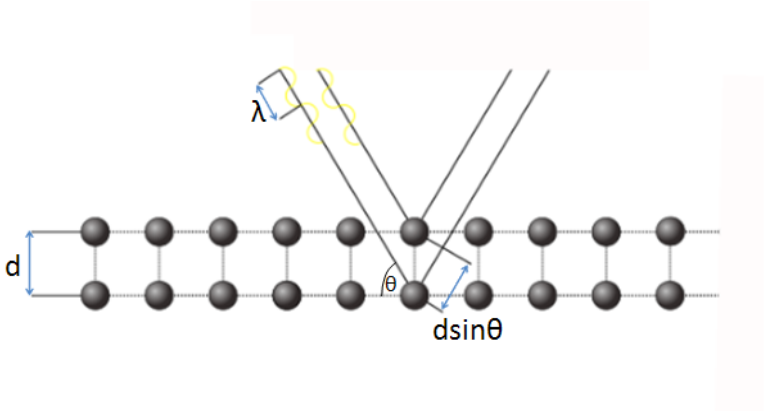

Figure 6.5: Bragg diffraction of coherent electron beams, by the first two planes of a crystal lattice.

Where,

λ – Wavelength

h – Planck's constant

m_0 – Electron rest mass

e – Charge on an electron

U – Accelerating voltage

c – Speed of light in a vacuum

n – Integer

d –Atomic plane spacing

θ – Angle of incident wave

The diffraction patterns produced by the crystal lattice are unique to its crystal structure and can be used to identify it, similarly to X-ray diffraction

techniques. The advantage of SAED over X-ray diffraction is that small localised areas within a single sample can be identified separately.

6.5 X-ray Photoelectron Spectroscopy

X-ray photoelectron spectroscopy (XPS) is a surface analysis technique capable of measuring the chemical composition, chemical state and bond energy of a material, for all elements with the exception of hydrogen and helium. XPS takes advantage of the photoelectric effect and a beam of X-rays is used to liberate photons and electrons from a surface. The X-ray energy is known; hence the electron binding energy can be determined by Equation (6.3).

$$E_{binding} = E_{photon} - (E_{kinetic} + \phi) \quad (6.3)$$

Where,

E – Energy

Φ – Work function of spectrometer

XPS measurements were performed using a VG Escalab 250 XPS with monochromated aluminium K-alpha X-ray source. The spot size was 500μm with a power of 150W. Detailed spectra of individual peaks were taken at an energy of 20eV. Etching was performed using an argon ion gun, calibrated to the sample, with a current of 0.1uA per mm^2. Binding energy was calibrated by setting the carbon 1s peak to 285eV. Detailed spectra had a Shirley background fitted to them and peaks were deconvoluted using mixed Gaussian-Lorentzian fits (using CASAXPS software).

6.6 Previously Mentioned Equipment

In addition to the aforementioned equipment, the following equipment was also used and has been described in Chapter 3: scanning electron microscope, energy dispersive X-ray spectrometer, inductively coupled plasma spectrometer and a centrifuge.

Chapter 7 Hip Simulator Materials and Methods

As with the tribometer, a number of different testing methodologies were employed on the hip simulator. These are referred to as Procedure 1, Procedure 2 and Procedure 3.

7.1 Hip Simulator Procedure 1 (long-term tests performed in 25% bovine serum)

In this procedure, the lubricant used was a 25% dilution of benchmark foetal bovine serum as previously mentioned. Hip bearing surfaces were tested for approximately 0.66 million seconds at 1Hz. At approximately 1/3 million cycles the test was stopped and the surfaces were rinsed with distilled water. The gaiter and base plate were cleaned with Trigene, rinsed and reassembled. Throughout the tests the OCP was monitored and sequential LPR measurements were performed every 10,000 cycles as described previously. Anodic and cathodic Tafel constants were taken as 120mV/dec. All measurements were performed on a Solartron SI 1280. Following testing, samples were stored in a desiccator in preparation for surface analysis. The samples were not weighed, since they were used for surface analysis. Hence, no attempt to remove the adhered tribological layers was made following testing. The tests conducted are summarised in Table 7.1

Test 1	1	2	3	4	5	6
Completed	No	Yes	No	No	Yes	Yes
Test duration (s)	Electrode failed at 200,000s	662,000	Electrode failed at 90,000s	Electrode failed at 230,000s	651,000	661,000
R_a head (nm)	4.4	4.8	4.3	4.8	4.3	4.3
R_a cup (nm)	6.6	6.0	6.9	6.1	6.4	6.6
Clearance (μm)	83.4	69.3	64.0	87.3	74.3	82.3
Notes						Data not available for initial 1000s

Table 7.1: Testing matrix for Procedure 1.

7.2 Hip Simulator Procedure 2 (short-term potentiostatic tests)

In order to assess the impact of tribology on corrosion over a small time scale, a number of short-term tests were performed. In these tests, an overpotential of 100mV was applied to the sample and the change in current was observed at a high sampling rate. A 100mV overpotential was chosen so that passivity was maintained outside of the wear scar but depassivation could still take place within the wear scar without producing an excessive corrosion current. This was done to observe the effect of both load and frequency on the current over a single cycle. The same lubricant and hip simulator set up was used as described in the previous procedure (Procedure 1). Additionally, a rotary variable resistor was attached to the

rear of simulator so that when it oscillated in the sagittal plane the resistance was varied. The resister was then connected to a voltage supply so that it acted as a potential divider. The oscillating potential output was sampled by an Autolab PGstat 101. This enabled measurements of current to be synchronised with the gait cycle. Due to the large number of tests being performed, a single sample was used to perform all of them. To limit the effect of wear on the signal, the conditions that were deemed to be less severe were tested first. To further limit the effect of wear on the bearing surface, all tests were performed for less than 1000s. Following testing at varying velocity and varying load the sample was removed. Using silicon carbide grit paper, the femoral head was roughened to approximately 80-90nm R_a, then to a coarser 140-179nm R_a. This was done by hand, using 1500-grit paper and the current was again monitored. The process was then repeated using 400-grit paper. The different test variables are summarised in Table 7.2.

Conditions	1 Hz Frequency	3.5kN Peak Load	Roughened Surface (1Hz 3kN)
1	1kN peak load	0.5Hz frequency	1500-grit (80-90nm R_a)
2	2kN peak load	0.75Hz frequency	400-grit
3	3kN peak load	1.25Hz frequency	N/A (140-179nm $R_{a)}$

Table 7.2: Testing matrix for Procedure 2.

7.3 Hip Simulator Procedure 3 (long-term tests performed in bovine serum diluted with phosphate buffered saline)

In this Procedure, 3 tests were performed under the same simulated gait cycle as the previous long-term tests (Procedure 1). The lubricant used

differed from that used in Procedure 1; instead European foetal bovine serum diluted to 17g/l with PBS was used, as discussed previously. The pH was buffered to 7.4 and the conductivity was measured as 14.6mS/cm. Tests were run for 1 million cycles in total, but were stopped every 333,000 cycles to permit replacement of the serum solution. The test samples were not removed from the simulator when the serum was replaced. Serum was drained from the simulator, and the test cell, then refilled and rinsed with distilled water 3 times before refilling with fresh serum. This was done in order to minimise disturbance to the tribofilm. At this point, a sample of the used serum was taken for ion analysis by (ICP-MS) (as described in section 3.6). Following testing, surfaces were rinsed with distilled water, weighed. After rinsing, the roughness and roundness of the bearing surfaces was tested using a Taylor Hobson Talysurf PGI 800. Finally, surfaces of the samples were cleaned vigorously with a solution of 5% nitric acid to remove most of the adherent protein layer, before repeated profilometry and mass loss measurements were undertaken. The third sample was not treated in this manner; instead, it was prepared for XPS analysis (as described in section 6.5). OCP and LPR were monitored as was described in the previous long-term tests (Procedure 1), and Tafel constants were determined by anodic and cathodic polarisation during simulated gait. In addition potentiostatic current measurements were also taken. All measurements were taken on an Autolab PGstat 101. This involved applying 100mV anodic potential to the sample (similar to the short-term tests described in Procedure 2) for 100s. This was performed 10 times throughout the entire test, at approximately 100,000-second intervals. Although polarisation of the sample can damage the surface, this effect was minimised by only applying 100mV for a brief amount of time (0.1% of the total test duration). In order to synchronise measurements of current with the gait cycle, the same method was employed for the short-term tests described in Procedure 2.

TEST	1	2	3
Completed	Yes (1 million s)	Yes (1 million s)	Yes (1 million s)
ICP-MS	Yes	Yes	Yes
Weight Loss	Cup and Head	Cup and Head	Cup only
XPS	No	No	Yes (Head)
Notes			Lab mishap lost data between 1200-135,000s.

7.3: Testing matrix for Procedure 3.

To supplement the analysis of the tribological performance of the bearing surfaces, the transient EHL models of the THRs under experimental conditions were established and solved. In the EHL models, the lubricating serum was modelled as an isoviscous, incompressible, Newtonian fluid with a viscosity of 0.0009 Pa.s. This is a reasonable approximation due the very high shear rates encountered in the joint (171). The CoCr alloy was considered as a linear elastic material with the elastic modulus of 210 GPa and Poisson's ratio of 0.3. The load was the actual loading cycle measured from the hip simulator. Only the flexion/extension velocity was considered, which was calculated from the actual measurement of the flexion and extension angle of the head. The governing equations of the EHL modes included the Reynolds equation, film thickness equation and load balance equations (172).

The details of the numerical method can be found elsewhere (173). It is only briefly described here. The numerical analyses were performed under a spherical coordinate system. The governing equations were non-dimensionalised to facilitate the numerical analysis and improve the stability of the numerical process. A cycle was divided into 128 time steps. At each time step, the Reynolds equation was solved using a multi-grid method; the elastic deformation of the bearing surfaces was calculated using a multi-level multi-integration technique (174, 175), and the load balance was satisfied through adjusting the eccentricities of the head according to the calculated load components from the film pressure. Three levels of grid were used in the multilevel solver. On the finest level, 257 nodes were arranged in both

the entraining and side leakage directions (172). Four simulation cycles were analysed.

Chapter 8 Hip Simulator Results

8.1 Electrochemical Results from Procedure 1 (long-term tests performed in 25% bovine serum)

8.1.1 Initial Response of Current and Potential

The measured open circuit potential for the metal-on-metal hip assemblies in static conditions was between -27mV and -79mV (vs. Ag/AgCl). This was substantially more noble than the standard reduction potentials of the major alloying elements of the metal. Such noble potentials indicate that the bearing surfaces were covered with a well-developed passive film, inhibiting anodic dissolution of the surface. The OCP of the bearings surfaces was also nobler than for the MoM pin/plate samples used in the tribometer. This would suggest that the passive film developed on the bearings was thicker or more uniform than that on the pin/plate. The passive film on the bearings was produced during the manufacturing, and passivation, process whilst the film on the pin/plate was developed in the laboratory, following the sample preparation outlined in section 4.2.

When the hip simulator was started, the motion and loading cycle began simultaneously. Initially, the loading cycle was lower than that desired but it was continually ramped-up over the first 10 cycles to reach the required value. Initiation of the hip simulator produced a simultaneous negative shift in the measured OCP, as shown in Figure 8.1. The magnitude of the change in OCP from static to dynamic conditions, for the first 10,000 cycles, is shown in Figure 8.2. The negative shift in OCP between static conditions and that observed after 10,000s was on average -253mV. The shifts for all the tests are shown in Figure 8.2. These observations indicate that the passive film was damaged by interaction of the opposing surfaces, leading to an increase in oxidation of the base alloy. This is an interesting finding

since it demonstrates that, although the hip simulator operated in a different lubricating regime to the tribometer, depassivation still occurred.

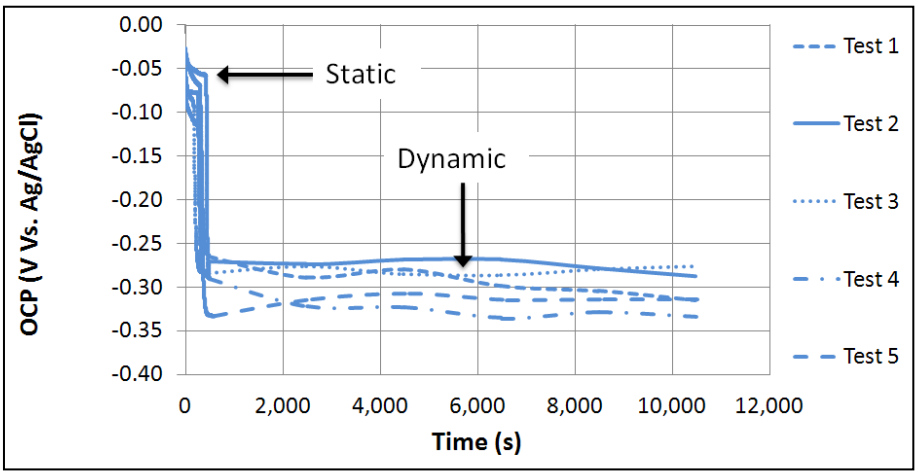

Figure 8.1: OCP response over the first 10,000 cycles (2h 47m).

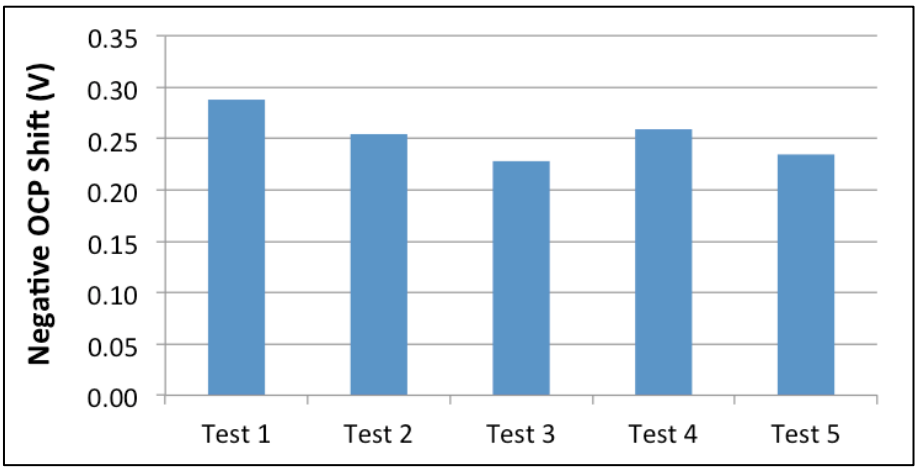

Figure 8.2: Shift in OCP from static to dynamic conditions over the first 10,000 cycles (2h 47m).

Depassivation of the surface was confirmed by the observation of a decrease in polarisation resistance following the onset of simulated gait. An example of this is given in Figure 8.3. The polarisation resistance was used to obtain the corrosion current (I_{corr}), as described in section 4.1.2. It is clear

from Figure 8.3 that the signal to noise ratio was large under static conditions. This may account for some variation in the calculated corrosion currents between separate tests, or in a single test over time. Anodic and cathodic Tafel constants of 120mV were used in the determination of the corrosion current from LPR data.

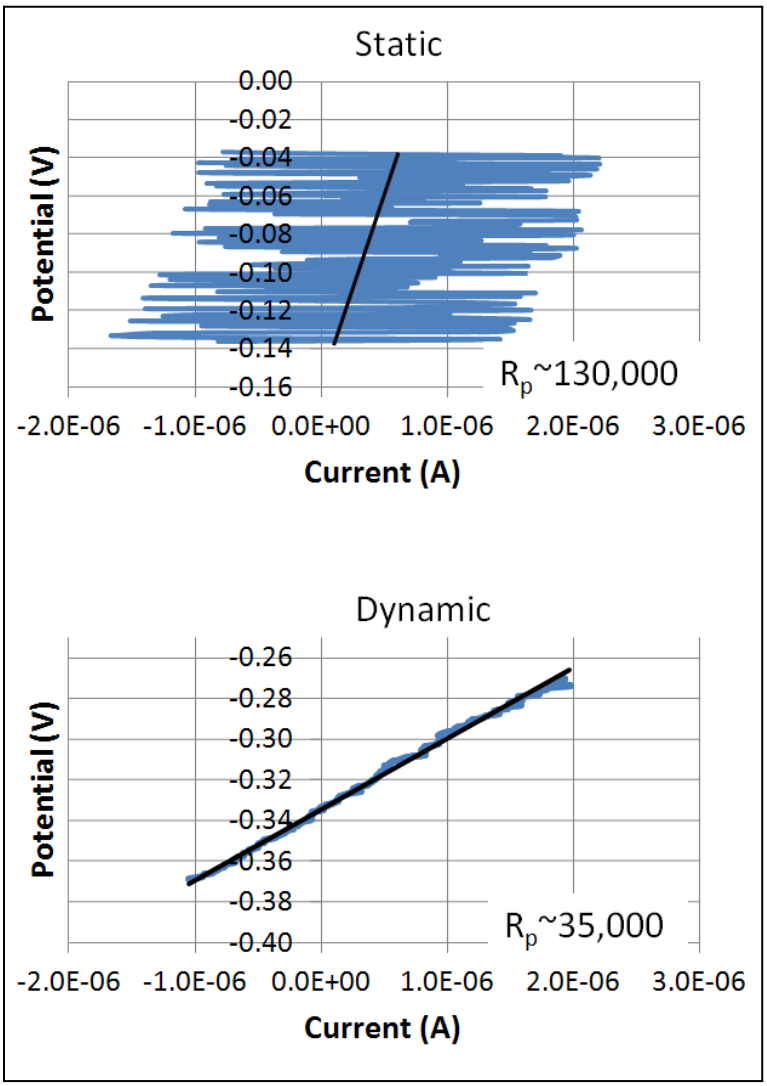

Figure 8.3: LPR measurements under static and dynamic conditions used to calculate polarisation resistance (R_p).

The variation in total corrosion current, as a result of wear-induced damage to the passive film, is shown on Figure 8.4. It can be seen that, over the first 10,000s, there was an average increase in the total corrosion current of

2.28μA (shown in Figure 8.5). From this, it was possible to estimate the average current density in the depassivated region of the surfaces. This is illustrated by Equations (8.1), (8.2) and (8.3).

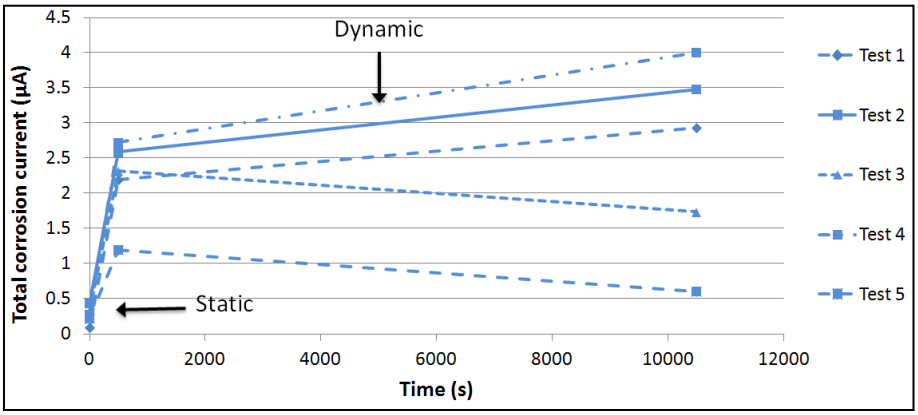

Figure 8.4: Variation of corrosion current over the first 10,000 cycles (2h 47m).

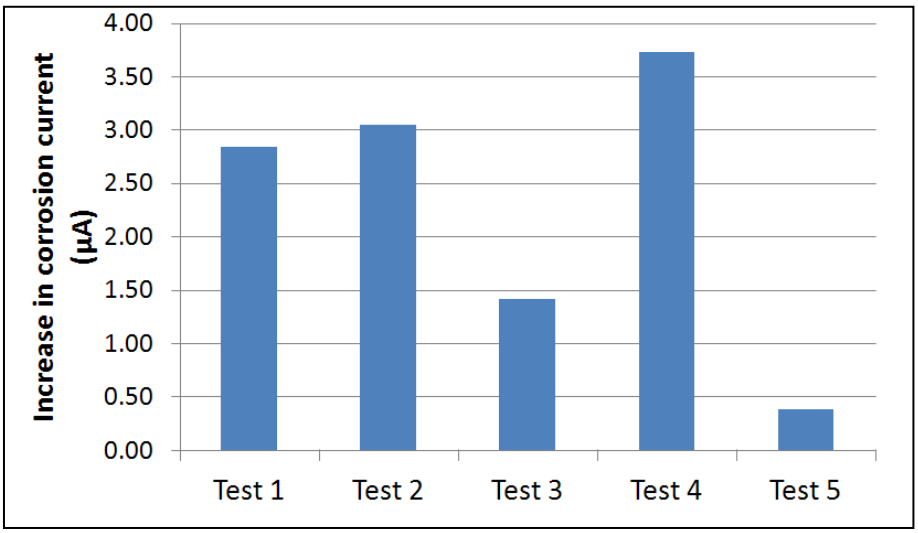

Figure 8.5: Increase in corrosion current over the first 10,000 cycles (2h 47m).

$$I_{Corr(wear\ scar)} = i_{corr(dynamic)} A_{wear\ scar} \tag{8.1}$$

$$I_{Corr(static)} = i_{corr(static)} A_{total} \tag{8.2}$$

$$I_{Corr(total)} = i_{corr(static)}(A_{total} - A_{wearscar}) + i_{corr(dynamic)}A_{wearscar} \quad (8.3)$$

Where,

I_{corr} – Total corrosion current

i_{corr} – Corrosion current density

The area of the wear scar can be estimated by calculating the size of the Hertzian contact patch between the head and cup, then calculating the distance that head moves across the cup surface during a single gait cycle. This produces a value that is an over estimate of the contact region. Since the hip is lubricated, the contact patch is smaller than that predicted by Hertzian analysis. Also, the load varies over a single cycle producing a changing wear scar size. It is also assumed that the current density on the head and cup are equal. Hence, this method gives an estimate of the maximum possible wear scar size. Using this method the maximum wear scar area was calculated to be 218mm^2, which accounted for 3.6% of the total exposed bearing surface.

Calculating the current density in this way assumes that it is uniform across the wear scar. This is unlikely, since there is a sliding point of contact between the surfaces. However, these assumptions give a basis for comparison and a similar analysis has been used to analyse other tribocorrosion systems (176). What is actually calculated is the average current density across the whole wear scar over a number of cycles. Figure 8.6 shows the variation in the estimated corrosion current density in the load bearing conjunction from static to dynamic conditions. Figure 8.7 shows the increase in corrosion current density within the wear scar, over the first 10,000s. By comparing Figures 8.5 and 8.7, it can be seen that the total corrosion current increased by just 9.6 times over the first 10,000 cycles, whereas the corrosion current density in the wear scar increased by close to 300 times. The wear scar current density in the hip simulator was substantially lower than that produced in the tribometer, by at least an order of magnitude. Two points can explain this. In the hip simulator, the current density was an underestimate due to the over estimate of the wear scar

area. In addition, the lubricating conditions are very much more severe in the tribometer as it resides in the boundary regime, hence depassivation is likely to be more severe.

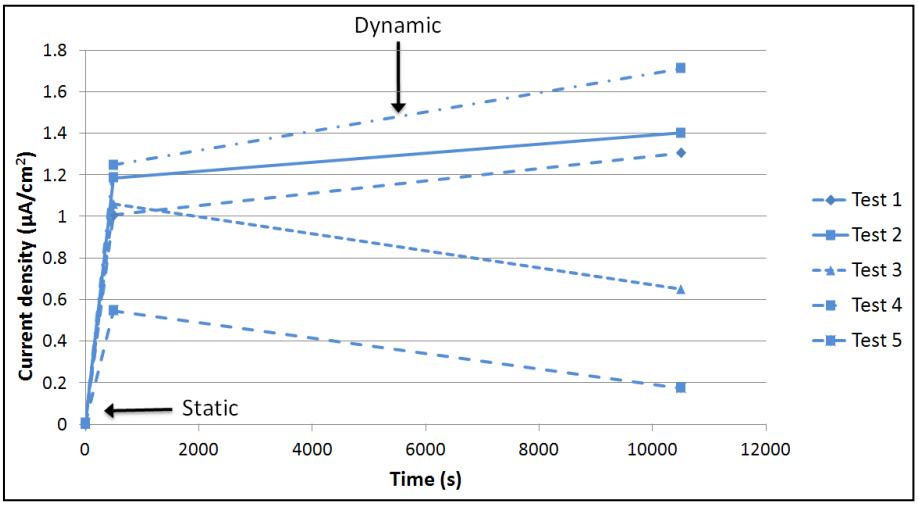

Figure 8.6: Variation of corrosion current density of the wear scar.

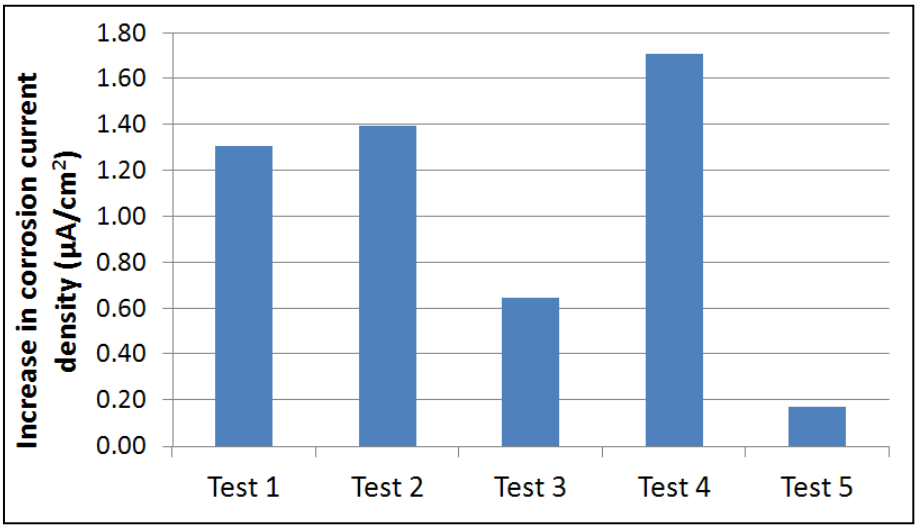

Figure 8.7: Increase in wear scar current density over the first 10,000 cycles (2h 47m).

Figure 8.6 shows that for two of the tests, the current density within the wear scar reduced from that measured immediately after motion was initiated to that measured at 10,000s. One cause of this may be the lack of a lubricating film under static conditions. Prior to motion, there is no entrainment velocity, which according to the modified Dowson-Hamrock equation (Equation

(2.10)) gives a predicted film thickness of zero, and hence no lubricating film. Hence, the initial cycle is performed in conditions comparable to dry conditions, which could result in very severe depassivation of the surface. This effect may be mitigated by the ingress of serum proteins into the clearance gap during static conditions, which may explain why it did not occur in all 5 tests.

8.1.2 Response of the current potential throughout the duration of the test

The long-term data from the tests that were performed for approximately 667,000 cycles are given below. For ease of interpretation, the corrosion current is plotted alongside the OCP for each test individually in Figures 8.8-8.10.

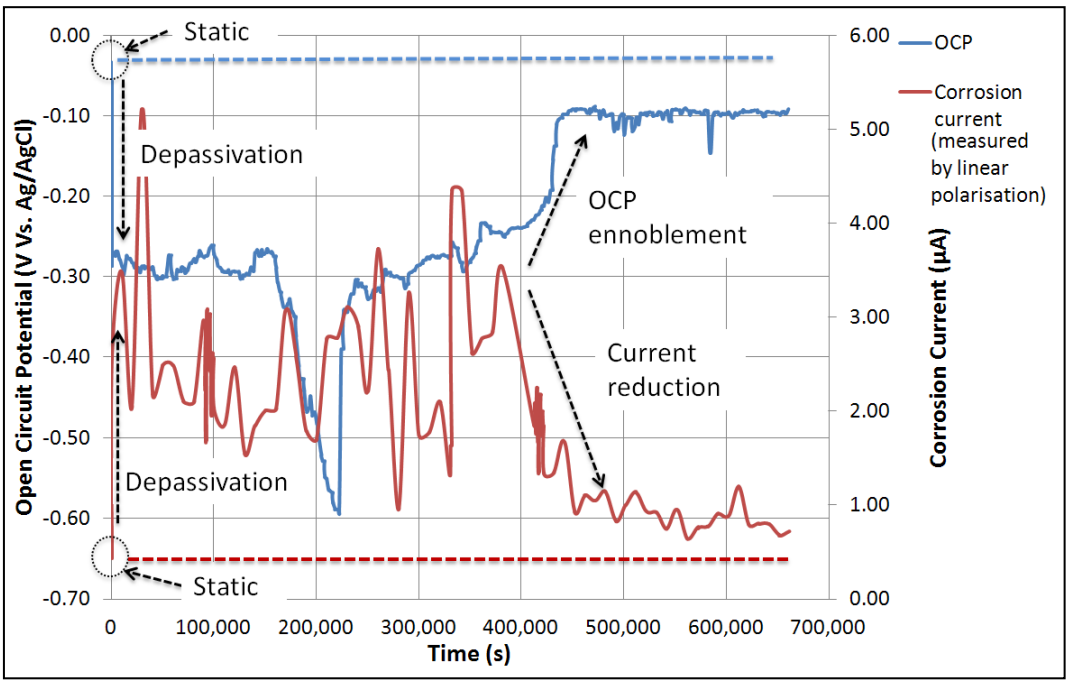

Figure 8.8: Variation of OCP and corrosion current throughout test 2.

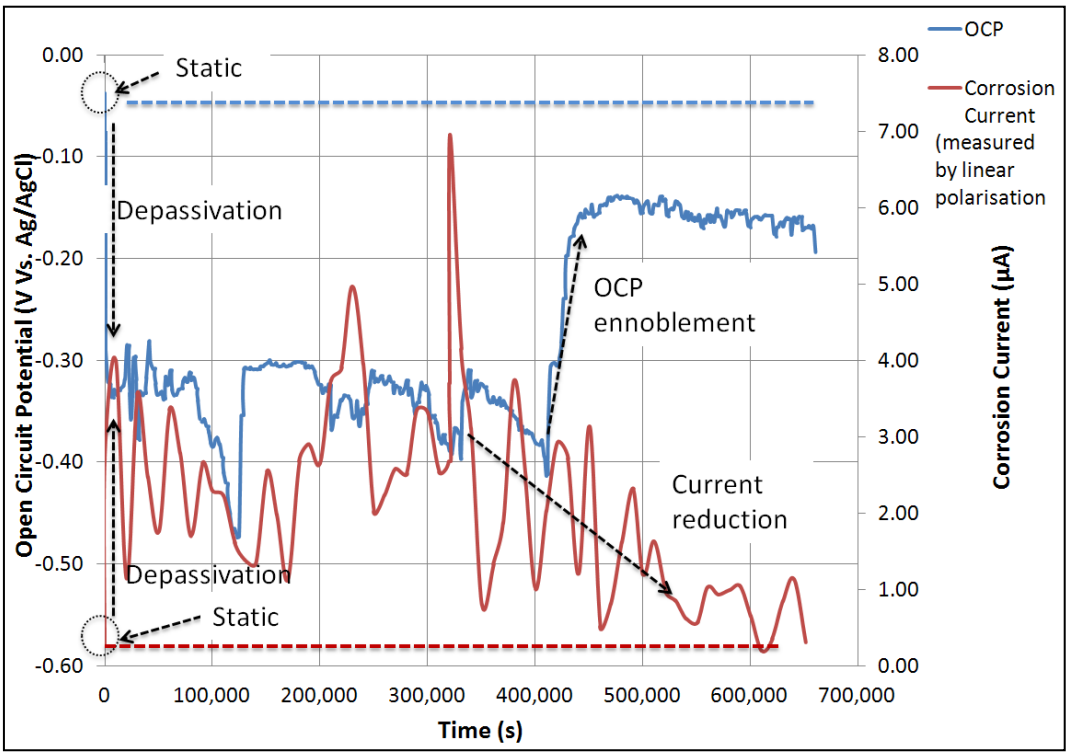

Figure 8.9: Variation of OCP and corrosion current throughout test 5.

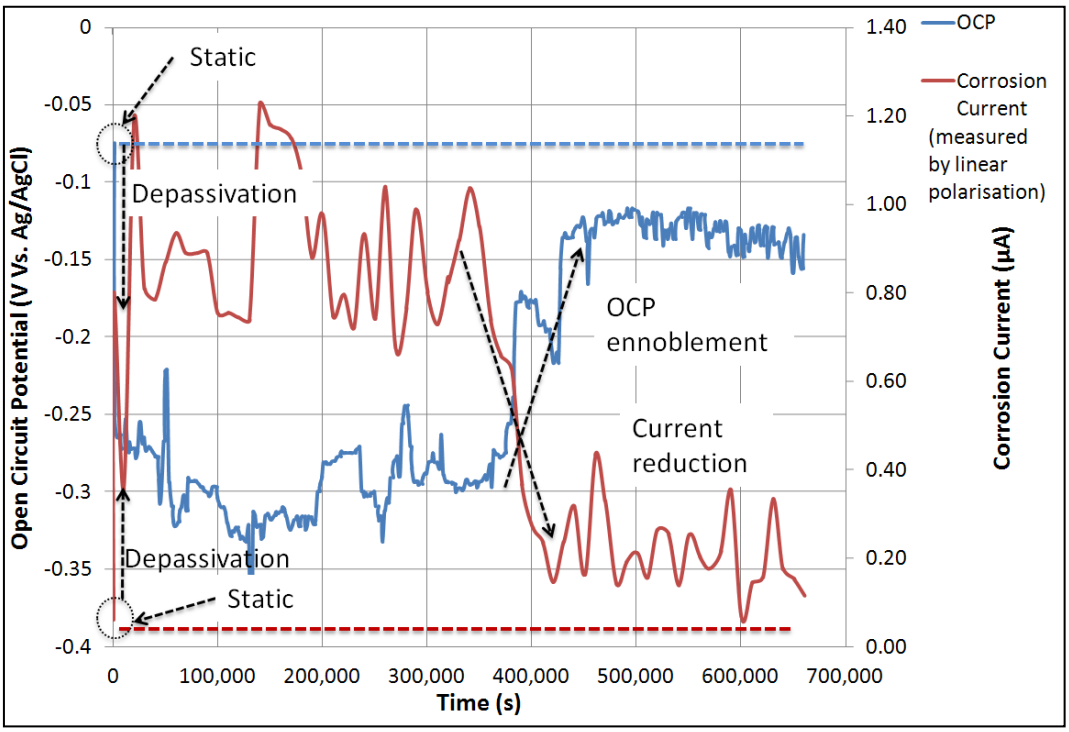

Figure 8.10: Variation of OCP and corrosion current throughout test 6.

Figures 8.8-8.10 have been labelled to identify the distinguishing features. The OCP and corrosion current under static conditions are circled, and a horizontal line has been extended from them. The reduction in OCP and corresponding increase in corrosion current are indicated by the vertical arrows labelled ‘depassivation’. In each of the tests there was ennoblement in the OCP and a corresponding reduction in corrosion current, which have been labelled accordingly.

The ennoblement of OCP in all 3 tests occurred between 350,000 and 450,000 cycles, and was between 169mV and 187mV. The OCP remained at an elevated level throughout the remainder of the tests. The ennoblement in OCP indicates a reduction in the thermodynamic drive for the surface to react. This can be interpreted as a level of recovery of the passive film taking place and is consistent with previous findings by Yan *et al* in both tribometer (88, 104, 161) and hip simulator studies (150, 177). A similar trend was observed for the corrosion current. Close to the time when the OCP was seen to ennoble, there was a reduction in corrosion current. This was more difficult to quantify due to the large oscillations in the measured signal. Reduction in the corrosion current confirmed, the inference from OCP that anodic dissolution of the surface had reduced. This could be caused by a number of different phenomena.

- The observed reduction was close to the timescale that has previously been reported for the running-in of MoM bearings (20, 92, 106). If the observed electrochemical response correlated with running-in, then the reduction in corrosion could either be attributed to mechanical or chemical causes.

- A reduction in surface roughness, or improved clearance or a combination of both could reduce the severity of mechanical contact. This would have the action of reducing the magnitude of the cyclic depassivation within the wear scar. A shift in the depassivation/repassivation equilibrium away from depassivation and would reduce the corrosion current.

- The build-up of tribochemical reaction layers could also produce a similar effect. If a tribolayer acted as a solid lubricant interposed between the surfaces, it could reduce the level of mechanical depassivation. It is worth noting that during the tests, neither the corrosion current nor the OCP returned to the levels recorded under static conditions. This indicated that, although some reduction had occurred, increased dissolution of the surface had arisen. Corrosion currents were converted into a cumulative mass loss using the Faraday equation (Equation (5.1)). The cumulative mass loss over the duration of the 3 tests is shown in Figure 8.11.

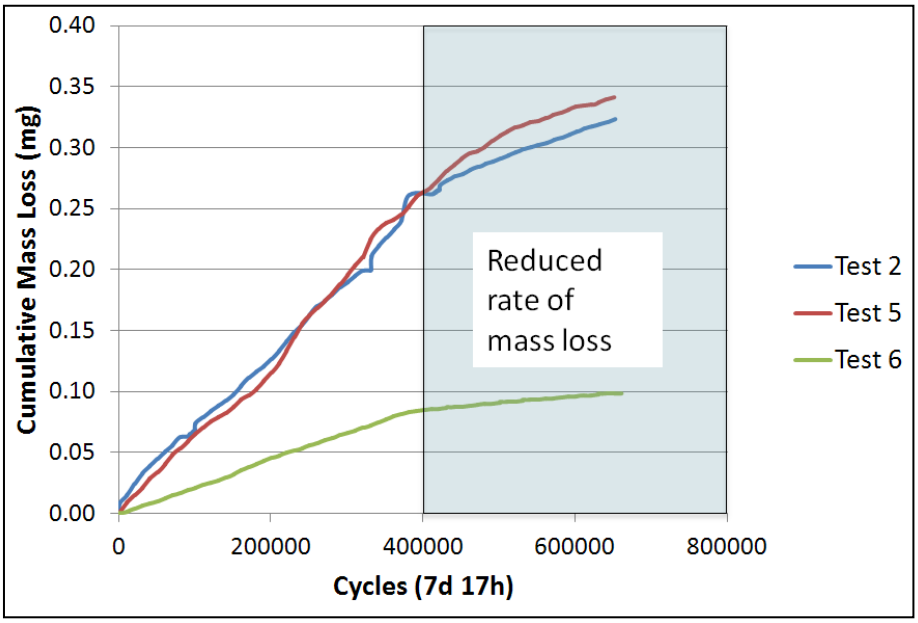

Figure 8.11: Cumulative electrochemical mass loss of test duration.

It can be seen that there was a remarkable agreement in the results between tests 2 and 5, however, the cumulative mass loss from Test 6 was substantially lower. It is not clear what caused this, although total weight loss measurements from previous studies have been shown to vary substantially over the first million cycles (74). From the sample of studies investigated by Dowson *et al* (74), a typical weight loss for a 36mm MoM joint with an average minimum film thickness of 18nm would be approximately 7mg for the first 0.67M cycles. Hence the amount of material liberated due to depassivation accounted for a substantial proportion of the expected total material lost over the test duration.

8.2 Electrochemical Results from Procedure 2 (short-term potentiostatic tests at +100mV Vs OCP)

8.2.1 Effect of Varying Load

For tests run at a frequency of 1Hz it was seen that increasing the load increased the current measured. When sampled at a frequency of 100Hz for 50s, the average current was 7.12μA, 7.2μA and 9.23μA for peak loads of 1kN, 2kN, and 3kN. These measured values are more than twice as great as those measured in the tests performed for an extended duration using linear polarisation. This indicated that enhanced dissolution was caused by the applied anodic potential. This is shown in Figures 8.12-8.14. It is clear from the figures that there was considerable oscillation of the current over a short time interval, as expected signal was cyclic and appeared too regular to be attributable to noise.

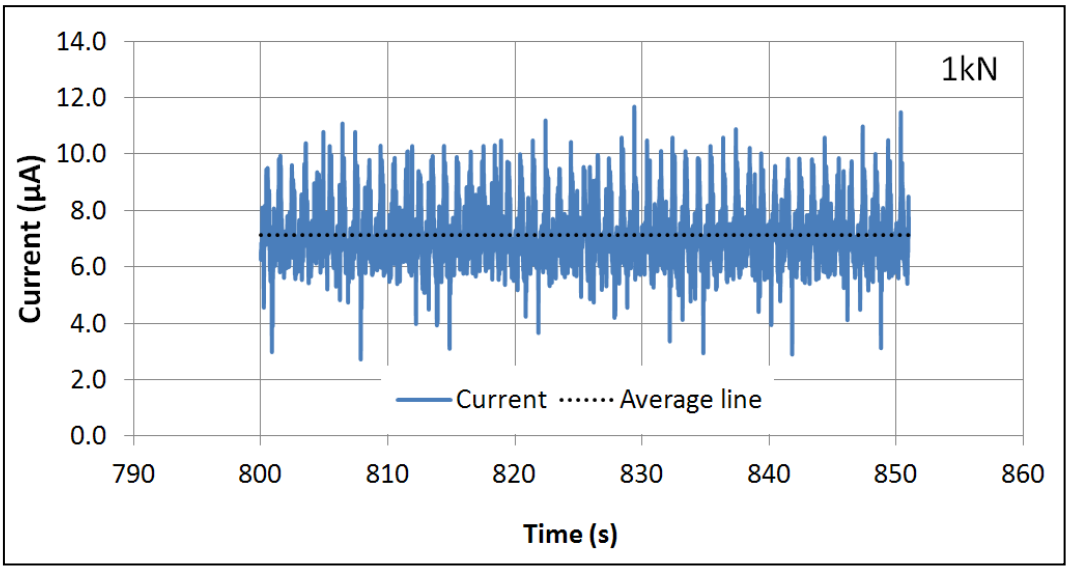

Figure 8.12: Potentiostatic current under 1kN peak load at 1Hz.

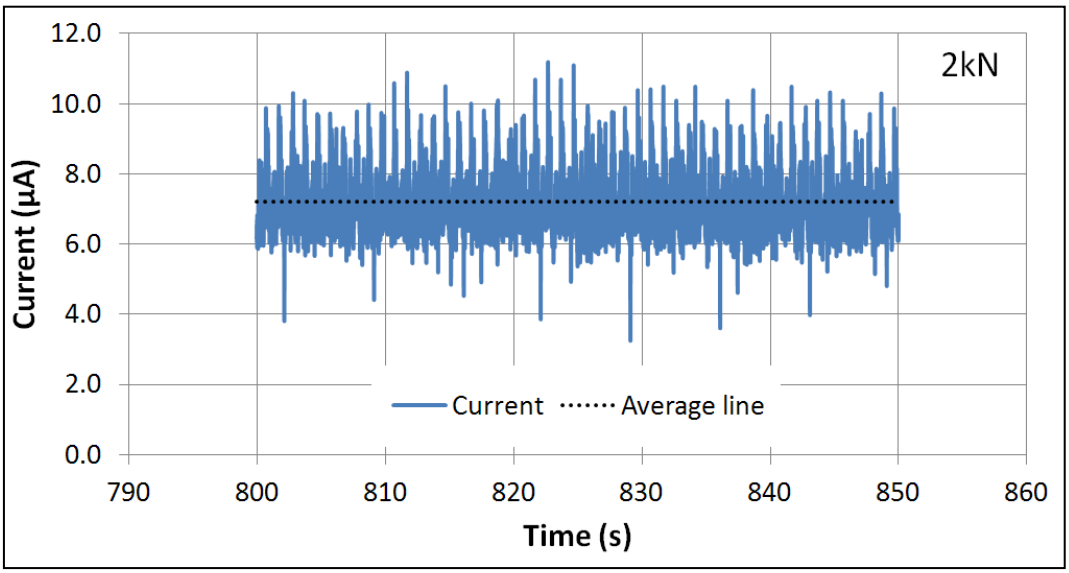

Figure 8.13: Potentiostatic current under 2kN peak load at 1Hz.

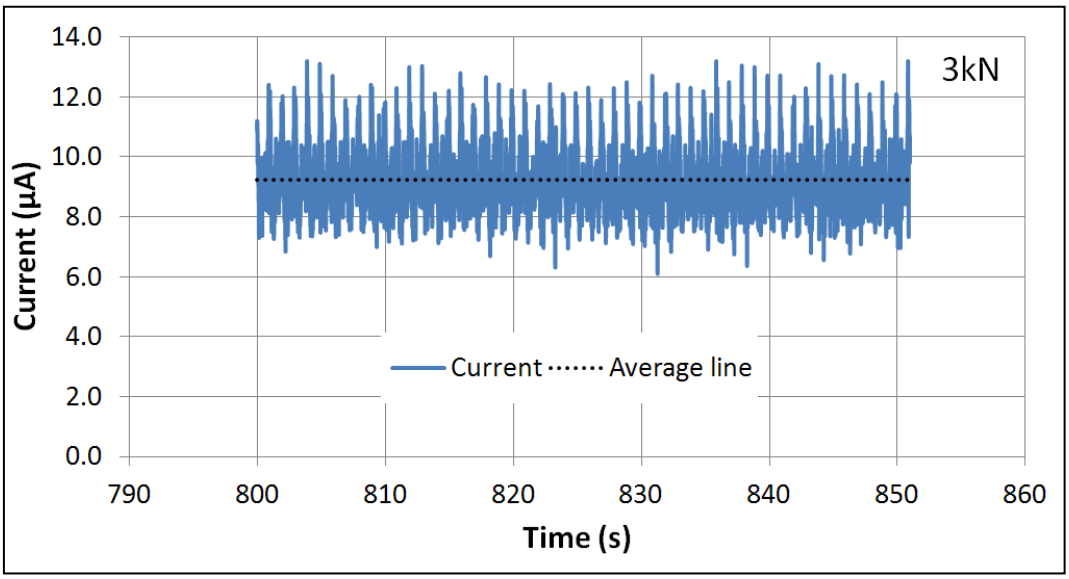

Figure 8.14: Potentiostatic current under 3kN peak load at 1Hz.

When looking at just 5s worth of data, it can be observed that the current followed a defined repetitive pattern at the same frequency as the gait cycle (1Hz) (Figures 8.15-8.17). This oscillating current reflected the variation in the anodic dissolution of the sample over a single cycle, caused by mechanical depassivation.

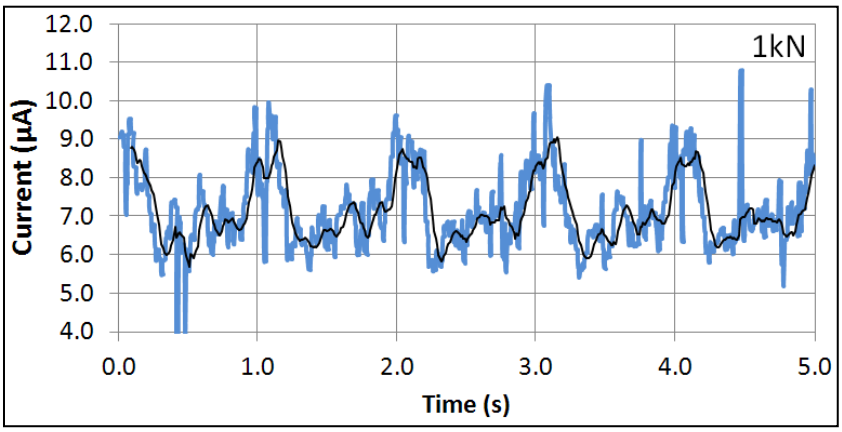

Figure 8.15: 5s of potentiostatic current sampled at 100Hz, tested under 1kN peak load at 1Hz overlaid with a 10-point moving average.

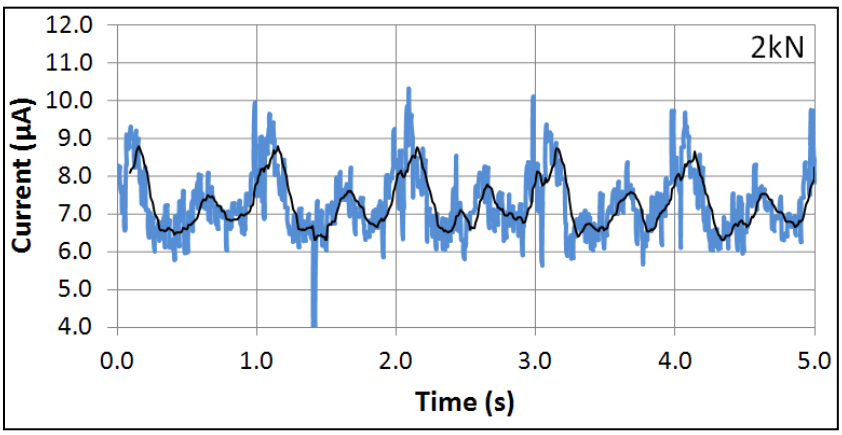

Figure 8.16: 5s of potentiostatic current sampled at 100Hz, tested under 2kN peak load at 1Hz overlaid with a 10-point moving average.

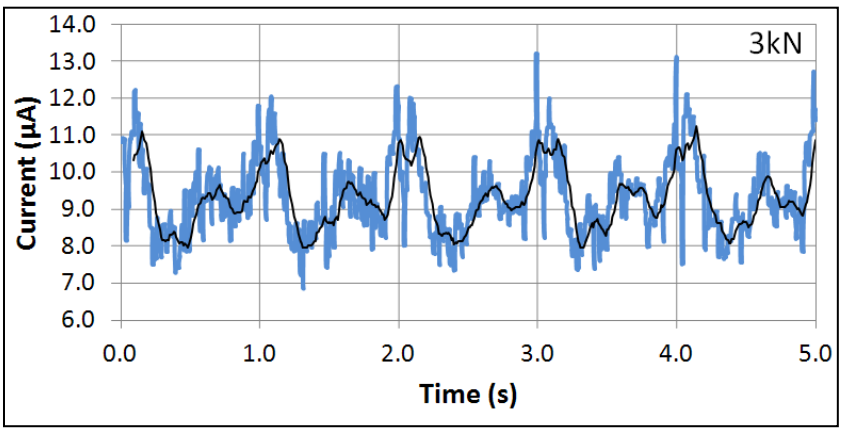

Figure 8.17: 5s of potentiostatic current sampled at 100Hz, tested under 3kN peak load at 1Hz overlaid with a 10-point moving average.

In each case the cyclic pattern appeared to consist of two peaks, with the larger of the two being forked. Upon increasing the load, the magnitude of whole signal of the current increased rather than just an increase in the magnitude of the peak. However, the range of the signal was also increased with an increasing load. A single current cycle is shown plotted alongside the applied loading cycle in Figure 8.18.

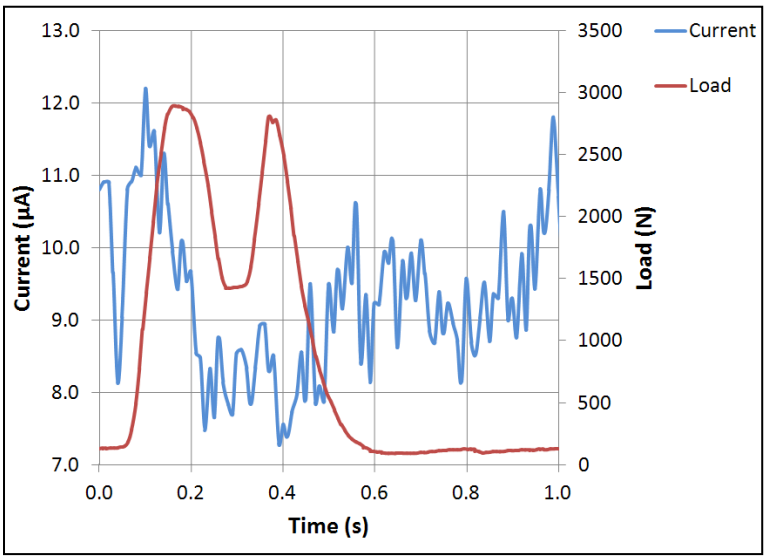

Figure 8.18: Potentiostatic current over one cycle synchronised with the applied load.

Clearly there was no direct correlation between the instantaneously applied load and the simultaneously measured current, but a general increase in current with increased load was observed. The increase in average current with peak load may be caused by a number of different factors.

- The predicted minimum EHL film thickness under steady load is a function of load$^{-0.21}$ (74) (Equation (2.10)). By reducing the minimum EHL film thickness, the lambda ratio is also reduced (Equation (2.7)). This causes an increase in the amount of load supported by asperity contact, as opposed to that supported by EHL film pressure. In addition, under dry contact, the Hertzian contact patch half width (a) increases as a function of load$^{1/3}$, shown in Equation (8.4).

- Furthermore, since the load is balanced by the plastic flow stress of the surface, increasing the load in dry conditions increases the real contact area proportionally. Although the samples were tested in lubricated conditions, some mechanical asperity contact took place. Since this was altered, the level of mechanical depassivation was also altered, giving rise to the measured corrosion current.

$$a = \left(\frac{3wR}{E'}\right)^{\frac{1}{3}} \tag{8.4}$$

Where,

a – Contact patch half width

w - Load

R – Effective radius

E' – Effective elastic modulus

8.2.2 The Effect of Gait Frequency

The effect of gait cycle frequency was not as clear as the effect of load. The average current over 50s when sampled at 100Hz was very similar (6.9μA, 6.6μA and 6.7μA at gait frequencies of 0.5Hz, 0.75Hz and 1.25Hz respectively). This is shown in Figures 8.19-8.21. Although the average current for the three conditions did not vary substantially, it can be seen from the figures that, at higher gait frequencies, there was a greater range in the measured current signal.

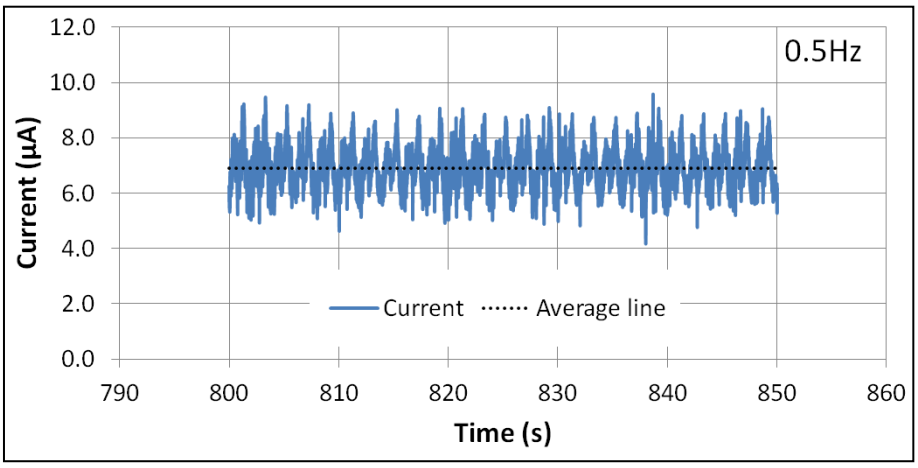

Figure 8.19: Potentiostatic current under 3.5kN peak load at 0.5Hz.

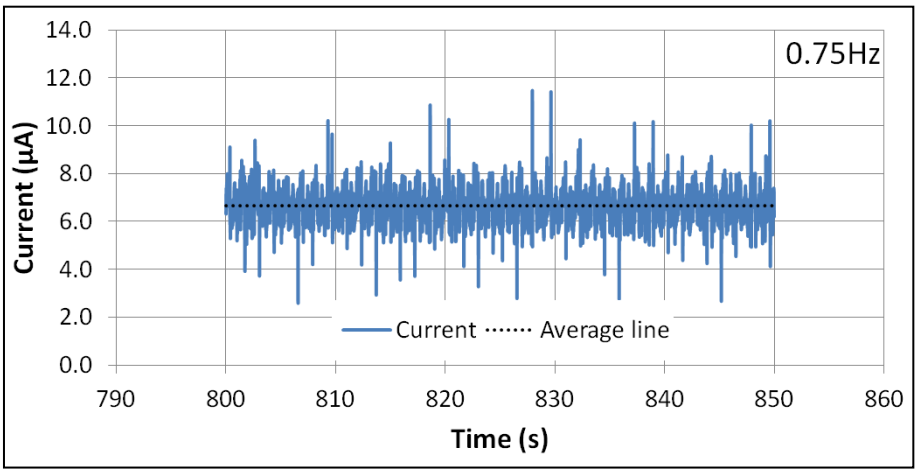

Figure 8.20: Potentiostatic current under 3.5kN peak load at 0.75Hz.

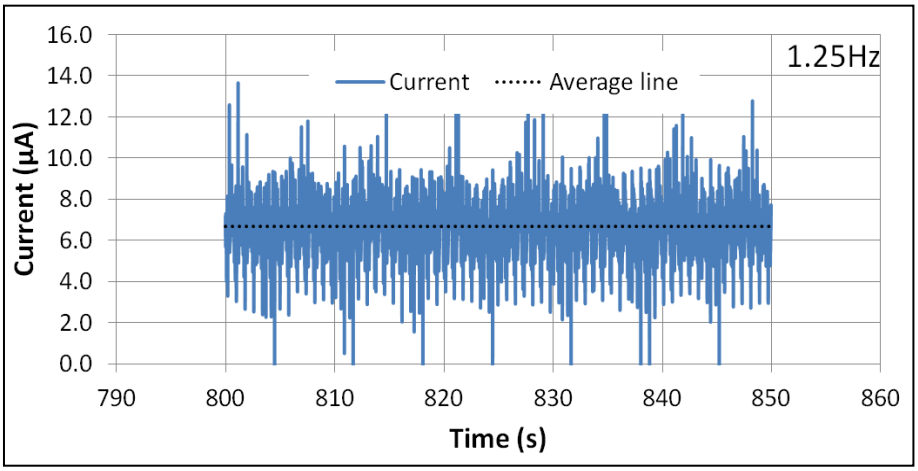

Figure 8.21: Potentiostatic current under 3.5kN peak load at 1.25Hz.

As before, the current oscillations over a single cycle can be interpreted when displayed over a smaller timescale as shown in Figures 8.22-8.24. It can be seen that, as gait frequency was increased, the current oscillation frequency also increased to match it. At a frequency of 0.5Hz, the current response was similar to that observed previously at 1Hz. There were two peaks per cycle, with the major occurring at the very start of each, and the minor occurring just past the midpoint. At 0.75Hz, the distinction between the major and minor peak was less apparent. A cyclic pattern, however, was still observed. At a frequency of 1.25Hz, the two-peaked cycle changed to one approximating a sinusoidal response, with a maxima located at the centre of each cycle.

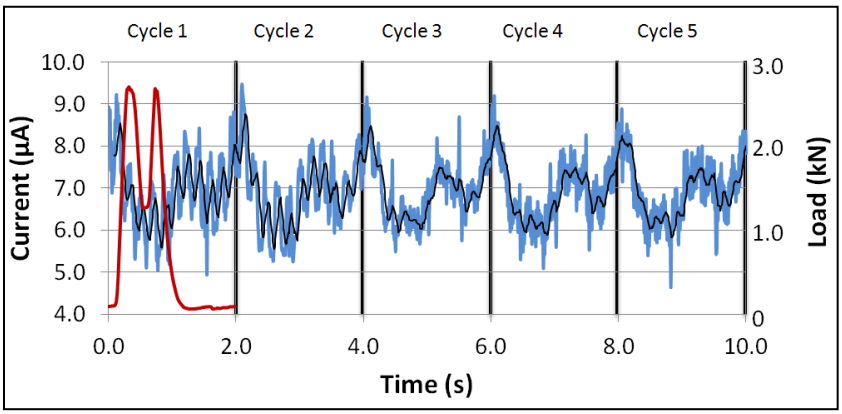

Figure 8.22: 5 cycles of potentiostatic current sampled at 100Hz, tested under a 3.5kN peak load at 0.5Hz overlaid with a 10-point moving average.

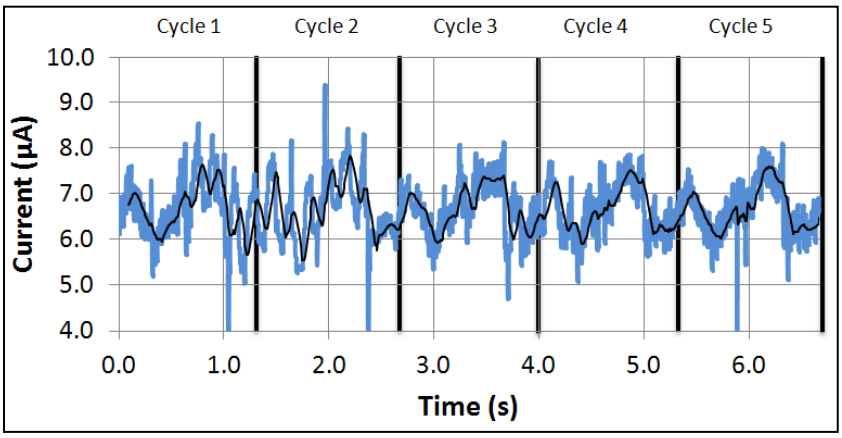

Figure 8.23: 5 cycles of potentiostatic current sampled at 100Hz, tested under a 3.5kN peak load at 0.75Hz overlaid with a 10-point moving average.

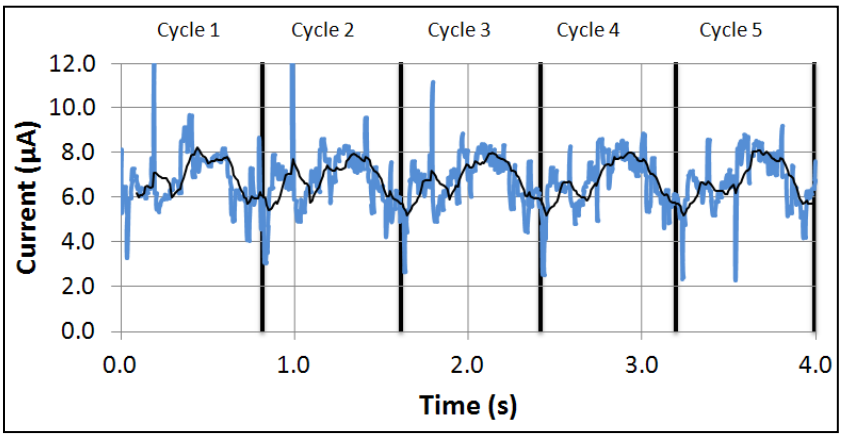

Figure 8.24: 5 cycles of potentiostatic current sampled at 100Hz, tested under a 3.5kN peak load at 1.25Hz overlaid with a 10-point moving average.

The lack of a clear trend between the average current observed over 50s and the applied gait frequency can be explained by a number of competing factors. In terms of EHL film thickness, a higher gait frequency produces a greater entrainment velocity and hence a thicker film. The predicted minimum EHL film thickness is a function of angular velocity$^{0.65}$ (74) (Equation (2.10)). This effect would produce a greater average minimum film thickness at higher frequencies and reduce the severity of asperity contact, since a greater proportion of the load would be supported by fluid pressure. A competing factor is that, at higher gait frequencies, the bearing surfaces undergo a greater relative sliding distance in the same amount of time. This results in a greater amount of wear, and therefore depassivation. A second mechanism then arises. At a higher gait frequency there is less time between the femoral head depassivating the same location on the acetabular cup. At a higher frequency, there is less time for the passive film to regenerate itself between successive cycles; hence, a greater current density will flow from the surface. Sun *et* al (67) demonstrated that cobalt chromium repassivates over a period of seconds following micro abrasion in solutions of NaCl and bovine serum. Where this was the case, repassivation produces an exponential decay in the corrosion current. An illustration of the repassivation process following abrasion is demonstrated in Figure 8.25. The small amount of change in the average current suggests that, over the range of frequencies tested, these factors largely cancel one another out. However, the change in appearance of the cyclic current response suggests that the depassivation mechanism was altered. Another factor, which is difficult to quantify, is the production of wear debris generated within the

bearing. Debris with a diameter greater than the minimum film thickness may cause depassivation when trapped in the joint capsule. At greater gait frequencies, the egress of the debris may be affected, as well as the particle morphology itself. Bowsher *et al* (96) demonstrated that, by altering the gait cycle, particle morphology was dramatically changed.

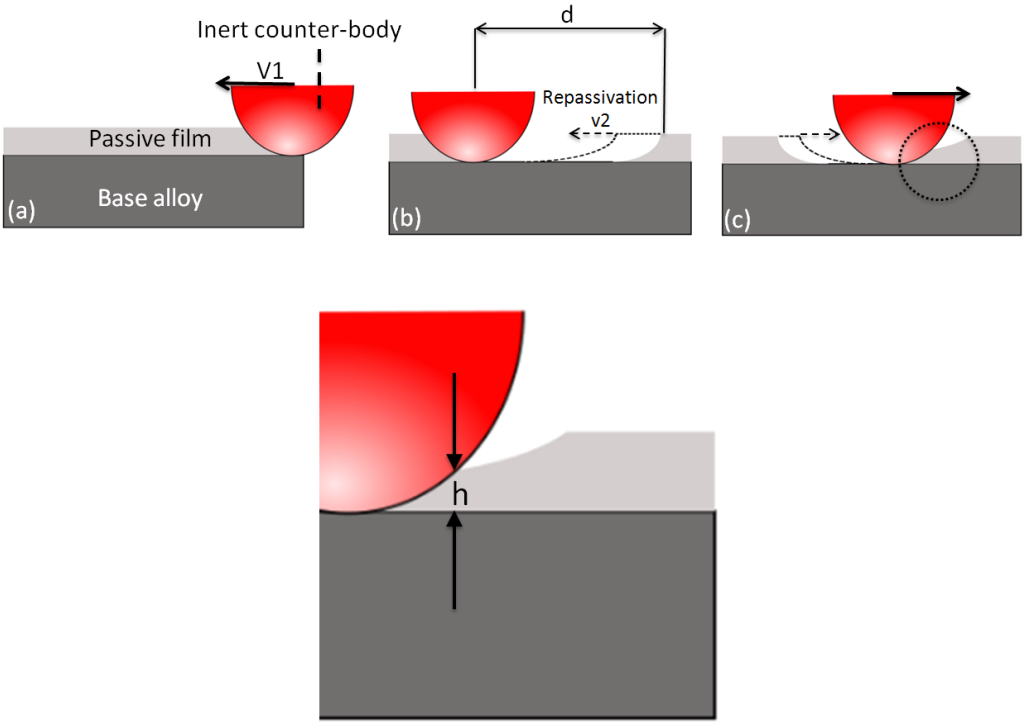

Figure 8.25: Depassivation/repassivation of a surface.

From Figure 8.25, the distance d depends on the sliding velocity (v1) and the rate of repassivation (v2). When reciprocating across a wear path of length d, the sliding velocity and repassivation velocity will determine the thickness of the passive layer (h) at a given location.

8.2.3 The Effect of Bearing Roughness

The effect of roughening the femoral head on the potentiostatic current signal is shown in Figures 8.26-8.27. The average currents over 100s were

8.79μA and 5.95μA respectively after roughening using 1500-(85nm R_a) and 400-grit -(155nm R_a) SiC paper, respectively. The peak load was 3kN and the gait frequency was 1Hz. Surprisingly, roughening of the surface did not produce an increase in corrosion current when compared to that measured at 1Hz and a 3kN maximum load. As mentioned previously, all tests were performed on a single bearing surface; hence in the later tests the surfaces had already been subjected to wear and corrosion. It was unexpected that upon increasing the roughness of the surface from that obtained by 1500-grit SiC paper to that obtained by 400-grit SiC paper, the average current was substantially reduced. Figures 8.26-8.27 both demonstrate a fairly constant current over 100s. This suggests that the effect of gradual wear did not cause the observations made, and it was caused by the increase in surface roughness.

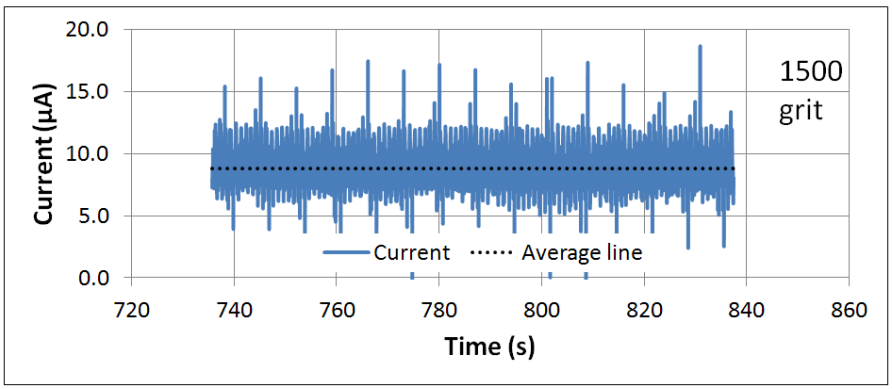

Figure 8.26: Potentiostatic current under 3kN peak load at 1Hz after roughening with 1500-grit SiC paper.

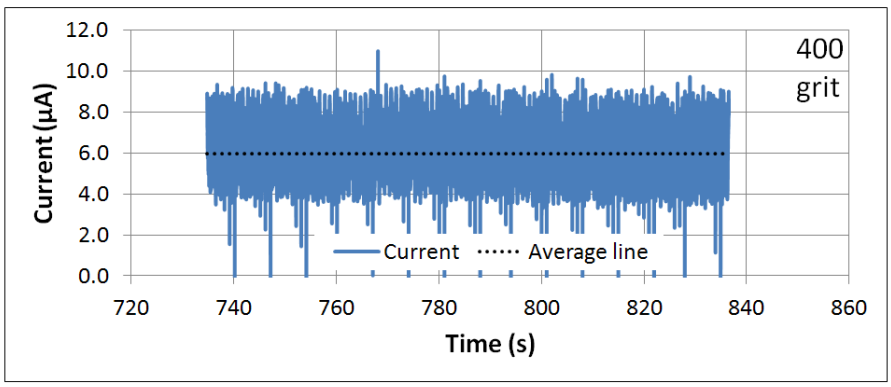

Figure 8.27: Potentiostatic current under 3kN peak load at 1Hz after roughening with 400-grit SiC paper.

Upon roughening the femoral head, the current exhibited a repetitive response at the gait frequency as was previously observed prior to roughening. The response contained the characteristic two-peaked profile previously mentioned, with peak positions occurring in similar locations throughout the cycle (see Figures 8.28 and 8.29). Interestingly, the signal resembled that produced at the same load and frequency prior to roughening. This is a significant finding. Prior to roughening, the surface roughness was below 10nm R_a on both the head and cup, however, following roughening this was substantially increased. The increase in roughness was sufficient to shift the theoretical lubrication regime towards more severe mixed lubrication. The only manifestation of the increase in contact severity was a sharpening of the measured signal. This suggests that the damage mechanism taking place was similar in both smooth and roughened systems. This may be explained by the presence of proteins. Although the minimum lubricating film thickness was predicted to be several tens of nanometres the protein molecules will result in a greater separation than this. It has been shown that protein lubricating films will behave differently to the EHL film (120, 132, 133), and can separate surfaces even when there is no entrainment velocity (81). Although, it must be considered that these findings were reported under steady-state conditions between a ball and plate configuration. It is feasible that at all points throughout the cycle the surfaces were partially separated by a combined proteinaceous and elastohydrodynamic film, whether they were roughened or smooth, hence the current cycle measured did not differ as dramatically as may have been expected.

The observation of decreasing current when surface roughness was increased, by using 1500-grit paper to 400-grit paper was unexpected. Classic lubrication analysis would suggest that a higher surface roughness would result in a greater degree of mechanical contact and hence depassivation. However, it has been demonstrated that upon increasing the nano-scale roughness of a metallic surface, the adsorption of bovine serum albumin was dramatically increased (178, 179). For platinum samples, it was found that an increase in surface R_a from 1.49nm to 4.62nm caused an increase in adsorption (normalised against increased surface area) by up to 34%, depending on the total protein concentration (178). Another possible explanation for the decreased current at an increased roughness could be the change in contact mechanics. By artificially roughening the surface the

asperity geometry may be altered in such a way that the net depassivation was less severe despite more severe contact taking place at asperity tips. The work of Johnson *et al* (180) suggests that asperity stiffness is considerably less than EHL film stiffness and large deformation occurs across them. This could alter the relative contribution of wear, corrosion and the synergy between the two. Hence, the total wear could be increased, despite a lower corrosion current being observed. This is illustrated in Figure 8.30.

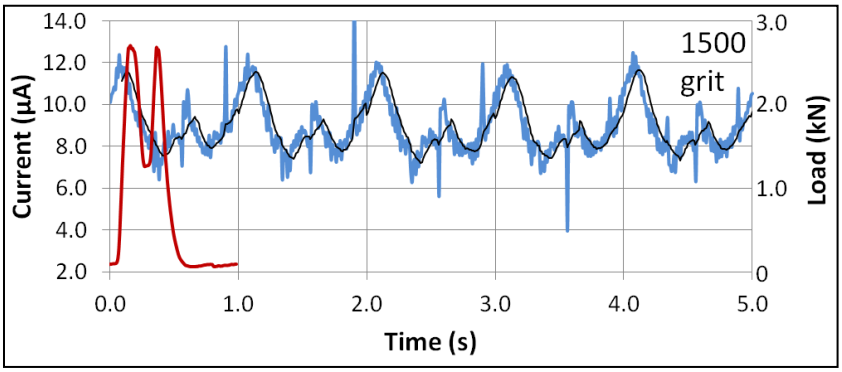

Figure 8.28: 5s of potentiostatic current sampled at 100Hz, tested under 3kN peak load at 1Hz after roughening with 1500-grit SiC paper overlaid with a 10-point moving average.

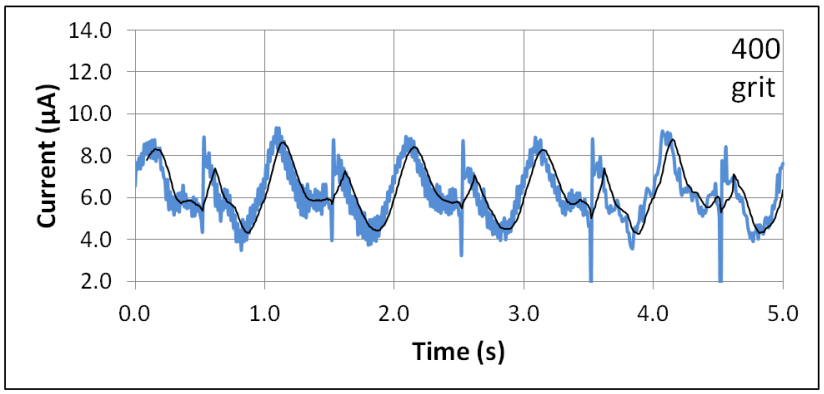

Figure 8.29: 5s of potentiostatic current sampled at 100Hz, tested under 3kN peak load at 1Hz after roughening with 1500-grit SiC paper overlaid with a 10-point moving average.

If the ratio between the total material removed and the amount of passive film removed is varied, it could affect the contribution of corrosion towards

material degradation. A situation could then arise in which an increase in the wear rate may not be related directly to an increase in the measured corrosion current.

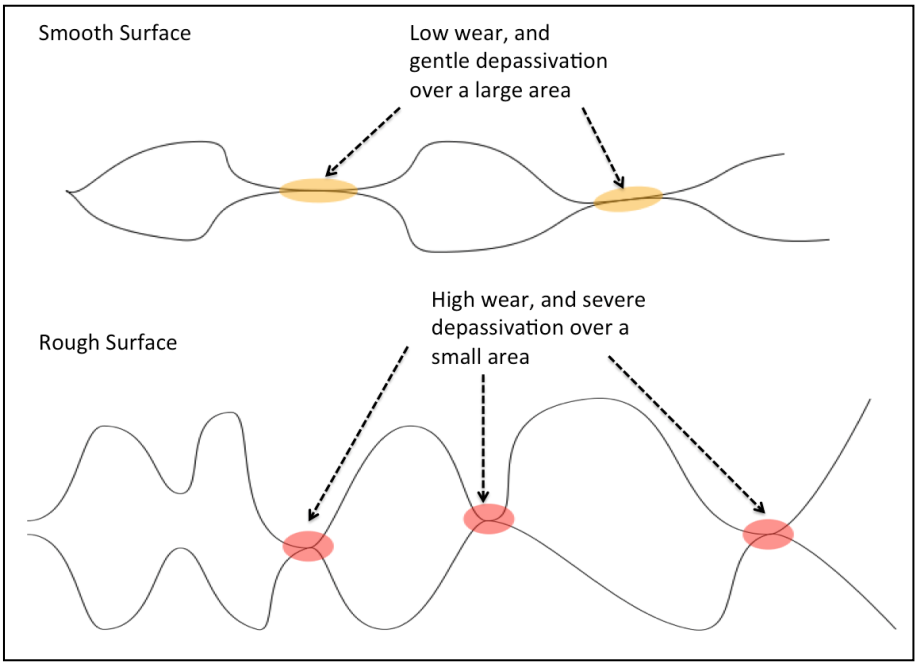

Figure 8.30: Asperity contact between rough and smooth surfaces.

The potentiostatic current measurements exhibit important and consistent features. The current varies over a single cycle, and this variation is affected by altering the simulator operating parameters (motion and load). The signal was also sensitive to roughening from 1200- to 400-grit SiC polishing paper. Analysis of these competing parameters is not trivial as they combine complex tribological concepts with depassivation kinetics.

These new findings on the interaction between tribology, corrosion and depassivation are most significant.

8.3 Electrochemical Results from Procedure 3 (long-term tests performed in bovine serum diluted with phosphate buffered saline)

8.3.1 Initial Features Response of Current and Potential measurements

The OCP in static conditions was on average -98mV (see Figure 8.31), which is slightly less noble than that observed in the previous long-term tests (Procedure 1). The different lubricant used in the two procedures can explain this, specifically the interactive effects of bovine serum albumin (BSA) and phosphate buffered saline (PBS) on CoCr. Munoz *et al* (42) demonstrated that phosphates can shift the OCP to nobler potentials, but the effect is reversed upon the addition of BSA. BSA and phosphates are both negatively charged at pH 7.4 and competitively adsorb onto the alloy surface. When this occurs, the role of albumin as an anodic catalyser dominates over the reduced mass transport caused by the two species. The overall effect is a reduction in OCP. It should be noted, here, that other studies suggest that competitive adsorption does not occur between albumin and phosphates and that protein concentration had no significant effects on corrosion current (181). The electrochemical impedance spectroscopy results presented, however, show that for solutions of 0.1M PBS the addition of bovine calf serum caused a reduction to R_f (the passive film resistance) by up to 23% (181). Although this change is not as substantial as that reported by Munoz *et al* (42), it demonstrates that BSA does affect the system, and hence must adsorb on to the surface.

Upon initiation of the loading cycle, the OCP shifted in the negative direction. This is consistent with the observations made in section 8.1 and was not unexpected, considering that the conditions were very similar, with the only variation being the serum solution used. The results are shown in Figure 8.32, it can be seen that there is limited data available for ‘Test 3’ this was

the result of a disruption to the measurement of corrosion which resulted in an absence of data between 1200s and 135,000s.

Figure 8.31: OCP in static conditions.

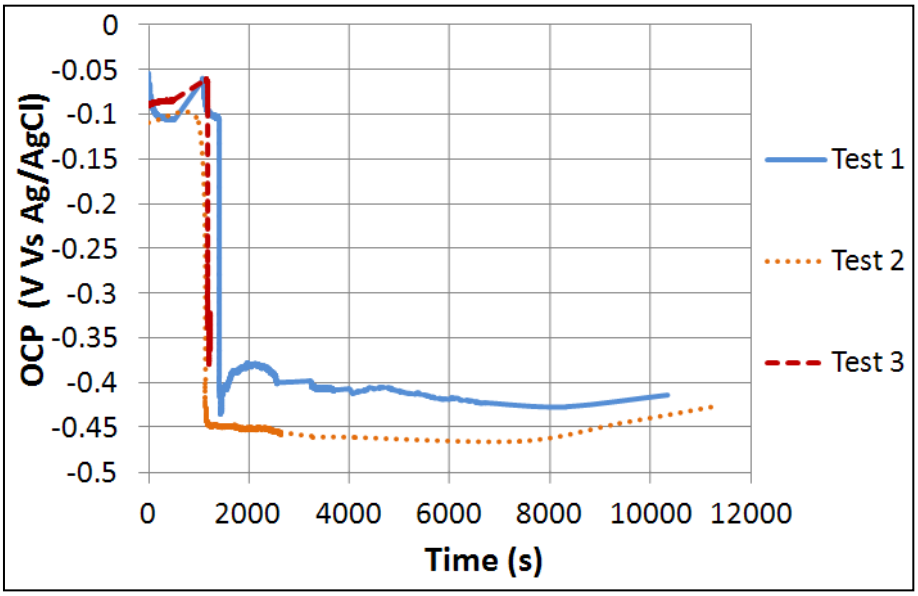

Figure 8.32: OCP response over the first 10,000s (2h 46m).

The immediate negative shift in potential associated with depassivation was approximately -300mV (see Figure 8.33). This was a marginally greater shift than that observed over the first 10,000s for the un-buffered tests in Procedure 1. This may be attributable to the different lubricant used. By using PBS to dilute the serum, as opposed to distilled water, the osmolality

of the solution was increased. This is manifested as an increase in the chloride ion concentration and the presence of phosphate ions (which were not present in the two previous procedures). In addition there is also a higher concentration of bovine serum albumin (17g/l as opposed to 11.1g/l), which has been shown to catalyse anodic dissolution of the alloy (42).

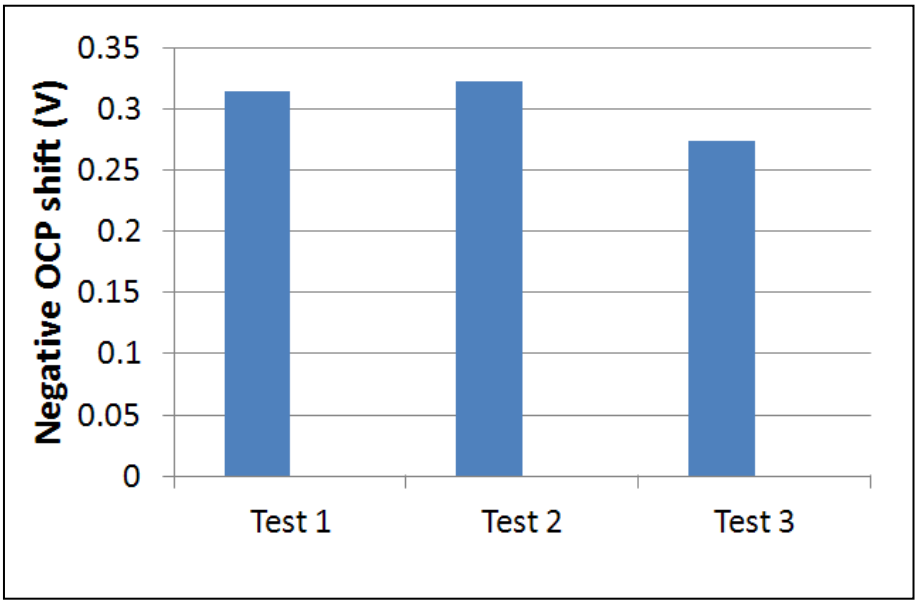

Figure 8.33: Immediate shift in OCP caused by depassivation.

The negative shift in OCP was met by a corresponding increase in corrosion current as discussed previously. The increase in corrosion current over the first 10,000s for Test 1 and Test 2 was 6.9μA and 7.7μA correspondingly (see Figure 8.34). As before, the current density can be estimated for the wear scar, (see in Figure 8.35). Both the current and wear scar current density were much greater than for any of the long-term tests conducted in un-buffered 25% serum solution (Procedure 1). An increase in corrosion current could be caused in two ways; a greater amount of depassivation could take place, the removal of more of the passive film, or a greater amount of alloy dissolution giving an equal amount of depassivation. The former relates to the lubricating properties of serum proteins and phosphates, whilst the latter relates to the corrosive properties of the lubricant.

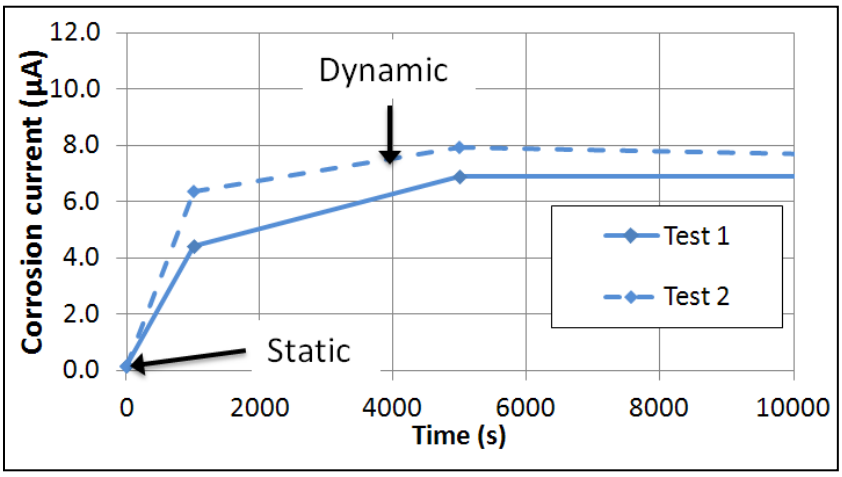

Figure 8.34: Variation of corrosion current over the first 10,000s (2h 46m).

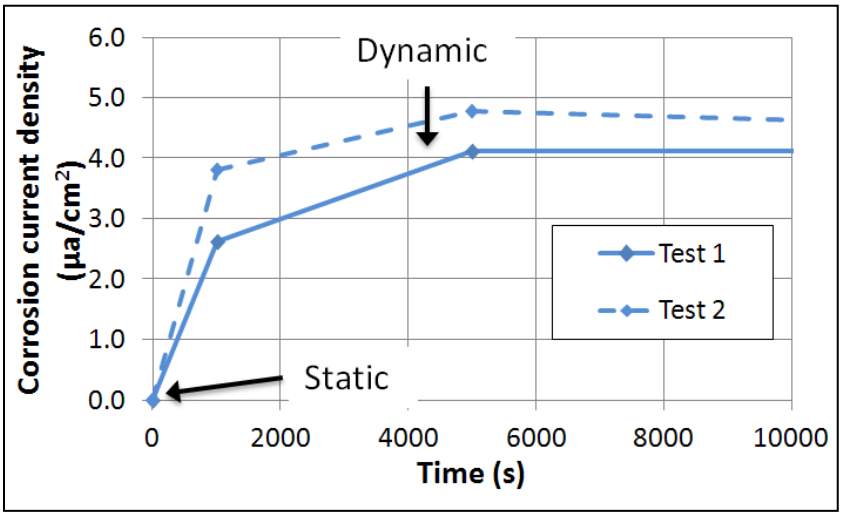

Figure 8.35: Variation of corrosion current density, in the wear scar, over the first 10,000s (2h 46m).

Phosphates adsorb strongly onto CoCr surfaces (42, 181). The presence of phosphates may reduce the total protein adsorption on to the surface, via competitive adsorption. As discussed in section 2.4.8, adsorbed proteins can act as boundary lubricants between CoCr sliding interfaces, thus reducing wear, and also reducing depassivation (128, 129, 134). These actions may explain the observation of increased corrosion currents compared to those measured in un-buffered 25% serum solution (Procedure 1). Alternatively, the increased current could be a purely attributable to changes in the serums properties as an electrolyte. This could be caused by the increased corrosivity of the different serum solution used. The corrosivity caused by the

increase in both protein and chloride concentration could offset the anodic inhibition caused by phosphate adsorption. This would also explain the more negative OCP measured in static conditions. Hence both chemical and mechanical factors may be relevant.

As with the previous long-term tests (Procedure 1), the corrosion current was calculated from linear polarisation resistance (LPR) measurements with Tafel constants calculated from Tafel plots performed at the end of the experiment. Example LPR plots taken in static and dynamic conditions are shown in Figures 8.36 and 8.37, Figure 8.38 shows an example Tafel plot.

As can be seen in Figures 8.36 and 8.37, noise was fairly large compared to the measured signal. Every effort was made to increase the signal to noise ratio, but, when measuring such low currents in a dynamically changing environment, there will always be difficulties in obtaining clean data. For this reason, it must be accepted that corrosion currents obtained from LPR measurements in these conditions contain a level of error. For the purpose of observing general trends in corrosion behaviour this does not pose an issue. It is more pertinent when attempting to convert corrosion measurements into an electrochemical mass loss. When this was the case it was assumed that due to the large amount of LPR measurements taken per test (approximately 100), errors due to noise or poor signal would largely average out.

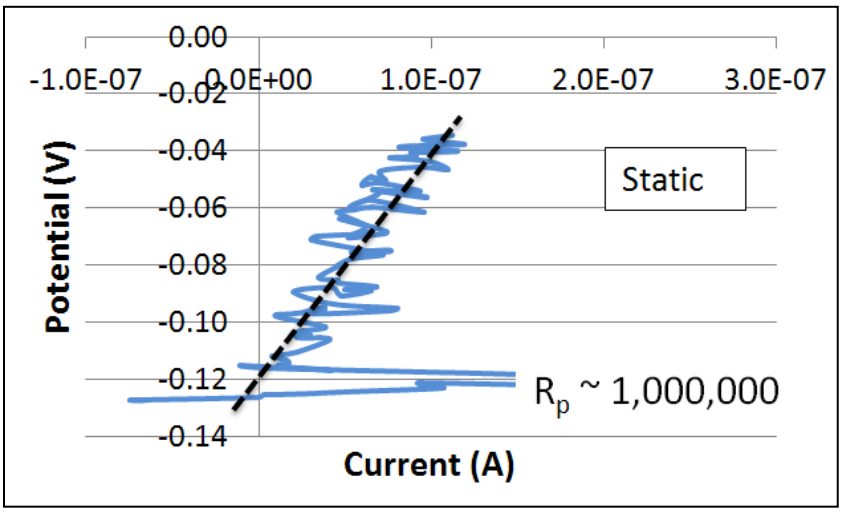

Figure 8.36: Linear polarisation in static conditions.

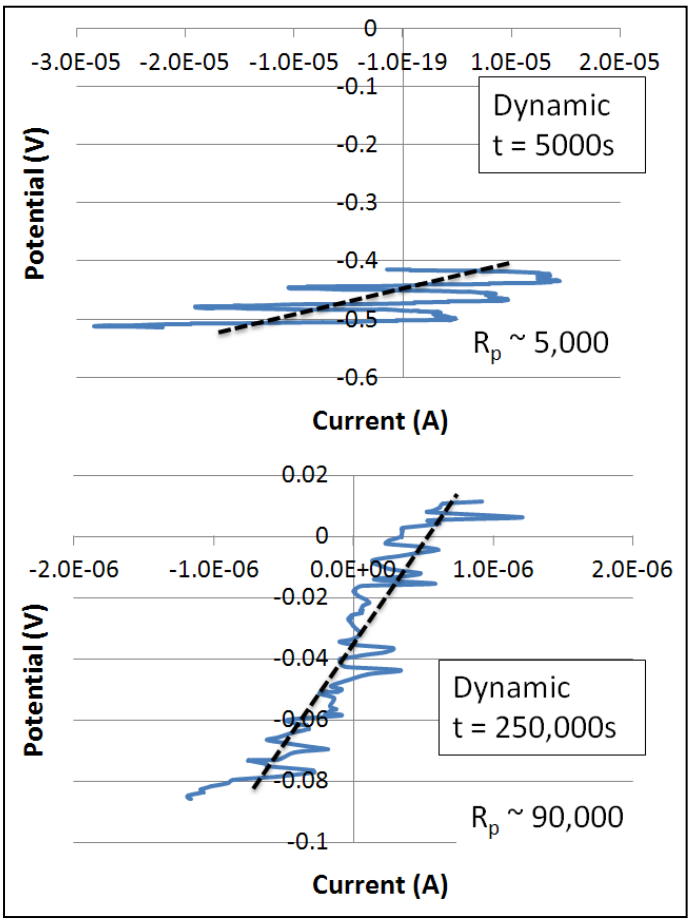

Figure 8.37: Linear polarisation in dynamic conditions at 5000s (1h 23m) and 250,000s (2d 21h 26m).

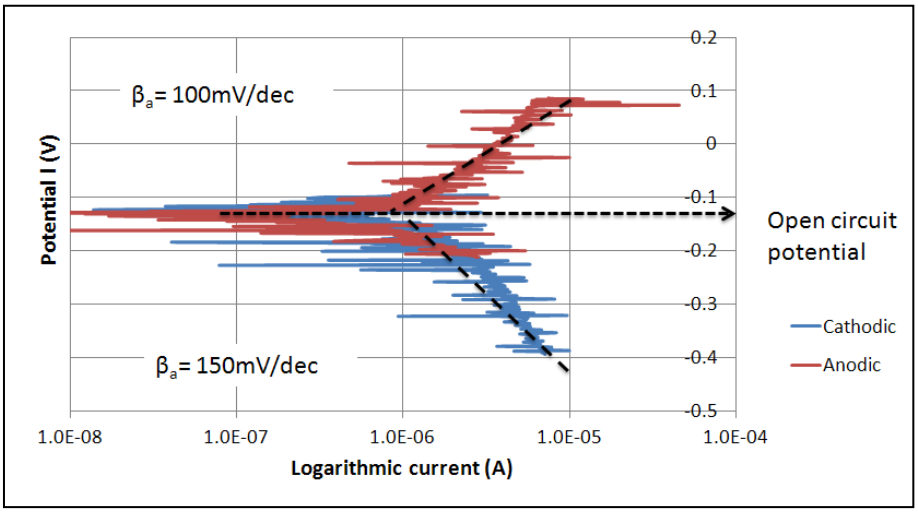

Figure 8.38: Tafel slope measured during normal simulated gait whilst lubricated with serum diluted with phosphate buffered saline following approximately 950,000s (10d 23h 53m).

8.3.2 Response of Current and Potential Over The Test Duration

The variation of both calculated corrosion current and OCP is shown for each of the three tests in Figures 8.39-8.41.

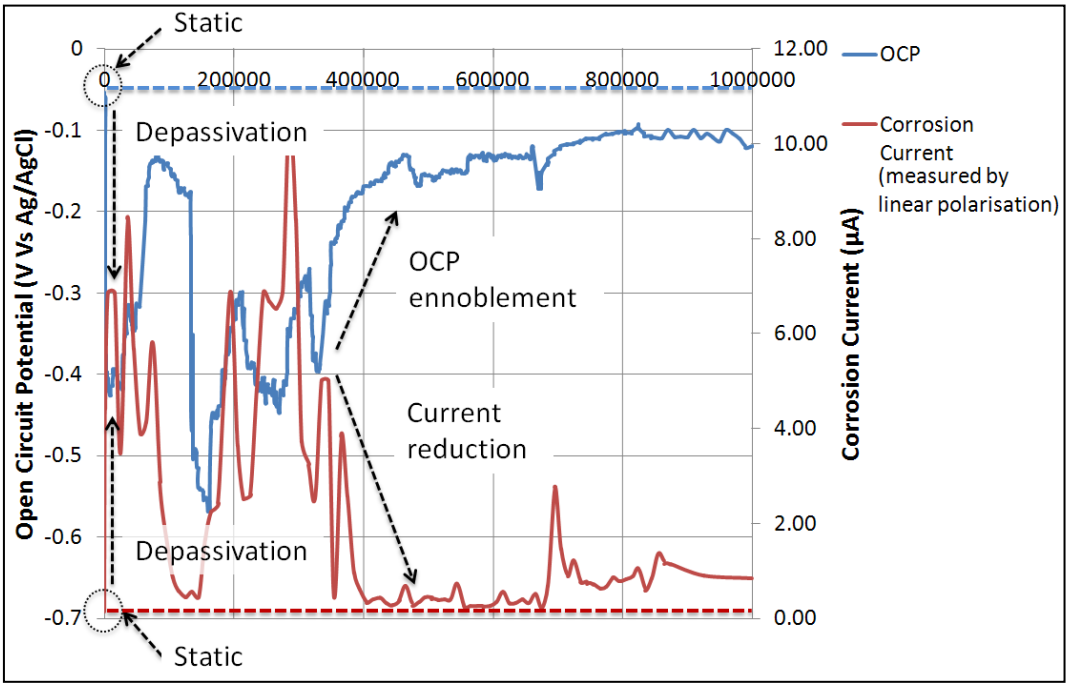

Figure 8.39: Variation of OCP and corrosion current over the duration of test 1, during normal simulated gait whilst lubricated with serum diluted with phosphate buffered saline.

Figure 8.39 shows a similar variation in corrosion current and open circuit potential as was observed in the previous long-term tests (Procedure 1). Initial depassivation occurred when the motion was initiated, shown by a negative shift in OCP and an increase in corrosion current. For the following 400,000 cycles (4d 15h 7m) there were large oscillations in both potential and current, although the values of each suggest that the bearing was in a state of depassivation. Following 400,000s (4d 15h 7m), partial repassivation appeared to have occurred, evident in the ennoblement in OCP and reduction in current. For the remainder of the test, the oscillation in OCP and corrosion current was diminished and the magnitudes of each suggest that the bearing remained in a state of partial repassivation. There was a

small temporary increase in current, which occurred at approximately 670,000 cycles (7d 18h 7m), corresponding to the second time the serum was changed.

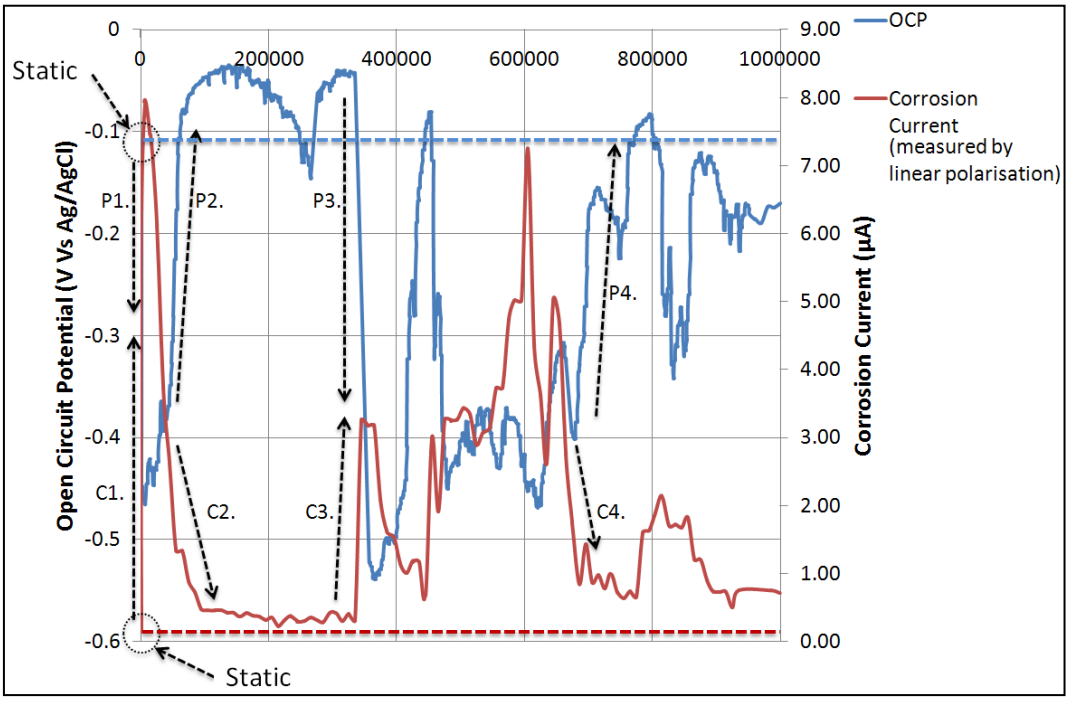

Figure 8.40: Variation of OCP and corrosion current over the duration of test 2, during normal simulated gait whilst lubricated with serum diluted with phosphate buffered saline.

Figure 8.40 shows that a more complex oscillation of current and OCP occurred for the second test than the first test. The same depassivation observations were made following the initial onset of the simulated gait cycle, shown by the arrows labelled P1 and C1. However, a large period of partial repassivation followed until approximately 330,000 cycles (3d 20h 30m), which corresponds to the first time the serum was changed. The current subsequently increased (arrow C3) and the OCP shifted in the negative direction (arrow P3). What followed were large fluctuations in current and potential, of similar magnitude to that of the first 400,000 cycles (4d 15h 7m) of Test 1 (Figure 8.39). Towards the final 300,000 cycles (3d 11h 20m), the general current trend appeared to have reduced somewhat (arrow C4), and the OCP shifted slightly in the noble direction, but neither appeared to have reached a steady state.

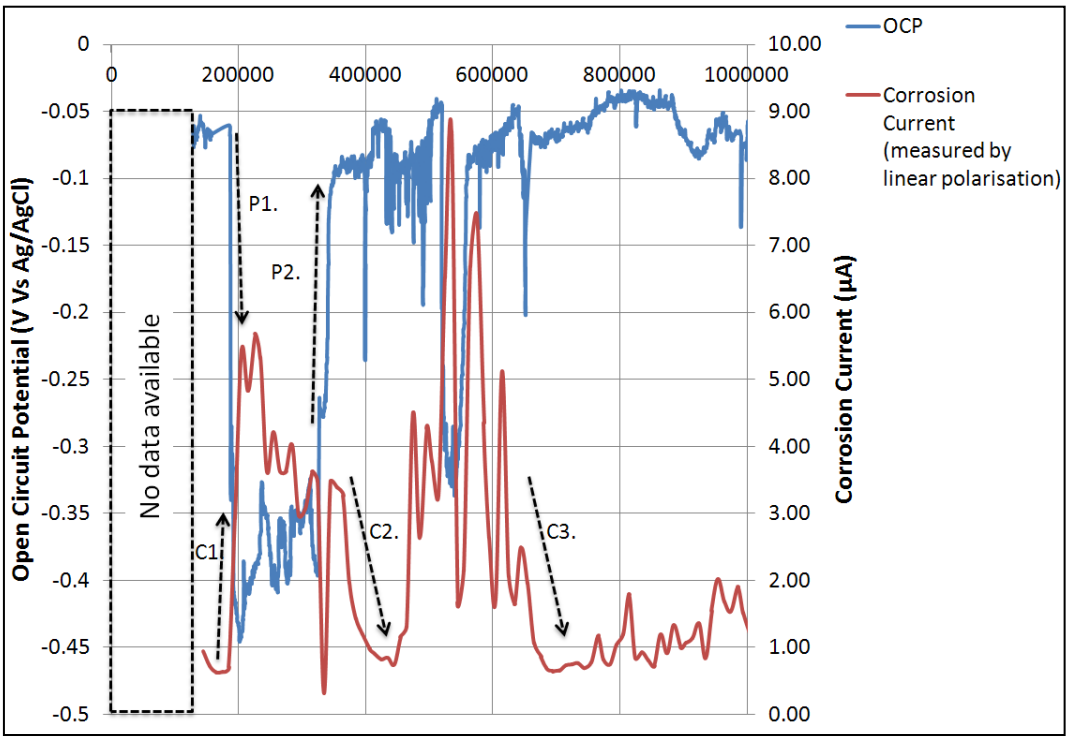

Figure 8.41: Variation of OCP and corrosion current over the duration of test 3, during normal simulated gait whilst lubricated with serum diluted with phosphate buffered saline.

Figure 8.41 shows the variation of current and OCP for the test. As mentioned previously, due to a disruption to measurement by the potentiostat there was no electrochemical data available for the period at the start of the test following the initial depassivation. In this period, however, the simulator was not stopped and the gait cycle continued; the only lapse was in the sampling of data. Following the recommencement of the signal, it can be seen that temporary ennoblement appeared to have occurred, as was seen in the previous test (Figure 8.40). This came to an abrupt end close to 200,000 cycles (2d 7h 33m). At this point there was a sharp negative shift in OCP (arrow P1) and a sharp increase in current (arrow C1). Repair of the passive film then appeared to occur between 350,000 (4d 1h 13m) and 400,000 cycles (4d 15h 7m). Arrow P2 shows ennoblement in OCP at this time, corresponding to the first time the serum was changed. This ennoblement lasted until around 500,000 cycles (5d 18h 53m). Depassivation then occurred again, resulting in corrosion currents approaching 9µA. This period of increased corrosion was short-lived, and the current returned to less than 2µA (arrow C3) where it remained for the

remainder of the test. This was mirrored in the behaviour of the OCP, which stayed at a noble potential for the final 300,000 cycles (3d 11h 20m).

8.3.3 Response of Potentiostatic Current over the duration of the tests

Figure 8.43 shows the average potentiostatic current over the duration of each of the three tests. Each data point represents the average current measured over a period of 100s at an applied potential of 100mV (Vs OCP). It can be seen that the shape of potentiostatic current over a single test resembled the general shape of the corrosion current for each of the tests shown in Figures 8.39-8.41. The magnitude of the current, however, was increased by the 100mV applied potential. The peak currents measured during potentiostatic polarisation were approximately double those measured under free corrosion conditions (corrosion current – I_{corr}). This effect is quantified by the Butler Volmer equation (Equation (10.2)) and is illustrated in Figure 8.42. Viewing the data in this way does little more than confirm the trends in corrosion current obtained through linear polarisation. In order to gain more information regarding the transient cyclic current, the data must be viewed over a smaller time scale.

$$I = I_{corr}\{exp - (\alpha nF\eta/RT) - exp((1-\alpha)nF\eta/RT)\} \quad (8.5)$$

I – External current density caused by applied overpotential

I_{corr} – Total corrosion current

α – Symmetry coefficient

F – Faraday constant

η – Dynamic viscosity

R – Ideal gas constant

T – Temperature

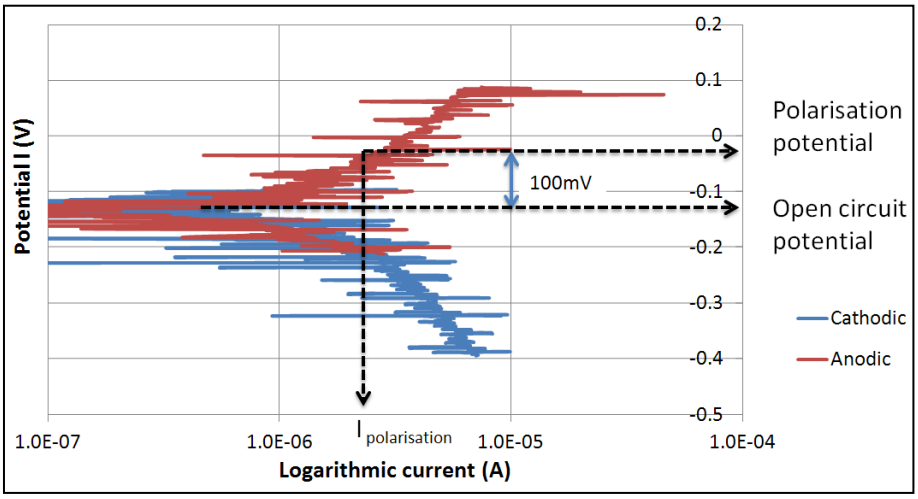

Figure 8.42: Tafel slope measured during normal simulated gait whilst lubricated with serum diluted with phosphate buffered saline following approximately 950,000s (10d 23h 53m). Indicating the polarisation potential of the potentiostatic measurements.

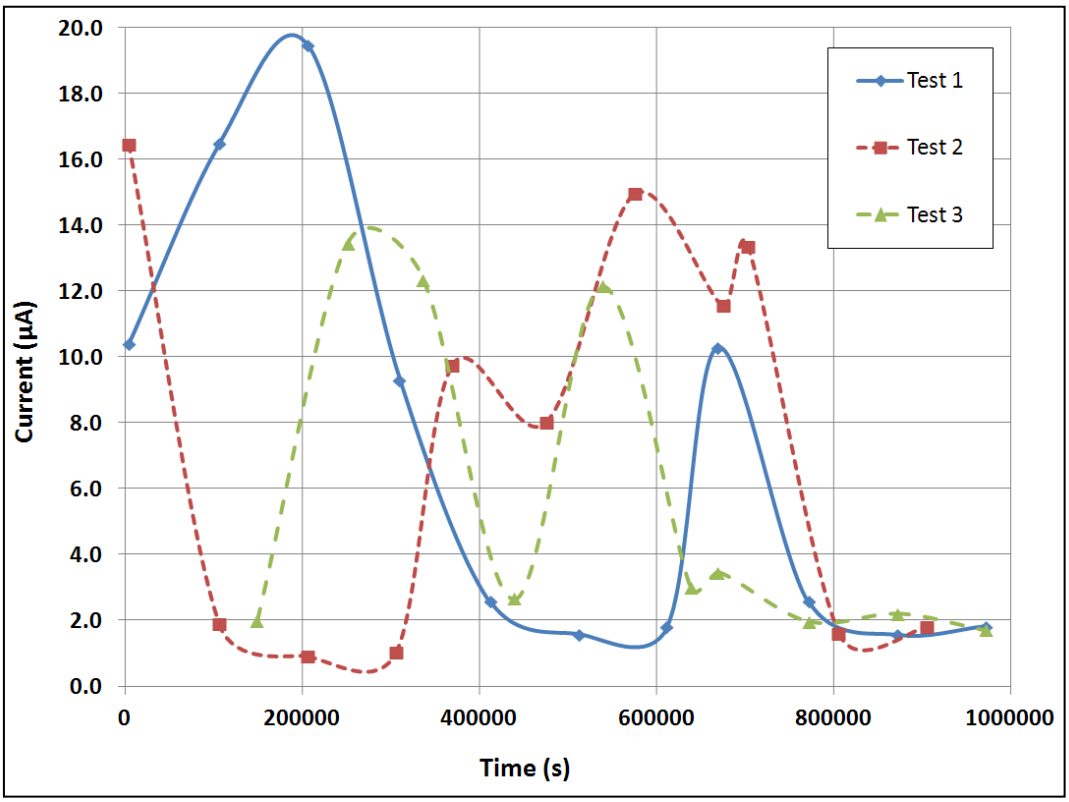

Figure 8.43: Variation of the potentiostatic current (averaged over each 100s measurements) over the three test durations.

When viewing the potentiostatic current over just a few seconds it can be seen that they took three forms. The first resembled the current trends observed from the previous short-term tests (Procedure 2). The current appeared to have cyclic periodicity equal to that of the gait frequency. The second was a current trace whose oscillations appeared to be noise, and showed no clear periodicity. The final was somewhere in between the previous two. Some periodicity could be identified, but no clear cyclic pattern was discerned. An example of each of the three trends is shown in Figure 8.44. Generally, a clear repetitive pattern was observed when the current was high. Little or no cyclic periodicity was usually associated with a low average current. The presence of periodicity for each of the potentiostatic current measurements is indicated in Figure 8.45.

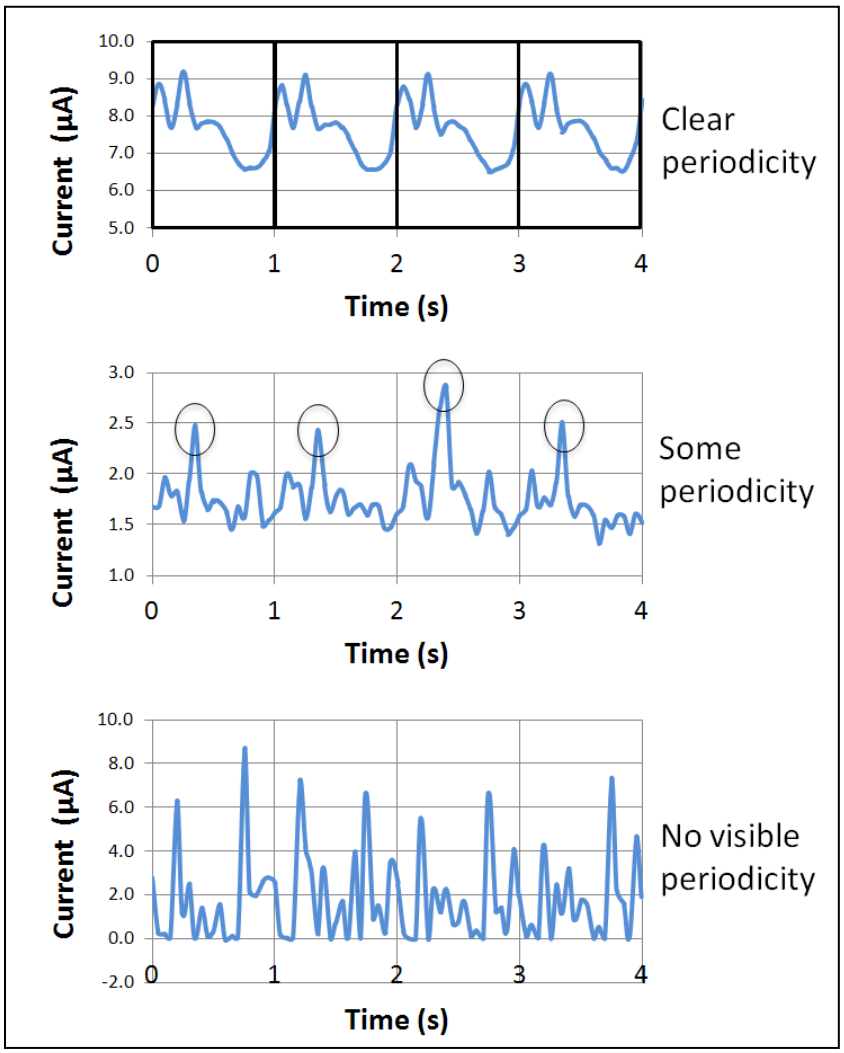

Figure 8.44 Potentiostatic current measurements showing varying levels of periodicity.

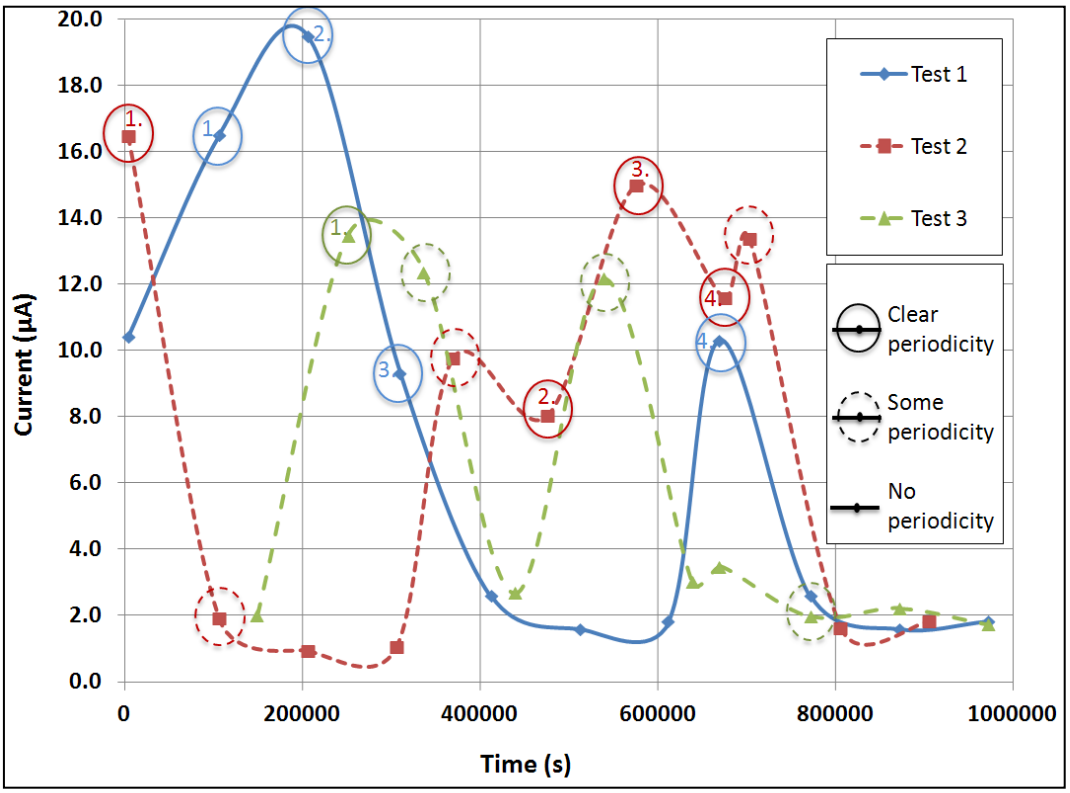

Figure 8.45: Variation of potentiostatic current with periodicity of signal indicated.

It can be seen that with the exception of two points, average potentiostatic current measurements below 4µA displayed no periodicity. Whilst all measurements above 4µA displayed at least some periodicity, and high average current measurements (above 14µA) all demonstrated clear periodicity. It should be noted that periodic trends were not all identical, although some similar features were identified. The location of minima and maxima during a cycle did not vary greatly from one measurement to the next, or indeed from one test to another. Figures 8.46-8.48 show 4s of data from potentiostatic measurements that displayed clear periodicity (as indicated in Figure 8.45)

Initially, plots were measured at a higher frequency of 40Hz, this was later reduced to 20Hz to make the current trend easier to observe without the need for plotting a moving average. Measurements taken during a single test have been plotted on the same figure. The Y-axis has been made arbitrary to facilitate comparison. The X-axis has been normalised to show the point at which current maxima and minima occur over a single gait cycle, that is to

say, the gait cycle has been synchronised with the electrochemical measurements.

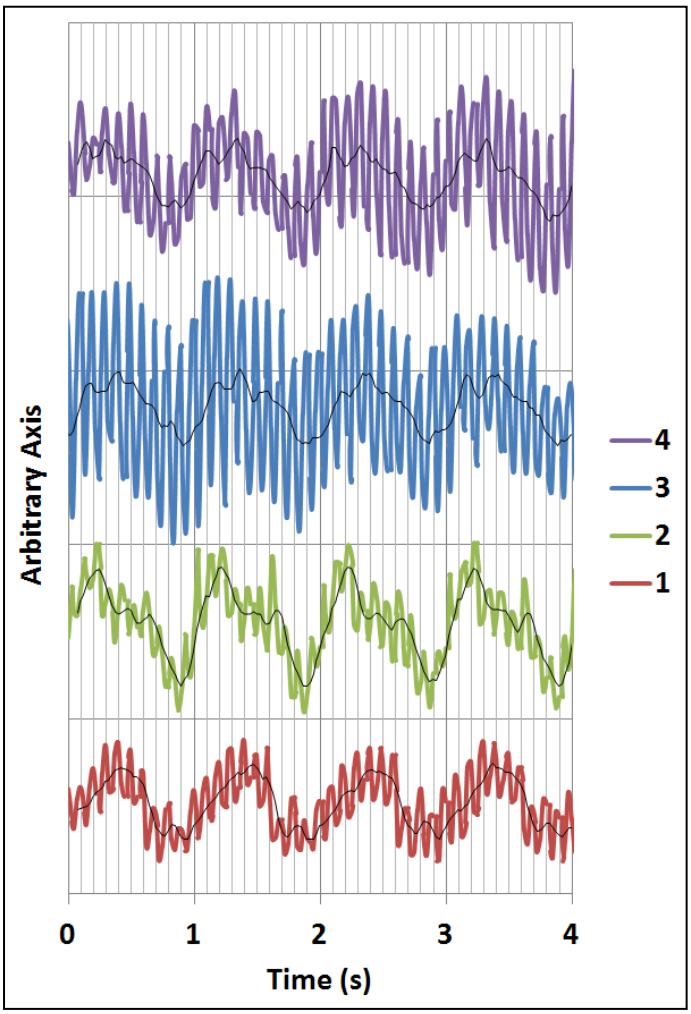

Figure 8.46: Periodic current measurements for Test 1, sampled at 40Hz and overlaid with a 4-point moving average. Numbers correspond to those labelled on Figure 8.45.

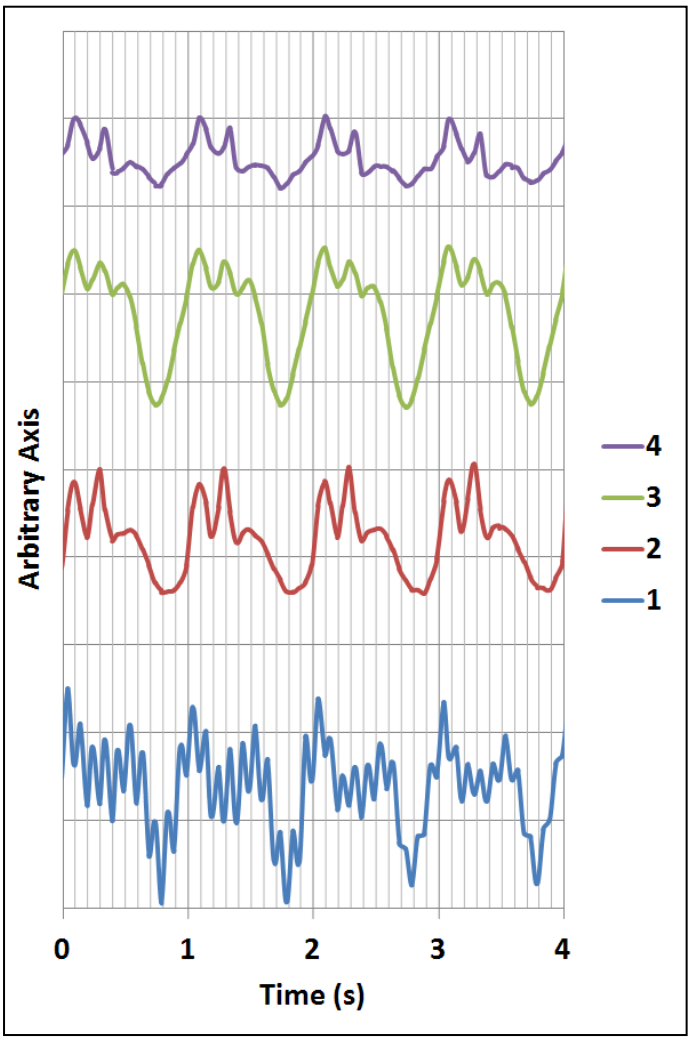

Figure 8.47: Periodic current measurements for Test 2 sampled at 20Hz. Numbers correspond to those labelled on Figure 8.45.

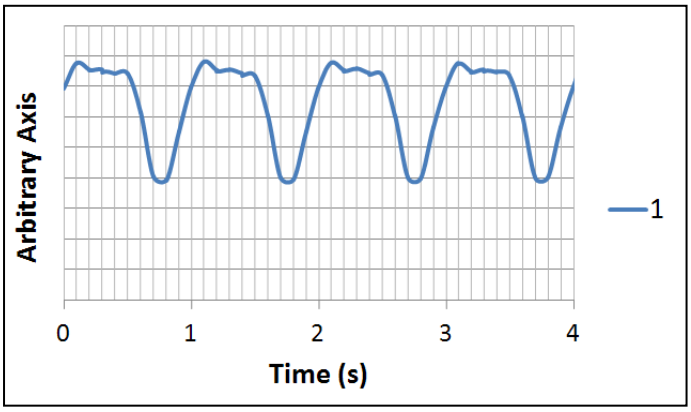

Figure 8.48: Periodic current measurement for test 3 sampled at 20Hz. Numbers correspond to those labelled on Figure 8.46.

It can be seen from Figures 8.46-8.48 that the current trend experiences a minima between 0.75s and 0.9s into the cycle. In addition the maxima often appears as two or perhaps three peaks, with the first occurring between 0.1s and 0.2s and the others following just after the midpoint of the cycle. The measurement shown in Figure 8.48 appears to contain a single broad maxima, however, upon close inspection three shallow peaks can be perceived within it. Differences in the signal can arise when comparing the data sampled at 40Hz to that sampled at 20Hz. Although a 4-point average serves to elucidate the general trend of the data it does not give a direct comparison of it.

It is interesting to see that during a single 1 million-cycle test, there are periods when the current is strongly influenced by the gait cycle and there are periods when it appears to be independent. Furthermore, when a strong dependence is observed, the current tends to be much greater than when no dependence is observed. It was found that when mechanically induced depassivation occurred, the corrosion current was also increased. Hence it may be inferred, that the periodic current signal is caused by periodic changes in the intensity of depassivation over a single gait cycle. Both load and velocity vary as a function of time in the latter case. Their interaction affects a number of different parameters that can influence depassivation kinetics such as: EHL film thickness, Hertzian contact area, actual contact area and contact pressure. In addition, the relative influence of these parameters would be expected to vary throughout the tests. This is caused by wear of the bearing surfaces. Wear causes changes to both the surface texture and the geometrical form of the bearing, and causes the production of debris at the interface. These changes influence both the contact mechanics and the lubrication regime, hence it is no surprise that the exact current signal changes from one measurement to the next. It is also of interest to seek an explanation for reductions in current. The association between low average current and the lack of periodicity within the current measurement suggest that some form of interruption to the mechanical depassivation cycle may have taken place. This could, for example, occur if the separation of the surfaces was enhanced by the interposition of a lubricating tribofilm, or an increase in the lubricant film thickness.

8.4 Degradation and material loss from Procedure 3 (long-term tests performed in bovine serum diluted with phosphate buffered saline).

8.4.1 Mass Loss

To assess the level of damage to the material surfaces, the head and cup from Tests 1 and 2 were weighed and the surface roughness was measured. This was not done for Test 3 as it was used for surface analysis as discussed later. In all 3 tests the metal ion concentrations were measured at 1/3, 2/3 and 1 million cycles. Mass loss and profilometry measurements were performed following rinsing in distilled water, then repeated following a more thorough cleaning with 5% nitric acid. Cleaning in acid was necessary to remove the tribofilm from the surface, which developed during the test. The presence and composition of the tribofilm is discussed in detail in Chapter 9. Figure 8.49 shows the mass loss over the duration of Test 1 and Test 2, following both rinsing and thorough cleaning.

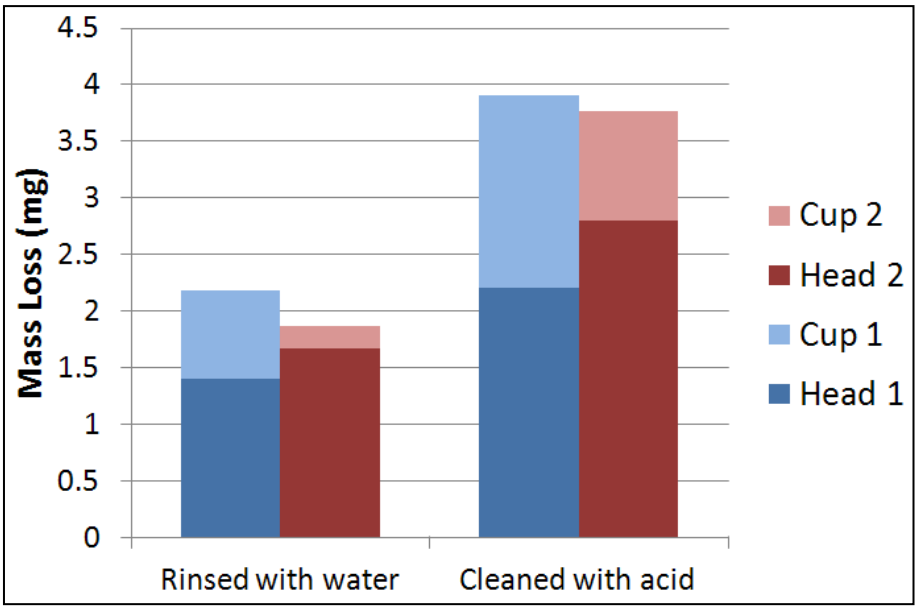

Figure 8.49: Total mass loss from Test 1 and Test 2.

It can be seen from Figure 8.49 that for both tests the head sustained a greater material loss than the cup. During motion, the load is applied vertically through the taper of femoral head, which differs from the loading experienced *in vivo*. This results in a contact point on the top pole of the femoral head regardless of the angle of flexion or extension. This causes it to be in a state of nearly constant depassivation. Whilst on the cup the contact point moves, consequently at a fixed location a depassivation/repassivation shifting equilibrium is established. Therefore, the degradation mechanism governing material loss is slightly different on the femoral head and the acetabular cup.

Figure 8.49 clearly demonstrates that the mass of the tribofilm is not trivial. By thoroughly cleaning the surfaces with a dilute nitric acid solution, approximately 1.5mg of additional material was removed. This was evident to the naked eye as the removal of a cloudy non-reflective layer from the whole surface, as well as dense black smears from around the wear scar. The total material losses of 3.9mg and 3.8mg in tests 1 and 2 give volumetric material losses of 0.47mm^3 and 0.45mm^3 respectively. These values are within the range of data analysed by Dowson (74).

8.4.2 Surface Roughness

Figure 8.50 gives the surface roughness values at the start of each test, then following rinsing and following thorough cleaning. Roughness was measured from three Talysurf line profiles taken from each head and cup.

The pre-test average surface roughnesses were between 4-7nm for all the surfaces measured. This is typical of current MoM bearing surfaces. Cups were slightly smoother than heads, but the difference was marginal. Following testing, the adherence of a substantial tribofilm increased the roughness of all the surfaces. It should be considered that although the profilometer imparts a low (10mN) load, its small (2μm radius) tip produces a large pressure, which may scratch the tribofilm during measurement (although this was not evident that this had occurred). This increase was markedly greater for the bearing used in Test 2. Following the removal of the

tribofilm, by cleaning with acid, the measured surface roughnesses were reduced. There was, however, an overall gain in the roughness of all the surfaces. Other studies have shown that following hip simulator testing, the surface roughness generally may decrease (26, 92) or increase (20, 26, 92). Most of the surfaces remained fairly smooth with R_a <15nm. The surface of cup 2, however, was an exception to this. Its roughness (R_a) increasing to 30nm.

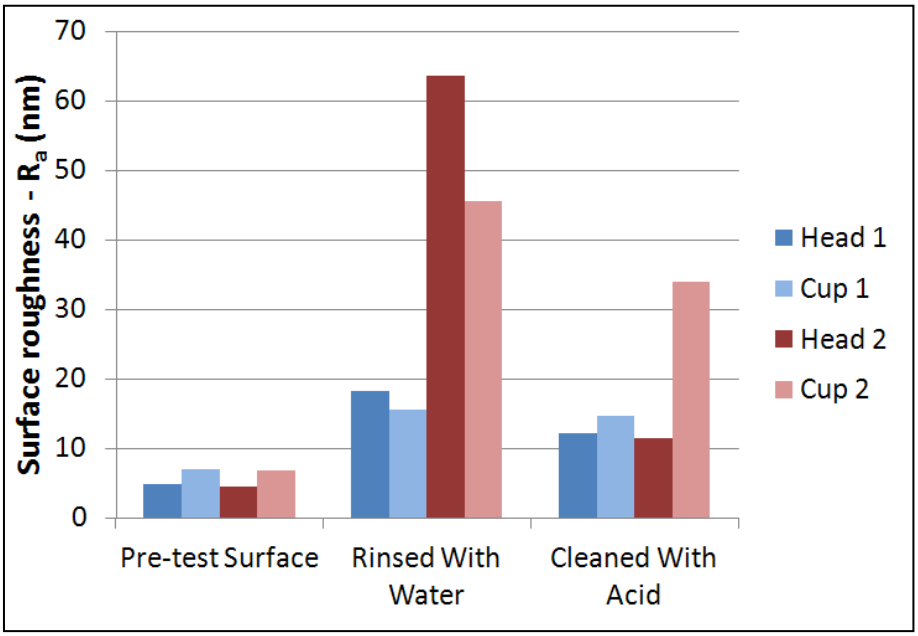

Figure 8.50: Surface roughness measured before testing and following it.

8.4.3 Bearing Clearance

The sphericity of the bearing surfaces were obtained from the profilometry traces. By subtracting the radii of the head from that of its corresponding cup the clearance of the assembly was obtained. Following testing, material loss caused local changes in the radii in the vicinity of the wear scars of both cups and heads. This was also measured, giving the effective clearance within the wear scar following testing. The measurements of clearance prior to testing, and from the wear scar following both rinsing and thorough cleaning are shown in Figure 8.51.

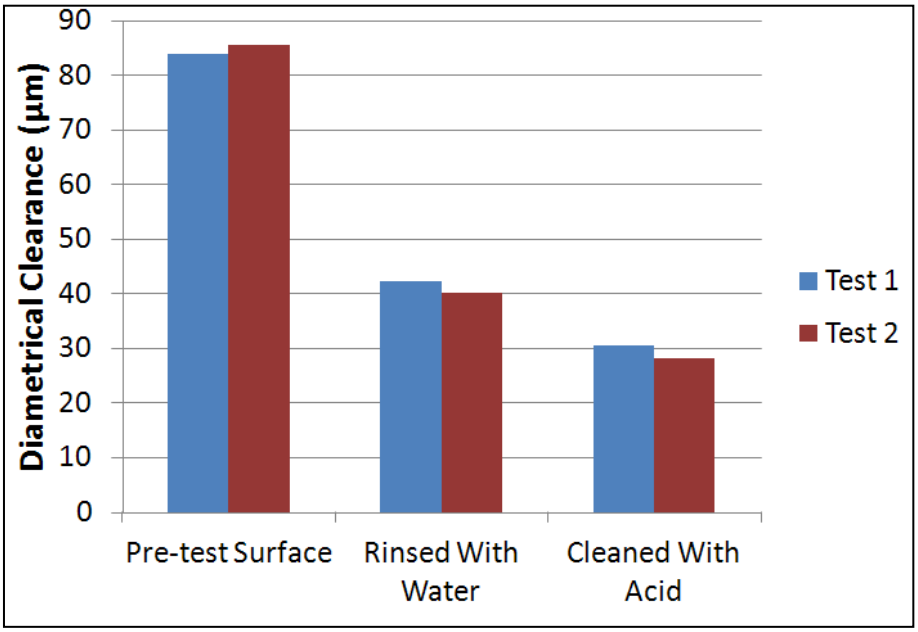

Figure 8.51: Diametrical clearance prior to, and following testing.

Following testing the diametrical clearance between the surfaces was found to have reduced. This is caused by an increase in radius on the head and a decrease in radius on the cup. Figure 8.51 shows that the clearance was lower when the tribofilm was present compared to when it was removed with dilute acid. Figure 8.53 and Figure 8.52 illustrate how these conformal changes to the bearing surface occur. According to EHL theory, an increase in the conformity between surfaces produces an increase in the lubricating film thickness. This is discussed in more detail in section 8.5.

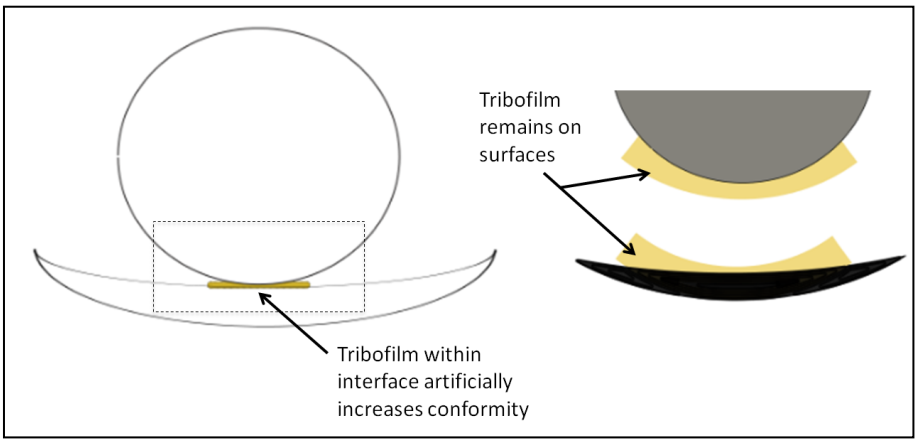

Figure 8.52: Tribofilm remains on surface following their separation.

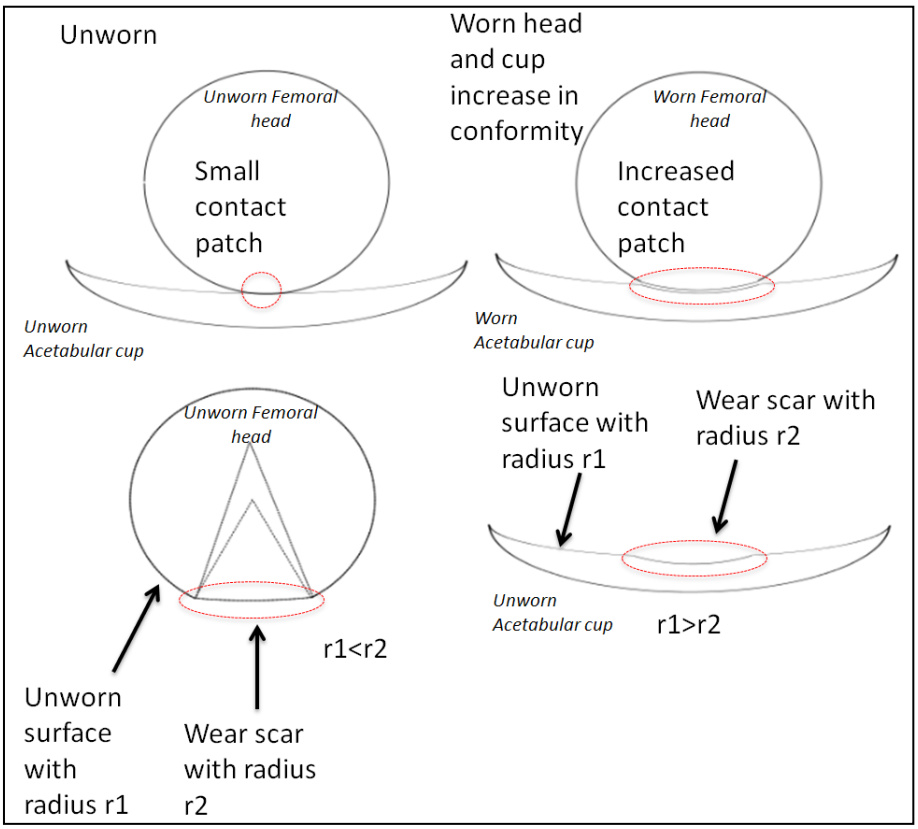

Figure 8.53: Conformal changes within the bearing following material loss and removal of the tribofilm.

8.4.4 Metal Ion Release

Figure 8.54 shows the different concentrations of metallic ions measured in each test solution by ICP-MS. In each case the major species present were cobalt, followed by chromium and finally molybdenum.

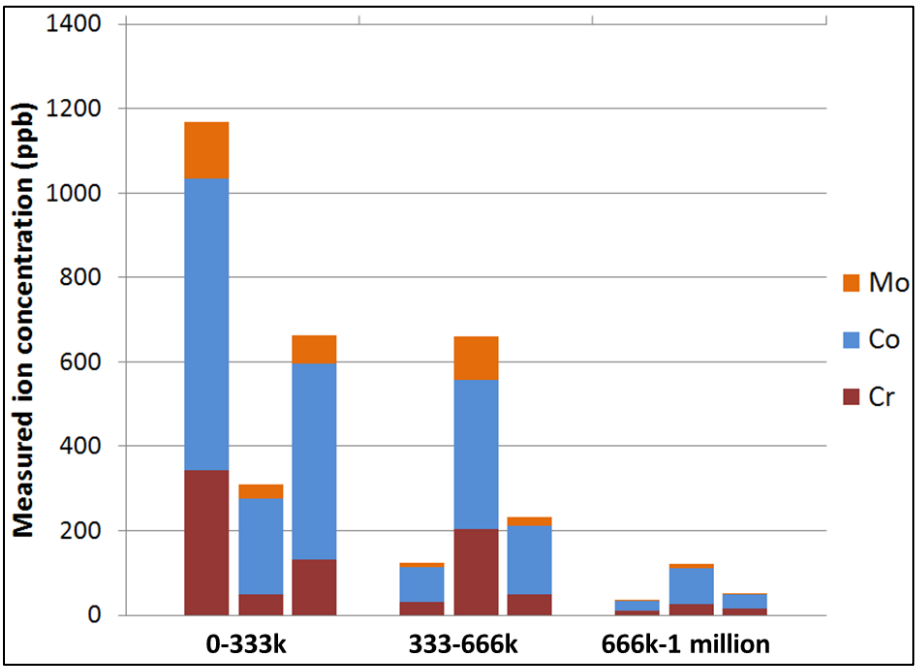

Figure 8.54: Metal ion concentrations measured from the bulk solution at 333k, 666k and 1 million cycles for each of the 3 tests.

The percentages of each element are shown in Figure 8.55 and can be compared with their abundance within the base alloy. The relative percentages of cobalt, chromium and molybdenum found in the alloy are as follows: 60.7%-69%, 26%-31.1% and 5%-7.2% respectively.

It follows that the measured concentrations of cobalt and chromium ions were equal or less than their stoichiometric proportions within the alloy. Molybdenum, was measured in slightly greater proportions in the ions. This could indicate one of three things.

- Molybdenum was preferentially removed from the alloy,
- Cobalt/chromium ions were removed from the sample,
- There was a source of ions present in the solution prior to testing.

ICP-MS measurements of the PBS solution prior to testing gave metal ion concentrations of 3.36, 0.12, and 1.57ppb for Cr, Co and Mo respectively. These low levels could provide some distortion or the results, but are not

great enough to increase the perceived concentration of Mo ions from below 7.2% to above 10%. It is known that proteins present in bovine serum will react with metal ions (41, 182). In the ICP-MS sample preparation the proteins are extracted from the solution. This results in extraction of any bound metal ions.

From Figure 8.54, it follows that there was a general trend of decreasing metal ion release as the tests progressed. This supported the electrochemical observations, which demonstrated that there was a decrease in corrosion current as the test progressed, and an ennoblement in OCP.

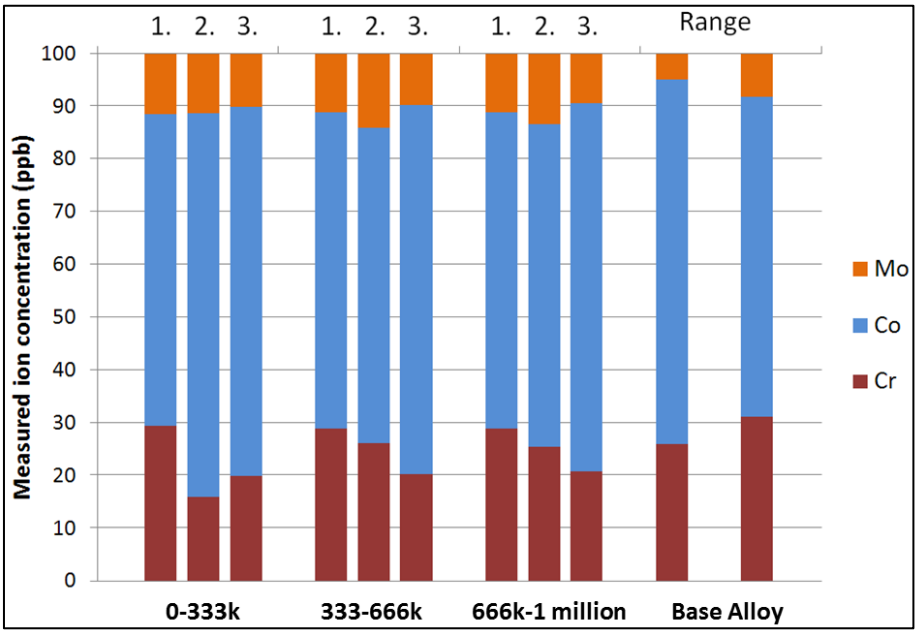

Figure 8.55: Ion percentages measured from the bulk solution at 333k, 666k and 1 million cycles for each of the 3 tests.

The measurements of corrosion current throughout the test were converted into a rate of mass loss using Faradays equation, (Equation (5.1)). This was then be compared to the progressive increase in the mass of metallic ions in the solution measured by ICP-MS. ICP-MS can be used to calculate the total mass of ions arising from both dissolution of the alloy surface and dissolution of particulate debris. Whereas the mass loss calculated from the corrosion current is only a measure of the dissolution of the bearing surfaces. The formation of ions from surface dissolution is calculated from the corrosion current. This is illustrated in Figure 8.56.

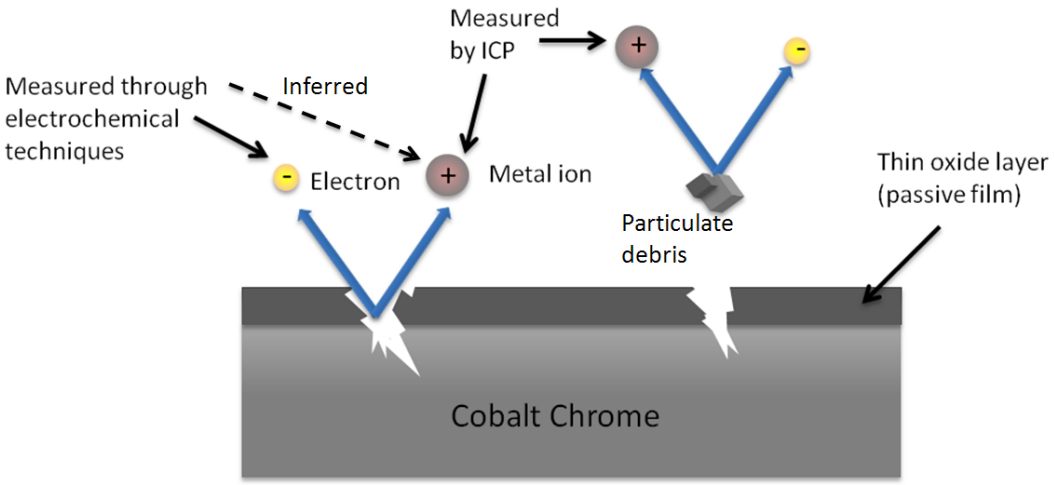

Figure 8.56: Sources of metal ions and techniques to measure them.

The progressive accumulation of ionic mass in the serum solution for each test is shown above the progressive release of ionic mass due to the corrosion current in Figure 8.57. As 'Test 3' contains an incomplete data set (as previously explained) the data was linearly interpolated between t=1200s (20m) and t=135,000s (1d 13h 30m). It is fully acknowledged that this may give rise to inaccuracies and has been considered in the analysis of the results.

As expected, Figure 8.57 demonstrates that the total mass of Co, Cr and Mo ions in the solution was markedly greater than the total release of ions from the bearing surface. The additional ions measured in the solution can be attributed to the dissolution of surface debris particulates. An interesting point to consider is the similarity in the trend of cumulative mass loss from corrosion and cumulative metal ion loss (particularly for Test 1 and Test 2. It is not as clear for Test 3, which may be ascribed to the missing corrosion data). This suggests that ions are liberated by particle dissolution within a short time frame, relative to the length of the test. If particle dissolution was a slow progress there would be a lag in the trend between the two graphs shown in Figure 8.57. The percentage contributions of particle dissolution and surface dissolution to total solution ion concentration are shown in Figure 8.58.

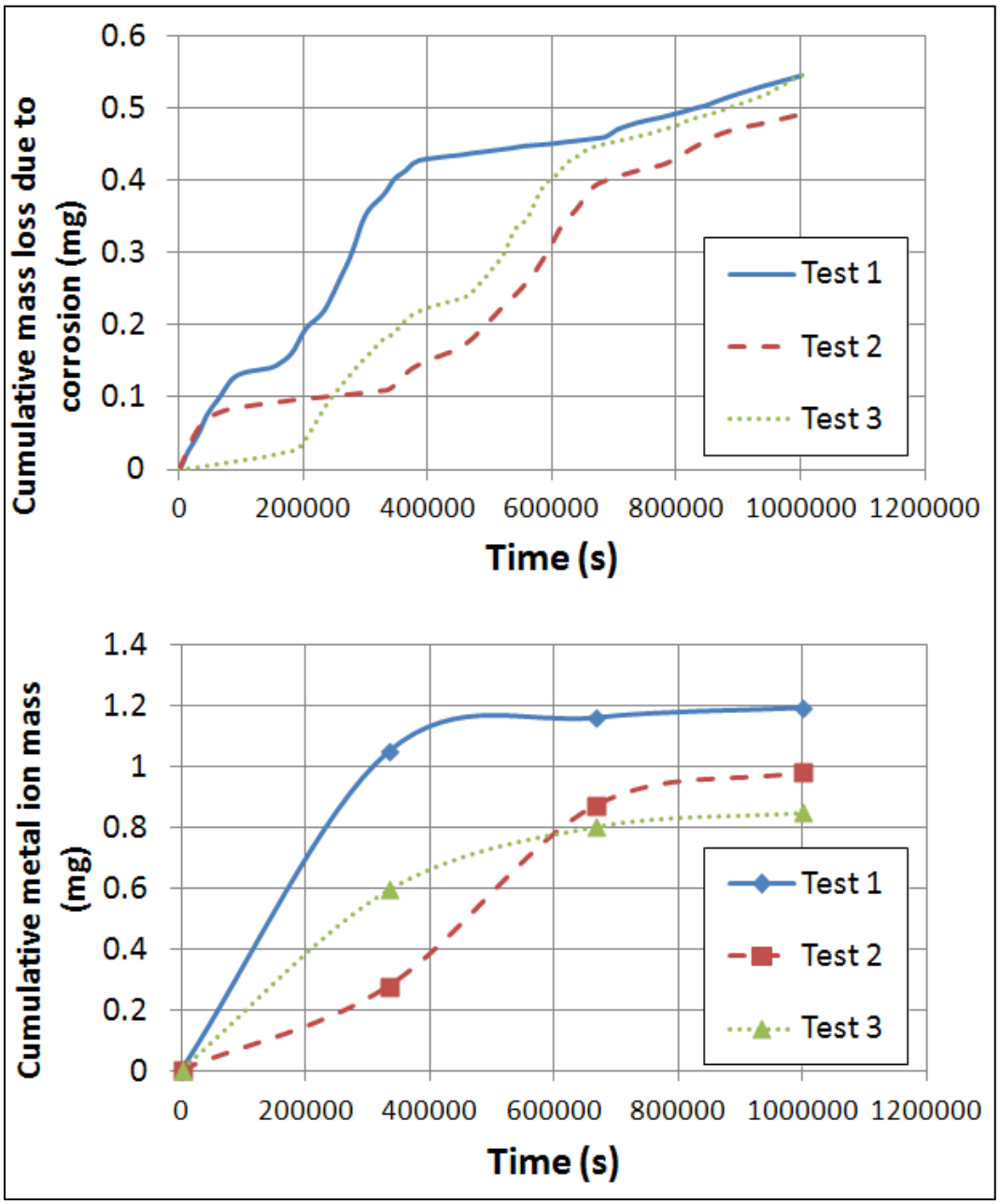

Figure 8.57: Cumulative mass loss due to corrosion (measured by LPR) (top) and ionic mass accumulation in solution (bottom) throughout the test duration (measured by ICP-MS).

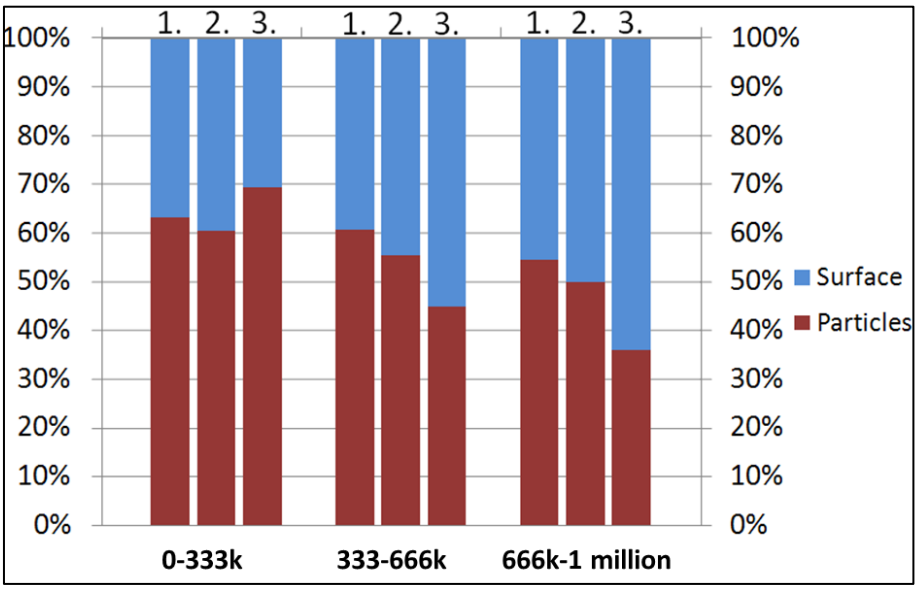

Figure 8.58: Percentage composition of particle and surface dissolution to total solution ion concentration for tests 1 2 and 3 at 333,000s (3d 20h 30m), 666,000s (7d 17h) and 1 million seconds of testing (11d 13h 19m).

For each of the three tests, the percentage of ions attributable to particle dissolution declined over the course of time. This may reflect a change in the mechanisms governing particle generation. It is possible that there was a progressive reduction in either the quantity or the average size of particles produced. Since the serum was changed every 1/3 of a million cycles, only surface changes could affect the degradation mechanism. These could either be geometrical changes such as reduced conformity or increased roughness, or they could be attributable to the development of a tribochemical layer.

By the end of the test it was apparent that metal ions were liberated in almost equal abundance, from both the surface and the debris. This is a noteworthy finding, and may be significant for the reduction of metal ion release from future metallic bearing designs.

In addition, it was possible to determine the individual contributions of pure corrosion (C), tribologically enhanced corrosion (C_W), and the sum of pure wear and corrosion enhanced wear ($W+W_C$), as shown in Equation (2.11) and Equation (2.12). Since the bearing surface used in 'Test 3' was reserved for XPS analysis, this procedure was only followed for Test 1 and Test 2. The results of which are shown in Figure 8.59.

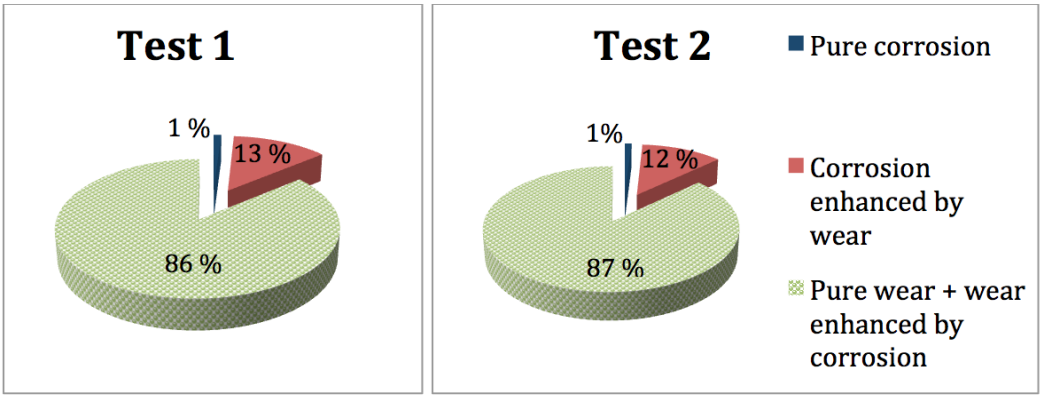

Figure 8.59: Contribution of corrosion towards total material loss for Test 1 and Test 2.

Pure corrosion was calculated by extrapolating the corrosion rate in static conditions, measured at the start of the test, over the test duration. Corrosion enhanced by wear was taken as the corrosion rate measured over the test duration minus the calculated pure corrosion. These measures of corrosion were converted into mass loss, as previously described, and subtracted from the total measured mass loss. This gave the combined contribution of pure wear and wear enhanced by corrosion. These two terms could not then be further separated without performing additional tests in the complete absence of corrosion.

In both tests pure corrosion accounted for approximately 1% of the total material loss. This is perhaps larger than expected, given that CoCr is considered a passive alloy. However, it should be considered that measurements of the passive current may contain a large amount of error due to the difficulty in accurately measuring such low values of current. Wear enhanced corrosion accounted for between 12-13% of the total mass loss over the test duration. This was greater than the fraction measured by Sun in a pin-on-disc tribometer. During 3-body abrasion of CoCr in serum, Sun (166) measured it as between 1.5-2.8% depending on the lubricant used.

8.5 Elastohydrodynamic film modeling

I would like to thank Dr Qingen Meng for running the simulations to determine the EHL film thickness discussed in this subsection.

The elastohydrodynamic film profile was computed using the velocity and loading cycle given in Chapter 6 with the omission of axial displacement. Results were produced for bearings with diametrical clearances of 85μm, and 58.5μm. The larger clearance reflects that of the bearing prior to wear, whilst the reduced clearance reflects that following conformal changes caused by wear. Figure 8.60 and 8.61 show the variation in minimum EHL thickness and corresponding lambda ratio (calculated from Equation (10.2)) over four cycles. The surface roughness used to calculate Lambda ratio from the computed minimum film thickness was based on that measured prior to and following testing, as shown in Figure 8.50. The surface roughness following testing was taken as the roughness, measured after cleaning with acid, since this represented the roughness of the actual metal surface and not the adhered tribofilm.

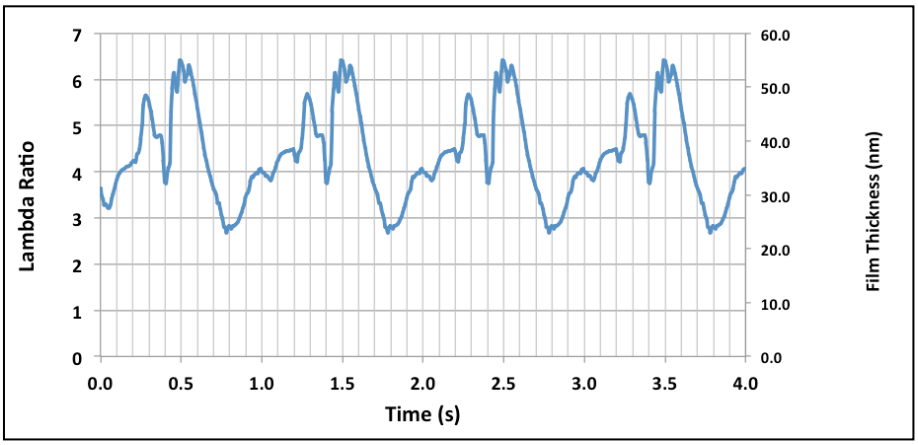

Figure 8.60: Cyclic variation of initial film thickness and lambda ratio.

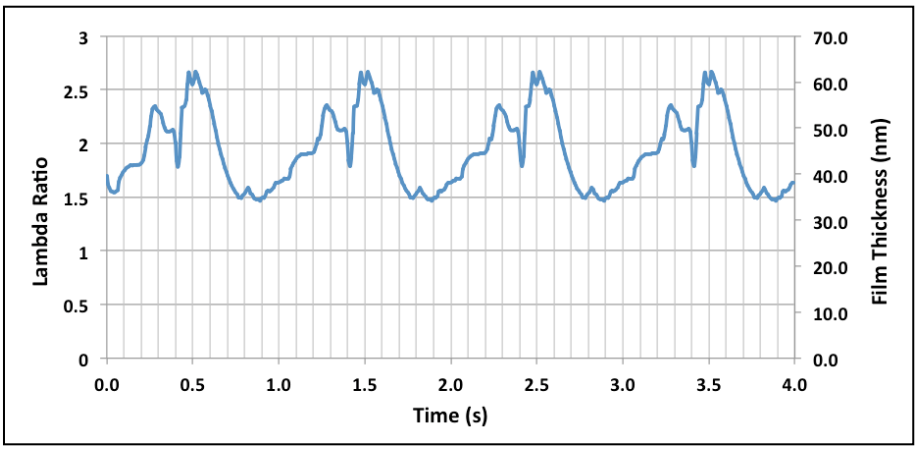

Figure 8.61: Film thickness and lambda ratio based on clearance and surface roughness after testing.

It can be seen from Figure 8.61-8.62 that the change in clearance did not alter the shape of the transient minimum EHL film thickness. It did, however, increase the overall thickness of the predicted film by approximately 10nm. There was an overall decrease in predicted lambda ratio when comparing the worn surface to the unworn surface, despite the increase in film thickness. This can be attributed to the increase in surface roughness measured at the end of the test (Figure 8.50), which was great enough to offset the increase in film thickness. From these results it can be inferred that the reduction in both depassivation and particle dissolution, towards the end of the tests, were not caused by increased separation of the surfaces by the EHL film. It appears that the tribofilm present on the surface may have acted as a lubricant, by separating the opposing surfaces and disrupting the interaction between the metal surfaces and hence the depassivation/repassivation cycle. Figures 8.60 and 8.61 only show the variation of minimum film thickness. A more complete understanding of the efficacy of the lubrication taking place can be obtained from the complete film contour at a given time.

The film thickness contour plots for the 85μm clearance bearing are given in Figure 8.62-8.65. Each plot shows the film thickness below 50nm across its polar axes, at 0.0625s increments.

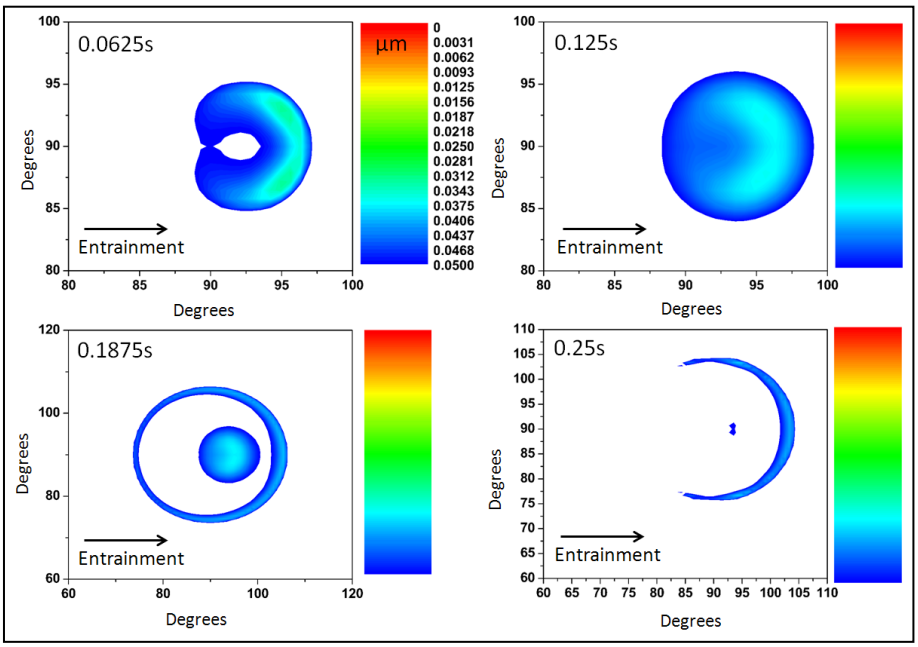

Figure 8.62: EHL film thickness contour plots between 0-0.25s (clearance 85µm).

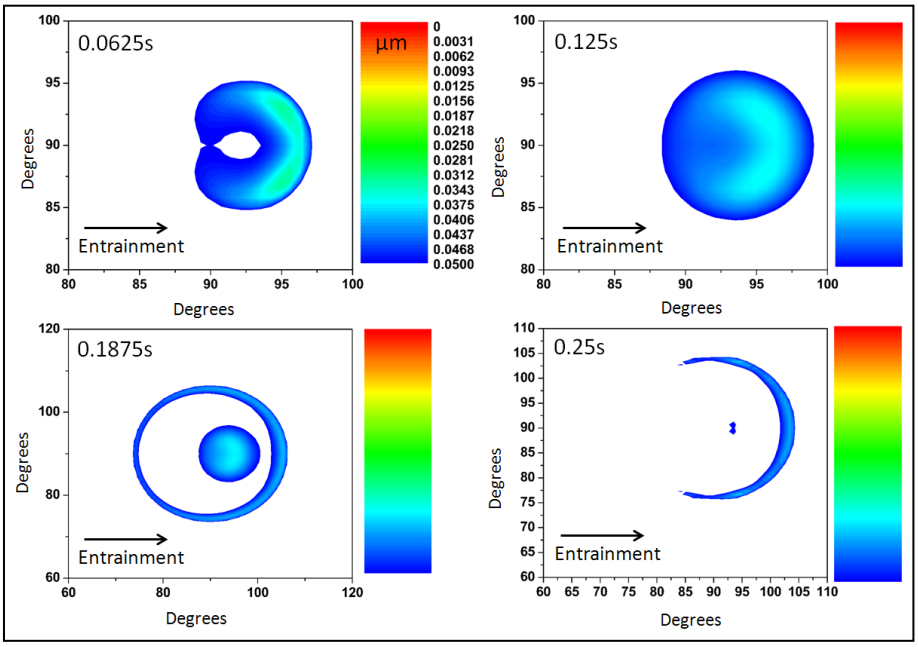

Figure 8.63: EHL film thickness contour plots between 0.25-0.5s (clearance 85µm).

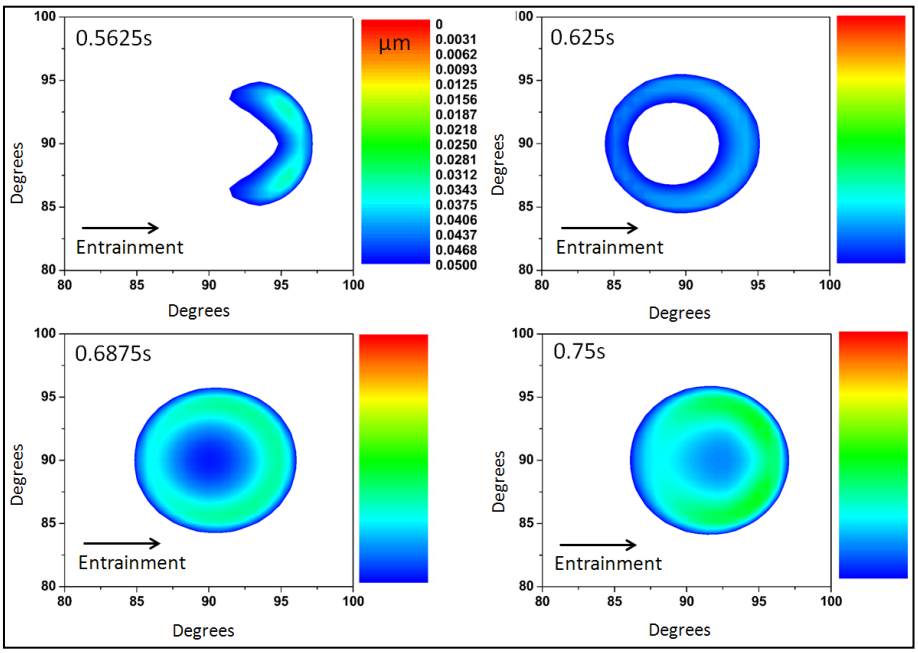

Figure 8.64: EHL film thickness contour plots between 0.5-0.75s (clearance 85µm).

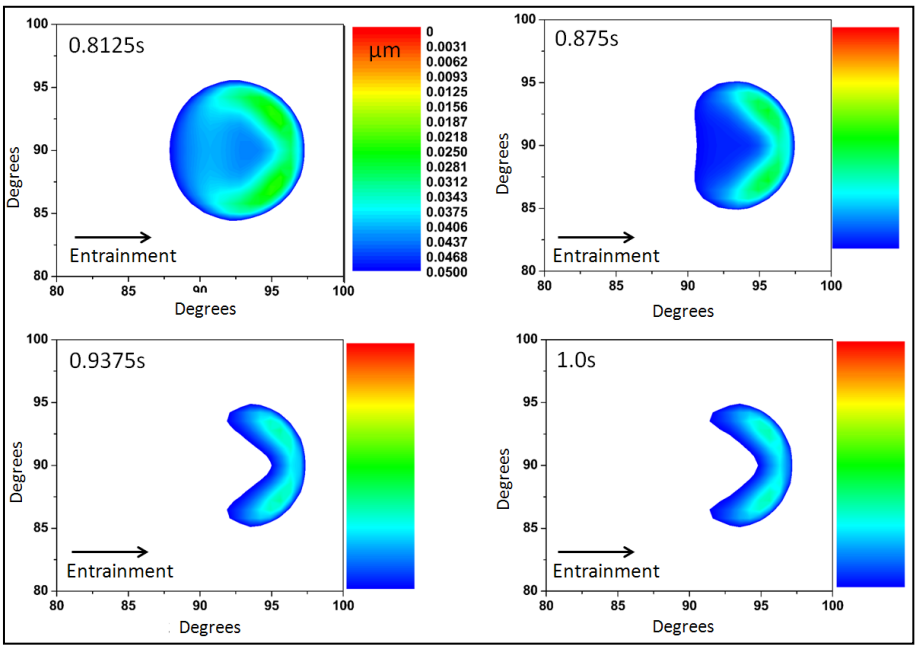

Figure 8.65: EHL film thickness contour plots between 0.75-1.0s (clearance 85µm).

The figures above illustrate the complexity with which the film profile evolves over a single cycle. Not only is there a variation in both central and minimum film thickness, but there is also a variation in the shape and area of the displayed film profile itself. Figure 8.64 shows that the thinnest film occurs at approximately 0.75s, and also spans the greatest area. Disregarding sliding velocity, it could be assumed that at this point in the cycle the most severe depassivation would take place. Conversely, at approximately 0.5s there appears to be the most superior lubricating film. The film thickness at this point is consistently thicker than 50nm. Hence, disregarding sliding velocity, it would be expected that the least severe depassivation would take place at this point.

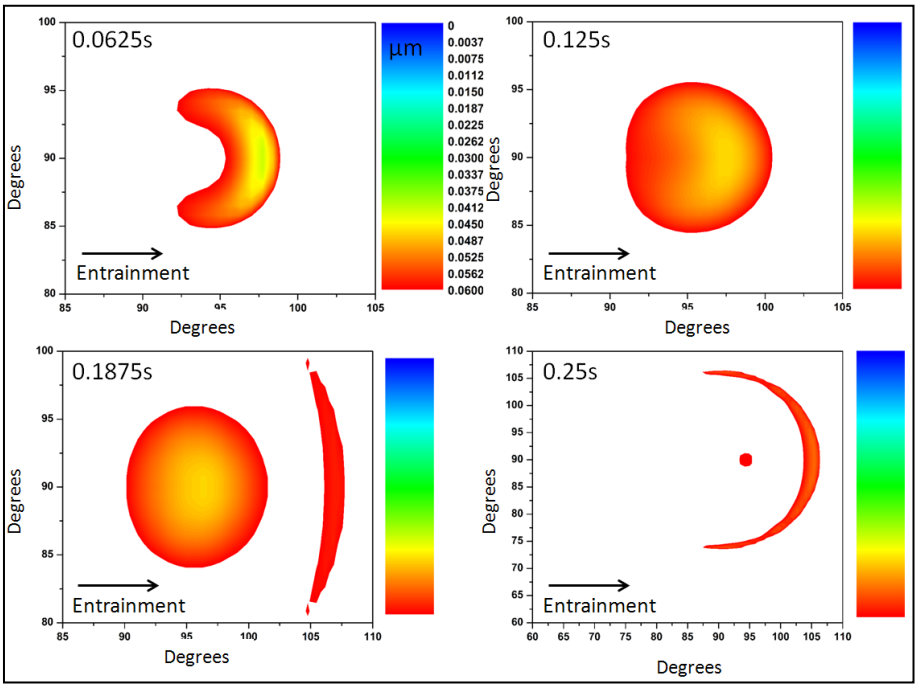

Figure 8.66: EHL film thickness contour plots between 0-0.25s (clearance 58.5µm).

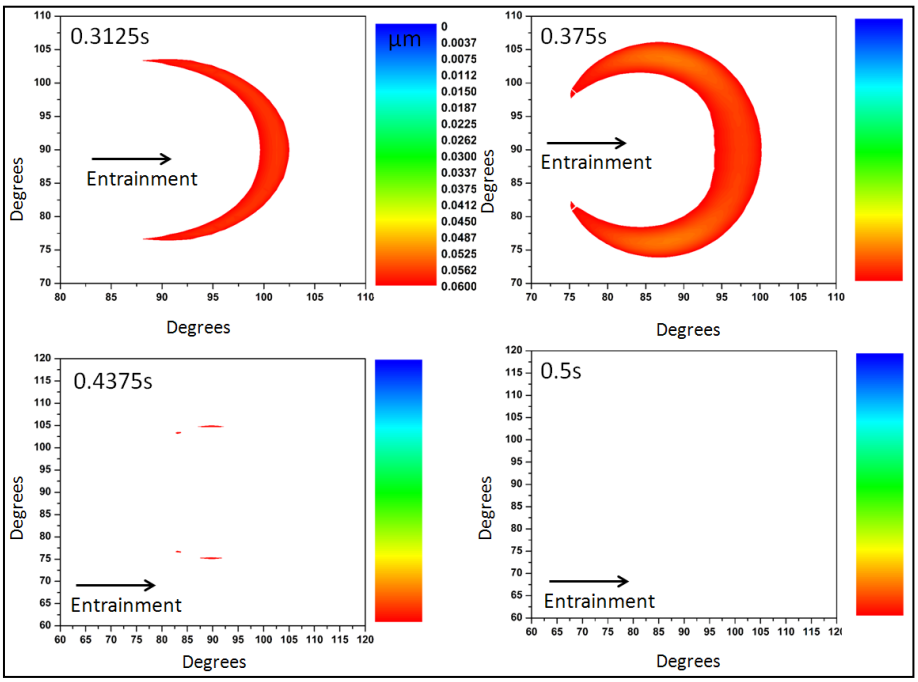

Figure 8.67: EHL film thickness contour plots between 0.25-0.5s (clearance 58.5µm).

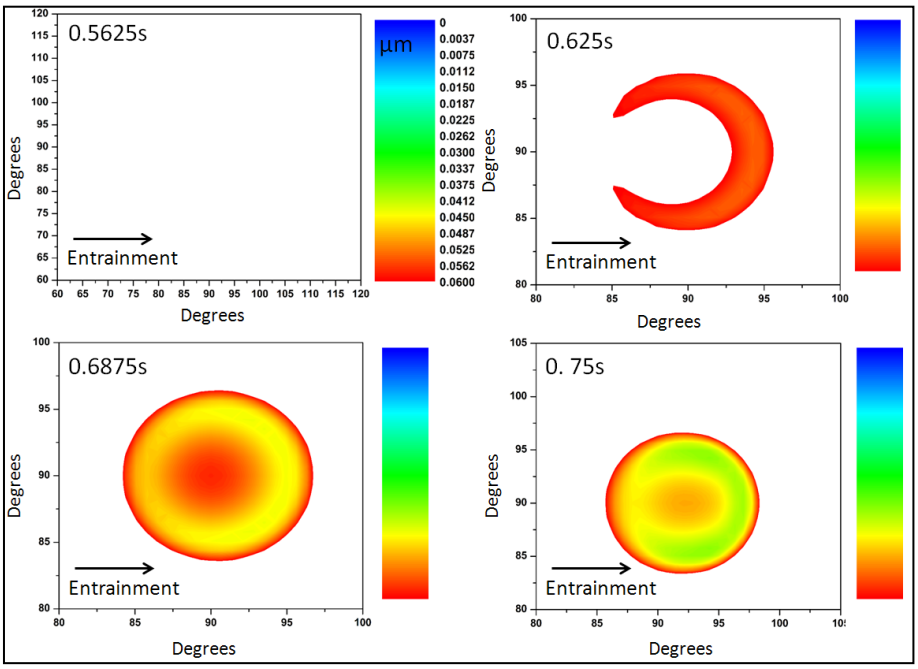

Figure 8.68: EHL film thickness contour plots between 0.5-0.75 (clearance 58.5µm).

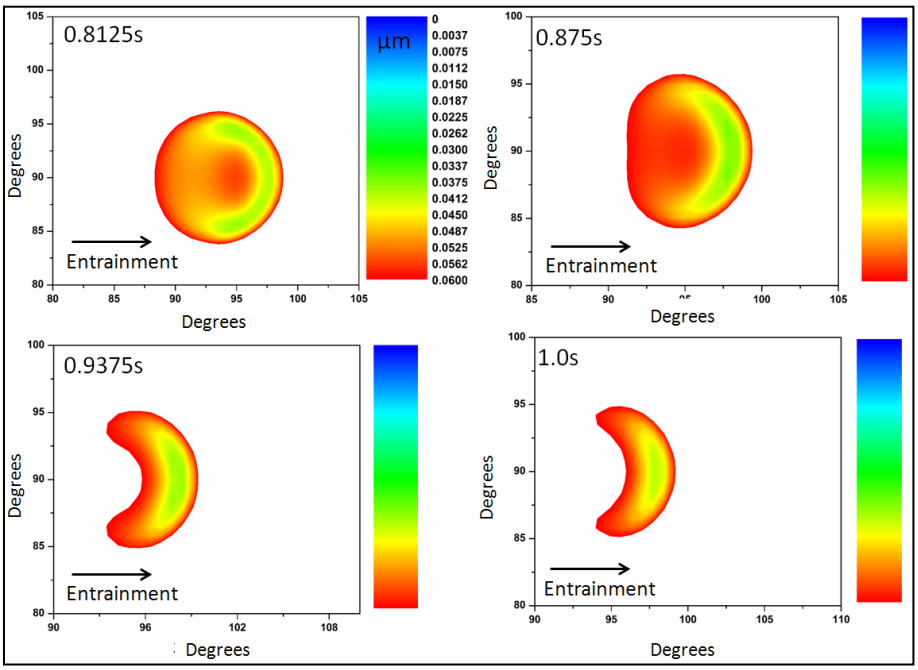

Figure 8.69: EHL film thickness contour plots between 0.75-1.0s (clearance 58.5µm)

Upon reducing the clearance changes to the shape of the film profile were not substantial. However, there was an overall increase in film thickness. Again, the regions of smallest film thickness and hence the most severe contact appeared to take place around 0.75s. The most substantial theoretical film thickness again appear to occur around 0.5s – 0.5625s. These points correspond well with the plot of minimum film thickness (Figure 8.61), indicating that it is a good indicator of the performance of the film as a whole.

8.6 Hip Simulator Summary

Depassivation occurred in the simulator at the onset of simulated gait. This was indicated by a negative shift in open circuit potential and a simultaneous increase in corrosion current.

After periods of sliding the corrosion current spontaneously reduced to a fraction of the value measured at the onset of simulated gait. The point at

which this occurred was affected by the composition of the serum solution used (protein and phosphate concentration).

Under potentiostatic conditions, the current displayed periodicity at the frequency of the gait cycle. The shape and magnitude of these current oscillations changed over the course of a long-term test and periods of oscillation ceased when repassivation was observed.

Metal ions were produced from both depassivation of the bearing surface and dissolution of the particulate debris in nearly equal volumes. The relative amount released from surface depassivation increased over duration of the tests.

Following a year's simulated gait (1 million cycles), the surface roughness and clearance had both increased. Elastohydrodynamic film thickness was calculated, based on the initial and final clearance of the bearing. When compared with the initial and final roughness of the surfaces the calculated lambda ratio was lower at the end of the test than prior to testing.

Chapter 9 Surface Analysis

9.1 Introduction

Surface analysis was undertaken on a number of hip simulator samples, tested both in Procedure 1 and Procedure 2. Transmission electron microscopy was used to observe subsurface changes to the microstructure. Furthermore, the composition and thickness of the adhered intact tribofilm was also investigated, in the transmission electron microscope (TEM), using selected area electron diffraction (SAED), electron energy loss spectroscopy (EELS) and energy dispersive X-rays (EDX). To supplement observations made on the TEM, X-ray photoelectron spectroscopy (XPS) was used to examine the tribofilm at a number of different splutter depths.

9.2 Transmission Electron Microscopy of the Worn and Unworn Surfaces

The sample preparation was undertaken as described previously in 6.2. Two surfaces were selected for analysis. One from within the wear scar of the femoral head, and one from the un-contacted region of the femoral head. SEM images of the two surfaces selected for sample preparation are shown in Figure 9.1. The surface were then milled away to leave a slide, which was then cut-out by the ion beam as shown in Figure 9.2. Once removed from the surface, the samples were thinned to the desired thickness (≈60nm) using the ion beam. The thinned samples are shown in Figure 9.3.

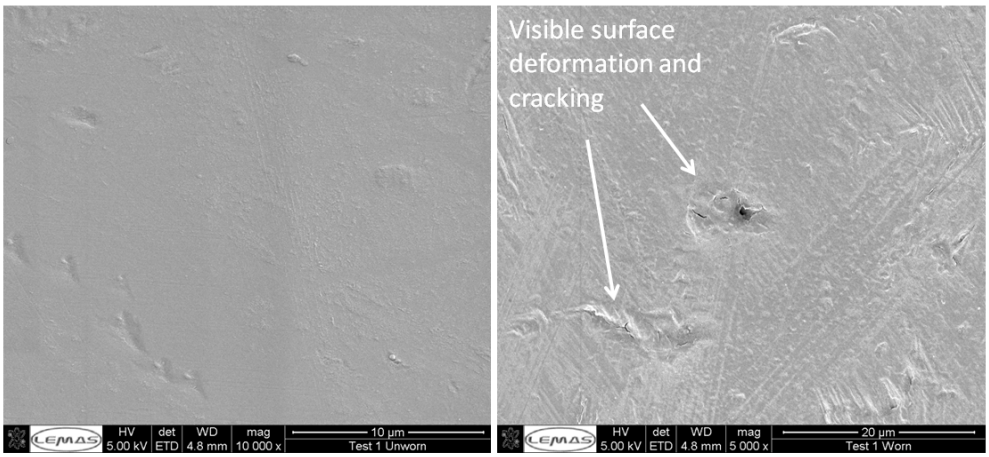

Figure 9.1: SEM images of the unworn (left) and worn (right) regions selected for TEM preparation.

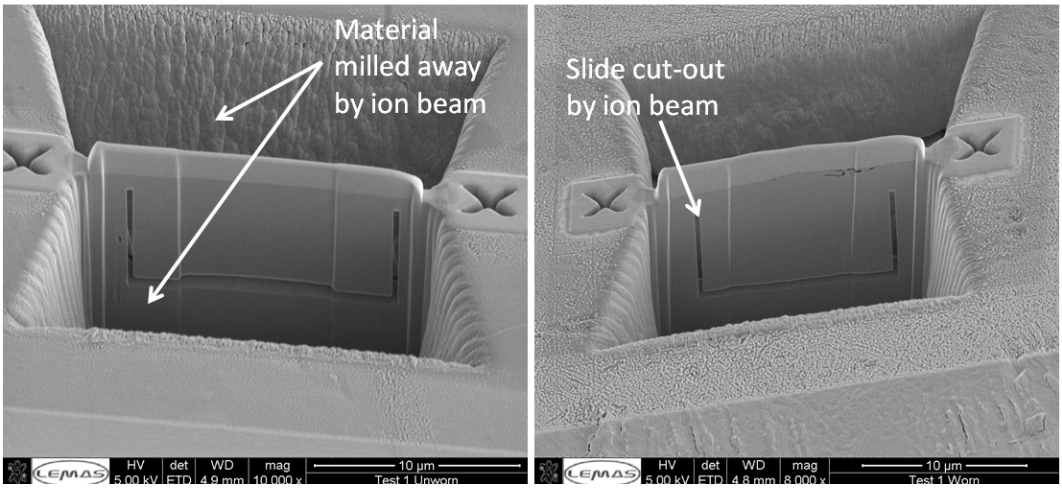

Figure 9.2: SEM image of TEM slide preparation from the unworn (left) and worn (right) regions.

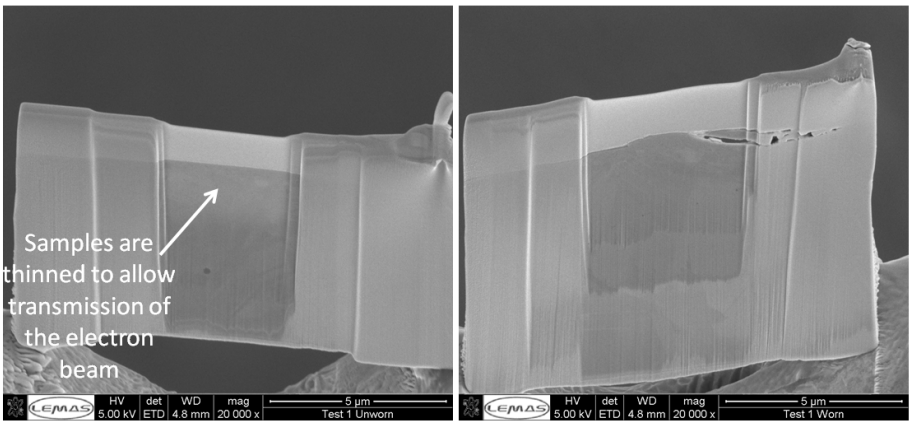

Figure 9.3: TEM slides, from the unworn (left) and worn (right) surfaces.

It can be seen from Figures 9.3 and 9.4 that the worn sample contains subsurface cracking. SEM images of the surface from the worn (contacting) region and unworn (non-contacting) region illustrate that damage to the surface took place as a result of the imposed, simulated walking cycle. Figures 9.3 and 9.4 show the formation of subsurface cracks in the contacting region. The crack was over 2μm in length and extended to a depth of approximately 200nm. Liberation of the material bordered by this crack (see Figure 9.4) would result in the release of a comparatively large particle (and possibly a number of smaller particles) when compared with the measured particles released from MoM articulations, both *in vivo* and *in vitro*. Studies have shown that an abundance of oval shaped sub-micron particles are produced along with larger rod-like particles, which can extend into the micron scale (57, 61, 62). Subsurface cracks of a similar scale to that shown in Figure 9.4 have been reported previously by Büscher *et al* (46). It was suggested that cracks such as these form along grain boundaries, resulting in delamination of the surface, however, the crack shown in Figure 9.4, occurred within the nano-crystalline region of the surface and not along a single grain boundary. No other cracks were observed in any regions of the prepared samples, although, the areas investigated by TEM account for an extremely small fraction of the bearing surfaces.

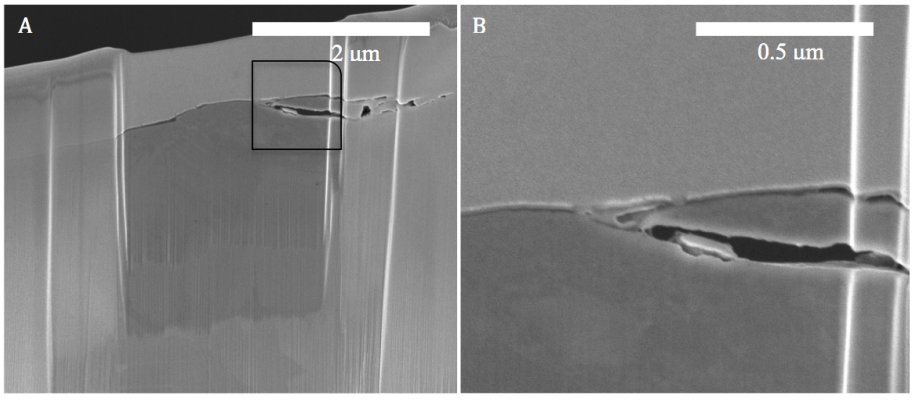

Figure 9.4: TEM slide of worn region showing subsurface crack and debris generation (A) and a higher magnification view of the cracked region (B).

TEM images of the samples revealed much greater detail, enabling analysis to be made of the subsurface. TEM imagery from both the non-contacting and the contacting regions revealed the existence of two distinct crystal

structures in the subsurface region (illustrated by circles labelled 1 and 2 in Figures 9.5 and 9.6). The dark field images shown in Figures 9.5B and 9.6B suggested that, close to the surface, the crystal structure was finer. This was established by the appearance of bright spots close to the surface, as opposed to the larger, uniform bright patches at submicron depths. Since only scattered light is captured during dark field imaging, only crystallites, which are orientated to give Bragg reflection at a specific angle, will light up. By measuring the diameter of different bright spots of the dark field image, the crystallite diameter close to the surface was estimated. Within the top 150nm of the unworn region the crystallite diameter appeared to be approximately 40nm, compared to 20nm diameter in the worn region (based on an average of 50 measurements of each). These observations are in agreement with published research by Pourzal *et al* (183), which identified a nano-crystalline layer with crystallites ranging from <15nm to 40nm in the worn and unworn regions of MoM prostheses tested *in vitro.* Furthermore, finer grains were identified within regions of the wear scar that had succumbed to either stripe wear or severe scratching as opposed to polishing (183, 184). One difference between those observations and those made in this study is that Pourzal *et al* (183) found finer crystallites in the non-contacting region than the contacting region. In addition the EDX revealed high amounts of silicon and carbon in this region and may be attributed to the polishing procedure undertaken in the manufacturing process.

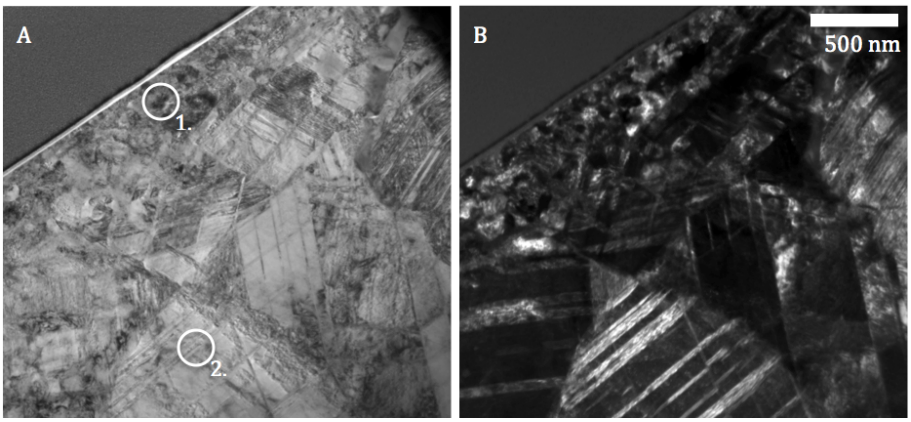

Figure 9.5: Bright and dark field TEM images of the unworn surface (A and B respectively).

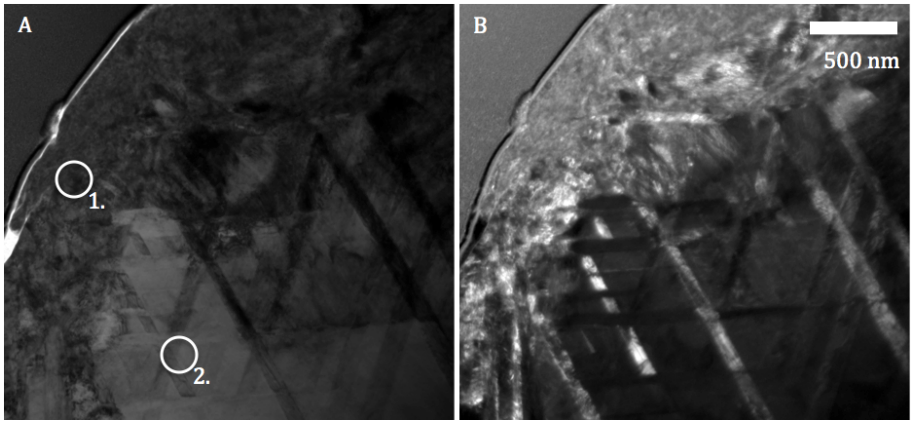

Figure 9.6: Bright and dark field TEM images of the worn surface (A and B respectively).

For added clarity, selected area electron diffraction (SAED) patterns were examined at different locations of the subsurface as demonstrated in Figures 9.7 and 9.8. The diffraction patterns observed in both the unworn and the worn surfaces both support the idea of a fine nano-crystalline structure existing in the uppermost layer of the surface. This is demonstrated by the ringed patterns shown in Figures 9.7A and 9.8A, indicative of multiple crystallites much smaller than the 300nm microscope aperture. The diffraction patterns shown in Figures 9.7B and 9.8B are indicative of a single crystal with a diameter greater in length than the aperture. The diffraction pattern in Figure 9.7B was indexed against ε-cobalt and indicates a hexagonal structure indicating the presence of strain-induced phase transformation, possibly caused in the manufacturing process. The diffraction pattern shown in Figure 9.8B was indexed against cobalt and indicates a cubic crystal structure demonstrating that even close to Martensitic bands (visible in Figure 9.6) there are regions of cubic structure. The diffraction patterns taken from the nano-crystalline region were also indexed against the hexagonally structured ε-cobalt. Comparing the ringed diffraction patterns from the unworn surface and the worn surface, it can be seen that the contacting region displayed a much more complete ring pattern. This supports the measurements from the dark field images, showing that the contacting region contained crystallites of a smaller average diameter. Observations of the depth of the nano-crystalline layer showed that it extended deeper in the contacting region to (approximately 250nm) compared to (150nm) in the non-contacting region. Pourzal *et al* (183) found that the formation of strain-induced phase transformations and,

consequently, a nano-crystalline layer, are caused under shear stress and have alluded to its significance in particle detachment and wear.

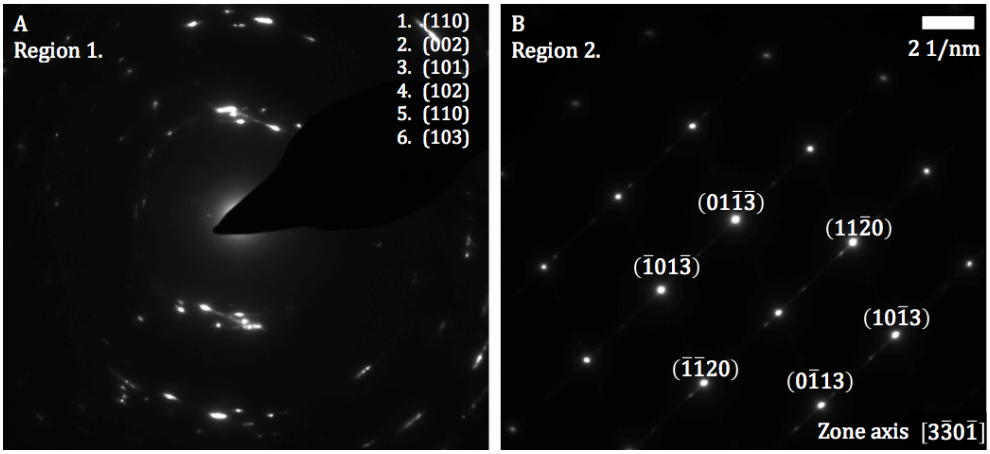

Figure 9.7: Selected area electron diffraction patterns taken from regions 1 and 2 of the unworn sample.

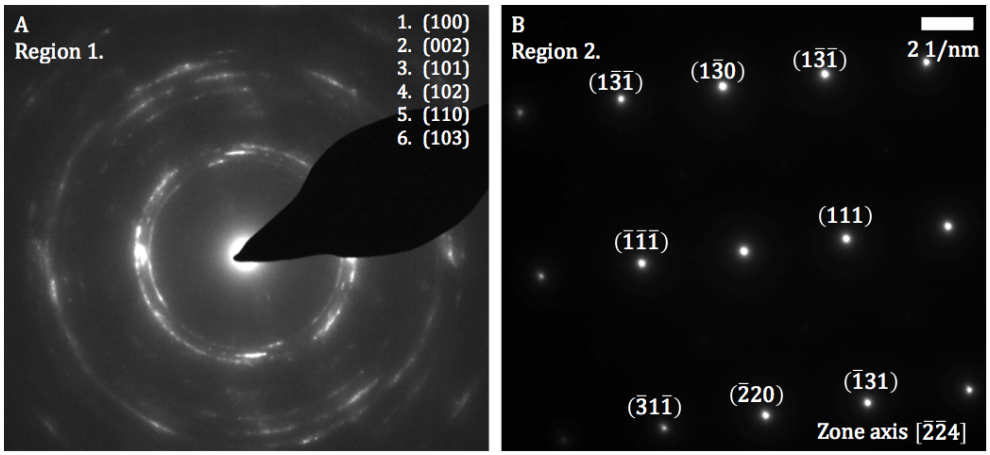

Figure 9.8 Selected area electron diffraction patterns taken form regions 1 and 2 of the worn sample.

9.3 Transmission Electron Microscopy of the Tribofilm

9.3.1 Introduction

Slides were prepared from areas on the femoral head displaying the most substantial tribofilm formation. These were identified as dark black regions located at the edge of the wear scars (see Figure 9.9). Upon rinsing the samples, it was discovered that a substantial amount of white precipitate was residing in the bearing interface. This was removed by rinsing and was stored in a desiccator for 24hrs, by which time it had formed a brittle black flake. This was placed in distilled water, ground into a powder and pipetted onto a TEM support grid to enable microscopic inspection and chemical analysis to be taken.

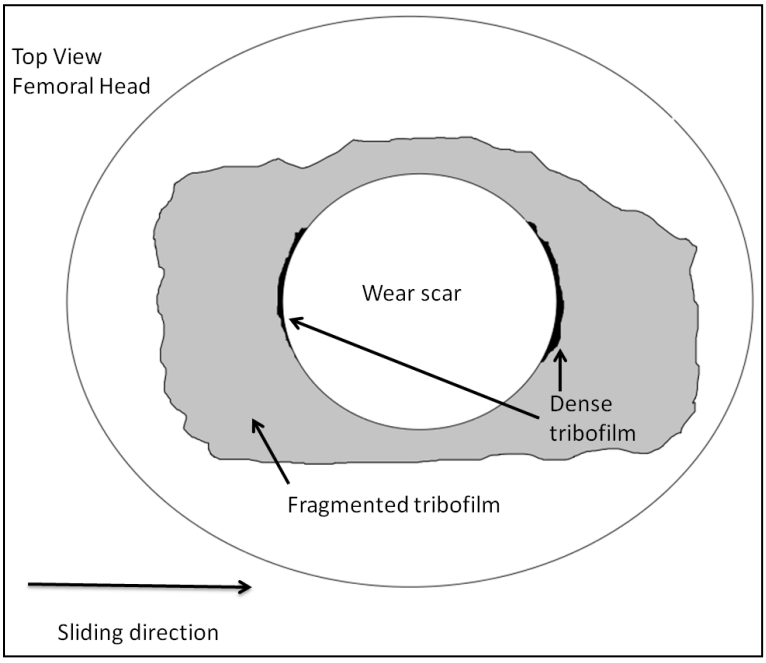

Figure 9.9: Illustration of femoral head, showing tribofilm and wear scar.

9.3.2 Tribofilm Images

TEM images show that the tribolayer thickness varied across the sample, depending on the topography of the underlying surface. In regions where the surface was flat there was little variation in tribolayer thickness; however, in regions where the surface was rough the layer appeared to fill in the crevices (see Figure 9.11). The could be due to material being forced into the surface cavities caused by the material roughness, or transformation of the surface into the observed tribofilm by chemical reaction, this is illustrated in Figure 9.10 Case 2, shown in Figure 9.10, and is supported by the apparent absence of a nanocrystalline layer beneath the tribofilm (see Figure 9.11). The nanocrystalline layer has been shown to exist on both the worn and unworn regions of the surface where the tribofilm is not present (see Figures 9.5 and 9.6). This implies that its removal was caused by a corrosion process as opposed to a purely wear process.

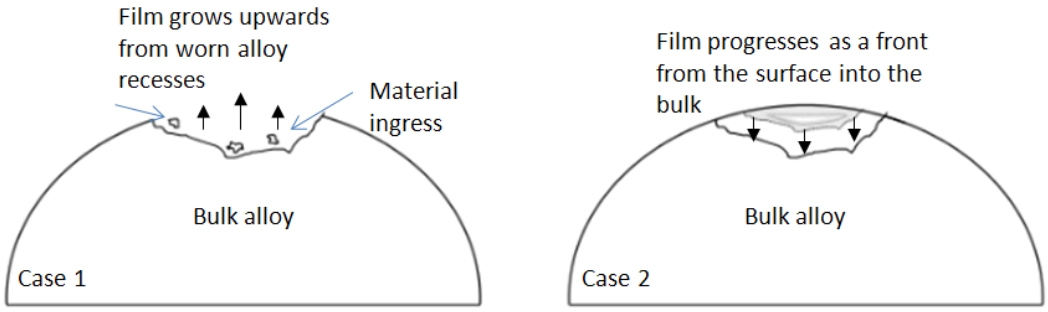

Figure 9.10: Mechanisms of tribofilm growth on the bearing surface

The range of thickness of the tribolayer was 200nm-740nm. The tribolayer in each case was found to contain embedded particles, these were either:

- Located at the surface/layer boundary (see Figure 9.12),
- Agglomerated within the layer (see Figure 9.13).
- Independently suspended within it (Figure 9.14).

Particles were typically smooth and oval shaped, however, some larger, jagged particles were identified at the surface/layer interface. The average length of oval particles was 24.2nm with a range of 8.3nm-75.7nm, whilst the average breadth was 14.9nm with a range of 3.6nm-34.4nm, giving an average aspect ratio of 1.7. These results were obtained from the measurement of 130 particles, identified from TEM images taken of the tribolayer.

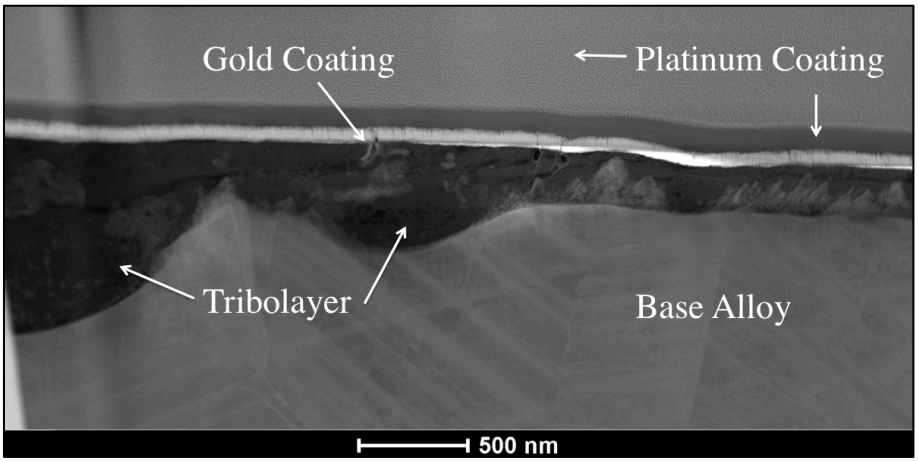

Figure 9.11: HAAD TEM image of bearing surface and tribolayer.

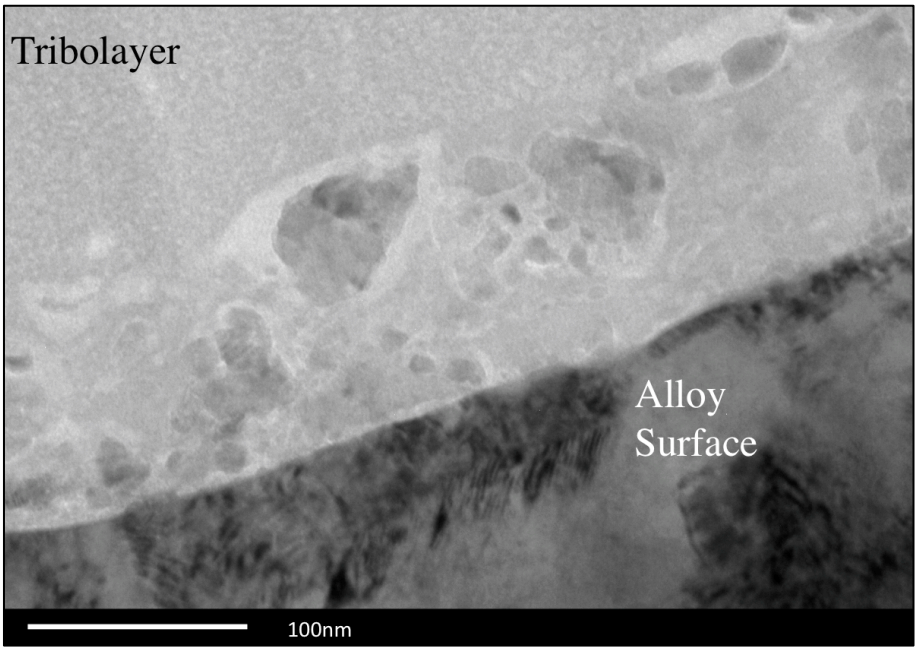

Figure 9.12: TEM image of particles located at the surface/tribolayer interface.

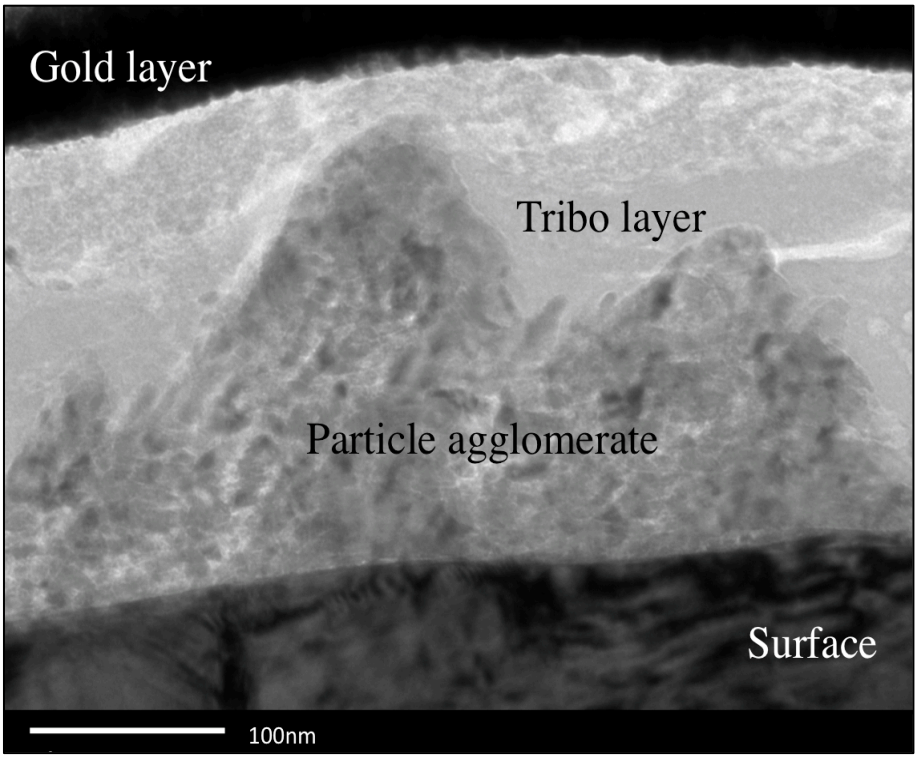

Figure 9.13: TEM image of agglomerated particles in the tribolayer.

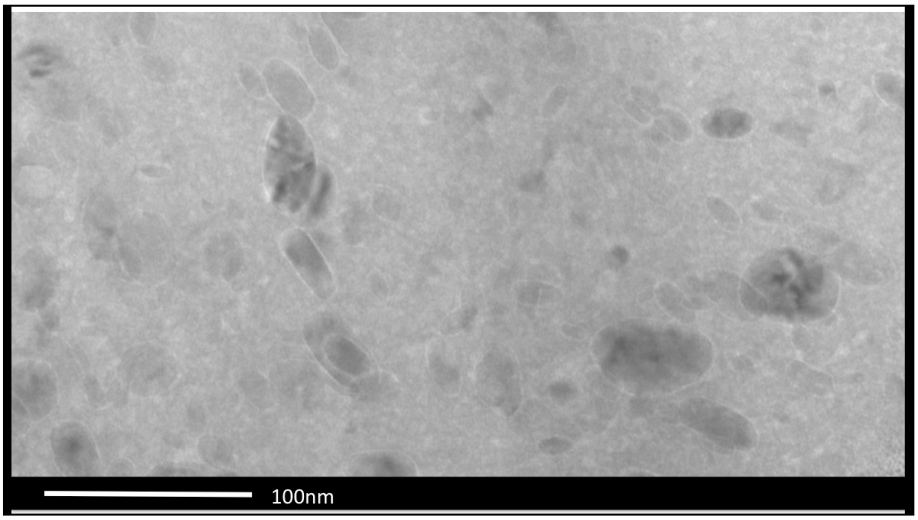

Figure 9.14: TEM image of particles suspended in the tribolayer.

9.3.3 Energy dispersive X-ray spectroscopy (EDX)

EDX mapping of the tribolayer revealed that it consisted of: carbon, calcium, cobalt, chromium, sulphur and oxygen. The particles embedded within the layer comprised cobalt and sulphur as shown in Figures 9.15 and 9.16. This was observed for each of the three types of particle described earlier. When employing EDX analysis there is overlap of the 2.293keV spectral peak of molybdenum and the 2.307keV spectral peak of sulphur. Figure 9.17 shows the absence of the 17.445eV spectral peak associated with molybdenum and confirmed that particles were indeed rich in sulphur, not molybdenum.

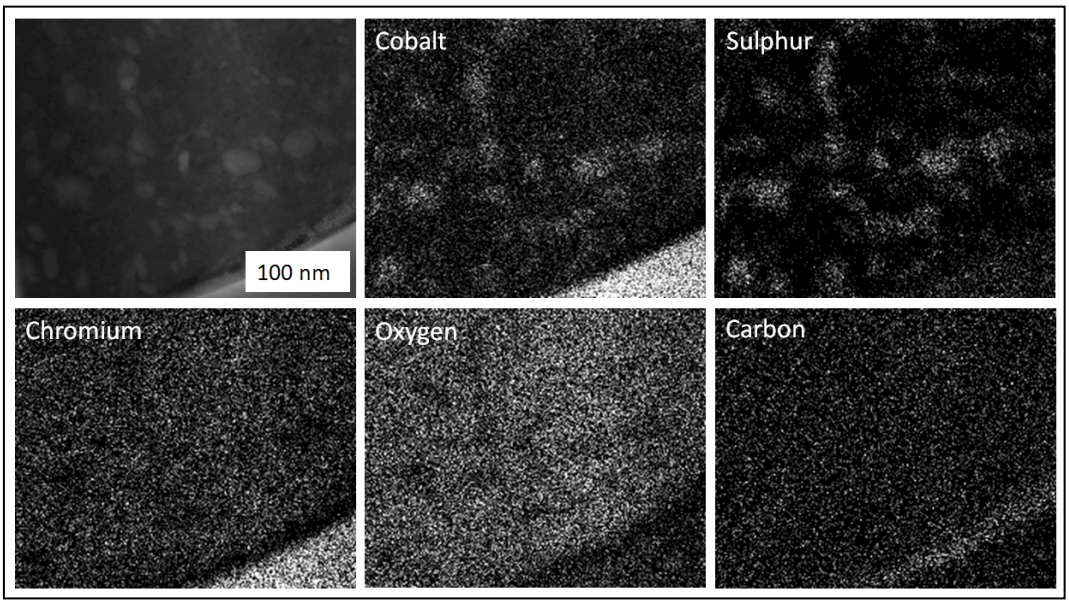

Figure 9.15: TEM image and corresponding EDX map of particles suspended in tribolayer.

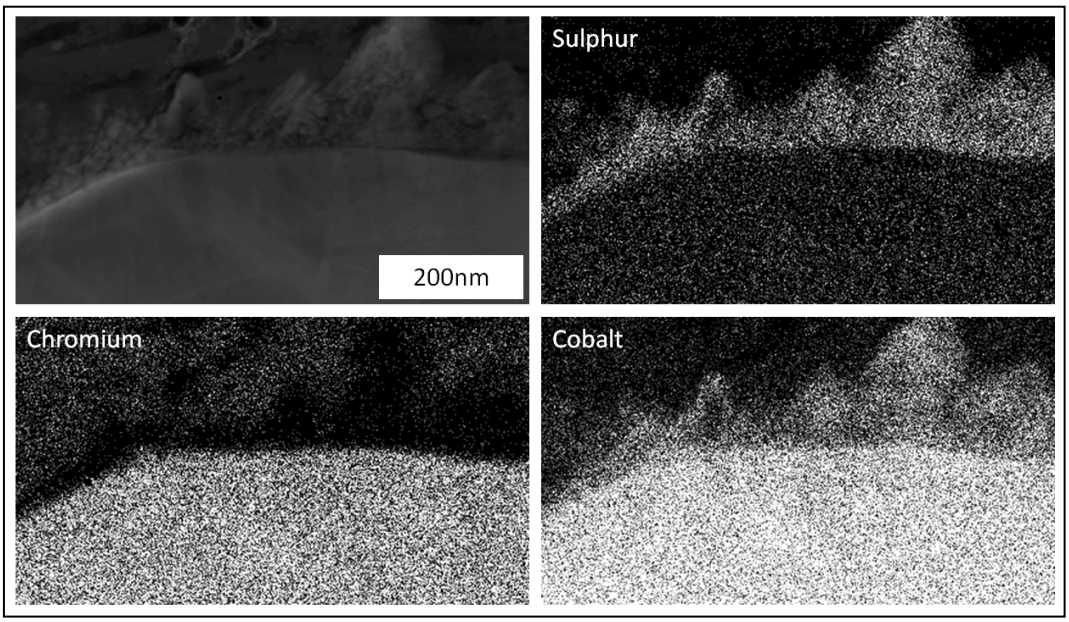

Figure 9.16: TEM image and corresponding EDX map of particles agglomerated in tribolayer.

It is possible to calculate standardless semi-quantification values from EDX spectra and maps using k-factors from the Oxford Instruments software (INCA). Absorption of light X-rays (i.e. from light elements) can result in errors in quant results, the magnitude of which is both sample and instrument dependent, more accurate results may be obtained using calibrated EDX, however for the purposes of this study this was not required. When this was applied to the particle agglomerates, it was found that their average elemental atomic composition was 59% cobalt and 41% sulphur. Particles at the surface/tribolayer interface (Figure 9.12) had an almost identical composition of 58% cobalt and 42% sulphur despite having a very different morphology. In regions of the tribolayer where particles were not observed, the average elemental composition was: 63% oxygen, 10% chromium, 14% carbon, 6% cobalt, 5% phosphorus and 3% calcium (total composition exceeds 100% due to rounding). Compositions were calculated from an average of 5 spectra collected at different locations. The probe size used was approximately 50nm. Example EDX spectra for the agglomerated particles and tribolayer are given in Figure 9.17.

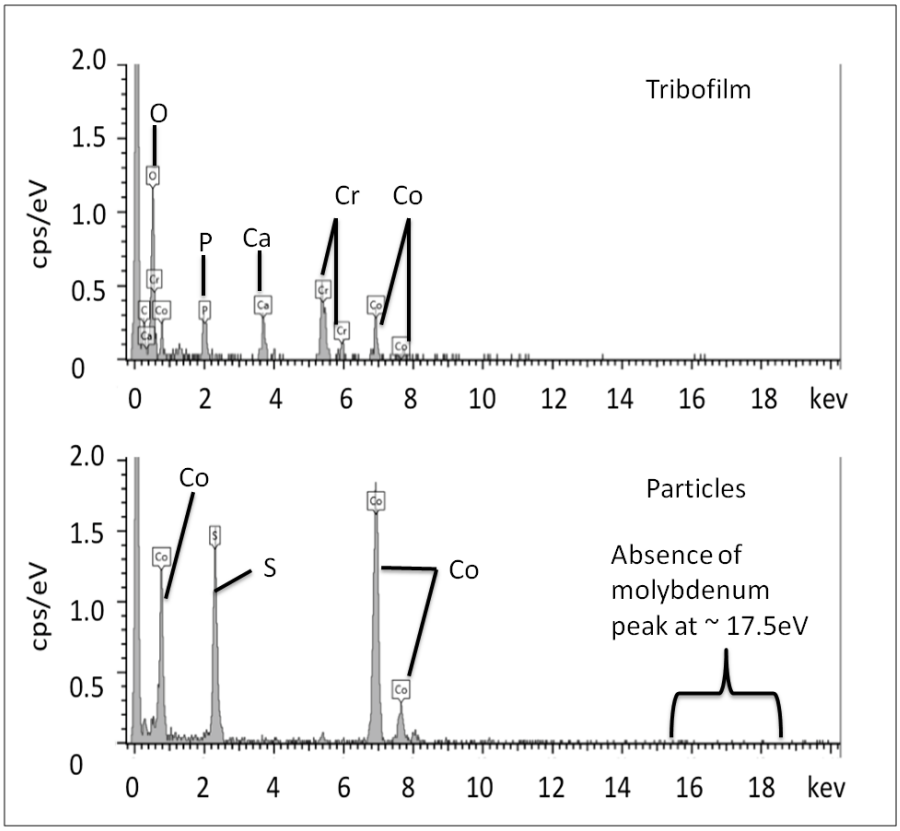

Figure 9.17: Example EDX spectra of tribolayer and agglomerated particles.

EDX spectra were taken from the base alloy at depths between 50 and 500nm beneath the tribolayer. It was found that at all depths the composition of the alloy was within the specified composition given by ASTM standard F1537-08. This indicated that a measurable amount of preferential leaching of alloying elements had not taken place. Spot EDX was also performed on the dehydrated protein precipitate. This revealed that it was predominantly comprised carbon, oxygen and nitrogen. The agglomerated particles within it contained chromium sulphur and cobalt in a ratio of 3.7;1.4;1 respectively.

EDX confirmed that the tribolayer was organometallic in nature, and rich in carbon, which is consistent with previous findings (102). From Figure 9.11 it can be seen that the tribolayer exists as a smooth layer across the roughened metal surface. Its appearance demonstrated that it smoothed the surface asperities. This is consistent with theories that suggest that it may operate as a solid lubricant (100-102). In addition, selected area electron diffraction patterns were obtained from regions of the layer deficient in particles, shown in Figure 9.18.

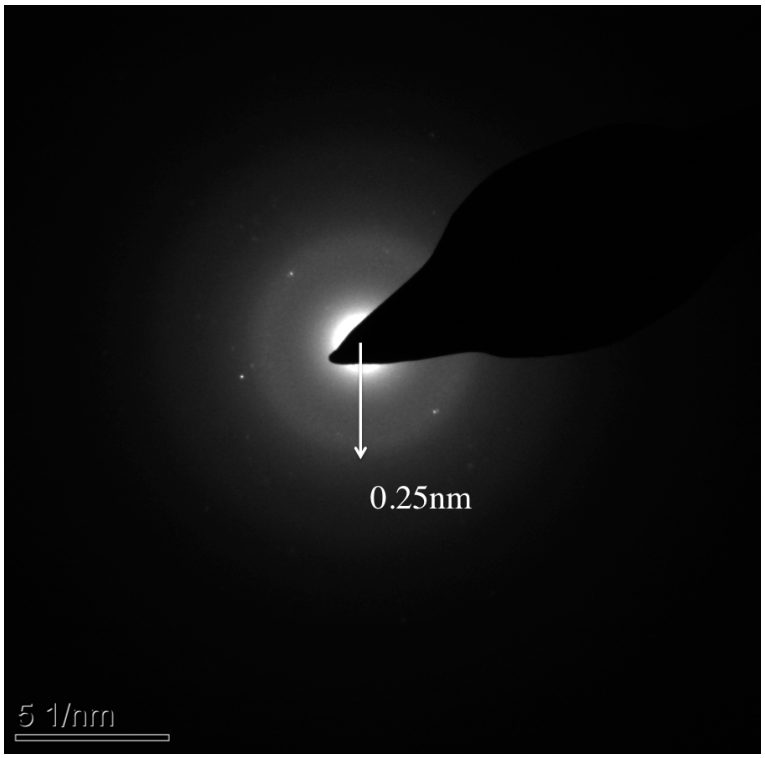

Figure 9.18: Selected area electron diffraction pattern from tribolayer containing no embedded particles.

Selected area electron diffraction patterns (as explained in section 6.4) taken from the tribolayer appear similar to those reported by Liao *et al* (100), however, the dominant spacing differs; d being measured to be approximately 0.25nm as opposed to 0.34nm. The 0.34nm spacing reported by Liao *et al* (100) correspond to the inter lamellae spacing found between the graphene sheets within graphite. When TEM images were taken of the tribolayer, at higher magnifications, no evidence of ranged ordering was observed (Figure 9.19), suggesting that graphitisation had not taken place within the tribolayer.

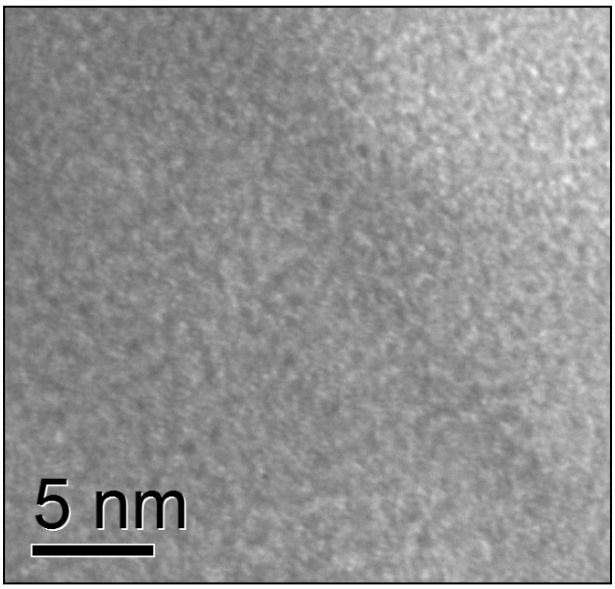

Figure 9.19: High magnification TEM image of tribolayer.

9.3.4 Electron Energy Loss Spectroscopy (EELS)

Core loss EELS spectra were obtained of the carbon k-edge from within the tribolayer. Figure 9.20 shows spectra collected from within the tribolayer, alongside spectra obtained from amorphous carbon and highly ordered pyrolytic graphite (HOPG), supplied by Agar Scientific. The spectrum obtained from the tribolayer has an appearance similar to that of amorphous carbon. It contains a sharp π^* peak close to 285eV followed by a broad σ* peak. Whereas, for HOPG both the π^* and σ^* peaks are sharper and more clearly defined.

It is well known that electron beam damage can affect the sp^2/sp^3 bonding ratio within carbon species (100, 185-187). To ensure that this was not taking place, a damage series was performed on a separate sample of the tribolayer. EELS spectra were taken periodically at a point within the tribolayer following exposure to the electron beam for 0,1,2,3,4,5 and 10 minutes; hence, the effect of electron fluence on EELS measurements was observed. The normalised periodic spectra obtained from the damage series are given in Figure 9.21. This shows that no discernable change in the EELS spectra was observed up to a total electron fluence of 1950e/nm^2 (t=600s).

Single spectra taken from different samples of the tribolayer were taken, at lower electron fluence, hence they were assumed to be free from significant beam damage.

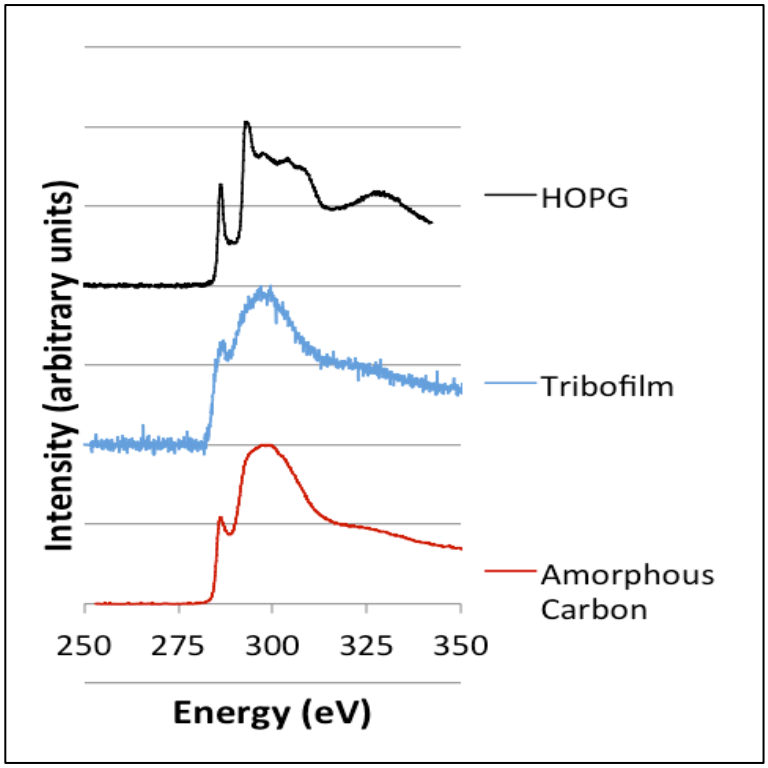

Figure 9.20: Electron energy loss spectra, taken from highly ordered pyrolytic graphite (HOPG), the tribolayer and amorphous carbon.

EELS C K-edge spectra taken from the tribolayer contained a prominent π^* pre-edge peak, similar to that measured in previous studies (100). However, the C K-edge spectra obtained more closely resembled that of amorphous carbon (100) rather than that of crystalline graphite. Using the Gaussian fitting procedure presented by Zhang *et al* (100, 187) the fraction of planar sp^2 bonded carbon atoms (planar sp^2 bonded carbon)/(total carbon), and hence the degree of graphitisation, was determined to be of the order of ≈65%. For comparison, the same technique was performed on an area of amorphous carbon TEM support film, which gave an sp^2 bonded carbon fraction of ≈73%. This was a considerably lower value than that determined by Liao *et al* (100) and this discrepancy may be attributed to the different fitting procedure used to determine the sp^2 bonded carbon fraction.

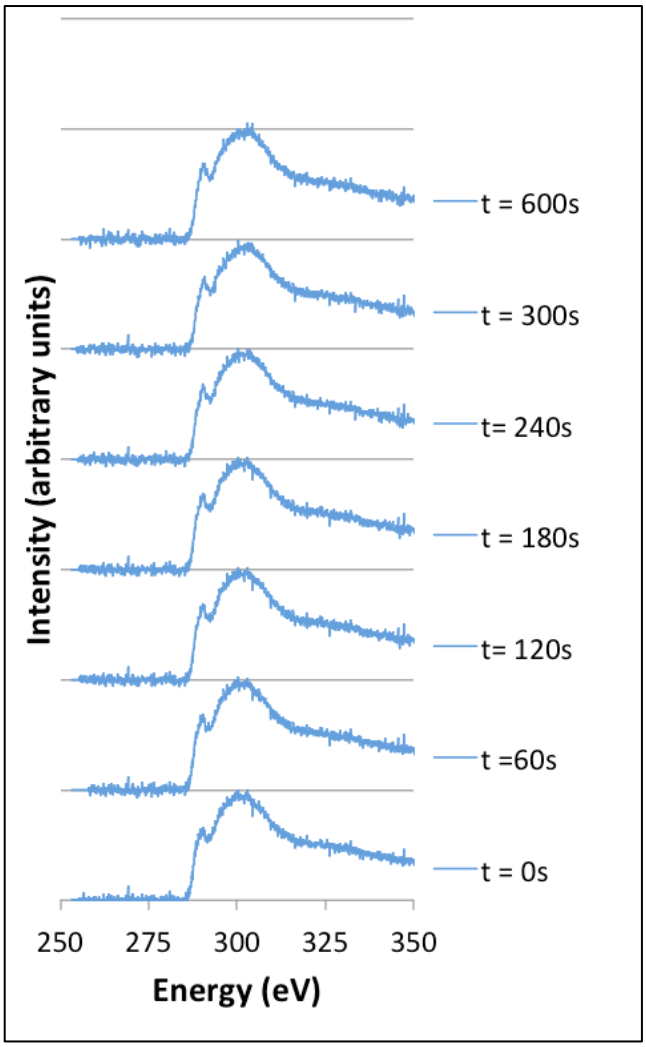

Figure 9.21: EELS spectra taken after increasing electron fluence.

It is noticeable that the measured π^* peak at the EELS C K-edge of the tribofilm was both asymmetric and also broad (relative to that observed in amorphous carbon or graphite). It was concluded that this π^* peak was, in fact, made up of two distinct peaks (see Figure 9.22). The lower energy loss peak (at ca. 285eV) may be associated with non-planar sp^2 bonded carbon and possibly also carbon (singly) bonded heteroatoms such as hydrogen, nitrogen and/or oxygen. This is supported by both the amorphous appearance of the region at high magnification (i.e. there is substantial curvature in the carbon-carbon bonds) as well as the high percentage of oxygen found to be present in the film (62.5%) as determined by TEM-EDX analysis. In addition, there may be hydrogen (and hence C-H bonding), which is extremely difficult to detect. Note if it is assumed that the π* peak at the EELS C K-edge of the tribofilm is composed of just a single peak caused

by planer sp^2 bonded carbon, the values for the degree of graphitisation calculated are much higher and may even exceed 100%. We believe this finding provides support for the interpretation of the π^* peak as being comprised of two separate peaks.

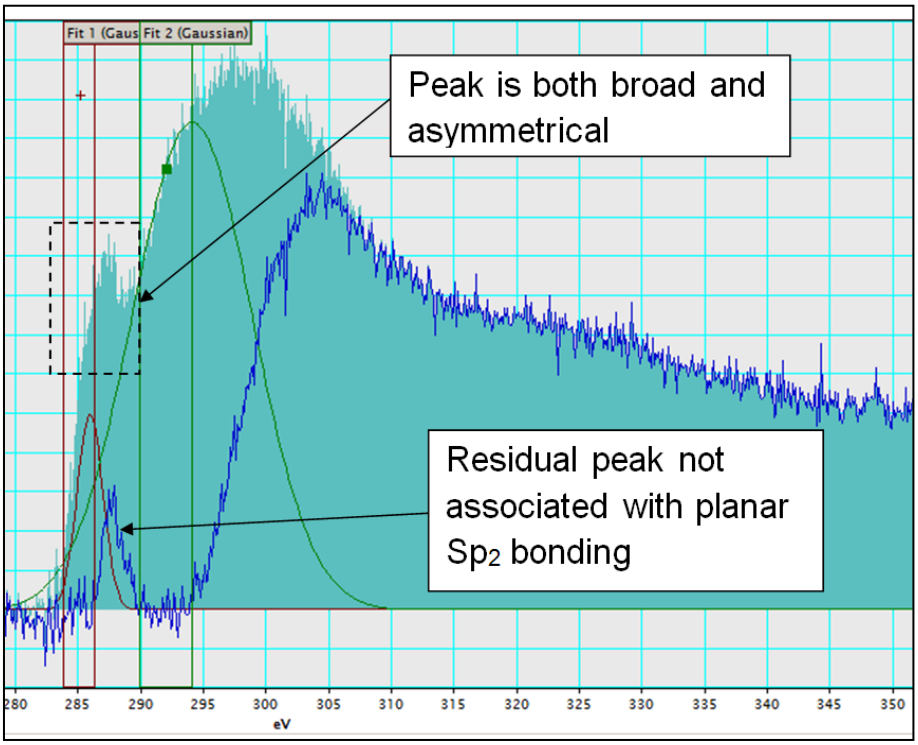

Figure 9.22: Fit used to estimate sp^2 bonding ratio in tribofilm.

9.3.5 Particle Composition

Particles suspended within the tribolayer were on average just 24nm in length and 15nm in width, which are smaller than typical particle sizes produced in MoM bearings, during simulator testing (the range of average sizes, reported for similar conditions, was from 20-135nm) (13, 62, 96, 108). In addition, the oval particles in the tribolayer appeared smoother than the oval particles previously imaged by Catelas *et al* (62) or Bowsher *et al* (96). The environment within the tribolayer could be responsible for this difference. Particles may be smoothed due to repeated impacts with one another caused by high shear rates across the tribolayer. Whereas those

that were liberated into the bulk solution were dispersed over a much greater area, and therefore particle-particle interaction is less likely. This is a similar mechanism to the saltation process that leads to the size reduction and smoothing of suspended pebbles in rivers (188, 189). Particles that were observed close to the interface between the alloy surface and the tribolayer (Figure 9.12), appeared more jagged and larger than those suspended within the layer. These could be newly formed particles that had not yet been dispersed throughout the layer, and had not reduced in size through abrasion induced smoothing. This mechanism is partly supported by the presence of particle agglomerations. Agglomerations show that particles do translate within the layer and come into physical contact with one another.

EDX revealed that particles comprised purely cobalt (58.2-58.6% - atomic) and sulphur (41.4-41.8% - atomic). No known sulphides of cobalt have a concentration of cobalt that great. This indicates that particles must also contain an amount of pure cobalt. Since the percentage composition of particles was independent of particle size, it is not feasible that particles contain a cobalt core surrounded by a cobalt sulphide layer. Instead, it appears that particles consist of a mixture of cobalt and cobalt sulphide. Electron diffraction patterns taken from the agglomerated particle were indexed against cobalt sulphide (Co_3S_4) as shown in Figure 9.23.

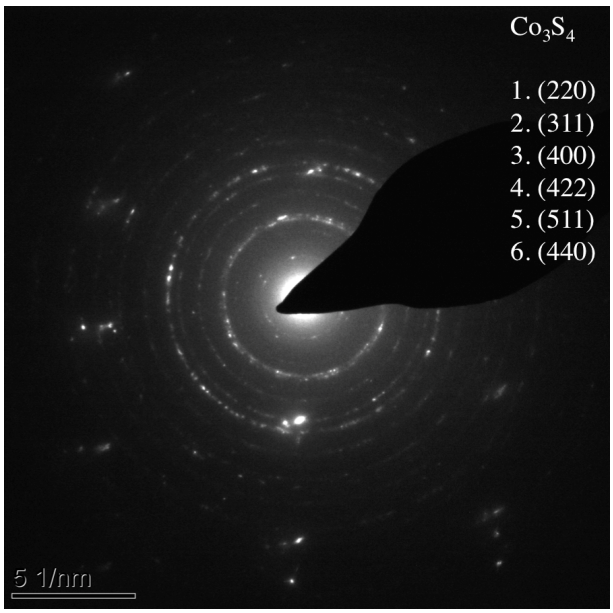

Figure 9.23: Electron diffraction taken from agglomerated particles, indexed against cobalt sulphide (Co_3S_4).

The absence of chromium within the embedded particles may explain the high level of chromium within the tribolayer. In the base alloy, the mass ratio of cobalt to chromium was between 2.8 to 1 and 2 to 1, whereas the average ratio detected in the tribolayer was 0.71 to 1. Measurements of the composition of the base alloy just below the tribolayer indicated that no preferential leaching of alloying elements had taken place. This suggests that particulate debris was the chief source of cobalt and chromium within the tribolayer. Furthermore, it appears that the concentration of cobalt within the embedded particles reduced the amount of freely available cobalt to distribute about the film, explaining the high ratio of chromium to cobalt within it. EDX indicated that preferential leaching of alloying elements did not take place in the bulk alloy beneath the tribolayer. This indicates that the presence of cobalt and chromium within the layer originates from both particles and oxidation of the topmost surface. The exact mechanism by which cobalt and chromium are separated from one another to leave cobalt rich particles embedded within a chromium rich tribolayer is still unclear.

9.3.6 Protein Precipitate

TEM images of the protein precipitate, collected from the bearing interface, revealed that it also contained particle agglomerates. They were observed to exceed 100nm in length and breadth (see Figure 9.24). The agglomeration of particles in these instances could be an artefact of the sample preparation. Dehydrating the precipitate and grinding it into a powder may cause agglomeration of particles contained within it.

Initially, the protein precipitate appeared milky in colour, but upon desiccating for 24 hours it became black and solidified. EDX confirmed that the solid precipitate was rich in carbon and contained metallic particles. EELS spectra of the carbon k-edge (see Figure 9.25) of the layer indicated that it also displayed a prominent π* pre-edge peak and 74% planar sp^2 bonding.

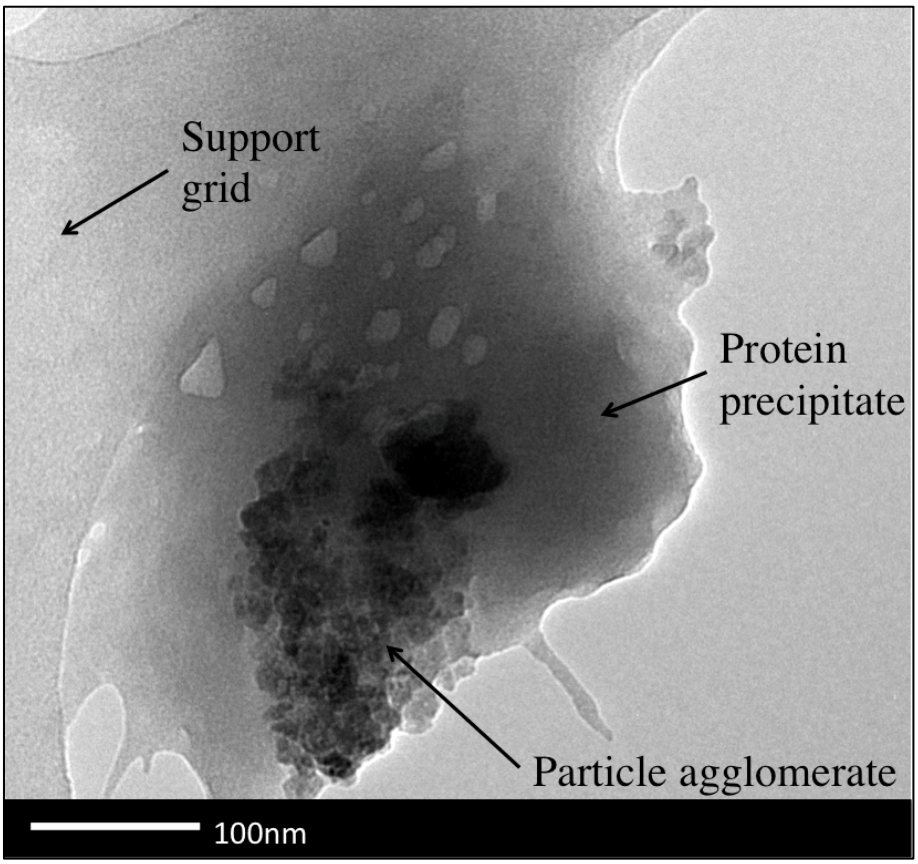

Figure 9.24: TEM image of dehydrated protein precipitate containing agglomerated particles.

It is clear that there are a number of similarities between the precipitated protein and the tribolayer. The presence of a high-carbon content and sulphur containing metallic particles may indicate that the precipitation of proteins from the solution is a precursor to tribolayer formation. The tribolayer itself contained cobalt and chromium and its entrapped particles were rich in sulphur, whereas the precipitate only contained cobalt and chromium within the entrapped particles, which were free of sulphur. This suggests that particles can react within the tribofilm and change in composition.

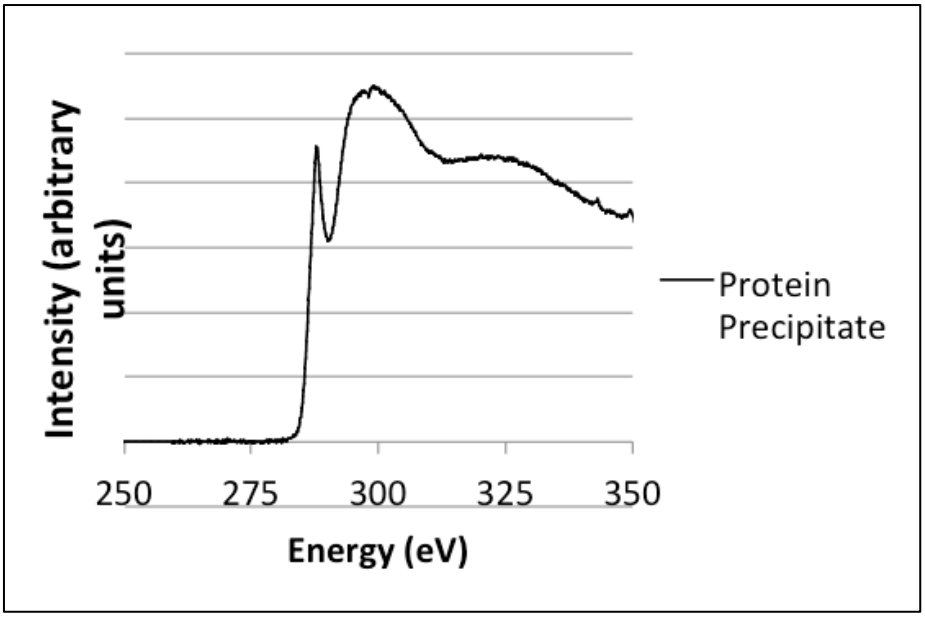

Figure 9.25: EELS spectra of desiccated protein precipitate.

9.4 XPS of Tribofilm

XPS was used to complement the TEM observations made of the tribofilm. Since XPS can be used to determine bond energies, more information about the chemistry of the film can be obtained compared to EDX. An XPS sample was prepared from the bearing surface of the 3rd test sample used in the long-term tests with buffered serum (Procedure 3). The sample was prepared as described in section 6.5. XPS spectra were taken at 23 depths following etching. The etching rate of the sample area was not uniform. Wyko non-contacting profilometry was used to confirm this following XPS analysis. The profile of the surface is shown in Figure 9.26. In addition, the tribofilm under examination was non-uniform and consisted of a complex chemical composition. This made prediction of an accurate etch-rate impossible. It is also important to consider the potential damage caused by argon ion beam etching on the tribofilm.

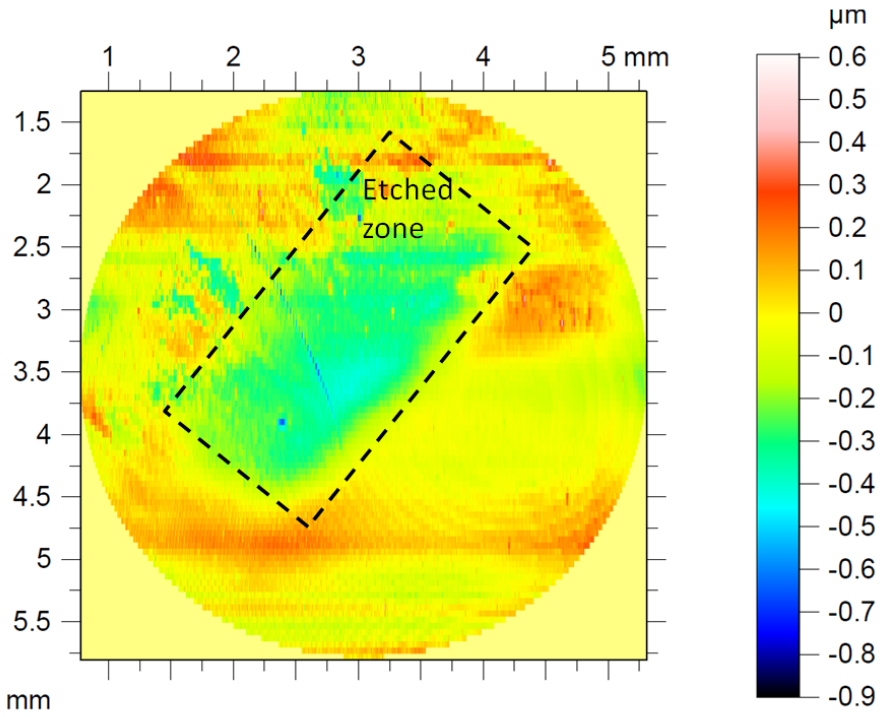

Figure 9.26: Sample surface following XPS 11,500s of etching.

In addition, the area investigated by XPS was approximately 0.5mm^2. This was very large relative to this thickness of the inhomogeneous tribofilm. As the etch depth was increased the amount of base alloy exposed to XPS analysis increased. For this reason percentage quantifications (which are only semi-quantitative of the base alloy relative to the tribofilm were not particularly useful, as they simply reflected the amount of base alloy protruding at a given etch depth. This is illustrated in Figure 9.27.

Some general trends can be, nevertheless, observed from the varying elemental compositions. The only elements found to increase in abundance were the main metallic elements found in the base alloy (Co, Cr and Mo), whilst all others decreased. The process of etching removes the tribofilm thus exposes more of the underlying surface as shown in Figure 9.27. Spectra obtained confirmed the presence of metal oxides as is constant with previous findings (34, 66, 68). The atomic composition of the tribofilm following different etch times is shown in Figures 9.28 and 9.29.

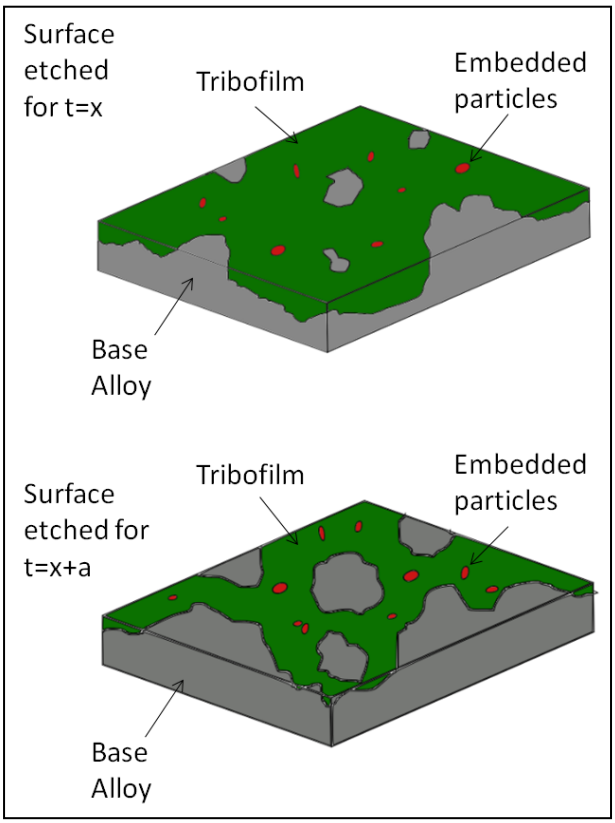

Figure 9.27: Diagram of XPS sample area following two different etch times highlighting their effect on the exposure of the base alloy.

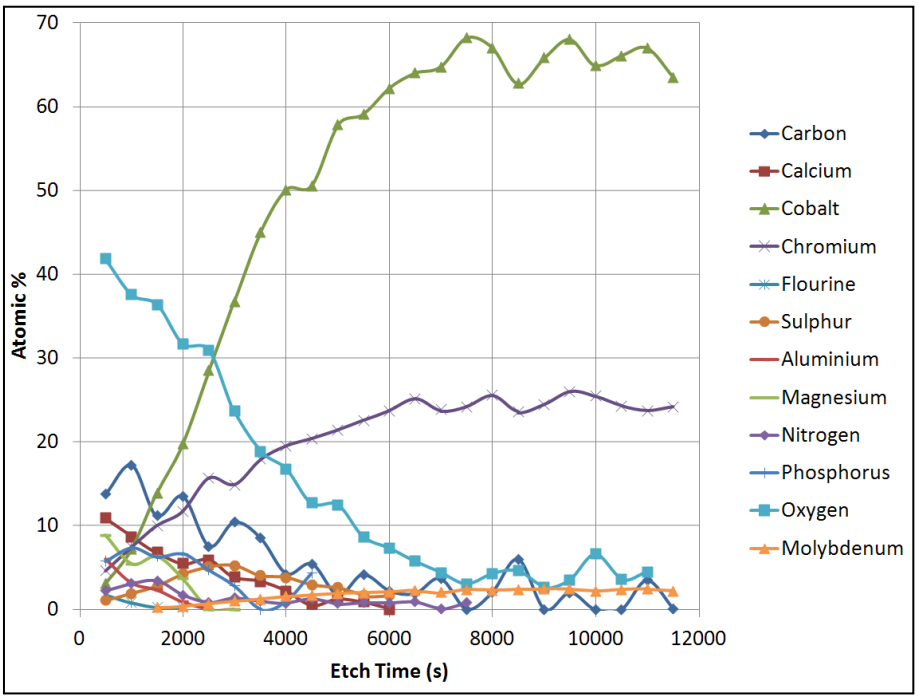

Figure 9.28: XPS elemental variation with etch time.

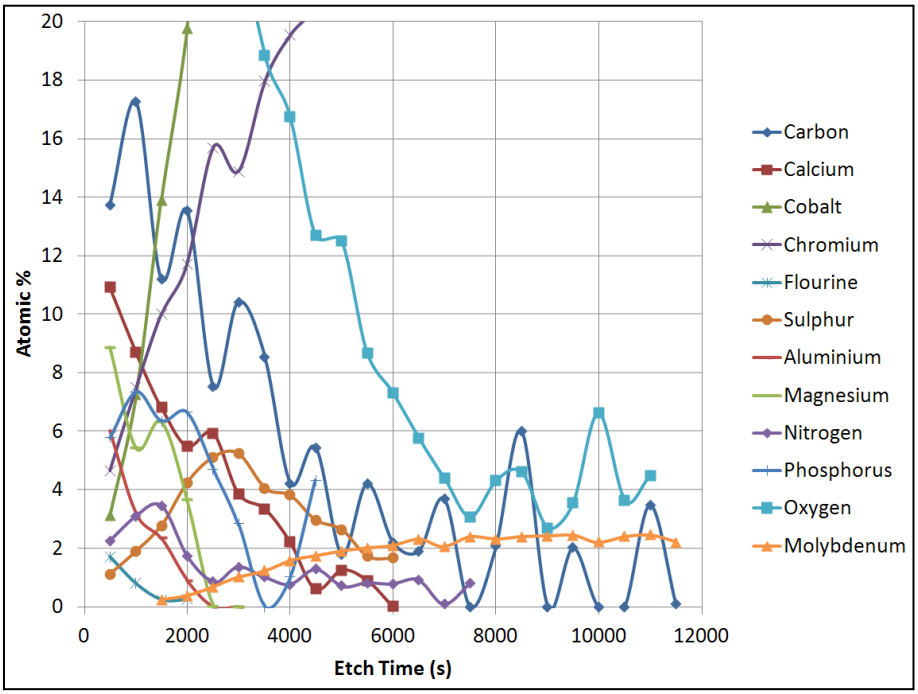

Figure 9.29: XPS elemental variation with etch time (reduced atomic %).

9.4.1 Sulphur

Sulphur was detected within the first 6000s of etching, after which its abundance was below the detection limit. The only species of sulphur detected was a sulphide (Figure 9.30) (190, 191). This can be attributed to the cobalt sulphide particles previously observed within the tribofilm film (Figure 9.16). This supports the SAED images suggesting that the cobalt and sulphur rich particles found within the film contained cobalt sulphide

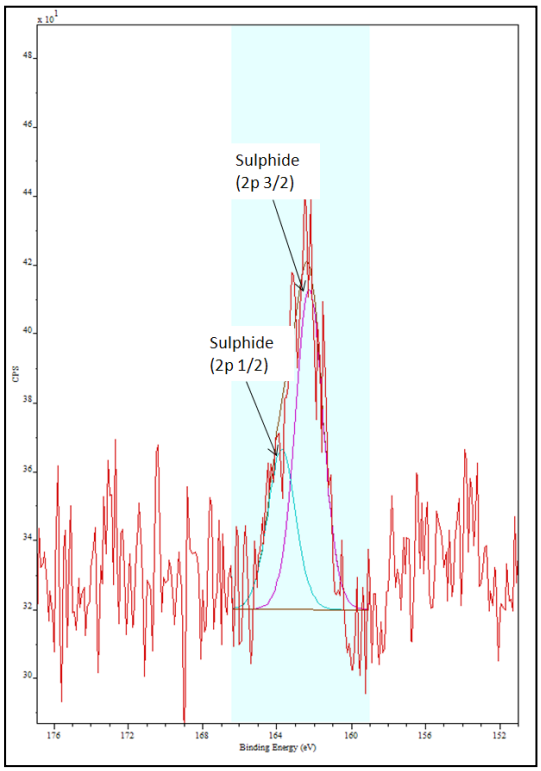

Figure 9.30: Deconvolution of sulphur 2p peaks.

9.5 Summary

Nanocrystallites were within the range reported by previous authors (46) and appeared to refine with strain. The tribological film produced on the surfaces contained both organic material, pure metal and metal oxides.

Analysis of the surfaces following long-term testing (Procedure 1 and Procedure 3) revealed the presence of recrystallisation and formation of a complex tribological layer at the bearing surfaces. This layer was measured between 200-740nm thick.

TEM imaging also revealed the presence of cobalt sulphide particles within the tribological layer, which were supported by XPS. Electron energy loss spectroscopy showed no evidence of graphitisation within the layer and was supported by selected area electron diffraction and transmission electron microscope images.

Chapter 10 Discussion

10.1 Tribometer and Simulator Comparisons

The tribometer was used to obtain an initial indication of the performance of bearing materials in conditions approximating those found *in vivo.* This enabled assessment of materials without undertaking the considerable time and expense of testing them in the hip simulator. The simulator was then used to perform a smaller number of tests in a more realistic environment. Although both systems were designed to approximate the *in vivo* environment, there were number of noteworthy differences between them. For this reason it is important to consider the validity of determining the tribocorrosion performance of bearing materials based on tribometer testing compared to simulator testing.

10.1.1 Comparison of Tribological Conditions

The comparative pressures and sliding velocities, produced in the simulator during simulated normal gait (Procedures 1 and 3) and tribometer during the highly loaded MoM tests (Procedure B), are shown in Figures 10.1 and 10.2. It can be seen that the sliding velocity (calculated from the sagittal displacement only) in the hip simulator reached a maximum of 44.5mm/s. In the tribometer, it was approximately 31.5mm/s. For an equally timed test, the sliding distance travelled in the simulator would exceed that in the tribometer by over 40%. In the hip simulator the surfaces were also subjected to biaxial motion. As discussed in 2.4.4 this has been shown to produce self-polishing of the surface, reducing the overall wear (86, 88, 91). The pressures generated in each system are somewhat different. The simulator produces a continually changing pressure, which repeats every cycle, whilst the tribometer maintains a pressure that does not vary over the course of one cycle. Initially, the pressure in the tribometer greatly exceeded that in the

simulator. However, over the course of the test it reduced until it fell below that produced in the simulator (Figure 10.2). Furthermore, the lubricating conditions produced in each system were very different. The tribometer operated in the boundary regime, with an estimated theoretical minimum film thickness below 1nm (calculated from Equation (2.9)). In the hip simulator, the bearing appeared to operate between the mixed- and fluid film-regime with a minimum film thickness of between 23nm and 54nm in each cycle.

By comparing the imposed tribological test conditions, it was clear that there were a number of different factors affecting the tribological severity of the two systems. It could be reasoned that the conditions imposed by the tribometer were the most aggressive. The fluid film conditions produced in the simulator, mean that the surfaces were partially separated during parts of each cycle, and hence were much closer to the conditions encountered *in vivo*.

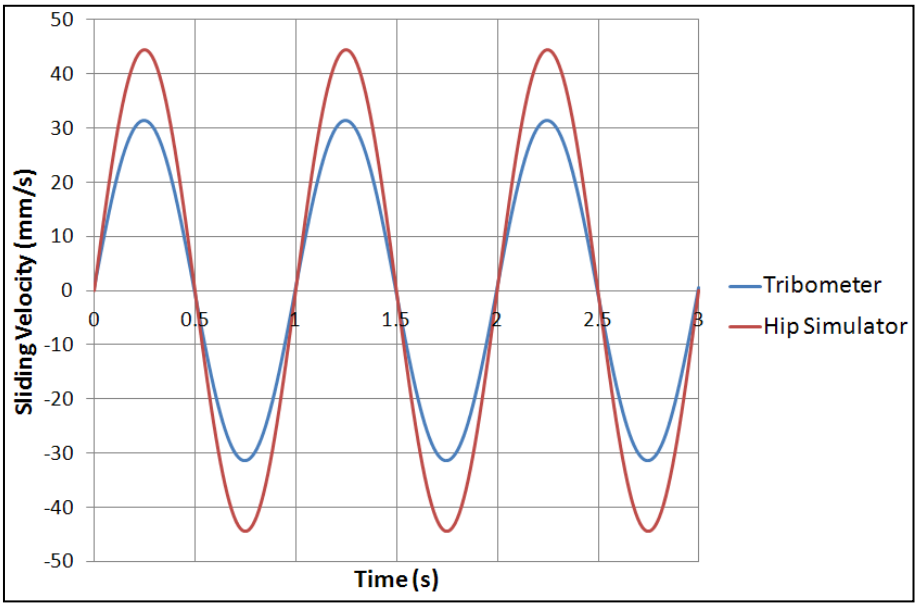

Figure 10.1: Instantaneous sliding velocity in hip simulator and tribometer.

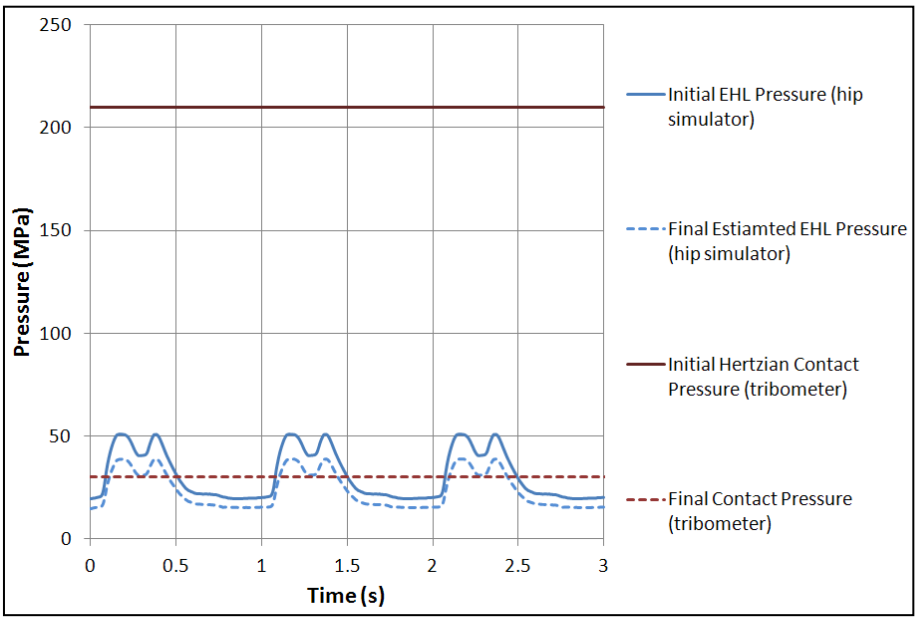

Figure 10.2: Variation in pressure between normal the hip simulator and the highly loaded tribometer.

10.1.2 Comparison of Electrochemical Responses.

In the tribometer, initial depassivation caused a rise in corrosion current, up to approximately 5μA (Figure 5.50) resulting greatly increased current density within the wear scar. In the hip simulator, the rise in corrosion, caused by depassivation during Procedure 1, which used the same un-buffered 25% serum lubricant as was used in the tribometer, was more modest; it rose to between 0.5μA and 4μA (Figure 8.34).

It has been demonstrated that galvanic coupling can occur between a depassivated wear scar and the surrounding passive alloy (114, 158, 176). For stainless steel submerged in sulphuric acid, this produced enhanced corrosion in regions adjacent to the wear track (158). During the analysis of the tests studied in this thesis, the lubricant was substantially less corrosive and there was no evidence of enhanced corrosion outside of the wear scar. Hence, increased corrosion, as a result of depassivation, has been considered to arise solely from within the wear scar. These values are average current densities taken over the entire wear scar. In reality the

current density varies across the wear scar itself. This is caused by the moving contact point between the surfaces and the continuous depassivation/repassivation cycle that takes place. It has been discussed by previous authors, and it has been suggested that galvanic coupling may occur between different locations within the wear scar itself (176, 192).

In the tribometer, 98% of the corrosion current was produced due to depassivation of the wear scar, despite it only accounting for 3-5% of the working electrode surface area. This resulted in a corrosion current density within the wear scar of between 30μA/cm^2 and 40μA/cm^2. The simulator responded quite differently. Between 85-87% of the corrosion current was produced from depassivation within the wear scar. The wear scar in this case accounted for 3.6% of the total exposed working electrode area, giving a corrosion current density within the wear scar of approximately 1 μA/cm^2.

The considerably lower wear scar current density produced in the hip simulator, compared to the tribometer, indicated that mechanical depassivation was less severe, despite producing similar total corrosion currents. This can be attributed to the larger area of the hip simulator test samples. The substantial reduction in corrosion current density, despite a greater sliding velocity and peak pressure, highlight the importance of lubrication between the surfaces.

In addition, the generation of debris within the joint simulator may cause a positive feedback with regards to wear. Yan *et al* (151) demonstrated that the introduction of cobalt nano-particles into the joint interface of an instrumented hip simulator caused a negative shift in OCP. The presence of 3rd-body abrasives was also found to affect the tribocorrosion performance of CoCr in a pin-on-disk tribometer (148, 166). This may have important ramifications when comparing findings from both the tribometer and hip simulator. The boundary lubricated conditions within the tribometer are likely to produce debris with a different morphology to those produced in the hip simulator. Furthermore, the egress of such particles from the sliding interface would be affected by the differences in geometry between the two systems.

10.2 Analysis of Simulator Test Protocol for Tribocorrosion

The development and use of hip joint simulators in the UK was first seen around the mid to late 1960's (193-195). These early machines did not closely resemble those in use today, and relied on hydraulics and spring loading to reproduce the loads experienced *in vivo* (194). Figure 10.3 shows one of the early simulators used by Duff-Barclay and Spillman (195), whilst that used by Dowson *et al* (193) is shown in Figure 10.4. It was not until the late 1980's that the modern style multi-station hip simulator was introduced into laboratory studies (196). Use of these early machines, was centered around the testing of materials that could be used as alternatives to PTFE for MoP hip replacements. Although wear was measured, the emphasis centered on the search for a material combination that produced low friction, approaching that achieved in natural mammalian joints (197). Whilst these simulators were designed to replicate conditions encountered *in vivo* ever more closely, there were no indications at the time that electrochemical conditions encountered in the body may contribute to implant performance.

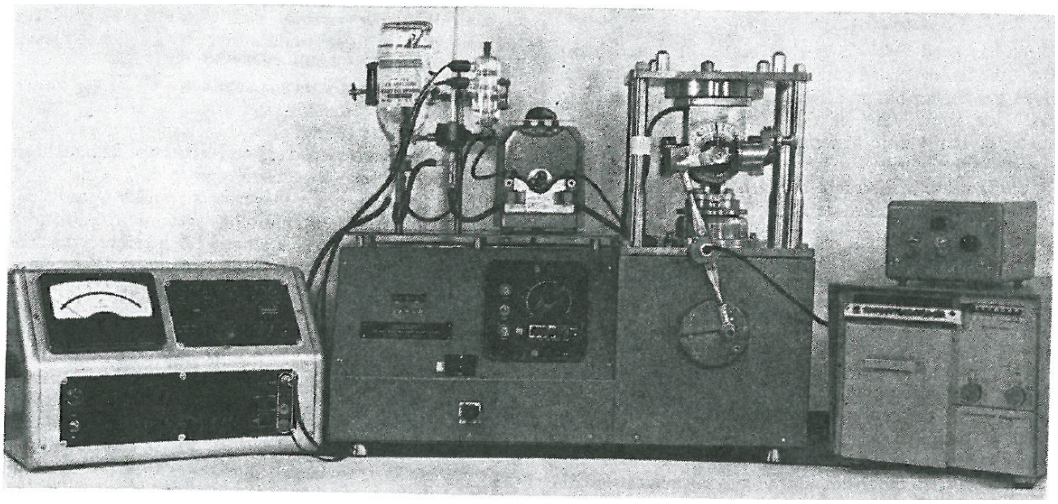

Figure 10.3: 'A human joint simulator' used by Duff-Barclay and Spillman (195).

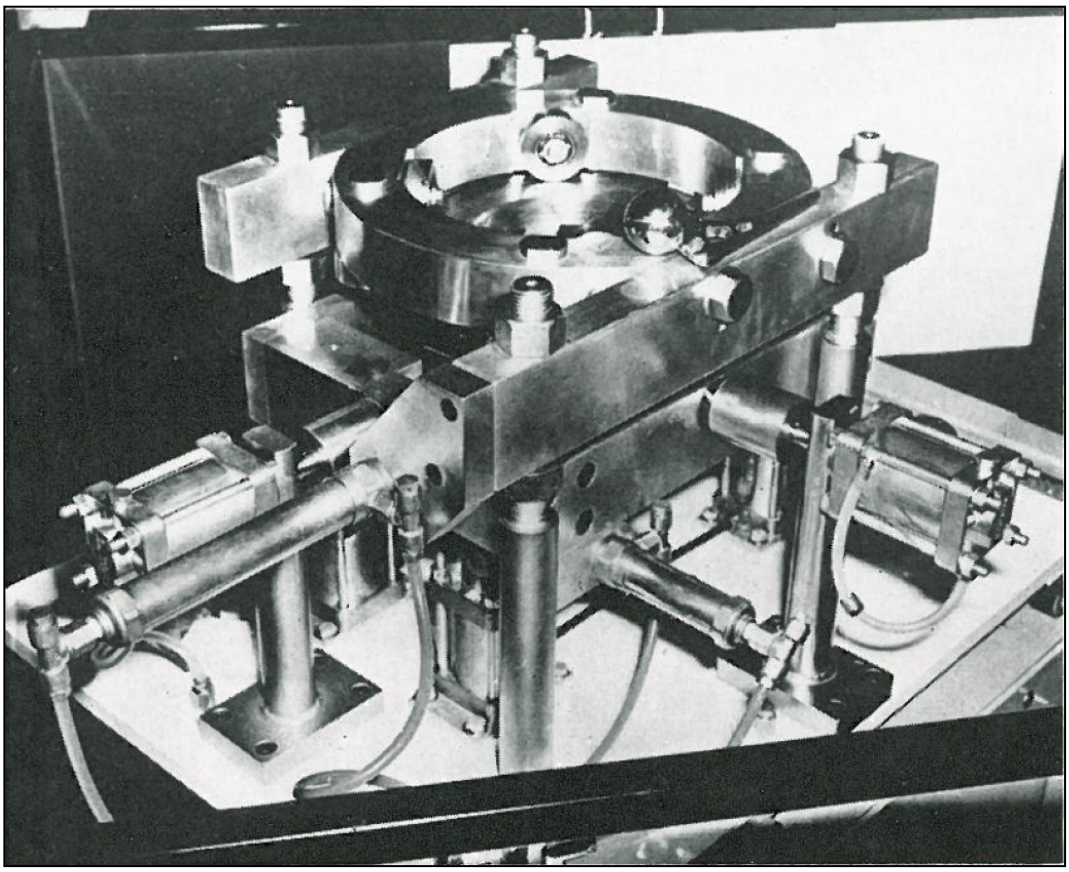

Figure 10.4 ‘ The upper part of the machine into which the joints are inserted’ used by Dowson *et al* (193).

There has been recently some concern that modern hip simulators reproduce a ‘best case’ scenario (198) since the placement of the joint can be rigorously controlled, and the gait cycle imparted typically follows standard walking conditions. Attempts have been made to increase the severity of loading in simulators, with the view to achieving wear rates that are closer to those produced *in vivo* (96, 155, 199-201).

Until recent years, the degradation of metallic bearing surfaces had been viewed as a purely mechanical process. It is now understood that this is not the case. The material degradation may also occur though a tribocorrosion mechanism (88, 89, 95, 104, 146, 147, 150, 161, 202, 203), where oxidation of the surface can also contribute significantly to material loss. This occurs both directly, as pure corrosion, and through the synergenistic interactions between wear and corrosion. Despite this, little effort has been made to

refine hip simulator testing techniques so that they can accurately reproduce the corrosion damage produced *in vivo*.

10.2.1 Effect of Simulated Gait Cycle on Corrosion Measurements

There are two obvious limitations that affect the level of corrosion damage in hip joint simulator tests.

The first concerns the level of pure corrosion. In the passive bearing surface this is generally extremely low, however, it occurs constantly irrespective of whether the bearing surfaces are in relative motion or not. Hence, when calculating the level of metal ions released due to pure corrosion the current must be estimated for performance over an entire year. In hip simulator studies, a year (31.5 million seconds) of use is typically represented by 1 million seconds of gait (or 1 million steps). Although this may represent, with fair accuracy, the amount of mechanical wear taking place, it only represents about 1/31.5 the level of pure corrosion taking place in a year. The static corrosion current was obtained from the long-term hip simulator tests (Procedures 1 and 3) and the increased ion release, caused by an additional 30.5 million seconds in static conditions, was estimated. When un-buffered 25% serum solution was used (Procedure 1), this would have produced an increase in mass loss between 0.8mg and 3.6mg. When phosphate buffered serum (Procedure 3) was used, it was between 0.3mg and 1.2mg. This considerably increases the contribution of pure corrosion to material degradation.

The second limitation relates to the level of wear enhanced corrosion. Following periods of depassivation the current is increased. When mechanical depassivation ceases the current reduces. It has been shown that for passive materials the current will decay exponentially (67, 204, 205). For stainless steels repassivating in tap water, following jet impingement, the repassivation kinetics have been found to obey a bi-exponential decay law (Equation (204)(10.1)(204). In this instance, the 2nd term relates to very rapid processes, such as the formation of a thin oxide layer, whilst the 3rd term

represents slower processes, such as the growth of the passive film. CoCr in bovine serum, following microindentation, was found to repassivate according to a first order exponential decay (Equation (10.2))(67).

$$i = i_s + i_1 exp\left(-\frac{t}{\tau_1}\right) + i_2 exp\left(-\frac{t}{\tau_2}\right) \quad (204)(10.1)$$

$$\mathrm{I} = \mathrm{I}_0 + \mathrm{A}_1 \exp\left(-\frac{\mathrm{t} - \mathrm{t}_0}{\tau}\right) \quad (10.2)$$

Where,

I – Current generated by indentation/abrasion

I_0 – Baseline current

A_1 – Constant determined experimentally

t - Time

t_0 – Time at 0 seconds

τ – Time constant for repassivation

i – Current density response to single particle impact

i_s – Stable current density in the absence of impingement

This does not imply that there is a progressive film growth whilst in bovine serum. However, the measurements that correlated with Equation (10.2) were only observed for 10 seconds of repassivation. It is possible that the term governing passive film growth for CoCr in bovine serum only becomes significant over a longer time frame and was unobservable in the study.

After periods of motion, follows a phase of time in which no motion is taking place, but the corrosion rate is still elevated (shown in Figure 10.5). *In vivo,* this would occur following every period of activity. Practically this may occur many times a day, and hence thousands or possibly tens of thousands of times a year. In a hip simulator this is only reflected once the gait cycle is interrupted. Interruptions occur when the simulator is stopped, to allow the serum to be replaced, and typically occurs between 2 and 4 times per million

cycles. This causes the amount of wear enhanced corrosion to be underestimated. This concept is supported by the work of Wimmer *et al* (87), who reported that in MoM pin-on-ball tests the total material degradation was greater in tests that had a 15s rest implemented between every 30s of motion, than those where motion was continuous.

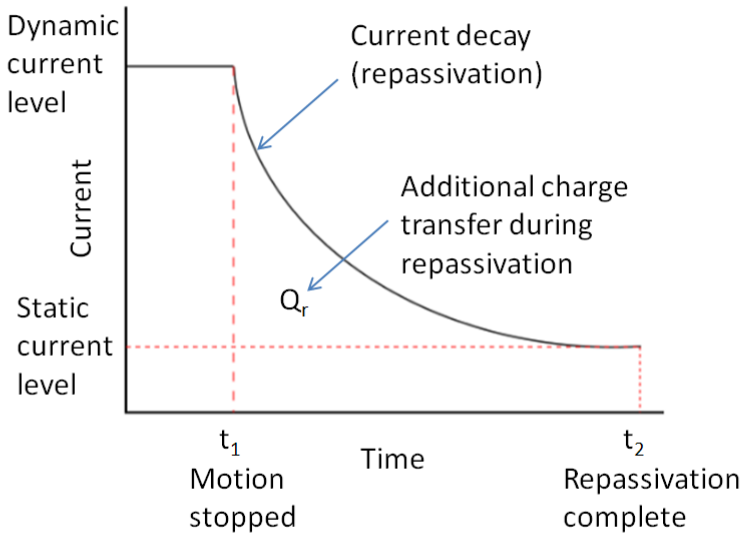

Figure 10.5: Schematic depicting the increased charge transfer during the repassivation of an active surface.

These concepts are illustrated in Figures 10.6 and 10.7. In Figure 10.7, the motion is split in to 3 segments; however, a much greater amount of discretisation is more realistic as long as it satisfies Equation (10.2) when considering the equivalent period of one year.

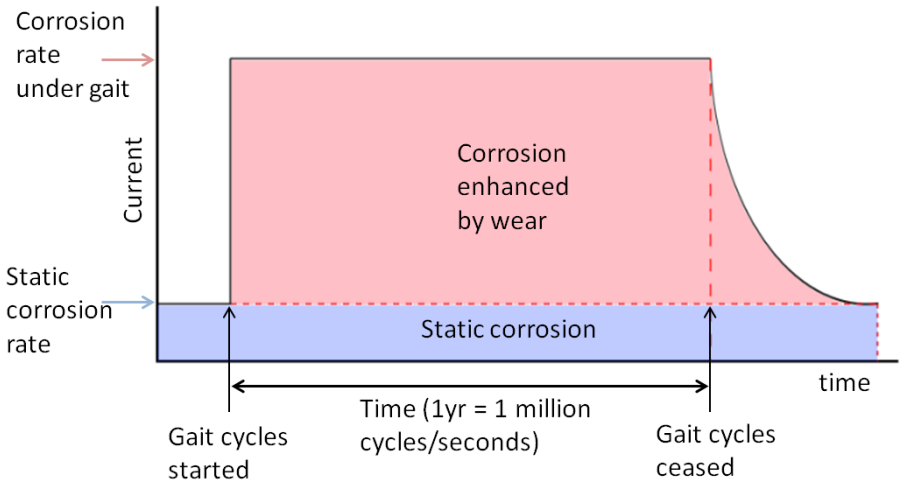

Figure 10.6: Simplified corrosion current diagram for an uninterrupted simulator test.

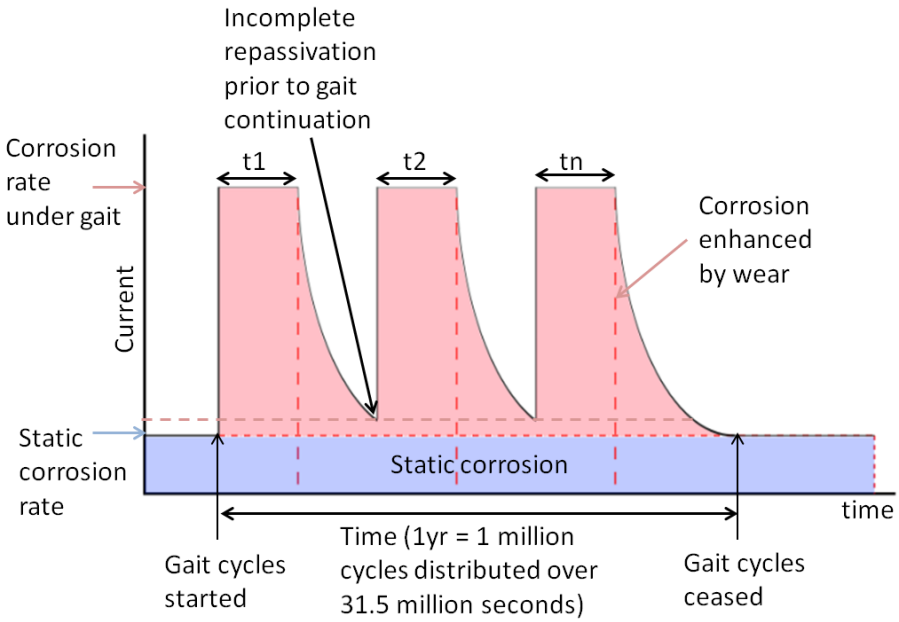

Figure 10.7: Simplified corrosion current diagram for an interrupted test run for 1 year.

$$\sum_{j=1}^{n} i(t_j).t_j = i(t_j)\times 10^6 \qquad (10.3)$$

Where,

t_j – Time of continuous gait

The total degradation can also be thought of as the combination of chemical dissolution and mechanical wear, shown in Equation (10.4) (202, 206, 207).

$$V_{tot} = V_{chem} + V_{mech} \quad (10.4)$$

Where,

V – Volume loss of material

In Equation (10.2), V_{chem} is the sum of alloy dissolution from both passive and active regions of the sample and can be thought of as C (pure corrosion) + C_w (wear enhanced corrosion). V_{mech} is the material loss through wear, and can be thought of as W (pure wear) + W_c (corrosion enhanced wear) Previous studies have characterised the degradation mechanism by the ratio of V_{chem}/V_{mech} (202, 206, 207). From the long-term measurements made in buffered serum solution, V_{chem}/V_{mech} was between 0.15 and 0.16, which is categorised as 'wear-corrosion'. If the V_{chem} is adjusted to include the additional contribution expected from 1 year (31.6M seconds) of static corrosion as opposed to just 1M seconds worth, then V_{chem}/V_{mech} increases to between 0.5 and 0.52. This is still in the 'wear-corrosion' regime (202, 206), but the amount of corrosion expected *in vivo* is still underestimated. It does not include the increased corrosion caused as a result of time dependent repassivation following brief periods of motion. It is feasible that during a testing procedure that represented the duration and frequency at which 1M steps are taken *in vivo,* the contribution of V_{chem} could become similar to V_{mech}, shifting the regime to one of 'corrosion-wear'. This would also distort the measurements of ion release from particles and depassivation. A more representative test would cause increased levels of metal ions, from both the additional corrosion of the surface and the longer exposure of particles to the serum.

10.2.2 Effect of Lubricant Composition

Two different lubricant compositions were used. The first comprised of 25% v/v bovine serum and distilled water, whilst the second was diluted to 18mg/l total protein concentration (approximately 33% v/v) with phosphate buffered saline (PBS). The choice of lubricant, for simulator testing, is not a simple decision, as a number of competing factors must be considered.

Ideally, the lubricant should behave as closely as possible to that found *in vivo*, in terms of both rheology and electrochemical properties. However, it is also important to be able to compare results with those already obtained in different laboratories and international standardisation should be as realistic as possible. Finally, practicality, in terms of cost and availability of certain fluids, can limit their use for *in vitro* studies.

Although 25% bovine serum diluted with distilled water is less physiologically relevant, in terms of osmolality, than bovine serum diluted to 17g/l with PBS (117), it has been used in many studies of MoM components (13, 98, 106, 111, 112, 150, 151, 177). This enables reasonable comparisons to be made with other studies. However, another factor to consider is the wide variability in the protein concentration of different types of bovine serum.

In the hip simulator, the differences between the un-buffered lubricant used in the Procedure 1 and the buffered lubricant in Procedure 3 produced some clear differences in the measured corrosion damage. The increased osmolality of the serum diluted with PBS resulted in a greater shift in OCP at the onset of motion (-303mV as opposed to -253mV), and a greater increase in corrosion current (≈7-8μA as opposed to 0.5-4μA).

Another difference observed between the two serum solutions used, was the unsteady nature of the current and potential when tested in the PBS containing lubricant. Rapid ennoblement of potential and simultaneous reductions in current were observed within the first few hundred thousand seconds, but were short-lived, as depassivation again followed. This did not occur for the tests conducted in serum that had been diluted with deionised water (Procedure 1), and partial repassivation did not usually occur until around 400,000 cycles (4d 15h 7m). The surface then appeared to remain in a state of partial repassivation for the remainder of the test.

These differences, observed between the two different procedures, may be attributed to five separate influences.

- The effect of protein concentration on corrosion.
- The effect of phosphate/chloride concentration on corrosion.
- The effect of different protein concentration on wear.
- The effect of increased phosphate ion concentration on wear
- The influences of phosphates and proteins on each other (synergy between the two).

The bovine serum used for the experiments discussed in this thesis contained 30g/l of serum albumin and 14,3g/l of serum globulins The addition of bovine serum albumin (BSA) to PBS has been shown to affect both the corrosion current and the OCP of CoCr alloys (42, 208, 209). The addition of the protein causes the OCP to shift in the negative direction. This has been explained by adsorption of albumin to the metal surface, which blocks the active sites available for oxygen reduction and reduces the cathodic current. However, it simultaneously increases the dissolution of the alloy, acting as an anodic catalyser (42, 208). Karimi *et al* (208) investigated the effect of BSA concentration on the OCP and corrosion current of CoCr. Upon increasing the concentration of BSA it was found that the OCP shifted negatively, but this effect reached a plateau at 4g/l. This was explained by the increased coverage of the adhered protein film blocking oxygen from reaching the surface. The effect on corrosion current was less clear. Corrosion current was determined by both electrical impedance spectroscopy and linear polarisation resistance. It was found that although the initial addition of BSA increased the corrosion current, there was no clear relationship between concentration and corrosion current. This is possibly attributable to competition between the diffusion barrier and increased anodic dissolution caused by the protein. Furthermore, it was also shown by Karimi *et al* (210) that the weight loss caused by the corrosion of CoCr alloys

was largely independent of albumin concentration between the range of 1-4g/l. The albumin concentration in this investigation was varied between 7.5g/l and 10g/l. The remaining protein concentration was made up by alpha- beta- and gamma-globulin.

By diluting serum with PBS solution as opposed to distilled water, the electrolytic properties of the lubricant were varied considerably. The increased concentration of dissolved ions causes an increase in osmolality of the solution (117). Osmolality is a measure of the direct ionic strength of the solution, and is roughly 6 times greater for PBS than distilled water. In addition, the increased concentration of phosphate and chloride ions has been shown to influence the corrosion rate of CoCr.

It has been shown that the presence of phosphate ions can inhibit the anodic dissolution of CoCr in an aqueous environment. However, this effect is inhibited by the presence of albumin, due to competitive adsorption on the material surface (42). It is well known that the presence of chlorides enhance pitting corrosion for many metals in aqueous conditions. Hoar and Mears (211) demonstrated that the current density of CoCr exposed to a physiologically representative salt and pH solution (known as Hank's solution) was increased upon increasing chloride concentration.

Proteins influence the tribological interactions between opposing surfaces in a number of ways. The presence of serum proteins can reduce the friction and wear between CoCr surfaces due to their boundary lubricating properties (128, 129, 134). Proteins also effect the tribological interaction of the opposing surfaces by forming adhered layers on the surfaces. These have been identified on both explants, and following *in vitro* testing (46, 87, 100-102, 106, 133). In addition, the presence of proteins has been found to increase the surface separation by a lubricant, resulting in a superior lubricating film when compared to more viscous solutions devoid of proteins (81, 135). The known influence of proteins on wear and lubrication, could suggest that their presence would result in a decrease in wear-induced depassivation and hence is the total measured corrosion response. During sliding, it has been shown that by increasing the serum concentration from 25% to 50%, the total wear rate can be reduced (44, 166). This was also found to occur when increasing albumin concentrations from 10g/l to 30g/l (212). Sun (44, 166) further demonstrated that, under abrasive wear, the increased protein concentration served to increase the total material degradation rate. However, the proportion of degradation attributable to

wear-enhanced corrosion was reduced. This resulted in a reduction in the measured corrosion current, in 50% serum when compared to 25%.

Because of the competitive adsorption that exists between phosphate ions and albumin (42), it is feasible that they could affect the formation of a biofilm on the bearing surface. It was shown that the organic layer formed on CoCr in the presence of albumin was thinner when phosphates were present. This may limit the lubricating properties of protein, which could result in a greater amount of wear-enhanced corrosion.

These competing factors may explain the differences observed between the results obtained for the two different serum solutions used (in Procedures 1 and 2). The greater protein concentration may explain how ennoblement of OCP occurred quicker. However, the interactive effects of phosphate ions could explain why this was short lived. Overall current densities were greater in the solution containing phosphates and an increased protein concentration (Procedure 3). This suggests that the improved lubrication afforded by the increased serum concentration was offset by the increased osmolarity of the solution caused by dilution with PBS.

In order to accurately reproduce the level of corrosion related damage produced *in vivo,* careful consideration must be exercised when selecting the lubricant used. As shown in this study, by replacing distilled water with PBS solution and slightly varying the protein concentration, vast changes in the corrosion current, and hence total damage, can be obtained. Hence, using currently accepted lubricant solutions (such as 25% bovine serum diluted with distilled water), the level of corrosion related damage can be grossly under represented, which results in an underestimation of the degradation as a whole.

10.3 Cyclic Depassivation Severity Factor

10.3.1 Introduction

It was shown in sections 8.2 and 8.3.3 that the potentiostatic current varied cyclically over a single gait cycle, and that the operational gait parameters influence both its shape and magnitude. The positions of maxima and minima in current were identified each cycle between 0.1-0.2s and 0.75-0.9s respectively. To explain these observations a mechanism for the generation of corrosion current over a single cycle is proposed.

10.3.2 Tribo-Corrosion Mechanism

It is proposed that the potentiostatic current produced is proportional to the instantaneous rate of passive film removal, due to increased charge transfer from the exposed alloy. This is determined by both the severity of mechanical, asperity contact between the opposing surfaces, and the relative sliding velocity between them. The applied load and the gait frequency/range govern this. However the relationship is complex owing to the presence of the EHL film generated in the interface.

In dry contact conditions, the contact between a loaded ball and cup can be thought of either in terms of real or apparent contact area. For an ideal elastic-plastic material the real contact area is the area over which the applied load is just supported elastically without further plastic deformation (see Equation (10.5))(10.2). This gives a real contact area that is proportional to the applied load.

$$w = p_0 a \tag{10.5}$$

Where,

w – Load

p_0 – Yield pressure

a – Real contact area

An EHL film reduces the real contact area by supporting a proportion of the load, by hydrodynamic action, reflected by the lambda ratio (Equation (2.7)). Determining the change in real contact area as a function of minimum EHL film thickness is not a trivial undertaking and beyond the scope of this study. For simplicity the degree of contact is assumed to be related to the lambda ratio and hence the minimum EHL film thickness. For a given degree of contact in mixed lubrication during the dynamic conditions encountered in each cycle, the severity of asperity contact is considered to be related to the applied load, the rate of passive film removal and the absolute sliding velocity of the joint.

By considering these points it is possible to produce a simple model to estimate the variation of the corrosion current over a single cycle, referred to as the severity factor. As an initial approach the severity factor as been defined in Equation (10.6).

$$I \propto \frac{w\Omega}{h_{min}} \tag{10.6}$$

Where,

I – Current generated by indentation/abrasion

w – Load

Ω – Angular velocity

h_{min} – Minimum elastohydrodynamic film thickness

The variation of the severity factor over a single cycle is shown in Figure 10.8.

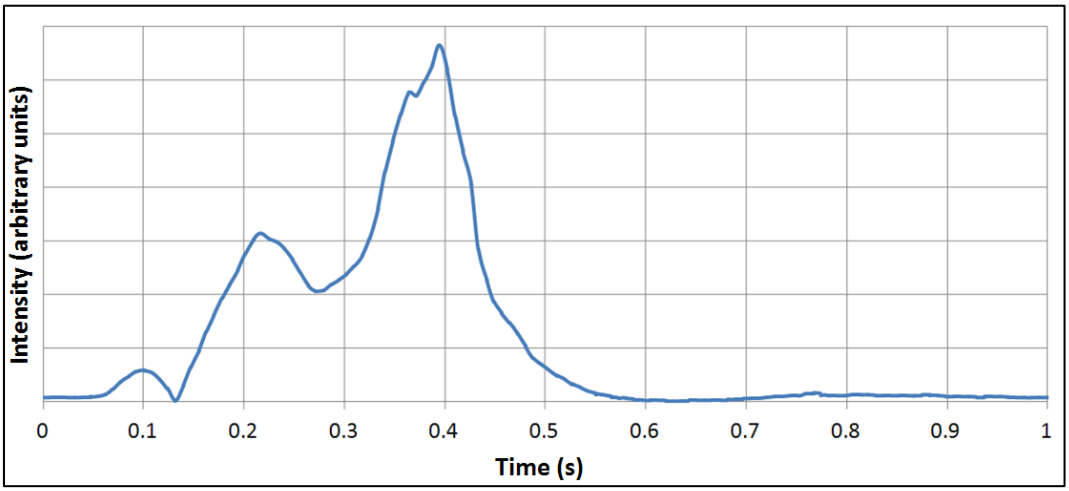

Figure 10.8: Variation of severity factor over a single cycle.

From Figure 10.8 it can be seen that there are three major peaks in depassivation severity, of different magnitudes, that occur at during each cycle. One peak at approximately 0.1s another at 0.2s and the third one at about 0.4s. From 0.6s onwards the severity factor drops to very small values. This reflects the comparatively low, and reasonably uniform, swing phase load. In this region the current would be expected to decay exponentially as previously discussed. This can be approximated by incorporating the repassivation model presented by Sun *et al* (67) (Equation (10.2)) for CoCr in 25% bovine serum solution, with a time constant of 180ms. The current decay has been included from the apex of the major peak (approximately 0.4s) to the start of the initial peak the cycle lasting about 1.1s (Shown in Figure 10.9).

Figure 10.10 shows the severity factor plotted on the same axis as the potentiostatic current responses already shown in Figures 8.48, and Figure 10.11 shows the severity factor combined with the repassivation current decay effect on the same axis as the current response. The current response bares some similarity to both the severity factor and the modified severity factor. Both contain two peaks per cycle and drop to a minimum within the swing phase. In particular, the modified severity factor most closely resembles the current response. However, there appears to be some

lag between the peaks and the current response, by approximately 0.2s. The initial peak in current at about 0.1s occurs almost simultaneously with the small peak in severity factor, although the reasons for this are not clear.

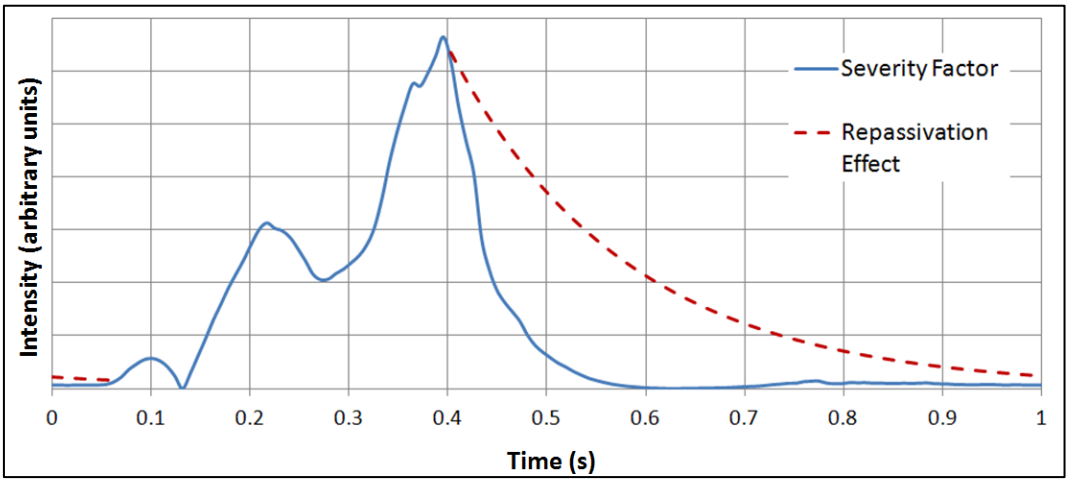

Figure 10.9: Variation of severity factor including the effects of repassivation.

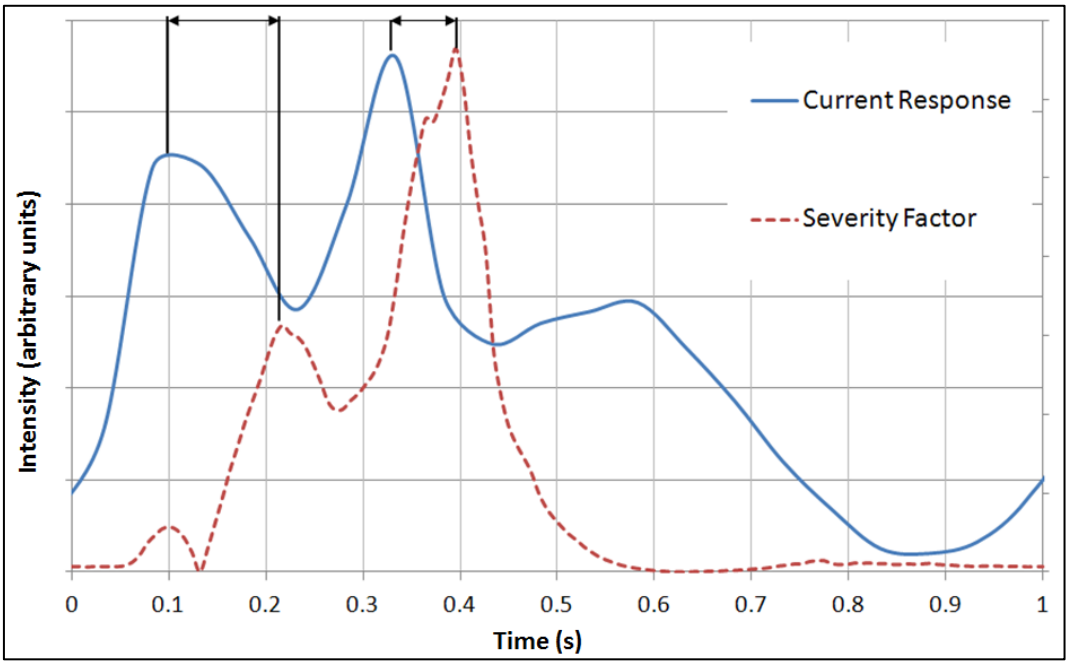

Figure 10.10: Severity factor and current response at approximately 400,000 cycles (4d 15h 7m).

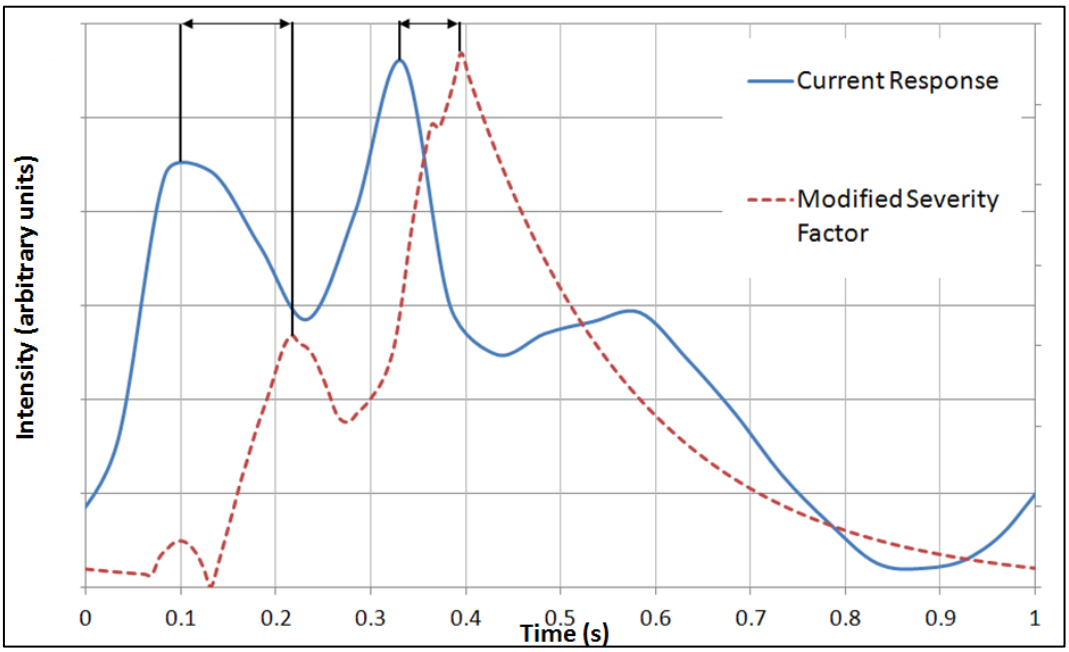

Figure 10.11: Modified severity factor and current response at approximately 500,000 cycles (5d 18h 53m).

Throughout the long-term tests the exact shape of the potentiostatic current responses changed. The exact reasons for this are not clear, but may be associated with progressive changes to the bearing surface caused by material transfer. Figure 10.11 shows the modified severity factor plotted against a current response measured later in the test. In this instance the current response has 3 clear peaks, which have been matched with the pre-peak, and the two major peaks of the severity factor. Although the relative magnitudes of the current peaks do not reflect the relative magnitudes of the severity factor, it produces a better fit than that shown in Figure 10.12. This is because the current slightly lags the severity factor, which can be justified by reaction kinetics.

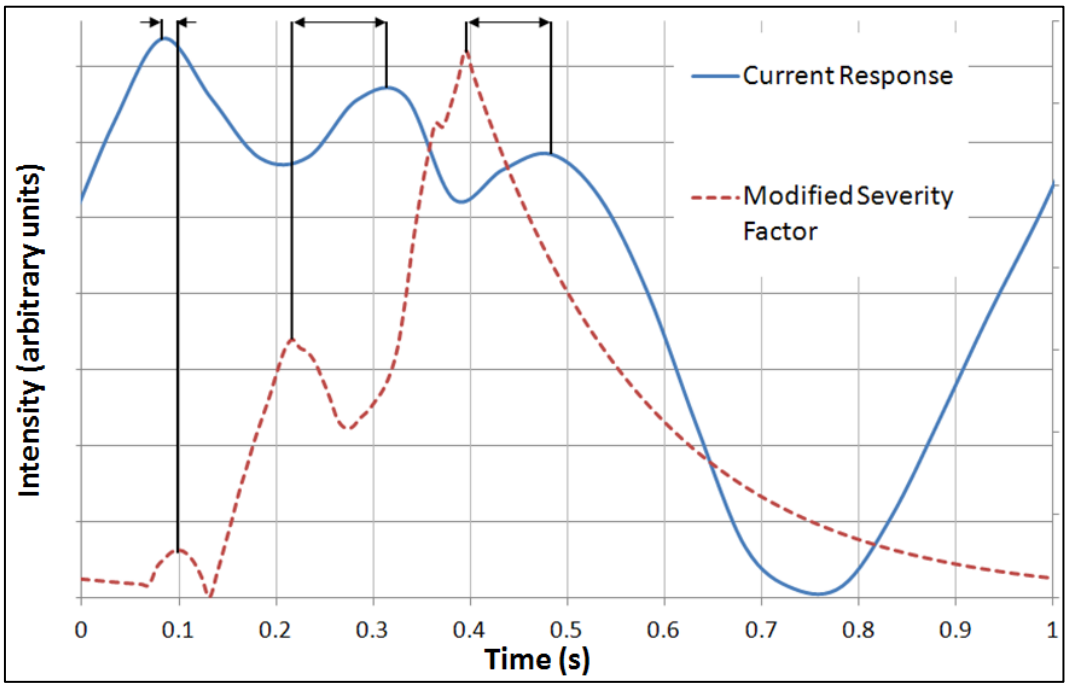

Figure 10.12: Modified severity factor and current response 2.

There are clearly differences between the shape of the severity factor and the measured current response. This may result from a number of factors.

- The system has been modeled around the initial bearing surface. However, the bearing surface changes rapidly, and continues to do so for the duration of the experiment.

- Debris is also generated, as discussed in 2.4.6. The debris size can easily exceed the minimum EHL film thickness. This can influence the mechanism of depassivation, and may either reduce it if the debris acts as mildly loaded rolling element bearings, or increase it by producing points of increased pressure and asperity interaction

- In addition, the film was considered to be Newtonian. This is a reasonable assumption for the bulk solution under the high shear rates encountered in the joint, but there may be issues with this when proteins precipitate from the solution, or adsorb on to the bearing surfaces. As discussed in 2.4.8, under some conditions proteins can form a gel-like layer at the bearing surface (120, 127, 132, 133). This layer may separate the surfaces at periods in which the EHL film is

thin, such as these at low entrainment velocities and high loads. Figures 10.13 and 10.14 highlight the differences between the theoretical system used to develop the lubrication model and the actual system encountered at the bearing interface.

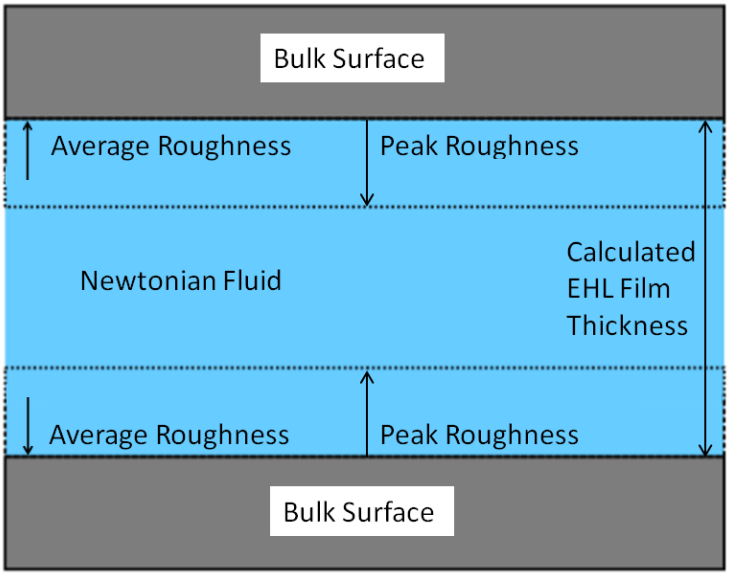

Figure 10.13: Theoretical model of lubrication within the bearing surface.

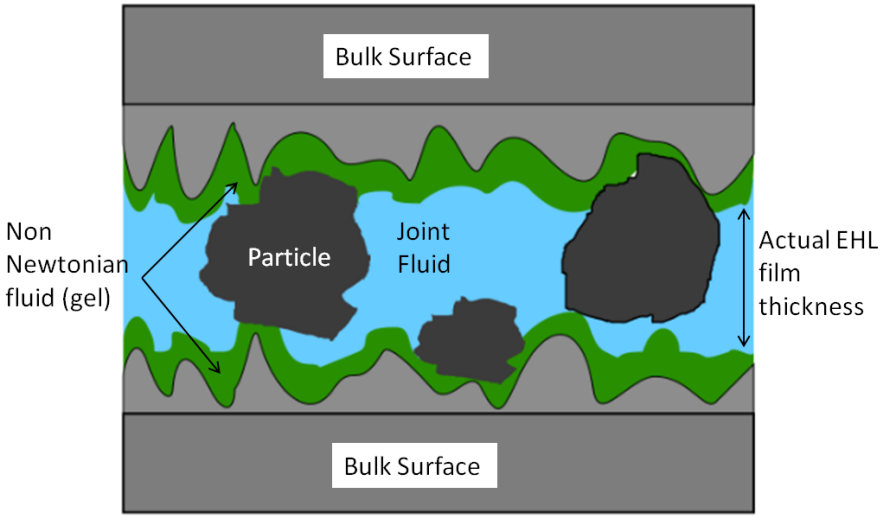

Figure 10.14: Representation of the lubrication when proteins and particles are present on the real bearing surfaces.

- Furthermore, the formation of a tribochemical reaction layer would serve to increase the complexity of the wear and lubrication reactions within the joint. This is discussed in more detail in section 10.4.

10.4 Tribofilm Formation and Importance

Formation of the tribofilm shown in 9.3 can have significant effects on the degradation of MoM hip prostheses. It was shown in both sections 8.1.2 and 8.3.2 that over extended periods of motion, within 1 million cycles, there was a spontaneous reduction in the corrosion current within the joint. This is shown in Figures 8.9-8.11 (from Procedure 1) and Figures 8.40-8.42 (from Procedure 3). The potentiostatic current traces shown in 8.3.3 indicate that upon reduction of the corrosion current, there was a disruption to the periodic current signal produced by the gait cycle. This must reflect that the surface depassivation/repassivation equilibrium was interrupted. Observations of running-in made by previous authors (14, 80, 83, 90, 93-96) would appear to confirm the observation that running-in is generally reflected in an increase in lambda ratio, caused by simultaneous smoothing of the surfaces and the increase in conformity, which facilities a shift to fluid film lubrication (20, 62, 92, 98). This could explain the electrochemical observations made, however, surface analysis of the bearing surfaces does not support it. It was shown in section 8.4 that, although the surfaces did increase in conformity, they also increased in roughness. By comparing the effects of increased roughness and increased conformity, it was shown in section 8.5 that there was an overall reduction in lambda ratio, caused by an increase in roughness of the underlying bearing alloy surfaces. This points towards the separation of the surfaces by a tribological film, rather than separation by the bulk lubricant.

The tribological layer, identified in Chapter 9, was found to exist mostly outside the wear scar (Figure 9.9). This may suggest that it does not participate substantially to the joint lubrication process. However, by considering the mechanism of growth of the wear scar, this can be shown to be incorrect. Figure 10.15 represents a top view of the wear scar and the location of the tribofilm. When wear proceeds, the wear scar grows

outwards, increasing in diameter. Figure 10.16 shows a side view of the worn femoral head. It is shown that the border between the wear scar and the unworn surface forms a wedge. This is due to the difference in radii inside and outside of the wear scar. For wear to proceed, this wedge must advance into the unworn region. However, the location of the densest regions of the tribofilm are at the border of wear scar and the unworn region of the head. Images taken of the tribofilm (see Chapter 9) show it is in excess of 700nm thick in places. This is substantially greater than either the maximum worn surface roughness (<70nm), or the maximum EHL film thickness (<65nm). Due to the thick coating it provides on the surface, and its ability to engulf wear debris, it appears to act as a solid lubricant or a grease. The idea of tribologically formed layers acting as solid lubricants has previously been proposed by Liao *et al* (100).

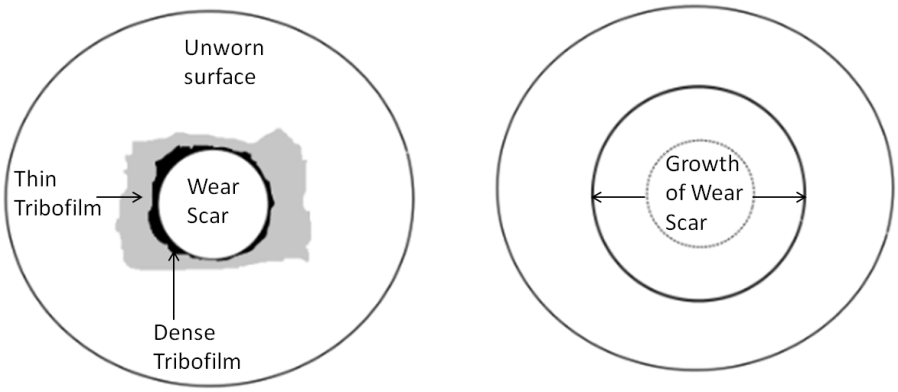

Figure 10.15: Location of tribofilm and growth of the wear scar.

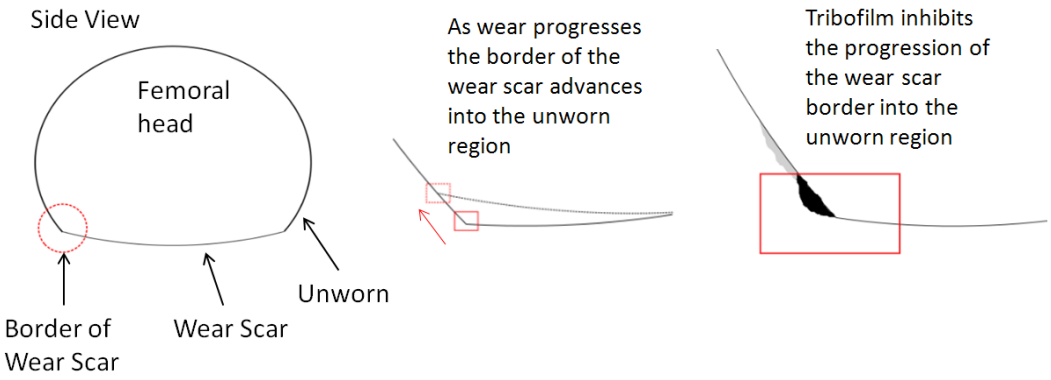

Figure 10.16: Diagram illustrating inhibition of wear by the tribofilm.

The model of lubrication proposed by Liao *et al* (100) proposes that the carbon-rich tribologically formed layer, on the surfaces of the bearing, is partially graphitised, forming nano-crystalline graphite. It was suggested that the lubricating properties of this layer are derived from the favorable lubricating properties of graphite in aqueous environments. The mechanism for graphitisation was not fully recognised. However, it was mentioned that high shear, elevated temperature and cobalt catalysis may be contributing factors.

Typically, graphitisation of amorphous carbon takes place between 2500-3000^{0}C (140, 141). It has been shown that this can be reduced by the presence of certain transition metals, such as cobalt, or by exposure to high shear rates (140, 141, 213, 214). Two mechanisms have been proposed for the catalysis of graphitisation by transition metals (214). The first relies on the metal acting as a solvent for carbon. Amorphous carbon is dissolved in a metallic melt. In this mechanism, graphite is formed by crystallisation from the melt upon cooling. The second is caused by the decomposition of carbides. Carbides decompose to produce metal and graphite (140). It has been suggested that both of these mechanisms may occur in tandem (214).

Decomposition of cobalt carbides has been shown to occur above 500^{0}C (213, 215). This is considerably greater than temperatures in the joint capsule. Frictional heating in MoP and CoP contact caused the bulk lubricant to increase to ≈43^{0}C (216). Even flash temperatures resulting from asperity/asperity contact are much lower than the temperatures required to decompose carbides. Using the Kuhlman-Wilsdorf approach (217, 218), the maximum flash temperatures were calculated for asperity interaction expected between metal-metal and carbide-carbide contacts in total hip replacements (87, 102) For opposing metal asperities, the flash temperature rise was only ≈5K. For opposing carbide contacts, it was considerably greater, rising to ≈34K. However, both of these temperature elevations are too low to promote the decomposition of metal carbides.

The action of shear has been shown to reduce the level at which graphitisation takes place (219). It was shown that graphitisation of anthracite could take place at 900^{0}C, with structural changes beginning at 700^{0}C, under the action of shear. At a pressure of 1GPa, and shear rates between 10^5-10^6s^{-1}, graphitisation was promoted by enhanced alignment of the basal structural units. For comparison, the shear rate of the EHL film over a single cycle in the hip simulator is shown in Figure 10.17. This was

calculated using Equation (10.2). Although the shear rate of the EHL film is great enough to enhance graphitisation of anthracite, the temperature required for graphitisation under these conditions is considerably greater than that found within the joint.

$$\tau = \frac{v}{h_{min}} \tag{10.7}$$

Where,

τ – Shear rate

v – Linear sliding velocity

h_{min} – Minimum elastohydrodynamic film thickness

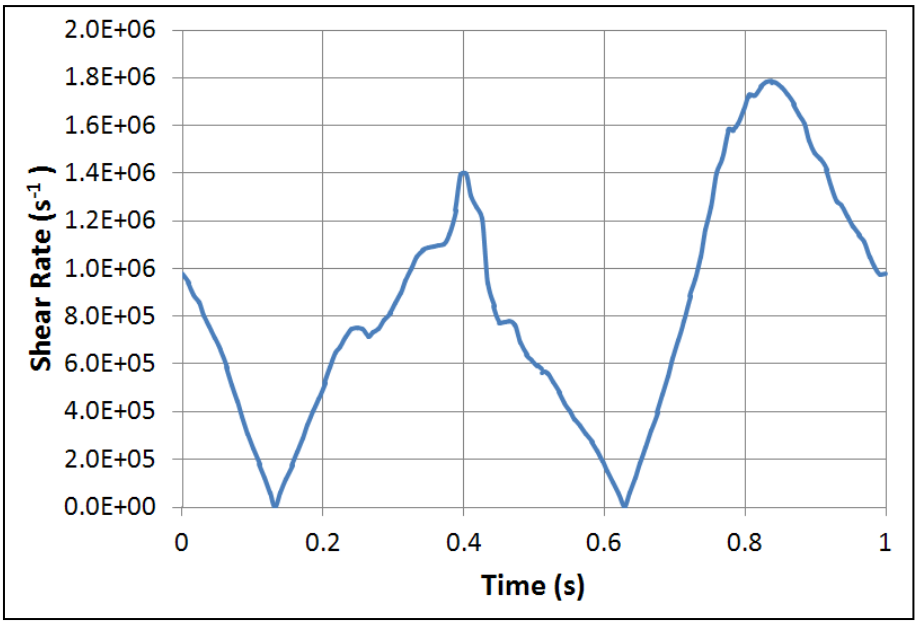

Figure 10.17: Shear rate of the EHL film over a single cycle.

Graphitisation was not observed within any of the tribolayers investigated in this study. In addition, possible mechanisms put forth by Liao *et al* (100) appear to require greater temperatures than can possibly be achieved within the bearing interface. Nevertheless, evidence for graphitisation was observed by Liao *et al*, and a lack of understanding of the mechanism may only highlight the specific conditions required for its formation. However, an

issue remains about its function as a lubricant. The lubricating properties of graphite arises from its layered graphene sheets, either by roll-up or shear of them in aqueous or atmospheric conditions (143, 220). In nano-crystalline graphite, these sheets are not present, as it does not contain long ranged ordering (221). This is shown in Figure 10.18.

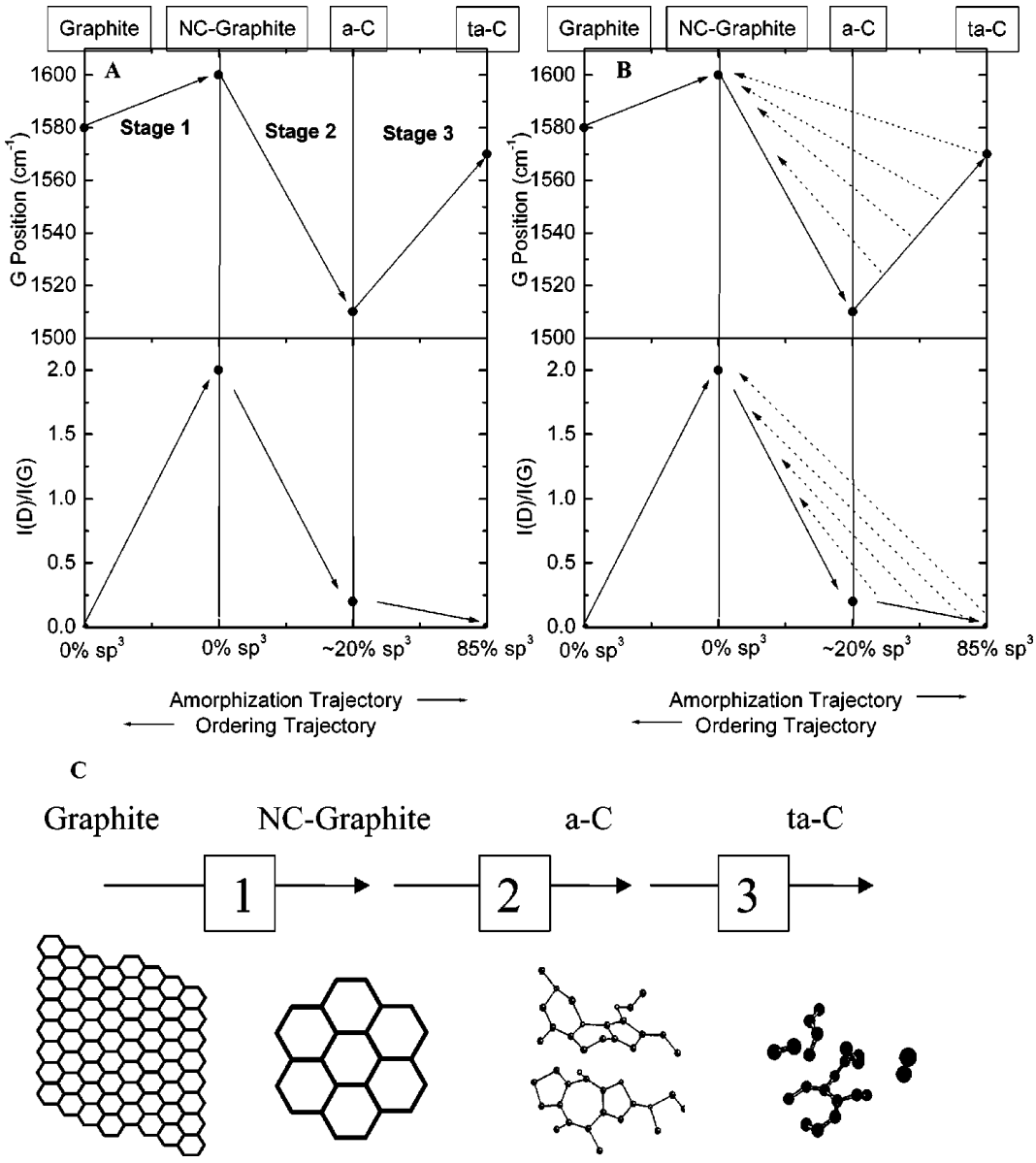

Figure 10.18: 'Three-stage model of the variation of the Raman *G* position and the *D* to *G* intensity ratio *I*(*D*)/*I*(*G*) with increasing disorder. The dotted left pointing arrows in (B) mark the non-uniqueness region in the ordering trajectory. (C) Shows the variation of the sp^2 configuration in the three amorphisation stages.' (221)

The location at which the tribofilm forms is defined by a sharp border. This may be explained by the contact mechanics at the border of the wear scar. As previously discussed, the head and cup wear together and the surfaces become more conformal within the wear scar. Conformal changes manifest themselves as an increase in effective local radius on the femoral head and a decrease in radius on the acetabular cup. This theoretically produces a very slight wedge at the border between unworn surface and the wear scar, which can be seen when the scales are greatly exaggerated (Figure 10.19).

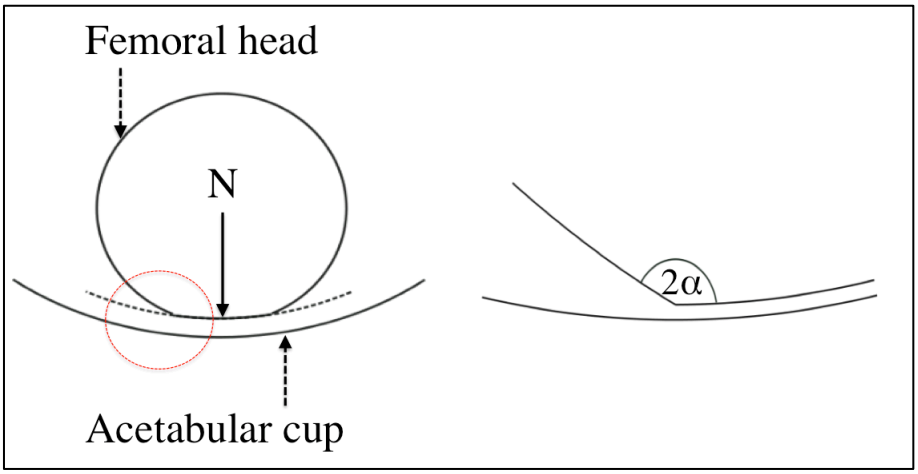

Figure 10.19: Wedge formation at edge of wear scar.

The angle alpha is close to 90^0 since the changes in radii are small, relative to the initial radius. However, it is not negligible and increases as a function of the half-width of the wear scar (a), shown in Figure 10.20. As the wear progresses, the radii of the head and cup tend to converge to a value midway between the two. The effect of wear scar half width on wedge angle (α) can be estimated. The change in (cot α) with respect to wear scar half width is shown in Figure 10.20.

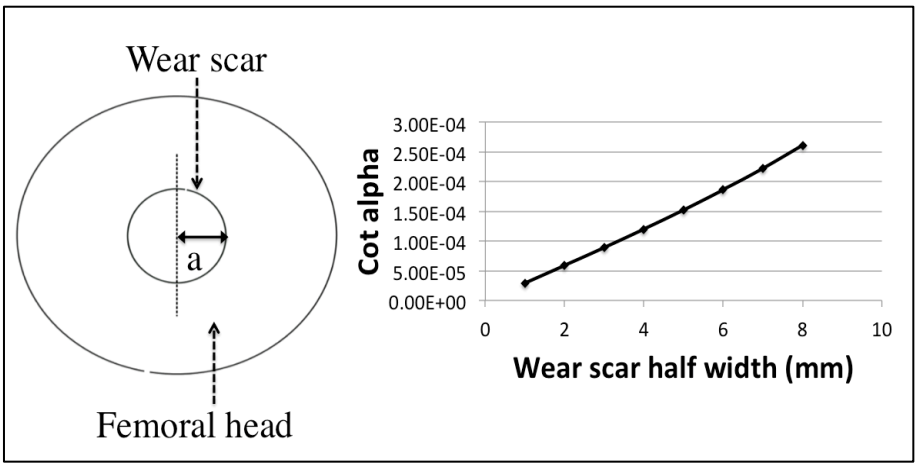

Figure 10.20: Effect of wear scar half width on wedge tip.

Johnson (222) has described the contact between a blunt-shaped wedge and a semi infinite elastic solid as depicted in Figure 10.21. The pressure distribution is represented by Equation 1, when α is close to 90^0 (222).

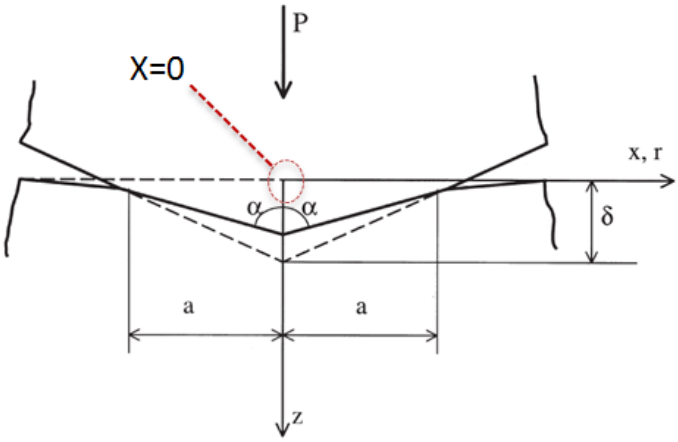

Figure 10.21: Contact of blunt wedge (222).

$$p(x) = \frac{E' \cot \alpha}{\pi cosh^{-1}\left(\frac{a}{x}\right)} \quad and \; P = \alpha E' \cot \alpha \text{ (222)} \tag{10.8}$$

Where,

E' – Effective elastic modulus

From Equation (10.2) and Figure 10.21, it can be seen then that, under dry conditions, the pressure rises to ∞ at x=0. By considering the presence of a blunt wedge on a worn femoral head, it is evident that there exists a region of increased pressure, at the border of the wear scar. It is this predicted region of very high pressure, which is where the thickest tribolayer formation occurs. The scraping action of the blunt wedge may serve to accumulate debris at its tip, or the increased contact pressure, and associated flash temperature it causes, may contribute to the formation of the tribofilm at this location. As the wear scar increases in diameter the wedge becomes more defined and the contact pressure increases.

Chapter 11 Conclusions and Future Work

11.1 Conclusions

The study reported in this thesis represents the first known simultaneous investigation of the tribology and corrosion governing important features of metal-on-metal hip joint replacement performance. Novel and significant findings are reported.

- Simulator measurements of tribocorrosion in a metal-on-metal joint.
- Mechanical wear loss.
- Corrosion current
- Elastohydrodynamic solutions for the specific conditions of simulator testing.
- The initial steps towards the development of a ‘severity factor’ which reflects current flow in a complete cycle of loading and motion have been achieved.

A number of concepts are presented regarding the tribocorrosion of biomaterials in different simulated conditions. Where results have been summarised some concluding points have be noted. However, a number of more general points relating to the key findings of the study as a whole are listed below.

- In the tribometer, polymer sliding will affect both the open circuit potential and corrosion current of a cobalt chromium alloy counter body. Although this produced an increase in the release rate of metal ions into the surrounding solution, when compared to MoM systems, the effect was trivial.

- For MoM systems, the corrosion current produced in the tribometer was influenced by the applied load. Larger loads resulted in more severe depassivation, due to the increased contact severity.

- The relative contribution of wear and corrosion, to total material loss, are influenced by the geometry of the working electrode and the sliding interface. The ratio of the size of the wear scar to the total electrode area should be considered when comparing results from different systems.

- The tribological conditions produced in the tribometer were more severe than the hip simulator for comparable contact pressures. This caused more severe depassivation leading to an increased corrosion current density in the wear scar.

- The severity of the boundary lubrication developed in the tribometer, was mitigated by the lubricating properties of serum proteins. Despite increasing corrosion in static conditions, proteins reduced corrosion in dynamic conditions by protecting the surfaces from depassivation.

- In the hip simulator, the electrochemical response was influenced substantially by the serum solution used. When a solution more physiologically representative than 25% V/V bovine serum was used, the corrosion current was increased.

- The corrosion current measured in the hip simulator varied considerably over a single cycle. This was caused by the effect of sliding velocity and load on the EHL film thickness and depassivation mechanics.

- Metal ion release from MoM bearings can be attributed to both surface depassivation and particle dissolution almost equally. Particles appear to release ions rapidly upon formation. They then became passivated and their dissolution rate is reduced.

- Tribologically formed layers are produced on the bearing surfaces following periods of wear. These layers contribute to the reduction of

wear and corrosion over time by acting as an interposition between the opposing surfaces.

- The thickness of tribologically formed layers can greatly exceed the height of the surface roughness and the EHL film thickness, thereby supporting a portion of the applied load.

- Wear debris is trapped in tribologically formed layers. These particles are subjected to mechanical abrasion and chemical oxidation, which produces smaller, smoother, cobalt sulphide ellipsoidal particles.

- Current hip simulator test protocols need to be revised for tribocorrosion systems in order to reflect more accurately the contribution of corrosion towards metal bearing degradation. Present methods are liable to under represent the influence of corrosion.

11.2 Future Work

There are many avenues of investigation which would build on the concepts developed in this thesis. A number of further investigations that could produce worthwhile information regarding the tribocorrosion of THRs are identified.

- Study the effect of bearing diameter on the tribocorrosion of either MoM or CoM systems.

- Large diameter bearings demonstrate favorable tribological properties due to increased EHL film thickness, however, larger bearing diameters produce an increased working electrode area with a larger wear scar. These two conflicting influences make it difficult to predict the performance of larger/smaller diameter bearings, and this challenge could be investigated.

- Study the tribocorrosion performance of bearings beyond the ‘running in’ phase could provide useful information relating to the long-term performance of metal-on-metal hip surfaces. Reductions in corrosion were observed which coincide with running in, however, tests were not continued past 1 million cycles. Analysis of the general corrosion current as well as its cyclic variability past 1 million cycles would provide information on the long term performance or hip joint bearings.

- Investigate the exact causes of cyclic current variation produced at the bearing interface. Combine EHL modelling with experimental measurements of cyclic corrosion current, to develop a complete model for cyclic depassivation could be obtained.

- Further investigation of the role of tribological formed layers should be undertaken. Study further the mechanisms leading to the formation of tribological films are still not fully understood. Information relating to their formation, and function, in the mitigation of corrosion and wear, could provide insights valuable for the development of new hip bearings.

- Investigation of multiple tribological interfaces that are electrochemically linked. Within a total hip replacement there are a number of interfaces that may become depassivated such as, the bearing, neck and stem. *In vivo* these interfaces are electrochemically linked and my drive or suppress corrosion on one another. Studying them together is paramount in understanding the system as a whole.

References

1. RegistryforEnglandandWales T. The National Joint Registry for England and Wales 9th Annual Report2012.

2. Birrell F, Johnell O, Silman A. Projecting the need for hip replacement over the next three decades: influence of changing demography and threshold for surgery. 1999.

3. Dixon T, Shaw M, Ebrahim S, Dieppe P. Trends in hip and knee joint replacement: socioeconomic inequalities and projections of need. Annals of the Rheumatic Diseases. 2004 July 2004;63(7):825-30.

4. Culliford DJ, Maskell J, Beard DJ, Murray DW, Price AJ, Arden NK. Temporal trends in hip and knee replacement in the United Kingdom: 1991 TO 2006. J Bone Joint Surg Br. January 1, 2010;92-B(1):130-5.

5. Meier B. As the use of metal-on-metal implants grows, studies raise concerns. The New York Times. 4//3/2010 ed2010.

6. Meier B. Concerns Over 'Metal on Metal' Hip Implants. The New York Times. 2010.

7. Savarino L, Granchi D, Ciapetti G, Cenni E, Greco M, Rotini R, et al. Ion release in stable hip arthroplasties using metal-on-metal articulating surfaces: A comparison between short- and medium-term results. Journal of Biomedical Materials Research Part A. 2003;66A(3):450-6.

8. Savarino L, Granchi D, Ciapetti G, Cenni E, Nardi Pantoli A, Rotini R, et al. Ion release in patients with metal-on-metal hip bearings in total joint replacement: A comparison with metal-on-polyethylene bearings. Journal of Biomedical Materials Research. 2002;63(5):467-74.

9. Weber BG. Total hip replacement: rotating versus fixed and metal versus ceramic heads. The Hip. 1981:264-75.

10. Dowson D. New joints for the Millennium: wear control in total replacement hip joints. Proceedings of the Institution of Mechanical Engineers, Part H: Journal of Engineering in Medicine. 2001;215(4):335-58.

11. Oral E, Godleski Beckos C, Malhi AS, Muratoglu OK. The effects of high dose irradiation on the cross-linking of vitamin E-blended ultrahigh molecular weight polyethylene. Biomaterials. 2008;29(26):3557-60.

12. Oral E, Christensen SD, Malhi AS, Wannomae KK, Muratoglu OK. Wear Resistance and Mechanical Properties of Highly Cross-linked, Ultrahigh Molecular Weight Polyethylene Doped With Vitamin E. The Journal of Arthroplasty. 2006;21(4):580-91.

13. Tipper JL, Firkins PJ, Besong AA, Barbour PSM, Nevelos J, Stone MH, et al. Characterisation of wear debris from UHMWPE on zirconia ceramic, metal-on-metal and alumina ceramic-on-ceramic hip prostheses generated in a physiological anatomical hip joint simulator. Wear. 2001;250(1-12):120-8.

14. Willert HG, Bertram H, Buchhorn GH. Osteolysis in alloarthroplasty of the hip. The role of ultra-high molecular weight polyethylene wear particles. Clinical orthopaedics and related research. 1990 (258):95-107.

15. Ingham E, Fisher J. The role of macrophages in osteolysis of total joint replacement. Biomaterials. 2005;26(11):1271-86.

16. Mevoy A, Jeyam M, Ferrier G, Evans CE, Andrew JG. Synergistic effect of particles and cyclic pressure on cytokine production in human monocyte/macrophages: proposed role in periprosthetic osteolysis. Bone. 2002;30(1):171-7.

17. Shetty VD, Villar RN. Development and problems of metal-on-metal hip arthroplasty. Proceedings of the Institution of Mechanical Engineers, Part H (Journal of Engineering in Medicine). 2006;220(H2):371-7.

18. Cooper RA, McAllister CM, Borden LS, Bauer TW. Polyethylene debris-induced osteolysis and loosening in uncemented total hip arthroplasty: A cause of late failure. The Journal of Arthroplasty. 1992;7(3):285-90.

19. Kadoya Y, Revell PA, Kobayashi A, Al-Saffar N, Scott G, Freeman MAR. Wear Particulate Species and Bone Loss in Failed Total Joint Arthroplasties. Clinical orthopaedics and related research. 1997;340:118-29.

20. Rieker C, Konrad R, Schon R, editors. In vitro comparison of the two hard-hard articulations for total hip replacements2001: Professional Engineering Publishing Ltd.

21. Roualdes O, Duclos M-E, Gutknecht D, Frappart L, Chevalier J, Hartmann DJ. In vitro and in vivo evaluation of an alumina-zirconia composite for arthroplasty applications. Biomaterials. 2010;In Press, Corrected Proof.

22. Vassiliou K, Scholes SC, Unsworth A. Laboratory studies on the tribology of hard bearing hip prostheses: ceramic on ceramic and metal on metal. Proceedings of the Institution of Mechanical Engineers, Part H (Journal of Engineering in Medicine). 2007;221(H1):11-20.

23. Tipper JL, Hatton A, Nevelos JE, Ingham E, Doyle C, Streicher R, et al. Alumina-alumina artificial hip joints. Part II: Characterisation of the wear debris from in vitro hip joint simulations. Biomaterials. 2002;23(16):3441-8.

24. Kumar P, Oka M, Ikeuchi K, Shimizu K, Yamamuro T, Okumura H, et al. Low wear rate of UHMWPE against zirconia ceramic (Y-PSZ) in comparison to alumina ceramic and SUS 316L alloy. Journal of Biomedical Materials Research. 1991;25(7):813-28.

25. Costa HL, Pandolfelli VC, de Mello JDB. On the abrasive wear of zirconias. Wear. 1997;203-204(0):626-36.

26. Spinelli M, Affatato S, Corvi A, Viceconti M. Ceramic-on-ceramic vs. metal-on-metal in total hip arthroplasty (THA): do 36-mm diameters exhibit comparable wear performance? Materialwissenschaft und Werkstofftechnik. 2009;40(1-2):94-7.

27. Yan Y, Neville A, Dowson D, Williams S. Tribocorrosion in implants--assessing high carbon and low carbon Co-Cr-Mo alloys by in situ electrochemical measurements. Tribology International. 2006;39(12):1509-17.

28. Varano R, Bobyn J, Medley J, Yue S. The effect of microstructure on the wear of cobalt-based alloys used in metal-on-metal hip implants. Proceedings of the Institution of Mechanical Engineers, Part H: Journal of Engineering in Medicine. 2006;220(2):145-59.

29. Agency MaHpR. Total hip replacement; All metal-on-metal (MoM) hip replacements (MDA/2012/008) 2012. http://www.mhra.gov.uk/Publications/Safetywarnings/MedicalDeviceAlerts/CON143782]. Available from: http://www.mhra.gov.uk/Publications/Safetywarnings/MedicalDeviceAlerts/CON143782.

30. M J Yaszemski DJT, K Lewandrowski, V Hasirci, D Altobelli, D L Wise. Biomaterials in Orthopedics: Marcel Dekkar, Inc; 2004.

31. Roberge PR, editor. Corrosion engineering principals and practices. 1st ed ed: The McGraw-Hil Companies, Inc.; 2008.

32. Goldberg JR, Gilbert JL. Electrochemical response of CoCrMo to high-speed fracture of its metal oxide using an electrochemical scratch test method. John Wiley & Sons, Inc.; 1997. p. 421-31.

33. Metikos-Hukovic M, Babic R. Passivation and corrosion behaviours of cobalt and cobalt-chromium-molybdenum alloy. Corrosion Science. 2007;49(9):3570-9.

34. Milosev I, Strehblow HH. The composition of the surface passive film formed on CoCrMo alloy in simulated physiological solution. Electrochimica Acta. 2003;48(19):2767-74.

35. Collier J, Surprenant V, Jensen R, Mayor M, Surprenant H. Corrosion between the components of modular femoral hip prostheses. Journal of Bone & Joint Surgery, British Volume. 1992 July 1, 1992;74-B(4):511-7.

36. Kop AM, Swarts E. Corrosion of a Hip Stem With a Modular Neck Taper Junction: A Retrieval Study of 16 Cases. The Journal of Arthroplasty. 2009;24(7):1019-23.

37. Mroczkowski ML, Hertzler JS, Humphrey SM, Johnson T, Blanchard CR. Effect of impact assembly on the fretting corrosion of modular hip tapers. Journal of Orthopaedic Research. 2006;24(2):271-9.

38. Oldfield JW, Sutton WH. Crevice Corrosion of Stainless Steels: II. Experimental studies. British Corrosion Journal. 1978;13(3):104-11.

39. Oldfield JW, Sutton WH. Crevice Corrosion of Stainless Steels: I. A Mathematical Model. British Corrosion Journal. 1978;13(1):13-22.

40. Oldfield JW, Sutton WH. New Technique for Predicting the Performance of Stainless Steels in Sea Water and other Chloride-containing Environments. British Corrosion Journal. 1980;15(1):31-4.

41. Clark GCF, Williams DF. The effects of proteins on metallic corrosion. Journal of Biomedical Materials Research. 1982;16(2):125-34.

42. Munoz AI, Mischler S. Interactive Effects of Albumin and Phosphate Ions on the Corrosion of CoCrMo Implant Alloy. Journal of The Electrochemical Society. 2007;154(10):C562-C70.

43. : Springer Science Business Media; 2007. Biomaterials an Introduction.

44. Sun D, Wharton JA, Wood RJK. Effects of proteins and pH on tribocorrosion performance of cast CoCrMo - a combined electrochemical and tribological study. Tribology - Materials, Surfaces & Interfaces. 2008;2(3):150-60.

45. Zhao J-C, Notis MR. Kinetics of the fcc to hcp phase transformation and the formation of martensite in pure cobalt. Scripta Metallurgica et Materialia. 1995;32(10):1671-6.

46. Büscher R, Täger G, Dudzinski W, Gleising B, Wimmer MA, Fischer A. Subsurface microstructure of metal-on-metal hip joints and its relationship to wear particle generation. Journal of Biomedical Materials Research. 2005;72B(1):206-14.

47. Huang P, Lopez HF. Athermal ε-martensite in a Co-Cr-Mo alloy: grain size effects. Materials Letters. 1999;39(4):249-53.

48. Remy L, Pineau A. Twinning and strain-induced f.c.c. - h.c.p. transformation on the mechanical properties of Co-Ni-Cr-Mo alloys. Materials Science and Engineering. 1976;26(1):123-32.

49. Remy L, Pineau A. Twinning and strain-induced F.C.C. - H.C.P. transformation in the Fe-Mn-Cr-C system. Materials Science and Engineering. 1977;28(1):99-107.

50. Huang P, López HF. Strain induced e-martensite in a Co-Cr-Mo alloy: grain size effects. Materials Letters. 1999;39(4):244-8.

51. Persson DHE, Coronel E, Jacobson S, Hogmark S. Surface analysis of laser cladded Stellite exposed to self-mated high load dry sliding. Wear. 2006;261(1):96-100.

52. Persson DHE, Jacobson S, Hogmark S. The influence of phase transformations and oxidation on the galling resistance and low friction behaviour of a laser processed Co-based alloy. Wear. 2003;254(11):1134-40.

53. Persson DHE, Jacobson S, Hogmark S. Effect of temperature on friction and galling of laser processed Norem 02 and Stellite 21. Wear. 2003;255(1):498-503.

54. Lhotka C, Szekeres T, Steffan I, Zhuber K, Zweymüller K. Four-year study of cobalt and chromium blood levels in patients managed with two different metal-on-metal total hip replacements. Journal of Orthopaedic Research. 2003;21(2):189-95.

55. Rasquinha VJ, Ranawat CS, Weiskopf J, Rodriguez JA, Skipor AK, Jacobs JJ. Serum Metal Levels and Bearing Surfaces in Total Hip Arthroplasty. The Journal of Arthroplasty. 2006;21(6, Supplement 1):47-52.

56. De Smet K, De Haan R, Calistri A, Campbell PA, Ebramzadeh E, Pattyn C, et al. Metal ion measurement as a diagnostic tool to identify problems with metal-on-metal hip resurfacing. The Journal of bone and joint surgery American volume. 2008;90 Suppl 4:202-8.

57. Huber M, Reinisch G, Trettenhahn G, Zweymüller K, Lintner F. Presence of corrosion products and hypersensitivity-associated reactions in periprosthetic tissue after aseptic loosening of total hip replacements with metal bearing surfaces. Acta Biomaterialia. 2009;5(1):172-80.

58. Case C, Langkamer V, James C, Palmer M, Kemp A, Heap P, et al. Widespread dissemination of metal debris from implants. J Bone Joint Surg Br. 1994 September 1, 1994;76-B(5):701-12.

59. Cobb A, Schmalzreid T. The clinical significance of metal ion release from cobalt-chromium metal-on-metal hip joint arthroplasty. Proceedings of

the Institution of Mechanical Engineers, Part H: Journal of Engineering in Medicine. 2006;220(2):385-98.

60. Sargeant A, Goswami T. Hip implants - Paper VI - Ion concentrations. Materials & Design. 2007;28(1):155-71.

61. Doorn PF, Campbell PA, Worrall J, Benya PD, McKellop HA, Amstutz HC. Metal wear particle characterization from metal on metal total hip replacements: Transmission electron microscopy study of periprosthetic tissues and isolated particles. John Wiley & Sons, Inc.; 1998. p. 103-11.

62. Catelas I, Bobyn JD, Medley JB, Krygier JJ, Zukor DJ, Huk OL. Size, shape, and composition of wear particles from metal-metal hip simulator testing: Effects of alloy and number of loading cycles. Journal of Biomedical Materials Research - Part A. 2003;67(1):312-27.

63. Browne M, Gregson PJ. Metal ion release from wear particles produced by Ti-6Al-4V and Co-Cr alloy surfaces articulating against bone. Materials Letters. 1995;24:1-6.

64. Hanawa T. Metal ion release from metal implants. Materials Science and Engineering: C. 2004;24(6-8):745-52.

65. Metikos-Hukovic M, Pilic Z, Babic R, Omanovic D. Influence of alloying elements on the corrosion stability of CoCrMo implant alloy in Hank's solution. Acta Biomaterialia. 2006;2(6):693-700.

66. Hodgson AWE, Kurz S, Virtanen S, Fervel V, Olsson COA, Mischler S. Passive and transpassive behaviour of CoCrMo in simulated biological solutions. Electrochimica Acta. 2004;49(13):2167-78.

67. Sun D, Wharton J, Wood R. Micro- and Nano-scale Tribo-Corrosion of Cast CoCrMo. Tribology Letters. 2011;41(3):525-33.

68. Kocijan A, Milošev I, Pihlar B. Cobalt-based alloys for orthopaedic applications studied by electrochemical and XPS analysis. Journal of Materials Science: Materials in Medicine. 2004;15(6):643-50.

69. Williams J, editor. Engineering Tribology. 2nd Edition ed. Cambridge, UK: Cambridge University Press; 2005.

70. T.E T. The theory of partial elastohydrodynamic contacts. Wear. 1972;21(1):49-101.

71. Wellauer E, J. AGMA experience in establishing coordinated gear rating standards. Japan Society of Mechanical Engineers1967.

72. D. Dowson GRH. Elasto-hydrodynamic Lubrication the Fundamentals of Roller Gear Lubrication 1st ed. Sved G, editor: Pergamon Press; 1966.

73. B J Hamrock DD. Elastohydrodynamci lubrication of elliptical contacts for materials of low elastic modulus - I -fully flooded conjunction. Trans ASME, J Lubric Technol. 1978;100(2):236-45.

74. Dowson D. Tribological principles in metal-on-metal hip joint design. Proceedings of the Institution of Mechanical Engineers, Part H: Journal of Engineering in Medicine. 2006;220(2):161-71.

75. Jin ZM, Dowson D, Fisher J. Analysis of fluid film lubrication in artificial hip joint replacements with surfaces of high elastic modulus. Proceedings of the Institution of Mechanical Engineers, Part H (Journal of Engineering in Medicine). 1997;211(H3):247-56.

76. Yew A, Udofia I, Jagatia M, Jin ZM. Analysis of elastohydrodynamic lubrication in McKee-Farrar metal-on-metal hip joint replacement. Proceedings of the Institution of Mechanical Engineers, Part H (Journal of Engineering in Medicine). 2004;218(H1):27-34.

77. Jin ZM, Dowson D. A full numerical analysis of hydrodynamic lubrication in artificial hip joint replacements constructed from hard materials. Proceedings of the Institution of Mechanical Engineers, Part C: Journal of Mechanical Engineering Science. 1999 April 1, 1999;213(4):355-70.

78. Cooke AF, Dowson D, Wright V. The rheology of synovial fluid and some potential synthetic lubricants for degenerate synovial joints. Engineering in Medicine. 1978;7(2):66-72.

79. Dowson D, Jin ZM. Metal-on-metal hip joint tribology. Proceedings of the Institution of Mechanical Engineers, Part H: Journal of Engineering in Medicine. 2006;220(2):107-18.

80. Dowson D, Hardaker C, Flett M, Isaac GH. A hip joint simulator study of the performance of metal-on-metal joints: Part I: The role of materials. The Journal of Arthroplasty. 2004;19(8, Supplement):118-23.

81. Dowson D, McNie CM, Goldsmith AAJ. Direct experimental evidence of lubrication in a metal-on-metal total hip replacement tested in a joint simulator. Proceedings of the Institution of Mechanical Engineers, Part C: Journal of Mechanical Engineering Science. 2000 January 1, 2000;214(1):75-86.

82. Smith SL, Dowson D, Goldsmith AAJ. The effect of femoral head diameter upon lubrication and wear of metal-on-metal total hip replacements. Proceedings of the Institution of Mechanical Engineers, Part H: Journal of Engineering in Medicine. 2001 February 1, 2001;215(2):161-70.

83. McNie CM, Dowson D. The effect of radial clearance on lubrication in a metal on metal joint tested in a hip jointsimulator. Tribology Series. Volume 38: Elsevier; 2000. p. 341-5.

84. Jacobs MA, Schmidt MB, Farrar R. The effect of clearance and diameter on debris generation in a metal-on-metal hip. The Journal of Arthroplasty. 1998;13(2):224.

85. Dowson D, Hardaker C, Flett M, Isaac GH. A hip joint simulator study of the performance of metal-on-metal joints: Part II: Design. The Journal of Arthroplasty. 2004;19(8, Supplement):124-30.

86. Tipper JL, Firkins PJ, Ingham E, Fisher J, Stone MH, Farrar R. Quantitative analysis of the wear and wear debris from low and high carbon content cobalt chrome alloys used in metal on metal total hip replacements. Journal of Materials Science: Materials in Medicine. 1999;10(6):353-62.

87. Wimmer MA, Loos J, Nassutt R, Heitkemper M, Fischer A. The acting wear mechanisms on metal-on-metal hip joint bearings: in vitro results. Wear. 2001;250(1-12):129-39.

88. Yan Y, Neville A, Dowson D, Williams S, Fisher J. Tribo-corrosion analysis of wear and metal ion release interactions from metal-on-metal and ceramic-on-metal contacts for the application in artificial hip prostheses.

Proceedings of the Institution of Mechanical Engineers, Part J: Journal of Engineering Tribology. 2008;222(3):483-92.

89. Figueiredo-Pina CG, Yan Y, Neville A, Fisher J. Understanding the differences between the wear of metal-on-metal and ceramic-on-metal total hip replacements. Proceedings of the Institution of Mechanical Engineers, Part H: Journal of Engineering in Medicine. 2008;222(3):285-96.

90. Wang A, Yue S, Bobyn JD, Chan FW, Medley JB, editors. Surface characterization of metal-on-metal hip implants tested in a hip simulator1999; Atlanta, GA, USA: Elsevier S.A.

91. Scholes SC, Unsworth A. Pin-on-plate studies on the effect of rotation on the wear of metal-on-metal samples. Journal of Materials Science: Materials in Medicine. 2001;12(4):299-303.

92. Vassiliou K, Elfick APD, Scholes SC, Unsworth A. The effect of 'running-in' on the tribology and surface morphology of metal-on-metal Birmingham hip resurfacing device in simulator studies. Proceedings of the Institution of Mechanical Engineers, Part H (Journal of Engineering in Medicine). 2006;220(H2):269-77.

93. Salesky WF, Fisher RM, Ritchie RO, Thomas G. Nature and origin of sliding-wear debris from steels1983. Medium: X; Size: Pages: 41 p.

94. Sikorski ME. The adhesion of metals and factors that influence it. Wear. 1964 1964/4//;7(2):144-62.

95. Yan Y, Neville A, Dowson D. Biotribocorrosion - an appraisal of the time dependence of wear and corrosion interactions: I. The role of corrosion. Journal of Physics D: Applied Physics. 2006;39(15):3200-5.

96. Bowsher J, Hussain A, Williams P, Shelton J. Metal-on-metal hip simulator study of increased wear particle surface area due to 'severe' patient activity. Proceedings of the Institution of Mechanical Engineers, Part H: Journal of Engineering in Medicine. 2006;220(2):279-87.

97. Chan FW, Bobyn JD, Medley JB, Krygier JJ, Tanzer M. Wear and Lubrication of Metal-on-Metal Hip Implants. Clinical orthopaedics and related research. 1999;369:10-24.

98. Ishida T, Clarke IC, Donaldson TK, Shirasu H, Shishido T, Yamamoto K. Comparing ceramic-metal to metal-metal total hip replacements - A simulator study of metal wear and ion release in 32- and 38-mm bearings. Journal of Biomedical Materials Research - Part B Applied Biomaterials. 2009;91(2):887-96.

99. Yan Y, Neville A, Dowson D. Biotribocorrosion of CoCrMo orthopaedic implant materials Assessing the formation and effect of the biofilm. Tribology International. 2007 2007/12//;40(10-12):1492-9.

100. Liao Y, Pourzal R, Wimmer MA, Jacobs JJ, Fischer A, Marks LD. Graphitic Tribological Layers in Metal-on-Metal Hip Replacements. Science. 2011 Dec;334(6063):1687-90. PubMed PMID: WOS:000298344000062. English.

101. Wimmer MA, Fischer A, Büscher R, Pourzal R, Sprecher C, Hauert R, et al. Wear mechanisms in metal-on-metal bearings: The importance of tribochemical reaction layers. Journal of Orthopaedic Research. 2009;28(4):436-43.

102. Wimmer MA, Sprecher C, Hauert R, Täger G, Fischer A. Tribochemical reaction on metal-on-metal hip joint bearings: A comparison between in-vitro and in-vivo results. Wear. 2003 2003/9//;255(7-12):1007-14.

103. St. John KR, Zardiackas LD, Poggie RA. Wear evaluation of cobalt–chromium alloy for use in a metal-on-metal hip prosthesis. Journal of Biomedical Materials Research Part B: Applied Biomaterials. 2004;68B(1):1-14.

104. Yan Y, Neville A, Dowson D. Understanding the role of corrosion in the degradation of metal-on-metal implants. Proceedings of the Institution of Mechanical Engineers, Part H: Journal of Engineering in Medicine. 2006;220(2):173-80.

105. Dobbs HS, Robertson JLM. Heat treatment of cast Co-Cr-Mo for orthopaedic implant use. Journal of Materials Science. 1983;18(2):391-401.

106. Bowsher JG, Nevelos J, Williams PA, Shelton JC. 'Severe' wear challenge to 'as-cast' and 'double heat-treated' large-diameter metal-on-metal hip bearings. Proceedings of the Institution of Mechanical Engineers,

Part H: Journal of Engineering in Medicine. 2006 February 1, 2006;220(2):135-43.

107. Varano R, Bobyn JD, Medley JB, Yue S. The effect of microstructure on the wear of cobalt-based alloys used in metal-on-metal hip implants. Proceedings of the Institution of Mechanical Engineers, Part H: Journal of Engineering in Medicine. 2006 February 1, 2006;220(2):145-59.

108. Brown C, Williams S, Tipper J, Fisher J, Ingham E. Characterisation of wear particles produced by metal on metal and ceramic on metal hip prostheses under standard and microseparation simulation. Journal of Materials Science: Materials in Medicine. 2007;18(5):819-27.

109. Catelas I, Campbell PA, Bobyn JD, Medley JB, Huk OL. Wear particles from metal-on-metal total hip replacements: Effects of implant design and implantation time. Proceedings of the Institution of Mechanical Engineers, Part H: Journal of Engineering in Medicine. 2006;220(2):195-208.

110. Shahgaldi B, Heatley F, Dewar A, Corrin B. In vivo corrosion of cobalt-chromium and titanium wear particles. J Bone Joint Surg Br. 1995 November 1, 1995;77-B(6):962-6.

111. Fisher J, Hu XQ, Stewart TD, Williams S, Tipper JL, Ingham E, et al. Wear of surface engineered metal-on-metal hip prostheses. Journal of Materials Science: Materials in Medicine. 2004;15(3):225-35.

112. Fisher J, Hu XQ, Tipper JL, Stewart TD, Williams S, Stone MH, et al. An in vitro study of the reduction in wear of metal-on-metal hip prostheses using surface-engineered femoral heads. Proceedings of the Institution of Mechanical Engineers, Part H: Journal of Engineering in Medicine. 2002 April 1, 2002;216(4):219-30.

113. Ortega-Saenz JA, Alvarez-Vera M, Hernandez-Rodriguez MAL. Biotribological study of multilayer coated metal-on-metal hip prostheses in a hip joint simulator. 2013.

114. Leslie IJ, Williams S, Brown C, Anderson J, Isaac G, Hatto P, et al. Surface engineering: A low wearing solution for metal-on-metal hip surface replacements. Journal of Biomedical Materials Research - Part B Applied Biomaterials. 2009;90(2):558-65.

115. Stamm B, Kuzun B, Filipov O, Reuter S, Erdmann I, Deuerler F, et al. Adjustment of wear particle size distribution of DLC coatings for tribological metal-on-metal pairing in artificial hip joints. Materialwissenschaft und Werkstofftechnik. 2009;40(1-2):98-100.

116. Balagna C, Faga MG, Spriano S. Tantalum-based multilayer coating on cobalt alloys in total hip and knee replacement. Materials Science & Engineering: C (Materials for Biological Applications). 2012 05/01;32(4):887-95.

117. Brandt JM, Brière LK, Marr J, MacDonald SJ, Bourne RB, Medley JB. Biochemical comparisons of osteoarthritic human synovial fluid with calf sera used in knee simulator wear testing. Journal of Biomedical Materials Research Part A. 2010;94A(3):961-71.

118. Mazzucco D, Scott R, Spector M. Composition of joint fluid in patients undergoing total knee replacement and revision arthroplasty: correlation with flow properties. Biomaterials. 2004;25(18):4433-45.

119. He XM, Carter DC. Atomic structure and chemistry of human serum albumin. Nature. 1992;358(6383):209-15.

120. Myant C, Underwood R, Fan J, Cann PM. Lubrication of metal-on-metal hip joints: The effect of protein content and load on film formation and wear. Journal of the Mechanical Behavior of Biomedical Materials. 2011;6(0):30-40.

121. Heuberger MP, Widmer MR, Zobeley E, Glockshuber R, Spencer ND. Protein-mediated boundary lubrication in arthroplasty. Biomaterials. 2005;26(10):1165-73.

122. Roba M, Naka M, Gautier E, Spencer ND, Crockett R. The adsorption and lubrication behavior of synovial fluid proteins and glycoproteins on the bearing-surface materials of hip replacements. Biomaterials. 2009;30(11):2072-8.

123. Nakanishi Y, Murakami T, Higaki H. Adsorption control of synovia constituents on artificial joint materials by means of an electric field: evaluation of tribological characteristics. Proceedings of the Institution of

Mechanical Engineers, Part H: Journal of Engineering in Medicine. 2000;214(2):181-92.

124. Serro AP, Gispert MP, Martins MCL, Brogueira P, Colaço R, Saramago B. Adsorption of albumin on prosthetic materials: Implication for tribological behavior. Journal of Biomedical Materials Research Part A. 2006;78A(3):581-9.

125. Pradier CM, Costa D, Rubio C, Compère C, Marcus P. Role of salts on BSA adsorption on stainless steel in aqueous solutions. I. FT-IRRAS and XPS characterization. Surface and Interface Analysis. 2002;34(1):50-4.

126. Gispert MP, Serro AP, Colaço R, Saramago B. Bovine serum albumin adsorption onto 316L stainless steel and alumina: a comparative study using depletion, protein radiolabeling, quartz crystal microbalance and atomic force microscopy. Surface and Interface Analysis. 2008;40(12):1529-37.

127. Mavraki A, Cann PM. Friction and lubricant film thickness measurements on simulated synovial fluids. Proceedings of the Institution of Mechanical Engineers, Part J: Journal of Engineering Tribology. 2009;223(3):325-35.

128. Sawae Y, Yamamoto A, Murakami T. Influence of protein and lipid concentration of the test lubricant on the wear of ultra high molecular weight polyethylene. Tribology International. 2008;41(7):648-56.

129. Walker PS, Erkman MJ. Metal-on-metal lubrication in artificial human joints. Wear. 1972;21(2):377-92.

130. Widmer MR, Heuberger M, Vörös J, Spencer ND. Influence of polymer surface chemistry on frictional properties under protein-lubrication conditions: implications for hip-implant design. Tribology Letters. 2001;10(1):111-6.

131. Uyen HMW, Schakenraad JM, Sjollema J, Noordmans J, Jongebloed WL, Stokroos I, et al. Amount and surface structure of albumin adsorbed to solid substrata with different wettabilities in a parallel plate flow cell. Journal of Biomedical Materials Research. 1990;24(12):1599-614.

132. Fan J, Myant CW, Underwood R, Cann PM, Hart A. Inlet protein aggregation: a new mechanism for lubricating film formation with model

synovial fluids. Proceedings of the Institution of Mechanical Engineers, Part H: Journal of Engineering in Medicine. 2011 July 1, 2011;225(7):696-709.

133. Fan J, Myant C, Underwood R, Cann P. Synovial fluid lubrication of artificial joints: protein film formation and composition. Faraday Discussions. 2012;156(0):69-85.

134. Mishina H, Kojima M. Changes in human serum albumin on arthroplasty frictional surfaces. Wear. 2008;265(5-6):655-63.

135. Scholes S, Unsworth A. The Effects of Proteins on the Friction and Lubrication of Artificial Joints. Proceedings of the Institution of Mechanical Engineers, Part H: Journal of Engineering in Medicine. 2006;220(6):687-93.

136. Maskiewicz VK, Williams PA, Prates SJ, Bowsher JG, Clarke IC. Characterization of protein degradation in serum-based lubricants during simulation wear testing of metal-on-metal hip prostheses. Journal of Biomedical Materials Research - Part B Applied Biomaterials. 2010;94(2):429-40.

137. Crockett R, Roba M, Naka M, Gasser B, Delfosse D, Frauchiger V, et al. Friction, lubrication, and polymer transfer between UHMWPE and CoCrMo hip-implant materials: A fluorescence microscopy study. Journal of Biomedical Materials Research - Part A. 2009;89(4):1011-8.

138. Scholes SC, Unsworth A. Comparison of friction and lubrication of different hip prostheses. Proceedings of the Institution of Mechanical Engineers, Part H: Journal of Engineering in Medicine. 2000 January 1, 2000;214(1):49-57.

139. Scholes SC, Unsworth A, Goldsmith AAJ. A frictional study of total hip joint replacements. Physics in Medicine and Biology. 2000;45(12):3721.

140. Marsh H, Warburton AP. Catalysis of graphitisation. Journal of Applied Chemistry. 1970;20(4):133-42.

141. Krivoruchko OP, Zaikovskii VI. A new phenomenon involving the formation of liquid mobile metal-carbon particles in the low-temperature catalytic graphitisation of amorphous carbon by metallic Fe, Co and Ni. Mendeleev Communications. 1998;8(3):97-9.

142. Lavrakas V. Textbook errors: Guest column. XII: The lubricating properties of graphite. Journal of Chemical Education. 1957 2012/07/05;34(5):240.

143. Bryant PJ, Gutshall PL, Taylor LH. A study of mechanisms of graphite friction and wear. Wear. 1964 1964/2//;7(1):118-26.

144. Barril S, Mischler S, Landolt D. Influence of fretting regimes on the tribocorrosion behaviour of Ti6Al4V in 0.9 wt.% sodium chloride solution. Wear. 2004;256(9-10):963-72.

145. Yan Y, Neville A, Dowson D. Biotribocorrosion - an appraisal of the time dependence of wear and corrosion interactions: II. Surface analysis. Journal of Physics D: Applied Physics. 2006;39(15):3206-12.

146. Sun D. Abrasion-corrosion of Cast CoCrMo in Simulated Hip Joint Environments. 2009.

147. Sun D, Wharton JA, Wood RJK. Abrasive size and concentration effects on the tribo-corrosion of cast CoCrMo alloy in simulated body fluids. Tribology International. 2009;42(11-12):1595-604.

148. Sun D, Wharton JA, Wood RJK. Micro-abrasion-corrosion of cast CoCrMo: effects of micron and sub-micron sized abrasives. Wear. 2009;267(1-4):52-60.

149. Mathew M, Jacobs J, Wimmer M. Wear-Corrosion Synergism in a CoCrMo Hip Bearing Alloy Is Influenced by Proteins. Clinical Orthopaedics and Related Research. 2012;470(11):3109-17.

150. Yan Y, Neville A, Dowson D, Williams S, Fisher J. The influence of swing phase load on the electrochemical response, friction, and ion release of metal-on-metal hip prostheses in a friction simulator. Proceedings of the Institution of Mechanical Engineers, Part J: Journal of Engineering Tribology. 2009;223(3):303-9.

151. Yan Y, Neville A, Dowson D, Williams S, Fisher J. Effect of metallic nanoparticles on the biotribocorrosion behaviour of Metal-on-Metal hip prostheses. Wear. 2009;267(5-8):683-8.

152. Landolt D, Mischler S, Stemp M, Barril S. Third body effects and material fluxes in tribocorrosion systems involving a sliding contact. Wear. 2004;256(5):517-24.

153. Goldberg JR, Gilbert JL. The electrochemical and mechanical behavior of passivated and TiN/AlN-coated CoCrMo and Ti6Al4V alloys. Biomaterials. 2004;25(5):851-64.

154. Goldberg JR, Gilbert JL. In vitro corrosion testing of modular hip tapers. Journal of Biomedical Materials Research Part B: Applied Biomaterials. 2003;64B(2):78-93.

155. Hertz H. On the contact of elastic solids. J reine angew Math. 1881;92(156-171):110.

156. Hickling A. Studies in electrode polarisation. Part IV.-The automatic control of the potential of a working electrode. Transactions of the Faraday Society. 1942;38:27-33.

157. Mischler S. Triboelectrochemical techniques and interpretation methods in tribocorrosion: A comparative evaluation. Tribology International. 2008;41(7):573-83.

158. Ponthiaux P, Wenger F, Drees D, Celis JP. Electrochemical techniques for studying tribocorrosion processes. Wear. 2004;256(5):459-68.

159. Stern M, Geary AL. Electrochemical polarization. Electrochemical Society -- Journal. 1957;104(1):56-63.

160. Pourbaix M. Atlas of Electrochemical Equilibria in Aqeuous Solutions. First English ed. Oxford: Pergamon Press; 1966.

161. Yan Y, Neville A, Dowson D. Tribo-corrosion properties of cobalt-based medical implant alloys in simulated biological environments. Wear. 2007;263(7-12):1105-11.

162. Garcia EM, Santos JS, Pereira EC, Freitas MBJG. Electrodeposition of cobalt from spent Li-ion battery cathodes by the electrochemistry quartz crystal microbalance technique. Journal of Power Sources. 2008;185(1):549-53.

163. Paul JP. Paper 8: Forces Transmitted by Joints in the Human Body. Proceedings of the Institution of Mechanical Engineers, Conference Proceedings. 1966 June 1, 1966;181(10):8-15.

164. Unsworth A. Tribology of artificial hip joints. Proceedings of the Institution of Mechanical Engineers, Part J: Journal of Engineering Tribology. 2006;220(8):711-8.

165. Makinson KR, Tabor D. Friction and transfer of polytetrafluoroethylene. Royal Society -- Proceedings Series A. 1964;281(1384):49-61.

166. Sun D, Wharton JA, Wood RJK, Ma L, Rainforth WM. Microabrasion-corrosion of cast CoCrMo alloy in simulated body fluids. Tribology International. 2009;42(1):99-110.

167. Williams RL, Brown SA, Merritt K. Electrochemical studies on the influence of proteins on the corrosion of implant alloys. Biomaterials. 1988;9(2):181-6.

168. http://www.spineuniverse.com/anatomy/anatomical-planes-body. Anatomical Planes of the Body 2012 [cited 2012 October]. Available from: http://www.spineuniverse.com/anatomy/anatomical-planes-body.

169. Brydson R. Electron Energy Loss Spectroscopy: BIOS Scientific Publishers Limited; 2001.

170. Daniels H, Brown A, Scott A, Nichells T, Rand B, Brydson R. Experimental and theoretical evidence for the magic angle in transmission electron energy loss spectroscopy. Ultramicroscopy. 2003;96:523-34.

171. Yao JQ, Laurent MP, Johnson TS, Blanchard CR, Crowninshield RD. The influences of lubricant and material on polymer/CoCr sliding friction. Wear. 2003 2003/9//;255:780-4.

172. Wang F, Jin Z. Transient Elastohydrodynamic Lubrication of Hip Joint Implants. Journal of Tribology. 2008;130(1):011007-11.

173. Meng QingEn; Gao LeiMing LF, Yang PeiRan, Fisher J, Jin ZhongMin. Transient elastohydrodynamic lubrication analysis of a novel

metal-on-metal hip prosthesis with an aspherical acetabular bearing surface. Journal of Medical Biomechanics. 2009;24(5):352-62.

174. Gao LM, Meng QE, Wang FC, Yang PR, Jin ZM. Comparison of numerical methods for elastohydrodynamic lubrication analysis of metal-on-metal hip implants: Multi-grid verses Newton-Raphson. Proceedings of the Institution of Mechanical Engineers, Part J: Journal of Engineering Tribology. 2007 February 1, 2007;221(2):133-40.

175. H VC. Multigrid solution of the EHL line and point contact problems. Twente: University of Twente; 1991.

176. Papageorgiou N, Mischler S. Electrochemical Simulation of the Current and Potential Response in Sliding Tribocorrosion. Tribology Letters.48(3):271-83.

177. Yan Y, Neville A, Dowson D, Williams S, Fisher J. Electrochemical instrumentation of a hip simulator: a new tool for assessing the role of corrosion in metal-on-metal hip joints. Proceedings of the Institution of Mechanical Engineers, Part H (Journal of Engineering in Medicine). 2010;224(H11):1267-73.

178. Dolatshahi-Pirouz A, Rechendorff K, Hovgaard MB, Foss M, Chevallier J, Besenbacher F. Bovine serum albumin adsorption on nano-rough platinum surfaces studied by QCM-D. Colloids and surfaces B, Biointerfaces. 2008;66(1):53-9.

179. Rechendorff K, Hovgaard MB, Foss M, Zhdanov VP, Besenbacher F. Enhancement of Protein Adsorption Induced by Surface Roughness. Langmuir. 2006 2012/09/26;22(26):10885-8.

180. Johnson KL, Greenwood JA, Poon SY. A simple theory of asperity contact in elastohydro-dynamic lubrication. Wear. 1972;19(1):91-108.

181. Ouerd A, Alemany-Dumont C, Normand B, Szunerits S. Reactivity of CoCrMo alloy in physiological medium: Electrochemical characterization of the metal/protein interface. Electrochimica Acta. 2008;53(13):4461-9.

182. Yang J, Black J. Competitive binding of chromium, cobalt and nickel to serum proteins. Biomaterials. 1994;15(4):262-8.

183. Pourzal R, Theissmann R, Morlock M, Fischer A. Micro-structural alterations within different areas of articulating surfaces of a metal-on-metal hip resurfacing system. Wear. 2009;267(5-8):689-94.

184. Pourzal R, Theissmann R, Williams S, Gleising B, Fisher J, Fischer A. Subsurface changes of a MoM hip implant below different contact zones. Journal of the Mechanical Behavior of Biomedical Materials. 2009;2(2):186-91.

185. McCulloch DG, McKenzie DR, Prawer S, Merchant AR, Gerstner EG, Kalish R. Ion beam modification of tetrahedral amorphous carbon: the effect of irradiation temperature. Diamond and Related Materials. 1997;6(11):1622-8.

186. Davis CA, Knowles KM, Amaratunga GAJ. Cross-sectional structure of tetrahedral amorphous carbon thin films. Surface and Coatings Technology. 1995;76-77, Part 1(0):316-21.

187. Zhang Z-l, Brydson R, Aslam Z, Reddy S, Brown A, Westwood A, et al. Investigating the structure of non-graphitising carbons using electron energy loss spectroscopy in the transmission electron microscope. Carbon. 2011;49(15):5049-63.

188. Pittman ED, Ovenshine AT. Pebble morphology in the Merced River (California). Sedimentary Geology. 1968;2(2):125-40.

189. Schumm SA, Stevens MA. Abrasion in Place: A Mechanism for Rounding and Size Reduction of Coarse Sediments in Rivers. Geology. 1973 January, 1973;1(1):37-40.

190. Yue GH, Yan PX, Liu JZ, Fan XY, Zhuo RF. Fabrication, structure, magnetic properties of highly ordered cobalt disulfide nanowire arrays. Applied Physics Letters. 2005;87(26):262505-3.

191. Galtayries A, Grimblot J. Formation and electronic properties of oxide and sulphide films of Co, Ni and Mo studied by XPS. Journal of Electron Spectroscopy and Related Phenomena. 1999;98-99:267-75.

192. Vieira AC, Rocha LA, Papageorgiou N, Mischler S. Mechanical and electrochemical deterioration mechanisms in the tribocorrosion of Al alloys in NaCl and in NaNO3 solutions. Corrosion Science. 2012;54(0):26-35.

193. D. Dowson PSW, M.D. Longfield, V. Wright. A Joint Simulator Machine For Load-Bearing Joints. Medical and Biological Engineering. 1970;8:37-43.

194. P. Walker DD, M. Longfield, V. Wright. A Joint Simulator. Annals of the Rheumatic Diseases 1968;27(503):104-9.

195. I. Duff-Barclay DTS. Total Human Hip Joint Prostheses - A Laboratory Study of Friction and Wear. Proceedings of the Institution of Mechanical Engineers. 1967;181(3):90-103.

196. Dowson D, Jobbins B. Design and Development of a Versatile Hip Joint Simulator and a Preliminary Assessment of Wear and Creep in Charnley Total Replacement Hip Joints. Engineering in Medicine. 1988 July 1, 1988;17(3):111-7.

197. J. Scales PK, D. Goddard, editor. Lubrication and Wear in Joints. London: Sector Publishing Limited; 1969.

198. Firkins PJ, Tipper JL, Saadatzadeh MR, Ingham E, Stone MH, Farrar R, et al. Quantitative analysis of wear and wear debris from metal-on-metal hip prostheses tested in a physiological hip joint simulator. Bio-Medical Materials and Engineering. 2001;11(2):143-57.

199. Williams S, Stewart TD, Ingham E, Stone MH, Fisher J. Metal-on-metal bearing wear with different swing phase loads. Journal of Biomedical Materials Research Part B: Applied Biomaterials. 2004;70B(2):233-9.

200. Stewart TD, Tipper JL, Insley G, Streicher RM, Ingham E, Fisher J. Long-term wear of ceramic matrix composite materials for hip prostheses under severe swing phase microseparation. Journal of Biomedical Materials Research Part B: Applied Biomaterials. 2003;66B(2):567-73.

201. Nevelos J, Ingham E, Doyle C, Streicher R, Nevelos A, Walter W, et al. Microseparation of the centers of alumina-alumina artificial hip joints during simulator testing produces clinically relevant wear rates and patterns. The Journal of Arthroplasty. 2000;15(6):793-5.

202. Mathew MT, Runa MJ, Laurent M, Jacobs JJ, Rocha LA, Wimmer MA. Tribocorrosion behavior of CoCrMo alloy for hip prosthesis as a function

of loads: A comparison between two testing systems. Wear. 2010;271(9-10):1210-9.

203. Hodgson AW, Mischler S, Von Rechenberg B, Virtanen S. An analysis of the in vivo deterioration of Co-Cr-Mo implants through wear and corrosion. Proceedings of the Institution of Mechanical Engineers, Part H (Journal of Engineering in Medicine). 2007;221(H3):291-303.

204. Lu BT, Luo JL, Mohammadi F, Wang K, Wan XM. Correlation between repassivation kinetics and corrosion rate over a passive surface in flowing slurry. Electrochimica Acta. 2008;53(23):7022-31.

205. Kim JD, Pyun SI. The effects of applied potential and chloride ion on the repassivation kinetics of pure iron. Corrosion Science. 1996;38(7):1093-102.

206. Stack MM, Abdulrahman GH. Mapping erosion-corrosion of carbon steel in oil exploration conditions: Some new approaches to characterizing mechanisms and synergies. Tribology International. 2010;43(7):1268-77.

207. Stack MM, Pungwiwat N. Erosion-corrosion mapping of Fe in aqueous slurries: some views on a new rationale for defining the erosion-corrosion interaction. Wear. 2004;256(5):565-76.

208. Karimi S, Nickchi T, Alfantazi A. Effects of bovine serum albumin on the corrosion behaviour of AISI 316L, Co-28Cr-6Mo, and Ti-6Al-4V alloys in phosphate buffered saline solutions. Corrosion Science. 2011;53(10):3262-72.

209. Williams DF, Clark GCF. The corrosion of pure cobalt in physiological media. Journal of Materials Science. 1982;17(6):1675-82.

210. Karimi S, Nickchi T, Alfantazi AM. Long-term corrosion investigation of AISI 316L, Co28Cr6Mo, and Ti6Al4V alloys in simulated body solutions. Applied Surface Science. 2012;258(16):6087-96.

211. Hoar TP, Mears DC. Corrosion-Resistant Alloys in Chloride Solutions: Materials for Surgical Implants. Proceedings of the Royal Society of London Series A Mathematical and Physical Sciences. 1966 October 18, 1966;294(1439):486-510.

212. Cong-Truyen D, Seonghun P, editors. Tribological Response of Cobalt-Chromium Femoral Head under Lubrication of Bovine Serum Albumin2010; Berlin, Germany: Springer Verlag.

213. Derbyshire FJ, Presland AEB, Trimm DL. Graphite formation by the dissolution-precipitation of carbon in cobalt, nickel and iron. Carbon. 1975;13(2):111-3.

214. Irving SM, Walker Jr PL. Interaction of evaporated carbon with heated metal substrates. Carbon. 1967;5(4):399-402.

215. Manning MP, Garmirian JE, Reid RC. Carbon deposition studies using nickel and cobalt catalysts. Industrial & Engineering Chemistry Process Design and Development. 1982 2012/10/19;21(3):404-9.

216. Bergmann G, Graichen F, Rohlmann A, Verdonschot N, van Lenthe GH. Frictional heating of total hip implants, Part 1: measurements in patients. Journal of Biomechanics. 2001;34(4):421-8.

217. Kuhlmann-Wilsdorf D. Demystifying flash temperatures II. First-order approximation for plastic contact spots. Materials Science and Engineering. 1987;93(0):119-33.

218. Kuhlmann-Wilsdorf D. Demystifying flash temperatures I. Analytical expressions based on a simple model. Materials Science and Engineering. 1987;93(0):107-18.

219. Wilks KR, Mastalerz M, Bustin RM, Ross JV. The role of shear strain in the graphitization of a high-volatile bituminous and an anthracitic coal. International Journal of Coal Geology. 1993;22(3-4):247-77.

220. Pertsin A, Grunze M. Waterâˆ’Graphite Interaction and Behavior of Water Near the Graphite Surface. The Journal of Physical Chemistry B. 2003 2012/10/19;108(4):1357-64.

221. Ferrari AC, Rodil SE, Robertson J. Interpretation of infrared and Raman spectra of amorphous carbon nitrides. Physical Review B. 2003;67(15):155306.

222. Johnson KL. Contact Mechanics: Cambridge University Press; 1985.